SLAC-R-918
March 2009

GRADUATE COURSE IN PHYSICS
UNIVERSITY OF PISA

The School of Graduate Studies in Basic Sciences 'GALILEO GALILEI'

Ph.D. Thesis:

Search for lepton flavour violating decays $\tau \to l K^0_S$ with the *BABAR* detector

Candidate:
Riccardo Cenci

Supervisor:
Prof. Francesco Forti

SLAC National Accelerator Laboratory, Menlo Park, Ca 94025

Work supported in part by US Department of Energy contract DE-AC02-76SF00515

Printed on January 29, 2009 using LaTeX 2ε

2 Kt

Contents

Introduction

The Standard Model of fundamental interactions has proven to be one of most precise verified physical theories of all times. Nonetheless, it is clear that extensions to the Standard Model are required to provide a satisfactory explanation of fundamental questions such as how fermion masses and generations arise and what dark matter is made. Evidence for new physics can be seen in the direct production and observation of new particles, by increasing the beam energy above the production threshold, but also by looking for the effects of these new particles in loop diagrams, by precision measurements performed at high luminosity machines.

Searching of processes involving flavour changing neutral currents transitions of charged leptons is promising. Neutrino physics provides unambiguous evidence for non-conservation of lepton flavour [1, 2]. We therefore expect this phenomenon to also occur in the charged lepton sector, although there is not yet experimental evidence. Current experimental searches look for different processes that involves lepton flavour violation (e. g. μ decays, μ/e conversion and τ decays) and more results are expected in the coming years (e. g. from the MEG experiment [3]).

Considering lepton flavour violation in τ decays, if the light neutrino mass matrix (m_ν) is the only source of this violation, flavour changing neutral currents transitions of charged leptons occur well below any realistic experimental sensitivity (with a branching fraction smaller than 10^{-14} for $\tau \to \mu ll$) [4]. Any occurrence of these decays with a higher branching fraction would be a clear sign of new physics. In many extensions of the Standard Model, the parameters space allows for lepton flavour violation τ decays just below the present experimental bounds. Rare flavour changing neutral current decays of the τ lepton are particularly interesting since lepton flavour violation sources involving the third generation are naturally the largest. Many theories beyond the Standard Model allow for $\tau \to l\gamma$ and $\tau \to lll$ decays, where $l = e, \mu$, at a level between 10^{-7} and 10^{-10}. Examples are:

- Little Higgs model with T-Parity;
- supersymmetric extension of Standard Model with additional heavy right-handed neutrinos, introduced via the seesaw mechanism, or R-parity violation;
- grand unification theory, such as minimal $SU(5)$;

- supersymmetric models with Higgs exchange.

According to some of these models, semi-leptonic neutrino-less decays involving pseudo-scalar mesons like $\tau \to lP^0$ where $P^0 = \pi^0, \eta, \eta'$ may be enhanced over $\tau \to lll$ decays. We will give a brief description of them in Chap. 1.

Most of the predictions for lepton flavour violation processes from these theories are within the experimental reach, but even if lepton flavour violation is observed in one channel, it would be difficult to discriminate between the various models. We need also the ratio of branching fractions to clearly distinguish between them. Therefore, each single decay mode is important. Also, if lepton flavour violation processes are not observed, it is useful to improve any upper limit to shrink the theoretical parameters phase space of Standard Model extensions or exclude completely some of them.

Currently the B-factories have the highest sensitivity to the very rare τ decays because of the highest available data sample of clean τ events ($\sim$ 1 billion of τ pairs in total). The purpose of this work is to search for $\tau \to lK^0_S$ decay using an integrated luminosity of $469\,\text{fb}^{-1}$ collected by the *BABAR* experiment. The present best upper limit at 90% confidence level has been published by the Belle Collaboration using a sample of 281 fb^{-1}: $\mathcal{B}(\tau \to eK^0_S) < 5.6 \times 10^{-8}$ and $\mathcal{B}(\tau \to \mu K^0_S) < 4.9 \times 10^{-8}$ [5]. Our upper limit estimations, at the same confidence level, are: $\mathcal{B}(\tau \to eK^0_S) < 3.3 \times 10^{-8}$ and $\mathcal{B}(\tau \to \mu K^0_S) < 4.0 \times 10^{-8}$, an improvement with respect to the previous result.

Other activities performed during Ph.D. period

During the Ph.D. period, aside from the analysis activity described in this thesis, I have also taken part in other activities of the Pisa *BABAR* group. The group, in addition to the responsibility of the *BABAR* silicon vertex tracker, is involved in an R&D project for a new pixel silicon detector to be used in a future flavour physics experiment at high luminosity [6]. I have personally participated in both activities.

During 2004, using a finite element simulation with the ISE-TCAD software, I have studied different configurations of the new silicon detectors to maximize the charge collection [7]. During 2005, 2007 and 2008 I spent most of the time at the Stanford Linear Accelerator Center working on the silicon vertex tracker of the *BABAR* experiment, responsible for operations and data monitoring. Further details on the activities performed there will be given at the end of Sec. 2.9.

Chapter 1

Lepton Flavour Violation in τ Decays

In this chapter we give a brief overview of various theoretical models that allow for lepton flavour violation (LFV) τ decays at a rate close to the present experimental limits and summarize available theoretical estimations for $\tau \to lK_s^0$ decay channel. A more complete review and other references about LFV in general can be found in [8]. Then we review the most recent experimental results in searching LFV decay of τ lepton and present an overview of our analysis to search for $\tau \to lK_s^0$ decay. In this chapter the charge for particles is irrelevant and then omitted.

1.1 Overview of theoretical models that allow LFV interactions

1.1.1 Little Higgs models

A group of non-super-symmetric models that include LFV processes are Little Higgs models. One of the most attractive is the Littlest Higgs model [9] with T-parity (LHT). The model is based on a two-stage spontaneous symmetry breaking occurring at the scale $f \gtrsim 500\,\text{GeV}$ and the electroweak scale v. The additional introduced gauge bosons, fermions and scalars are sufficiently light enough to be discovered at LHC and this models include also a dark matter candidate. While the models without T-parity show results close to the Standard Model (SM) predictions, a very different situation is expected in the LHT model, where the presence of new flavour violating interactions and mirror leptons with masses of order 1 TeV can change the SM expectations by up to 45 orders of magnitude, bringing the relevant branching fractions for LFV processes close to the bounds available presently or in the near future.

While the possible enhancements of LFV branching fractions in the LHT model are interesting, such effects are common in many other new physics models, such as the minimal super-symmetric SM, and therefore cannot be used to distinguish between them. How-

ever, correlations between various branching fractions should allow a clear distinction of the LHT model from the minimal super-symmetric SM (MSSM). Any difference between these ratios of branching fractions (BFs) from the predictions of the MSSM or the LHT model could confirm one model and exclude the other one. Of particular interest are the ratios $\mathcal{B}(l_i \to eee)/\mathcal{B}(l_i \to e\gamma)$, where $l_i = \tau, \mu$, that are $\mathcal{O}(1)$ in the LHT model but strongly suppressed in super-symmetric models even in the presence of significant Higgs contributions. As shown in Fig. 1.1, assuming $f = 1\,\text{TeV}$, scenarios with LHT and MSSM contributions (blue dots) and with only MSSM (red dots) can be easily distinguished [10].

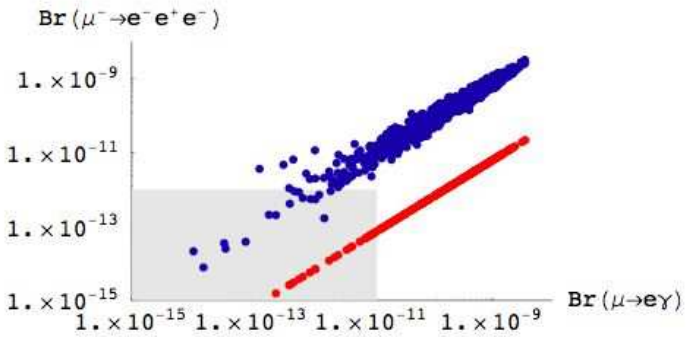

Figure 1.1: Correlation between $\mathcal{B}(\mu \to e\gamma)/\mathcal{B}(\mu \to eee)$ in the LHT model (blue dots). The red dots represents the dominant contribution in the MSSM. The gray region is allowed by the present experimental bounds.

The existing constraints on LFV τ decays are still relatively weak, so that they presently do not provide a useful constraint on the LHT parameter space. However most BFs in the LHT model, after imposing the constraints on $\mu \to e\gamma$ and $\mu \to eee$, can reach the present experimental upper bounds and are very interesting in view of forthcoming experiments.

1.1.2 Super-symmetric extension of Standard Model

In the low energy SUSY extensions of the SM the flavour and CP-violating (CPV) interactions would originate from the misalignment between fermion and sfermion mass eigenstates. Understanding why all these processes are strongly suppressed is one of the major problems of low energy SUSY. The absence of deviations from the SM predictions in LFV and CPV (and other flavour changing processes in the quark sector) experiments suggests the presence of a small amount of fermion-sfermion misalignment.

Assuming a see-saw mechanism with three heavy right-handed neutrinos, the effective light-neutrino mass matrix and its misalignment depend on Yukawa couplings between left- and right-handed neutrinos, the latter being a potentially large source of LFV. A complete determination of LFV interactions magnitude would require a complete knowledge

of the neutrino Yukawa matrix which is not possible using only low-energy observables from the neutrino sector. This is in contrast with the quark sector, where Yukawa couplings are completely determined in terms of quark masses and CKM matrix elements. As a result, the predictions of flavour changing neutral current effects in the lepton sector usually have sizable uncertainties.

Making assumptions on neutrino mass matrices, we can reduce the number of free parameters and estimate some BFs for LFV decays. In the case of degenerate heavy neutrino masses, the LFV observables depend mainly on the orthogonal matrix R [11]. R can be parametrized using three complex mixing angles written as $\theta_j = x_j + iy_j$, with $j = 1, 2, 3$. The BFs for $\mu \to e\gamma$ and $\tau \to \mu\gamma$ are shown in Fig. 1.2 for a hierarchical and degenerate light neutrino masses versus y. The typical mass for heavy neutrinos is $M_R = 10^{12}\,\text{GeV}$ and x_j's are assumed scattered over $0 < x_j < 2\pi$.

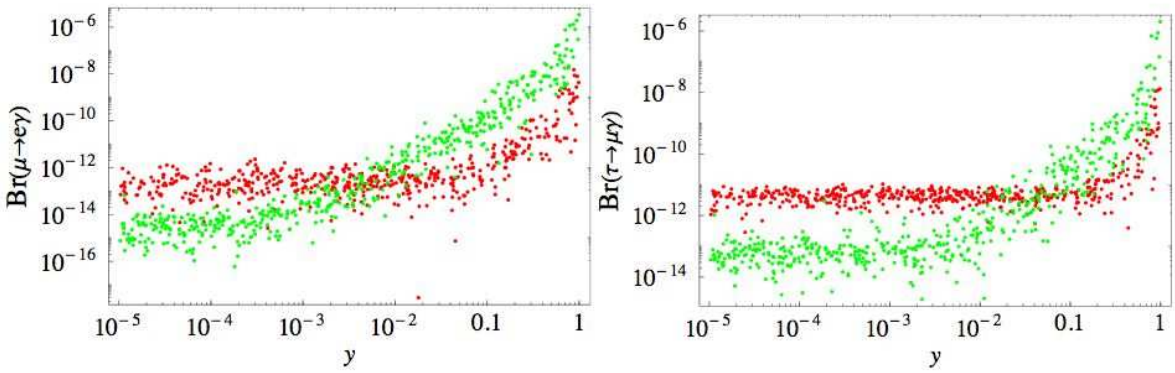

Figure 1.2: Degenerate heavy neutrinos: LFV branching fraction versus y for fixed $M_R = 10^{12}\,\text{GeV}$ for hierarchical (dark red) and degenerate (light green) light neutrino masses.

Instead, in case of hierarchical spectrum of heavy Majorana neutrinos, $M_1 \ll M_2 \ll M_3$, taking $M_1 = 10^{10}$ and $x_2 \sim x_3 \sim n \cdot \pi$, experimental bounds on $\mathcal{B}(\mu \to e\gamma)$ can be used to constrain the heavy neutrino scale, here represented by the heaviest right handed neutrino mass M_3 [12], as shown in Fig. 1.3.

Quantitatively, the present bound on $\mathcal{B}(\mu \to e\gamma)$ already constrains M_3 to be smaller than $\approx 10^{13}\,\text{GeV}$, while the MEG experiment at PSI is sensitive to $M_3 \leq \mathcal{O}(10^{12})\,\text{GeV}$.

A more precise estimation could be done for the ratio between different LFV observables. Consequently, bounds on one LFV decay channel (process) will limit the parameter space of the LFV mechanism and thus lead to bounds on the other LFV decay channels (processes). In Fig. 1.4, the correlation induced by the type I seesaw mechanism between $\mathcal{B}(\mu \to e\gamma)$ and $\mathcal{B}(\tau \to \mu\gamma)$ is shown, and the bounds induced by the former on the latter can be easily read off.

Interestingly, these bounds do not depend on whether hierarchical or quasi-degenerate heavy and light neutrinos are assumed. Note that the present upper bound on $\mathcal{B}(\mu \to e\gamma)$

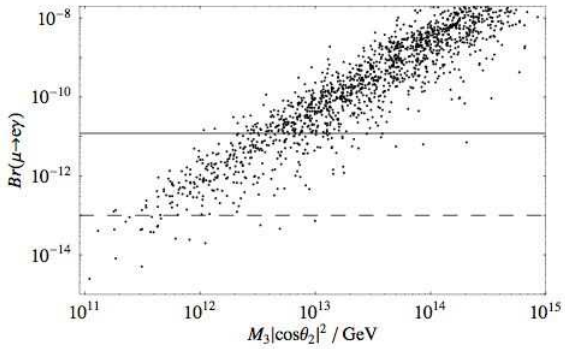

Figure 1.3: $\mathcal{B}(\mu \to e\gamma)$ vs $M_3|cos(\theta_2)|^2$ in case of hierarchical spectrum of heavy Majorana neutrinos for $M_1 = 10^{10}\,\text{GeV}$ and $x_2 \approx x_3 \approx n \cdot \pi$. All other seesaw parameters are scattered in their allowed ranges for hierarchical light and heavy neutrinos. The solid (dashed) line indicates the present (expected future) experimental sensitivity.

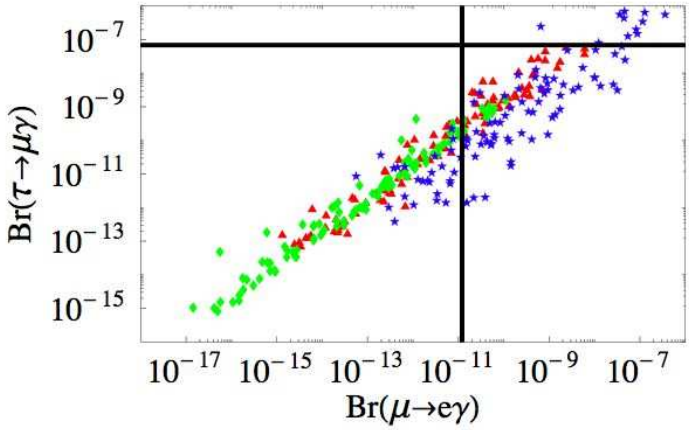

Figure 1.4: $\mathcal{B}(\tau \to \mu\gamma)$ versus $\mathcal{B}(\mu \to e\gamma)$ in MSSM scenario, with neutrino parameters scattered within their experimentally allowed ranges [13]. For quasi-degenerate heavy neutrino masses, both hierarchical (triangles) and quasi-degenerate (diamonds) light neutrino masses are considered with real R and $1011\,\text{GeV} < M_R < 1014.5\,\text{GeV}$. In the case of hierarchical heavy and light neutrino masses (stars), the x_i are scattered over their full ranges $0 < x_i < 2\pi$ and the y_i and M_i are scattered within the bounds demanded by leptogenesis and perturbativity. Also indicated are the present experimental bounds $\mathcal{B}(\mu \to e\gamma) < 1.2 \times 10^{-11}$ and $\mathcal{B}(\tau \to \mu\gamma) < 6.8 \times 10^{-8}$ [14, 15].

implies a stronger constraint on $\mathcal{B}(\tau \to \mu\gamma)$ than its expected future bound ($\mathcal{O}(10^{-9})$). The above results were derived in the simplifying case of a real R matrix. If the $\mu \to e\gamma$ and $\tau \to \mu\gamma$ decays will be observed, the ratio of interest can give unique information on the origin of the lepton flavour violation.

1.1.3 Super-symmetric grand unified theories

Other predictions for LFV processes can be obtained by embedding the SUSY model within a grand unified theory (GUT), such as minimal $SU(5)$, which incorporate the triplet see-saw mechanism. Using a minimal $SU(5)$ GUT, a very predictive scenario can be obtained with only three free parameters: the triplet mass M_T, the effective SUSY breaking scale B_T and the coupling constant λ [16, 17]. The phenomenological predictions more important and relevant for LHC, the B-factories, the incoming MEG experiment or the forecast Super Flavour factory, concern the sparticle and Higgs boson spectra and the LFV decays. The ratio of BFs for the radiative decays are $\mathcal{B}(\tau \to \mu\gamma)/\mathcal{B}(\mu \to e\gamma) \sim 300$ and $\mathcal{B}(\tau \to e\gamma)/\mathcal{B}(\mu \to e\gamma) \sim 0.2$ with the neutrino mixing parameter $\theta_{13} = 0$. If $\theta_{13} = 0.2$, the two ratios became ~ 2 and ~ 0.1 respectively. The other LFV processes are also correlated to the radiative ones in a model-independent way, as shown in Fig. 1.5.

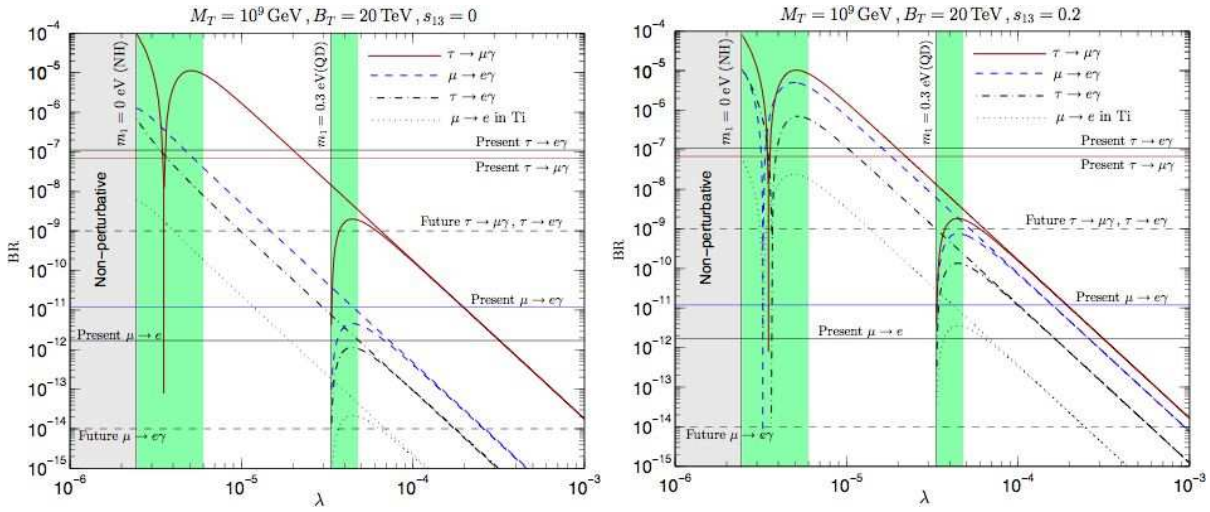

Figure 1.5: Branching fractions of several LFV processes as a function of λ according a minimal $SU(5)$ GUT model. The left (right) vertical line indicates the lower bound on λ imposed by requiring perturbativity of the Yukawa couplings $Y_{T,S,Z}$. The regions in green(grey) are excluded by the perturbativity requirement.

1.1.4 R-parity violation

In SUSY extensions of the SM, baryon and lepton numbers are no longer automatically protected. This is the main reason for introducing R-parity. The R quantum number is defined as $R = (-1)^{3B+L+2S}$, where B, L and S stand for baryon, lepton number and spin of the field, respectively. This ensures $R = +1$ for all particles and $R = -1$ for all super-particles, and conservation of R implies that super-particles must occur in pairs in all allowed Feynman vertexes. However, R parity is a discrete symmetry imposed by hand (to make the parameters space of the model more restricted and tractable) and in the

absence of R parity odd terms allowed by renormalizability and gauge invariance must be included in the super-potential of MSSM,

$$W = \frac{1}{2}\lambda_{ijk} L_i L_j E^c_k + \lambda'_{ijk} L_i Q_j D^c_k + \frac{1}{2}\lambda''_{ijk} U^c_i D^c_j D^c_k, \tag{1.1}$$

where there is summation over the generation indexes $i, j, k = 1, 2, 3$, and summation over gauge indexes is understood. L, Q, U, D and E denote, respectively, $SU(2)_L$ doublet lepton and quark super-fields, and $SU(2)_L$ singlet up, down, and charged lepton super-fields. With many new couplings (which can theoretically be complex) the phenomenology is immensely richer, but at the same time less predictive. In addition, while R-conserving effects can affect low-energy processes only through loops, the R-violating ones can show up in tree-level slepton o squark mediated processes, competing with the SM. In LFV case, the processes are forbidden in the SM and it can be taken only the amplitude that comes from R parity violating (RPV) SUSY, ignoring R-conserving effects and further coupling phases. For this model we do not have predictions for LFV processes but mostly upper limits on the trilinear couplings λ_{ijk}, λ'_{ijk} and λ''_{ijk} [18].

1.1.5 Higgs-mediated lepton flavour violation in super-symmetry

An independent (and potentially large) class of LFV contributions to rare decays comes also from the Higgs sector: if the slepton mass matrices have LFV entries and the effective Yukawa interaction includes non-holomorphic couplings, Higgs-mediated LFV amplitudes are necessarily induced [19]. Interestingly enough, gauge- and Higgs-mediated LFV amplitudes lead to very different correlations among LFV processes [19–23].

SM extensions containing more than one Higgs doublet generally allow flavor-violating couplings of the neutral Higgs bosons with fermions. Such couplings, if unsuppressed, will lead to large flavor-changing neutral currents in direct opposition to experiments. The possible solution to this problem involves an assumption about the Yukawa structure of the model. A discrete symmetry can be invoked to allow a given fermion type to couple to a single Higgs doublet, and in such a case flavour changing neutral currents are absent at tree level. While processes like $l_i \to l_j\gamma$ can be mediated only by a one or more loop Higgs exchange, $l_i \to l_j l_k l_k$ ones receive contribution also from tree level exchange. However, if the main two loop contribution in $l_i \to l_j\gamma$ arise from the exchange of a W boson, it becomes larger than one loop term and increases the BF over the $l_i \to l_j l_k l_k$ one, as shown in Fig. 1.6.

Again, only the correlations among the rates of the above processes are the signature of the Higgs-mediated LFV and allow us to discriminate between different SUSY scenarios.

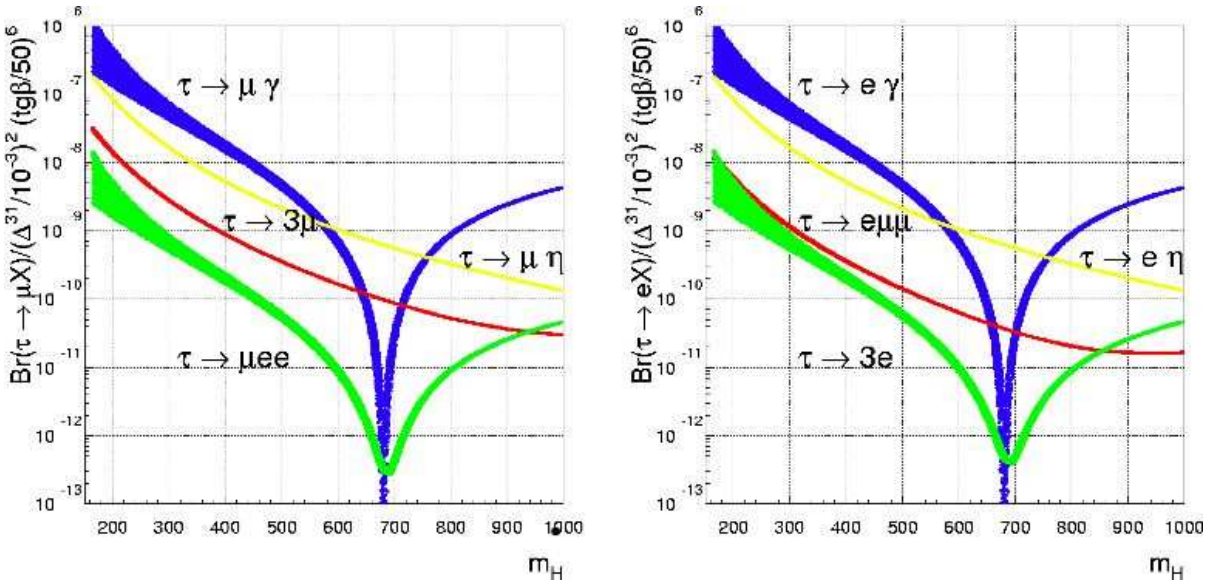

Figure 1.6: Branching fractions of various $\tau \to \mu$ and $\tau \to e$ processes vs the Higgs boson mass m_H in the decoupling limit as reported in [22]. $X = \gamma, \mu\mu, ee, \eta$.

1.1.6 Comparison between different models

The possible enhancements of LFV τ branching fractions in models detailed above are really interesting, but such effects are also similar and therefore cannot be used to distinguish these models. However, as stated previously, correlations between those branching fractions should allow a clear distinction between them. Table 1.1.6 shows a comparison between the estimations for ratios of some relevant BFs computed using different models [10].

Ratio	LHT	MSSM (w/o Higgs)	MSSM (with Higgs)
$\mathcal{B}(\tau \to \mu\mu\mu)/\mathcal{B}(\tau \to \mu\gamma)$	$0.4 - 2.3$	$\sim 2 \cdot 10^{-3}$	$0.06 - 0.1$
$\mathcal{B}(\tau \to e\mu\mu)/\mathcal{B}(\tau \to e\gamma)$	$0.3 - 1.6$	$\sim 2 \cdot 10^{-3}$	$0.02 - 0.04$
$\mathcal{B}(\tau \to eee)/\mathcal{B}(\tau \to e\mu\mu)$	$1.3 - 1.7$	~ 5	$0.3 - 0.5$
$\mathcal{B}(\tau \to \mu\mu\mu)/\mathcal{B}(\tau \to \mu ee)$	$1.2 - 1.6$	~ 0.2	$0.08 - 0.15$
$\mathcal{B}(\tau \to eee)/\mathcal{B}(\tau \to e\gamma)$	$0.4 - 2.3$	$\sim 1 \cdot 10^{-2}$	$\sim 1 \cdot 10^{-2}$
$\mathcal{B}(\tau \to \mu ee)/\mathcal{B}(\tau \to \mu\gamma)$	$0.3 - 1.6$	$\sim 1 \cdot 10^{-2}$	$\sim 1 \cdot 10^{-2}$

Table 1.1: Comparison of various ratios of branching fractions in the LHT model and in the MSSM without and with significant Higgs contributions.

1.2 Theoretical estimations of branching fraction for $\tau \to lK_S^0$ decay

A theoretical estimation of $\tau \to lK_S^0$ BF has been calculated using the extension of the SM by heavy neutrinos [24]. This extension is based on adding n_R $SU_L(2) \times U(1)$ singlet Dirac heavy neutrinos to n_G SM neutrinos. Heavy neutrinos should have large mixing with the SM leptons and large masses for obtaining observable LFV decay rates.

Since the new neutrinos are $SU_L(2) \times U(1)$ singlets, the structure of lepton interaction vertexes in the weak basis is the same as in the SM. However, in a transition to the mass-basis, non-degeneracy of neutrinos leads to the Cabibbo-Kobayashi-Maskawa (CKM) type matrix (B_{ln}) in the charged current (CC) nlW vertexes, where n's and l's are neutrinos and leptons. Therefore, this model, except for SM parameters, depends only on parameters defining B matrix and on heavy-neutrino masses, but they are undetermined even for the simplest case with two additional heavy neutrinos because there are $n_G n_R$ independent angles and $(n_G - 1)(n_R - 1)$ independent phases of B matrix. Since the B matrix elements are unknown, the amplitudes of LFV cannot be evaluated exactly. Only upper bounds of the amplitude can be found starting from deviations of lepton-flavour-conserving process from SM, like low-energy tree level processes [25].

For all the decays involving these new neutrinos, all amplitudes can approximately be expressed in terms of combinations of B matrix elements and λ ratios, where $\lambda_i = m_{N_i}^2/m_W^2$ and N_i are massive neutrinos. Keeping only the leading terms in the large-mass limit of heavy neutrinos, the theoretical upper bounds for $\tau \to lK_S^0$ processes are of the order 10^{-16}.

From another point of view, the R-parity violating SUSY model allows for LFV decays but, as stated before, instead of computing an estimation of the upper bounds, the current experimental bounds are used to compute limits on the parameters of the models [26].

For the L-violating processes only λ and λ' type couplings (defined in 1.1.4) are involved. Taking non-zero $\lambda\lambda'$ coupling, the generic process $\tau \to lP$ (where $l = e, \mu$ and $P = \pi, \eta, K^0$, generic pseudo-scalar meson) is fairly clean from a theoretical point of view and they can occur with an squark o sneutrino propagator mediating the decay.

Assuming all λ products to be real and positive, all measured upper limits for $\tau \to lK_S^0$ decays can be substituted to obtain an upper limit for those products. In the work published in [26], old values for BF upper limits ($\sim 10^{-3}$) are used to obtain limits for λ's couplings. The results relevant to $\tau \to lK_S^0$ decays are summarized in Tab. 1.2 [26], but better bounds on $\lambda\lambda'$ products will be available once current experimental results are incorporated.

$\lambda\lambda'$	Final state	Bound
(123)(221)	eK^0	4.7×10^{-2}
(132)(112)	μK^0	4.1×10^{-2}
(231)(212)	eK^0	4.7×10^{-2}
(233)(321)	μK^0	4.1×10^{-2}
(123)(121)	μK^0	4.1×10^{-2}
(131)(112)	eK^0	4.7×10^{-2}
(133)(321)	eK^0	4.7×10^{-2}
(232)(212)	μK^0	4.1×10^{-2}

Table 1.2: Bounds on R-parity $\lambda\lambda'$ type products for $\tau \to lK^0$ decays.

1.3 Experimental limits and reaches for LFV τ decays

Present generation B-factories operating around the $\Upsilon(4S)$ resonance also serve as τ-factories because the production cross sections $\sigma_{b\overline{b}} = 1.1\,\text{nb}$ and $\sigma_{\tau^+\tau^-} = 0.9\,\text{nb}$ are quite similar at center-of-mass energy near $\sqrt{s} = 10.58\,\text{GeV}$. *BABAR* and BELLE have thus been able to reach the highest sensitivity to LFV τ decays. The sensitivity, or expected UL, is defined as the UL value obtained using the background expected from Monte Carlo (MC) instead of observed events. Experimentally, LFV τ decays can be conveniently classified as $\tau \to \mu\gamma$, $\tau \to lll$ and $\tau \to lh$ where l is either an electron or muon and h represents a hadronic system (e.g. π^0, η, η', K^0_S, etc.).

The experimental signature for LFV τ decays is extremely clean. In $e^+e^- \to \tau^+\tau^-$ events at $\sqrt{s} \sim m_{\Upsilon(4S)}$, the event can be divided into hemispheres in the center-of-mass frame, each containing the decay products of one τ lepton. Furthermore, unlike SM τ decays which contain at least one neutrino, the measured energy of τ daughters has a peak at half the center-of-mass energy and the total invariant mass of the daughters is centered around the mass of the τ lepton. The mass and energy resolution are different for each decay, but they show always a long radiative tail due to initial and final state radiation, and bremsstrahlung.

The principal sources of background are radiative QED (*dimuon* or *Bhabha*) and continuum ($q\overline{q}$) events as well as $\tau^+\tau^-$ events with a mis-identified standard model decay mode. There is also some irreducible contribution from $\tau^+\tau^-$ events with hard initial state radiation in which one of the τ's decays into a mode with the same charged particle as the signal. For example, $\tau \to \mu\nu\overline{\nu}$ decays accompanied by a hard γ is an irreducible background in the $\tau \to l\gamma$ search.

The general strategy to search for the neutrino-less decays is to define a signal region in the two dimensional energy-mass plane of the τ's daughters and to reduce the background

expectation from well-known processes inside the signal region by optimizing a set of selection criteria based on missing momentum, particle identification and other variables related only to one of the two hemispheres. The analysis is performed in a blind fashion by excluding events in the region of the signal region until all optimisations and systematic studies of the selection criteria have been completed. Selection criteria are optimized using control samples, data sidebands and MC extrapolation to the signal region to yield the lowest expected upper limit under the no-signal hypothesis.

Currently *BABAR* and Belle have recorded integrated luminosities of $\mathcal{L} \sim 500\,\text{fb}^{-1}$ and $850\,\text{fb}^{-1}$, respectively, which correspond to a total of more than one billion of τ pairs. The analysis of these data samples is ongoing and published results include only part of the data analyzed. No signal has yet been observed in any of the probed channels and the individual experiments have each set 90% confidence level (CL) limits between 10^{-7} and 10^{-8} for the most part of decay channels. In the absence of signal, for large numbers of background events N_{bkg}, the 90% CL upper limit for the number of signal events can be given as $N_{90}^{UL} \sim 1.64\sqrt{N_{bkg}}$, whereas for small N_{bkg} a value for N_{90}^{UL} is obtained using the method described in [27], which gives for $N_{bkg} \sim 0$, $N_{90}^{UL} \sim 2.4$. Then the 90% CL branching fraction upper limit is computed as

$$\mathcal{B}_{90}^{UL} = \frac{N_{90}^{UL}}{2\varepsilon N_{\tau\tau}} = \frac{N_{90}^{UL}}{2\varepsilon\mathcal{L}\sigma_{\tau\tau}}, \tag{1.2}$$

where $N_{\tau\tau} = L\sigma_{\tau\tau}$ is the number of τ-pairs produced in e^+e^- collisions; $\mathcal{L}$ is the integrated luminosity, $\sigma_{\tau\tau}$ is the τ-pair production effective cross section and ε, is the channel reconstruction efficiency. The most recent results of these searches are summarized in Tab. 1.3.

The considerable experience developed in searching for these decays in large data sets enables us to make projections of the sensitivities to these decays with a SuperB-factory delivering a 10-fold to 100-fold increase in the data set. We express the experimental reach in terms of the *expected 90% CL upper limit* that can be reached assuming no signal and, for brevitys sake, we refer to this as the *sensitivity*. Depending upon the nature of backgrounds contributing to a given search, two extreme scenarios can be envisioned in extrapolating to higher luminosities:

- if the expected background is kept below $\mathcal{O}(1)$ events, while maintaining the same efficiency, and no signal events would be observed, the upper limit on branching fraction at 90% CL $\mathcal{B}_{90}^{UL}$ is $\propto 1/\mathcal{L}$, e. g. $\tau \to \mu\mu\mu$;

- if there is background now already and no reduction could be achieved in the future measurements, $\mathcal{B}_{90}^{UL}$ is $\propto 1/\sqrt{\mathcal{L}}$.

However, while the $\sqrt{\mathcal{L}}$ scaling is highly pessimistic, the other scenario is equivalent to a statement that the analysis can be performed maintaining the same efficiency and

	BABAR		Belle	
Channel	$\mathcal{L}(\,\mathrm{fb}^{-1})$	$\mathcal{B}_{90}^{UL}(10^{-8})$ [Ref.]	$\mathcal{L}(\,\mathrm{fb}^{-1})$	$\mathcal{B}_{90}^{UL}(10^{-8})$ [Ref.]
$\tau \to e\gamma$	535	1.2 [28]	211	11 [29]
$\tau \to \mu\gamma$		4.5 [28]		6.8 [15]
$\tau \to lll$		$2.0 - 4.1$ [30]	376	$4 - 8$ [31]
$\tau \to e\pi^0$	401	8 [32]	339	13 [33]
$\tau \to \mu\pi^0$		12 [32]		11 [33]
$\tau \to e\eta$		9.2 [32]		16 [33]
$\tau \to \mu\eta$		6.5 [32]		15 [33]
$\tau \to e\eta'$		16 [32]		24 [33]
$\tau \to \mu\eta'$		13 [32]		14 [33]
$\tau \to ehh'$	671	$4.4 - 8.7$ [34]	221	$12 - 32$ [35]
$\tau \to \mu hh'$		$3.4 - 15$ [34]		$7 - 48$ [35]
$\tau \to eK_S^0$	282	5.6 [5]	469	3.3 [36]
$\tau \to \mu K_S^0$		4.8 [5]		4.0 [36]
$\tau \to e\rho$	543	6.3 [37]	451	4.3 [36]
$\tau \to \mu\rho$		6.8 [37]		0.8 [36]
$\tau \to eK*$		7.8 [37]		5.6 [36]
$\tau \to \mu K*$		5.9 [37]		16 [36]
$\tau \to e\overline{K}*$		7.7 [37]		4.0 [36]
$\tau \to \mu\overline{K}*$		10 [37]		6.4 [36]
$\tau \to e\omega$		7.3 [37]		3.1 [36]
$\tau \to \mu\omega$		13 [37]		18 [36]

Table 1.3: Current observed upper limits on LFV τ decays as from *BABAR* and Belle last results with the used integrated luminosity.

backgrounds as the current one. Therefore, a SuperB-factory should not only provide more statistics but also a higher resolution or other handles to reject the backgrounds.

Again for $\tau \to l\gamma$, there is an *irreducible background* from $\tau \to \mu\nu\overline{\nu}$ (ISR) in which the photon from initial state radiation can be combined with a lepton to form a candidate that accidentally overlaps with the signal region. For a projection of the upper limit, we therefore consider a *realistic* scenario in which this source of background is present at the rate determined with the existing analysis, while all other backgrounds are suppressed with minimal cost to the signal efficiency. Note, however, that improvements on this realistic scenario are possible if the $l\gamma$ mass resolution is improved, which could be achieved by improving the spatial resolution of the electromagnetic calorimeter, comparing to the present B-factories.

The situation for the other LFV decays, $\tau \to lll$ and $\tau \to lh$, is even more promising, since these modes do not suffer from the aforementioned backgrounds from ISR. In this case, one can project sensitivities assuming N_{bkg} is comparable to backgrounds in existing

analysis for approximately the same efficiencies. Table 1.3 summarizes the sensitivities for various LFV decays.

Channel	Sensitivity
$\mathcal{B}(\tau \to \mu\gamma)$	2×10^{-9}
$\mathcal{B}(\tau \to e\gamma)$	2×10^{-9}
$\mathcal{B}(\tau \to \mu\mu\mu)$	2×10^{-10}
$\mathcal{B}(\tau \to eee)$	2×10^{-10}
$\mathcal{B}(\tau \to \mu\eta)$	4×10^{-10}
$\mathcal{B}(\tau \to e\eta)$	6×10^{-10}
$\mathcal{B}(\tau \to eK_S^0)$	2×10^{-10}

Table 1.4: Expected 90% CL upper limits on LFV τ decays with 75 ab^{-1} assuming no signal is found and reducible backgrounds are small ($\sim \mathcal{O}(1)$ events) and the irreducible backgrounds scale as $\mathcal{L}$.

1.4 Overview of the analysis for searching $\tau \to lK_S^0$

In this analysis we search for $\tau \to lK_s^0$ decay using data collected by the *BABAR* detector at the PEP-II asymmetric energy storage ring. Charged particles are detected and their momenta measured by both a silicon vertex tracker, consisting of 5 layers of double-sided detectors, and a 40-layer central drift chamber operating in a 1.5 T axial magnetic field. Charged particle identification (PID) is provided by the energy loss in the tracking devices and by the measured Čerenkov angle from an internally reflecting ring-imaging Čerenkov detector covering the central region. Photons and electrons are detected by a CsI(Tl) electromagnetic calorimeter. The calorimeter is surrounded by an instrumented flux return. The detector is detailed in Chap. 2. The analyzed data sample corresponds to an integrated luminosity of $469\,\text{fb}^{-1}$ collected from e^+e^- collisions and the total number of τ pairs $N_{\tau\tau}$ is 431×10^6. The MC simulated samples of signal and background events have been used to estimate the signal efficiency ε and the expected number of background events N_{bkg}. The charged tracks reconstruction and the particle identification, described in Sec. 3.1 and 3.2, are fundamental to a good efficiency and the best background rejection. For the electron and muon decay mode we use the same technique with a slightly different selection detailed in Chap. 4.

For this analysis, two different stages of events selection are used: a loose selection stage with enough statistics to estimate the shape of background distributions and a tight one in which the cuts have been optimized to obtain the lowest value for the upper limit sensitivity. There is also an additional stage of selection referred to as preselection and introduced only for technical purpose to reduce the number of possible combinations when

reconstructing τ candidates. Events are first selected using global event properties (thrust magnitude, charge and topology of the event, one or more reconstructed K^0_S) in order to reject background events with high multiplicity from $b\overline{b}$, $c\overline{c}$ and *uds* processes. All tracks (photons) are required to be reconstructed within a fiducial region. K^0_S candidate are reconstructed only in $K^0_S \to \pi^+\pi^-$ decay mode. The amount of background events due to $b\overline{b}$, *dimuon* and *Bhabha* processes are negligible after these selection criteria have been applied. For each events, two hemispheres are defined in the CM using the plane perpendicular to the thrust axis [38] calculated using tracks and calorimeter energy deposits without an associated track. The hemisphere that contains the reconstructed momentum of signal τ candidate is referred to as the signal side and the other hemisphere as the tag side. Candidate τ pair events are required to have three reconstructed charged particle tracks on the signal side and only one in the tag side. Only for the electron channel events with three reconstructed tracks on the tag side are also retained.

The signal τ candidates are examined in the two dimensional distribution of ΔE_τ vs. ΔM_τ where ΔM_τ is defined as the difference between the invariant mass of the reconstructed τ and the world average value [39], and ΔE_τ is defined as the difference between the energy of the reconstructed τ and the expected τ energy, half the center-of-mass total energy. The signal τ candidates are reconstructed by combining one K^0_S candidate with another track and fitting the whole decay tree, while requiring that the K^0_S decay products form a vertex, the track and the K^0_S come from the interaction point and the K^0_S mass is constrained to the nominal value. To improve the energy resolution, a bremsstrahlung recovery procedure is applied for the $\tau \to eK^0_S$ decay mode only: before the fit, the track candidate to be a lepton is combined with up to three photons contained in a small cone around the track direction. The lepton track is also requested to be loosely identified as electron or muon. For the muon channel the loose selection ends here. Instead for the electron channel further requests on the K^0_S candidate, like the flight length significance, are needed to obtain a reasonable agreement between data and MC shape. These requirements are also applied later to the muon channel candidates for the tight selection.

Most of the background surviving after the loose selection for both channels comes from charm decays such as $D \to K^0_S\pi$ and $D \to K^0_S\ell\nu$ and from combinations in the *uds* events of a true K^0_S and a fake lepton. To avoid bias from adapting the selection requirements to the data, the tight selection has been optimized in a blind way, without looking at the data in the rectangular region around the signal peak on $\Delta E_\tau/\Delta M_\tau$ plane. The optimization criterion is to obtain the lowest value for the upper limit sensitivity. For the tight selection we apply a tighter PID selector and requirements on missing momentum ($\Upsilon(4S)$ momentum minus all track candidates and all unmatched calorimeter deposits), number of photons on tag side and a *constrained* version of invariant mass on tag side. The main systematic sources (e.g. tracking and PID) for the efficiency are evaluated and

included in the final estimation of upper limit.

Since no evidence for a signal is found, 90% confidence level limits have been determined according to the modified frequentist analysis (or CL_s method) which has been already employed in $\tau \to \mu\gamma$ *BABAR* analysis [15] and was developed in the Higgs boson search at LEP [40]. In order to define the statistics test $Q = \mathcal{L}(S+B)/\mathcal{L}(B)$ (likelihood ratio between the signal plus background and background only hypothesis), a highly discriminant variable has been constructed by evaluating the χ^2 from a geometrical and kinematical fit with the additional constraints of ΔM_τ and ΔE_τ equal to 0 ($\chi^2_{\rm full}$). The MC signal shape has been determined from the distributions of events after the tight selection, while the MC background shape from the distributions after the loose selection, to have a decent number of events. The normalization of the expected background has been checked using data outside the signal region. The statistical and systematic uncertainties are included by the CL_s method in the final estimation of the upper limit.

Upper limits on branching fractions at 90% confidence level are calculated as

$$\mathcal{B}(\tau \to l K^0_S) < \frac{s_{90}}{2\varepsilon N_{\tau\tau}} \tag{1.3}$$

where s_{90} is the limit for the signal yield at 90% confidence level obtained using the CL_s method.

Upper limits have been also determined exploiting another technique that gives a similar but lower sensitivity, so it is used only as cross-check. For this method, the selection has been slightly tightened to reduce the background as much as possible. The background estimation in the signal region is obtained by extrapolating the event density in the lateral side-band regions in the ΔM_τ distribution after the loose selection. The fitted background distribution is normalized according to the number of data events in the sidebands after the tight selection. The upper limits on the branching fractions at 90% confidence level for this cross-check are finally calculated using the POLE program [41], an implementation of Feldman-Cousins method [42] that includes the efficiency and background uncertainties.

Chapter 2

Experimental Apparatus

BABAR is an High Energy Physics experiment installed at the Stanford Linear Accelerator Center (SLAC), California. It was designed and built by a large international team of scientists and engineers in the 90s, with a comprehensive physics program consisting of the systematic measurement of *CP* violation in the B meson system, precision measurements of decays of bottom and charm mesons of the τ lepton, and search for rare processes. The experiment consists of a detector [43] with the same name built around the interaction region of the high luminosity e^+e^- asymmetric collider PEP-II [44]. The data collection is now over and the machine and the detector are currently being dismantled. In this chapter the main features of the final design and performances of PEP-II collider and *BABAR* detector are described.

2.1 The PEP-II B Factory

The PEP-II B Factory is an asymmetric-energy e^+e^- collider designed to operate at a center-of-mass (CM) energy of 10.58 GeV, corresponding to the mass of the $\Upsilon(4S)$ vector meson resonance (see Fig. 2.1).

The effective cross section[1] for the production of the $\Upsilon(4S)$ at $\sqrt{s} = 10.58\,\text{GeV}$ is about 1.1 nb, and the $\Upsilon(4S)$ decays almost exclusively into $B^0\overline{B}^0$ or B^+B^- pairs. The design peak luminosity was foreseen to be $\mathcal{L} = 3 \times 10^{33}\ \text{cm}^{-2}\text{s}^{-1}$ and was reached in 2001. During year 2006 – thanks to higher beam currents, improved beam orbits and focusing – PEP-II has achieved a stable luminosity of $1.2 \times 10^{34}\,\text{cm}^{-2}\text{s}^{-1}$, thus producing B meson pairs at a rate greater than 13 Hz, which translates to about 20 millions of $B\overline{B}$ pairs in one month of continuous running, and provides an ideal laboratory for the study of B mesons.

[1] The effective cross section is lower (about one third) than the peak cross section (3.6 nb) due to the energy spread (3-6 MeV) of the beams and to initial state radiation.

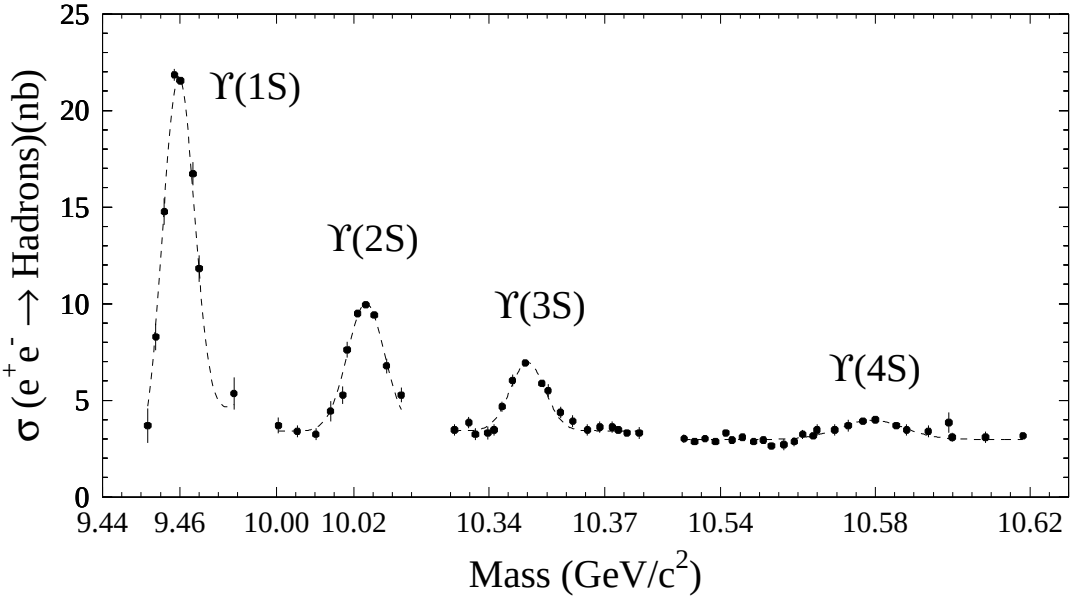

Figure 2.1: The first four S-wave Υ resonances shown with the hadronic cross section versus CM energy/c^2 in the Υ mass region. The $\Upsilon(4S)$ is the third radial excitation of the ground state. Its larger width corresponds to the fact that the $\Upsilon(4S)$ is just above threshold for strongly decaying to $B^0\overline{B}^0$ and B^+B^- pairs.

The effective cross sections of the main physics processes in PEP-II are listed in Table 2.1. The *Bhabha* processes includes electrons and positrons within the polar angle

$e^+e^- \rightarrow$	Cross section (nb)
uds	2.09
$c\overline{c}$	1.30
B^+B^-	0.525 (peak 1.8)
$B^0\overline{B}^0$	0.525 (peak 1.8)
Bhabha (SP-2400)	25.5
$\mu^+\mu^-$	1.16
$\tau^+\tau^-$	0.919 ± 0.003

Table 2.1: Effective cross sections of the main physics processes at $\sqrt{s} = M(\Upsilon(4S))$ The cross section for e^+e^- is referred to the volume of the *BABAR* electromagnetic calorimeter, which is used to trigger these events.

range from 15° to 165° in CM system. This corresponds to a polar angle range from about 18° to 131° in the laboratory (LAB) system. No radiative *Bhabha* sample is added.

At the peak of the $\Upsilon(4S)$ there is a non-negligible amount of continuum $e^+e^- \to q\overline{q}$ (q=u,d,s,c) and $e^+e^- \to ll(l = e, \mu, \tau)$ events. To study the background events due to these processes, part of the data is collected at a CM energy 40 MeV below the $\Upsilon(4S)$ peak, where $B\overline{B}$ production is not allowed. This data sample corresponds to about 1/10 of the sample taken at the $\Upsilon(4S)$ peak.

2.1.1 PEP-II layout

In PEP-II, the electron beam of 9.0 GeV collides head-on with the positron beam of 3.1 GeV resulting in a boost for the CM system of $\beta\gamma \approx 0.56$ in the LAB frame. The asymmetry of the machine is motivated by the need to separate the decay vertexes of the two B mesons. The boost makes it possible to reconstruct the decay vertexes of the two B mesons and to determine their relative decay times, since the average separation between the two B vertexes is $\beta\gamma c\tau \approx 250\mu$m. One can therefore measure the time dependent decay rates and CP-asymmetries.

The different beam energies require a two rings configuration, as shown in Fig. 2.2. The parameters of PEP-II rings are summarized in Tab. 2.2.

Parameters	Units	Design	Aug 2006
Energy (E) HER/LER	GeV	9.0/3.1	9.0/3.1
Current (I) HER/LER	A	0.75/2.15	1.87/2.90
Peak luminosity	$\mathrm{cm}^{-2}\mathrm{s}^{-1}$	3.0	12.0
Integrated luminosity	fb^{-1}/month	3.3	20.0

Table 2.2: PEP-II beam parameters; both design values and values achieved in colliding beam operation during year 2006 are given. HER and LER refer to the high energy e^- and low energy e^+ ring, respectively.

Electrons and positrons are accelerated from the 3 km long SLAC linear accelerator (LINAC) and accumulated into two 2.2 km long storage rings, called HER (high-energy ring) and LER (low-energy ring) respectively. A fraction of electrons instead of being delivered to the HER is further accelerated to an energy of 30 GeV and sent to a target where positrons are produced. In proximity of the interaction region, the beams are focused by a series of offset quadrupoles (Q1, Q2, Q4, Q5 in Fig. 2.5) and bent by means of a pair of samarium-cobalt dipole magnets (B1), which allow the bunches to collide head-on. The tapered B1 dipoles, located at $\pm$21 cm on each side of the interaction point (IP), and the Q1 quadrupoles operate inside the field of the *BABAR* superconducting solenoid, while Q2, Q4, and Q5, are located outside or in the fringe field of the solenoid.

The interaction region is enclosed in a water-cooled beam pipe consisting of two thin layers of beryllium (0.83 mm and 0.53 mm) with a 1.48 mm water channel in between.

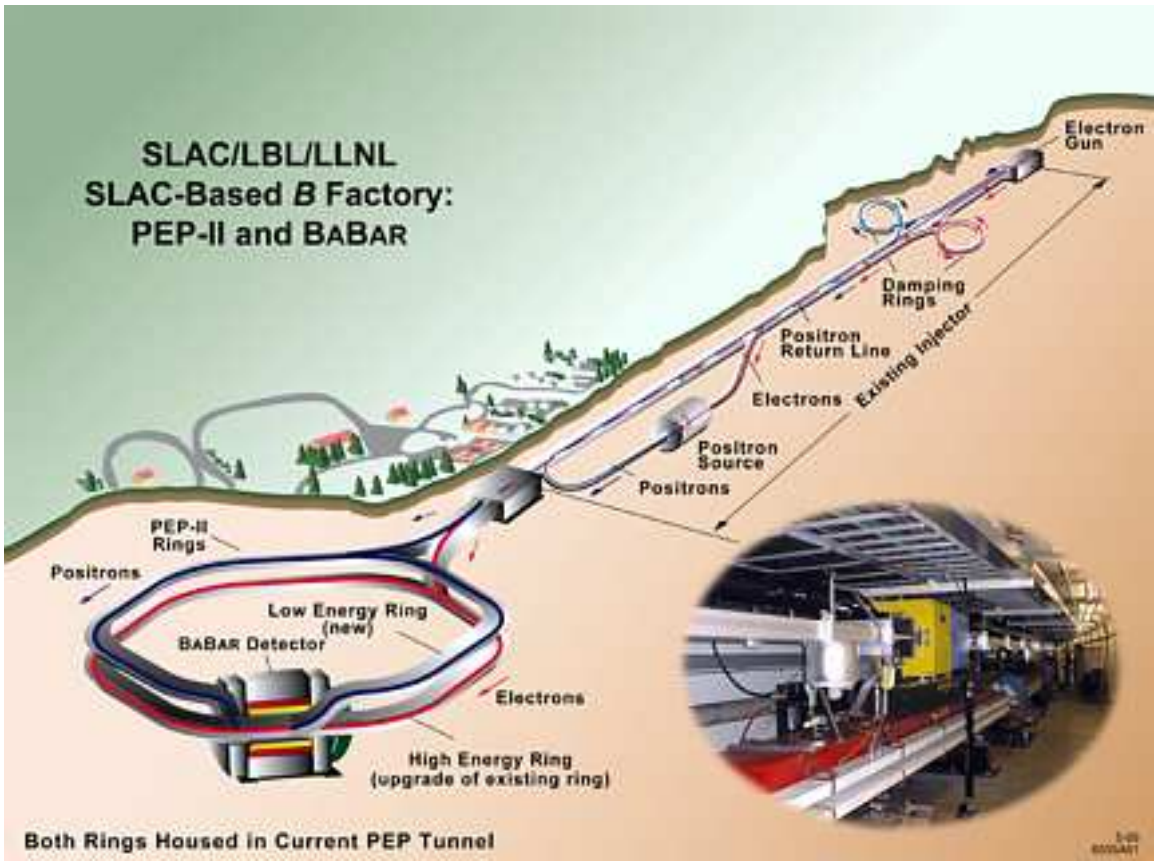

Figure 2.2: PEP-II overview.

To attenuate synchrotron radiation, the inner surface of the pipe is gold-plated (approximately 4 μm). The total thickness of the central beam pipe section at normal incidence corresponds to 1.06% of a radiation length. The beam pipe, permanent magnets, and the silicon vertex tracker (SVT) are assembled, aligned, and then enclosed in a 4.4 m long support tube. This rigid structure is inserted into the *BABAR* detector, spanning the IP.

2.1.2 Monitoring beam parameters

The beam parameters that are most critical for the *BABAR* data analysis are the luminosity, the energies of the two beams and the position and size of the luminous region.

Luminosity

While PEP-II uses a high-rate luminosity sampling radiative *Bhabha* scattering to provide a fast relative measurement of the luminosity for operations, *BABAR* derives the absolute luminosity off-line from QED processes, primarily e^+e^-, and $\mu^+\mu^-$ pairs. The best estimate for the relative error is 0.8% for the data taken until Summer 2003 and 0.49% for the remaining data [45]. A good estimate of this uncertainty is crucial for the analysis that depends strongly from the luminosity value, like measurements and upper limit

estimations of branching fractions.

Beam Energies

During operation, the mean energies of the two beams are calculated from the total magnetic bending strength (including the effects of off-axis quadrupole fields, steering magnets, and wigglers) and the beam orbits. While the systematic uncertainty in the PEP-II calculation of the absolute beam energies is estimated to be $5-10$ MeV, the relative energy setting for each beam is accurate and stable at about 1 MeV. The energy spread of the LER and HER is 2.3 and 5.5 MeV, respectively. To ensure that data are recorded close to the peak of the $\Upsilon(4S)$ resonance, the observed ratio of $B\overline{B}$ enriched hadronic events to lepton pair production is monitored on-line. At the peak of the resonance, a 2.5% change in the $B\overline{B}$ production rate corresponds to a 2 MeV change in the CM energy, a value that is close to the tolerance to which the energy of PEP-II can be held. However, a drop in the $B\overline{B}$ rate does not distinguish between energy settings above or below $\Upsilon(4S)$ peak. The sign of the energy change must be determined from other indicators. The best monitor and absolute calibration of the c.m. energy is derived from the measured CM momentum of fully reconstructed B mesons constrained with the known B meson mass. An absolute error of 1.1 MeV can be obtained for an integrated luminosity of 1 fb^{-1}. This error is equally limited by the knowledge of the B mass and the detector resolution.

Beam Size and Position

The size and position of the luminous region are critical parameters for the time-dependent analysis[2] and their values are monitored continuously on-line and off-line. The vertical size is too small to be measured directly. It is inferred from the measured luminosity, the horizontal size, and the beam currents; it varies typically by 1-2 μm. The transverse position, size and angles of the luminous region relative to the *BABAR* coordinate system are determined by analysing the distribution of the distance of closest approach to the z-axis of the tracks in well measured two-track events as a function of the azimuth ϕ. The longitudinal parameters are derived from the longitudinal vertex distribution of the two tracks. The uncertainties in the average beam position are of the order of a few μm in the transverse plane and about 100 μm along the collision axis. No significant variation in the beam position, compared to the measurement uncertainties, is found over periods of about 1–2 hours, indicating that the beams are stable over that period. The measured horizontal and longitudinal beam sizes, corrected for tracking resolution, are consistent with those measured by PEP-II.

[2]Or whenever a primary decay vertex is evaluated with the beam-spot constraint.

2.1.3 PEP-II performances

PEP-II has delivered luminosity starting from October 1999 till April 2008, and since then *BABAR* has recorded a total integrated luminosity of 531 fb^{-1}, mostly at $\Upsilon(4S)$ resonance peak plus small samples around $\Upsilon(2S)$ and$\Upsilon(3S)$ ones (see Fig. 2.3).

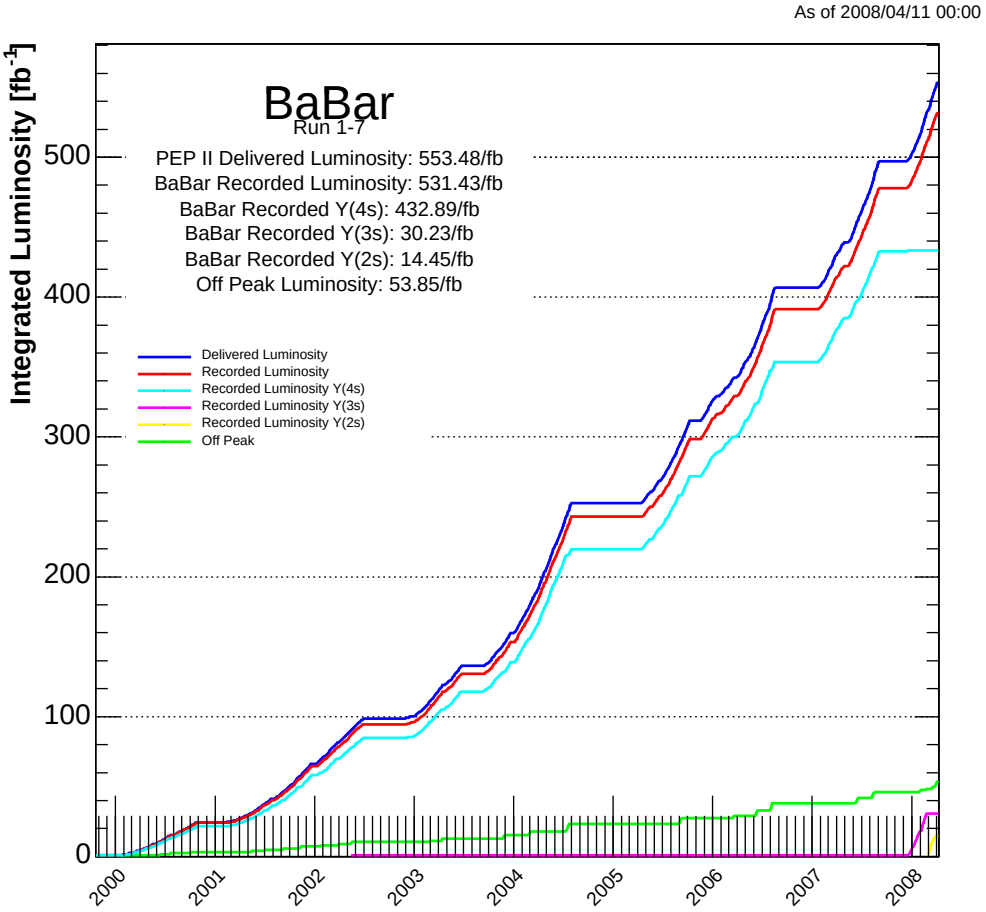

Figure 2.3: Total luminosity delivered by PEP-II from October 1999 to April 2008. The luminosities integrated by *BABAR* at different resonances is also shown.

Some off-peak luminosity has been collected, 40 MeV below each resonance peak, plus a scan from $\Upsilon(4S)$ till 11.2 GeV with 5 MeV steps, for a total amount of 54 fb^{-1}. Every single run of data has been checked and some of them have been rejected because of poor quality due to technical problem with the detector or bad conditions for the machine background. As shown in Table 2.2 [44, 46], PEP-II has already surpassed its design performances, both in terms of the instantaneous luminosity (by a factor 4) and the monthly integrated luminosity (by a factor 6).

The progress in the instantaneous luminosity is mainly due to the increase of the beam currents and improved focusing and beam orbits. A significant improvement to the inte-

grated luminosity has been achieved between December 2003 and March 2004 with the implementation of a novel mode of operation of PEP-II called "trickle injection" which increases the production of $B\overline{B}$ pairs by up to 50 percent (see Fig. 2.4). Until the end of 2003, PEP-II typically operated in a series of 40 minute fills during which the colliding beams coasted: at the end of each fill, it took about three to five minutes to replenish the beams for the next fill, and during this period the *BABAR* data acquisition system had to be turned off for the high background conditions, affecting detector safety and data acquisition dead-time. With the new technique, the *BABAR* detector can take data virtually uninterrupted while the LINAC continuously refills the beams with small injections at lower rate, replacing particles that are lost in collisions in the *BABAR* interaction region. After more than a year of testing, trickle injection was introduced first in December 2003 in the low energy ring, bringing the B Factory a 30% increase in output. In March 2004, trickle injection for the high energy ring was implemented, thus providing an additional 15% increase. The advantages of this novel mode of operation go beyond just the increase in luminosity: continuous injection makes the storage of particles more stable, so that PEP-II rings are easier to operate and beam losses are far less frequent than with the previous operational mode.

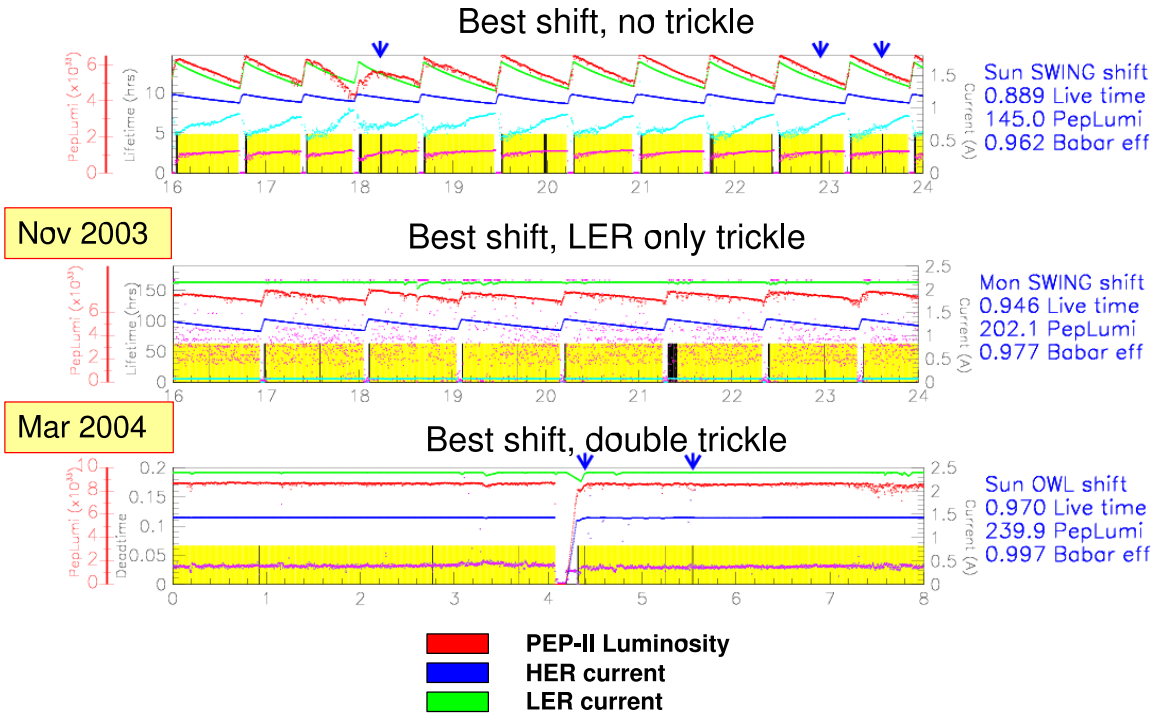

Figure 2.4: Comparison of the best 8-hour periods of data taking for three different mode of operation of PEP-II: no trickle injection (top), trickle injection of the low energy ring only (middle), and trickle injection of both beams (bottom).

2.2 Overview of the *BABAR* detector

The design of the *BABAR* detector has been optimized for *CP* violation studies, but it is also well suited for searches of rare decays of B and τ. To achieve the goal of performing accurate event reconstruction there are many requirements:

- a large acceptance and uniform efficiency, in particular down to small polar angles relative to the boost direction, to avoid particle losses;
- excellent detection efficiency for charged particles down to 60 MeV/c and for photons down to 25 MeV;
- good momentum resolution to kinematically separate signal from bkg;
- excellent energy and angular resolution for the detection of photons from π^0 and radiative B decays in the range from 25 MeV to 4 GeV;
- very good vertex resolution, both transverse and parallel to the beam;
- identification of electrons and muons over a wide range of momentum, primarily for the detection of semi-leptonic decays used to tag the B flavor and for the study of semi-leptonic and rare decays;
- identification of hadrons over a wide range of momentum for B flavor tagging as well as for the separation of pions from kaons;
- a highly efficient, selective trigger system with redundancy so as to avoid significant signal losses and systematic uncertainties.

Also other technical issues have been addressed in order to deal with a very large amount of data over many years:

- low noise electronics and data acquisition systems of high flexibility and operational stability;
- high degree of reliability of components and frequent monitoring and automated calibrations, plus control of the environmental conditions to assure continuous and stable operation;
- an on-line computing and network system that can control, process, and store the expected high volume of data;
- detector components that can tolerate significant doses of radiation and operate under high background condition.

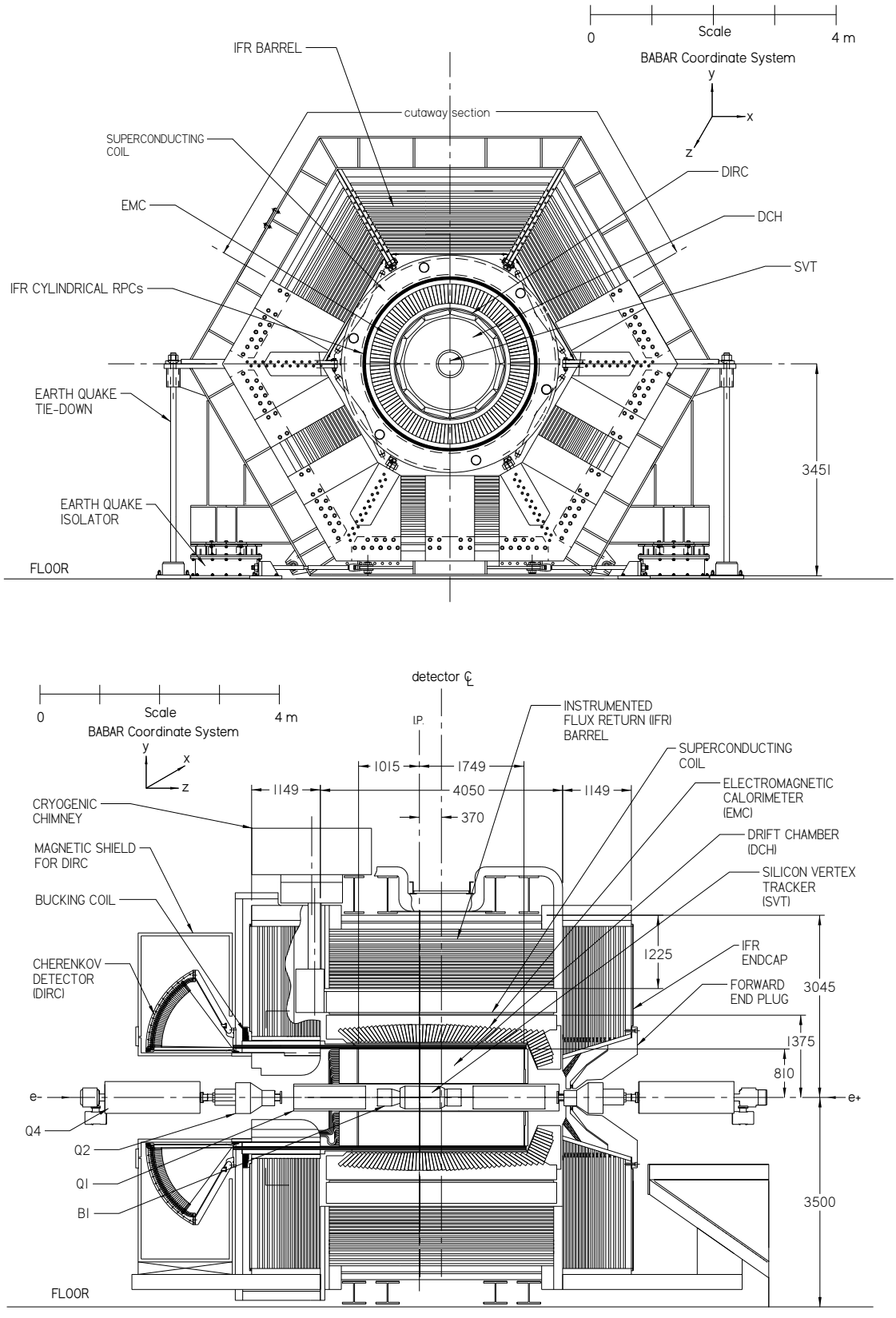

Figure 2.5: *BABAR* detector front view (top) and side view (bottom).

The *BABAR* detector (see Fig. 2.5), designed and fabricated by a collaboration of 600 physicists of 75 institutions from 9 countries, meets all these requirements, as will be shown in the next sections of this chapter.

An overview of the polar angle (θ) coverage, the segmentation and performance of the *BABAR* detector systems is summarized in Table 2.2. The *BABAR* superconducting solenoid, which produces a 1.5 T axial magnetic field, contains a set of nested detectors, which are – going from inside to outside – a five layers silicon vertex tracker (SVT), a central drift chamber (DCH) for charged particles detection and momentum measurement, a ring-imaging Čerenkov radiation detector (DIRC) for particle identification (PID), and a CsI(Tl) crystal electromagnetic calorimeter (EMC) for detection of photons and electrons. The calorimeter has a barrel and an endcap which extends it asymmetrically into the forward direction (e^- beam direction), where many of the collision products emerge. All the detectors located inside the magnet have full acceptance in azimuth (ϕ). The instrumented flux return (IFR) outside the cryostat is composed of 18 layers of steel, which increase in thickness outwards, with in-between 19 layers of planar resistive plate chambers (RPC) or limited streamer tubes (LST) in the barrel and 18 in the end-caps. The IFR allows the separation of muons and charged hadrons, and also detect penetrating neutral hadrons. As indicated in Fig. 2.5, the right-handed coordinate system is anchored to the main tracking system, the drift chamber, with the z-axis coinciding with its principal axis. This axis is offset relative to the beam axis by about 20 mrad in the horizontal plane. The positive y-axis points upward and the positive x-axis points away from the center of the PEP-II storage rings.

Since the average momentum of charged particles produced in B meson decay is below 1 GeV/c, the errors on the measured track parameters are dominated by multiple Coulomb scattering, rather than by the intrinsic spatial resolution of the detectors. Similarly, the detection efficiency and energy resolution of low energy photons are severely impacted by material in front of the calorimeter. Thus, special care has been given to keep the material in the active volume of the detector to a minimum. Figure 2.6 shows the distribution of material in the various detector systems in units of radiation lengths. Specifically, each curve indicates the material a particle traverses before it reaches the first active element of a specific detector system.

In the following sections there is a detailed description of each sub-detector and their performances. During the whole life of the experiment, there have been many efforts to recover from technical problems and to improve calibration and PID. Here some plots will be provided to give a general idea of performances, but for a more detailed description of PID techniques that directly affect this analysis see Section 3.2.

System	Polar angle coverage	Channels	Layers	Segmentation	Performance
SVT	[20.1,150.2]°	150K	5	50-100 μm $r-\phi$ 100-200 μm z	$\sigma_{d_0} = 55\,\mu$m $\sigma_{z_0} = 65\,\mu$m
DCH	[17.2,152.6]°	7,104	40	6-8 mm drift distance	$\sigma_\phi = 1$ mrad $\sigma_{\tan\lambda} = 0.001$ $\sigma_{p_T}/p_T = 0.47\%$ $\sigma(dE/dx) = 7.5\%$
DIRC	[25.5,141.4]°	10,752	1	$35 \times 17\,\text{mm}^2$ $(r\Delta\phi \times \Delta r)$ 144 bars	$\sigma_{\theta_C} = 2.5$ mrad per track
EMC(C)	[27.1,140.8]°	2×5760	1	$47 \times 47\,\text{mm}^2$ 5760 crystals	$\sigma_E/E = 3.0\%$ $\sigma_\phi = 3.9$ mrad
EMC(F)	[15.8,27.1]°	2×820		820 crystals	$\sigma_\theta = 3.9$ mrad
IFR(C)	[47,123]°	22K+2K	19+2	20-38 mm	90% $\mu^\pm$ eff. 6-8% $\pi^\pm$ mis-id
IFR(F)	[20,47]°	14.5K	18	28-38 mm	(loose selection, 1.5–3.0 GeV/c)
IFR(B)	[123,154]°	14.5K	18	28-38 mm	

Table 2.3: Overview of the coverage, segmentation, and performance of the *BABAR* detector systems. The notation (C), (F), and (B) refers to the central barrel, forward and backward components of the system, respectively. Performance numbers are quoted for 1 GeV/c particles, except where noted.

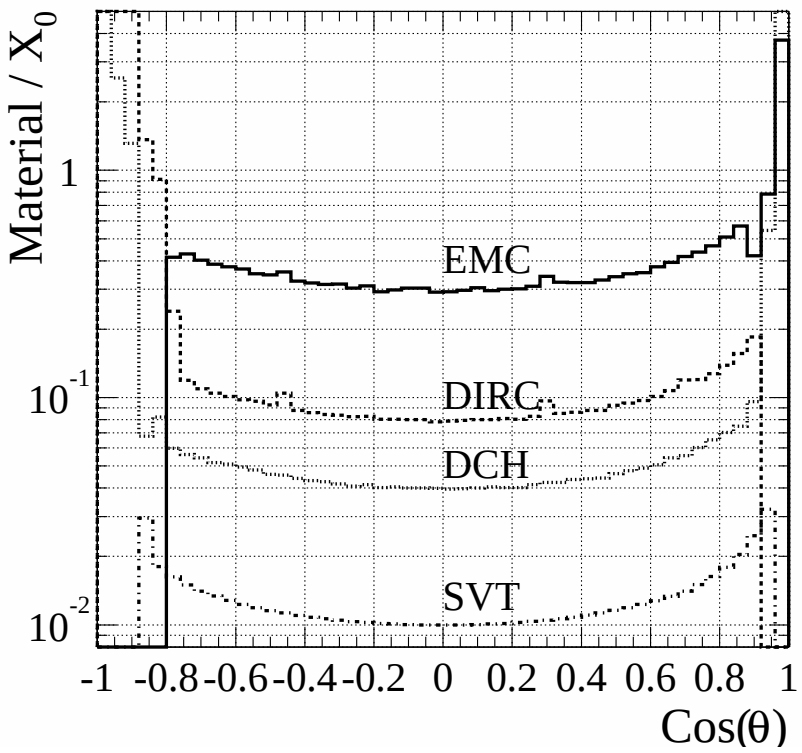

Figure 2.6: Amount of material (in units of radiation lengths) which a high energy particle, originating from the center of the coordinate system at a polar angle θ, traverses before it reaches the first active element of a specific detector system.

2.3 The Silicon Vertex Tracker

The SVT sub-detector provides a precise measurement of the decay vertexes and of the charged particle trajectories near the interaction region. The mean vertex resolution along the z-axis for a fully reconstructed B decay must be better than $80\,\mu$m in order to avoid a significant impact on the time-dependent CP asymmetry measurement precision; a $100\,\mu$m resolution in the $x-y$ transverse plane is necessary in reconstructing decays of bottom and charm mesons, as well as τ leptons.

The SVT also provides standalone tracking for particles with transverse momentum too low to reach the outer tracker, like soft pions from D^* decays and many charged particles produced in multi-body B meson decays. The choice of a vertex tracker made of five layers of double-sided silicon strip sensors allows a complete track reconstruction even in the absence of the drift chamber information.

Finally, the SVT supplies PID information both for low and high momentum tracks. For low momentum tracks the SVT $\mathrm{d}E/\mathrm{d}x$ measurement is the only PID information available, for high momentum tracks the SVT provides the best measurement of the track angles, required to achieve the design resolution on the Čerenkov angle measured by the DIRC.

2.3.1 Detector layout

The Silicon Vertex Tracker is composed of five layers of $300\,\mu$m thick, double-sided microstrip detectors [47]. The total active silicon area is 0.96 m^2 and the material traversed by particles at normal incidence is 4% X_0. The geometrical acceptance is 90% of the solid angle in the CM system.

The silicon detectors and the associated readout electronics are assembled into mechanical units called *modules*. The inner three layers are barrel-shaped and are composed by six modules each. They are placed next to the interaction region, at radii 3.3, 4.0 and 5.9 cm from the beam axis (Fig. 2.3.1 and 2.3.1), and provide an accurate measurement of the track impact parameters along z and in the $x-y$ plane. The outer two layers, composed by 16 and 18 modules (Fig. 2.3.1), have a peculiar arch structure to reduce the incident angles of particles going in the forward and backward direction; their barrel parts are placed at radii between 12.7 and 14.6 cm from the beam axis. They permit an accurate polar angle measurement and, along with the inner three layers, enable standalone tracking for particles with low transverse momentum p_T. Full azimuthal coverage is obtained by partially overlapping adjacent modules, either by tilting them in ϕ by 5° (inner layers) or by staggering them (outer layers); this overlap is also advantageous for alignment. The polar angle coverage is $20.1° < \theta_{\mathrm{LAB}} < 150.2°$.

Each silicon detector consists of a high-resistivity n^- bulk implanted with p^+ strips on one side and orthogonally-oriented n^+ strips on the other side. The strips are AC-

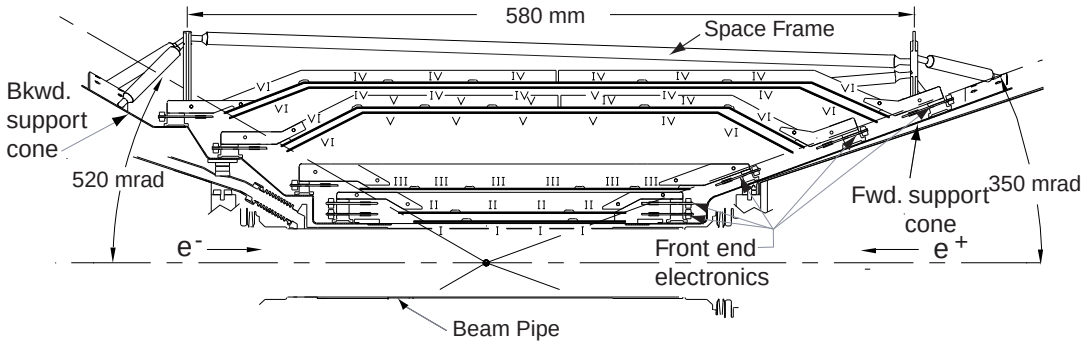

Figure 2.7: Schematic view of the SVT: longitudinal section.

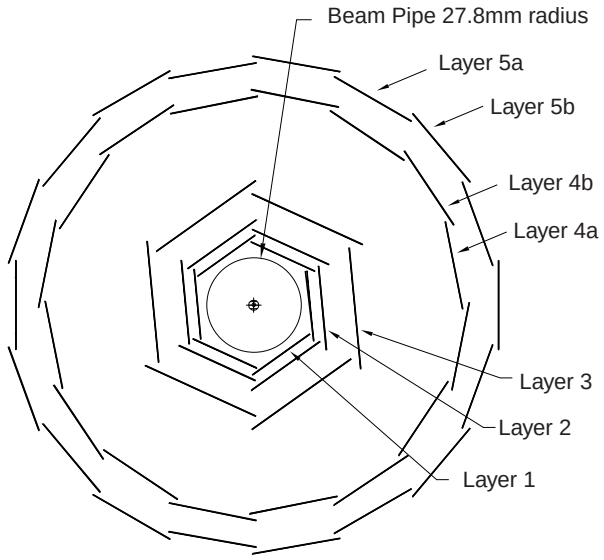

Figure 2.8: Schematic view of SVT: transverse section.

coupled to the electronics via integrated decoupling capacitor. The detectors are operated in reverse mode at full depletion, with bias voltage $V_{\rm bias}$ typically 10 V higher than the depletion voltage $V_{\rm depl}$ (which lies in the range 25 V – 35 V). The strips are biased through polysilicon resistors (4-20 MΩ) and the detector active area is surrounded by an implanted guard ring that collects the edge currents and shapes the electric field in the active region. The n^+ strip's insulation is provided by surrounding each n^+ strip with a p implant called *p-stop*, so as to achieve an inter-strip resistance greater than 100 MΩ at the operating bias voltage. The strip readout pitch varies with the layer (1-5) and the side of the sensors (z, ϕ) from a minimum of 50 μm to a maximum of 210 μm.

2.3.2 Detector performance

Hit efficiency and resolution

The SVT hit efficiency is determined by comparing the number of hits found by a half-module and assigned to a reconstructed track with the number of tracks that cross the half-module. Excluding 5 out of 208 defective readout sections, the combined hardware and software efficiency is measured to be about 97%.

Figure 2.3.2 shows the measured SVT spatial hit resolution in z and $r-\phi$ for the five layers, as a function of the track incident angle with respect to the silicon wafer plane. The resolution is determined from the distribution of the distance in the wafer plane between the hit and the track trajectory of high-momentum tracks. The track trajectory uncertainty contribution is subtracted to obtain the hit resolution, which varies between 15 and 50 microns.

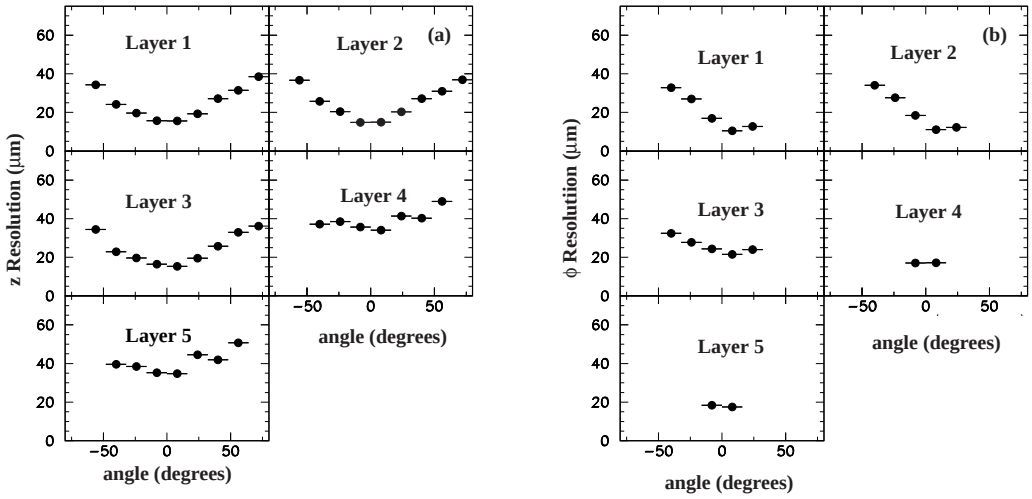

Figure 2.9: SVT hit resolution in the z (a) and ϕ (b) coordinate, in microns.

Tracking efficiency and track parameter resolution

A comparison of the detected slow pion spectrum with the Monte Carlo prediction is presented in Fig. 2.3.2 [43]. Based on this agreement, the detection efficiency is estimated to be 20% for particles with transverse momenta of 50 MeV/c, rapidly increasing to over 80% at 70 MeV/c.

For the purpose of most physics analysis, charged tracks are defined by five parameters $(d_0,\ \phi_0,\ \omega,\ z_0,\ \tan\lambda)$ at the track's point of closest approach (POCA) to the z axis, and the associated error matrix. d_0 and z_0 are the distances from the origin to this POCA in the transverse (x, y) plane and along the z axis respectively. ϕ_0 is the angle between the transverse component of the track tangent vector at this POCA and the x axis. λ is the

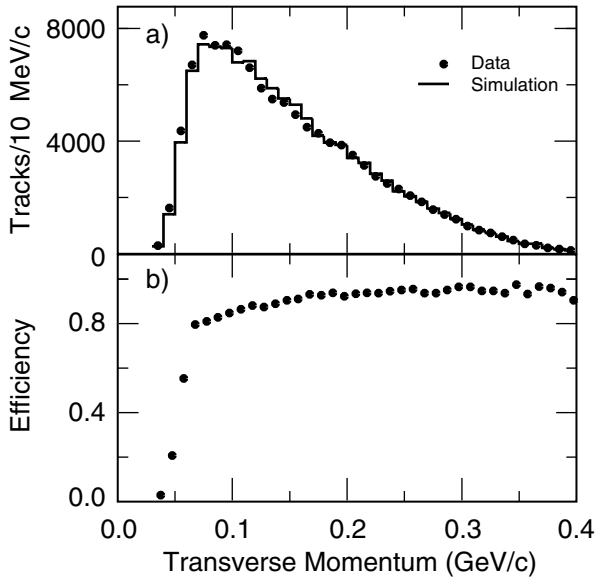

Figure 2.10: Monte Carlo studies of low momentum tracks in the SVT: (a) comparison between data and simulation of the transverse momentum spectrum of soft pions in $D^{*+} \to D^0\ \pi^+$, and (b) efficiency for slow pions detection estimated from simulated events.

angle between the transverse plane and the track tangent vector at this POCA (the so called "dip" angle). ω is the curvature of the track. The charge of the track is incorporated in the signing convention for ω, while the sign of d_0 is determined from the angular momentum of the track w.r.t. the x axis. d_0, ϕ_0, z_0 and $\tan\lambda$ resolutions are dominated by the resolution of the SVT, while ω (and therefore p_T) resolution is dominated by the drift chamber. Track parameter resolution is monitored online in promptly reconstructed Bhabha and $\mu^+\mu^-$ events and is further investigated offline, after the data is fully reconstructed, on tracks in hadronic events or in dedicated cosmic ray runs. Figure 2.11 shows the d_0, z_0, ϕ_0 and $\tan\lambda$ resolutions determined from cosmic ray muons with transverse momenta above 3 GeV/c: they are measured to be

$$\sigma_{d_0} = 23\,\mu\text{m}, \qquad \sigma_{\phi_0} = 0.43\,\text{mrad}$$

$$\sigma_{z_0} = 29\,\mu\text{m}, \qquad \sigma_{\tan\lambda} = 0.53 \cdot 10^{-3}$$

Figure 2.3.2 [48] shows the d_0 and z_0 resolutions as a function of p_T as determined from tracks in hadronic events.

For this study, the tracks not being examined were fit to the same vertex, and the d_0 and z_0 with respect to this vertex were calculated. These were accumulated and a Gaussian fit was made to the negative part of the distribution (particle lifetime can contribute to the positive part of both the d_0 and z_0 distributions). Requirements were also made on event thrust and vertex χ^2 to reduce the effect of decay lifetimes on this measurement.

The contributions from the vertex errors were accumulated and fit for, and removed from the measured resolutions in quadrature. The d_0 and z_0 resolutions measured are about 25 and 40 μm respectively at $p_T = 3\,\mathrm{GeV}/c$, in good agreement with resolutions measured in cosmic ray studies.

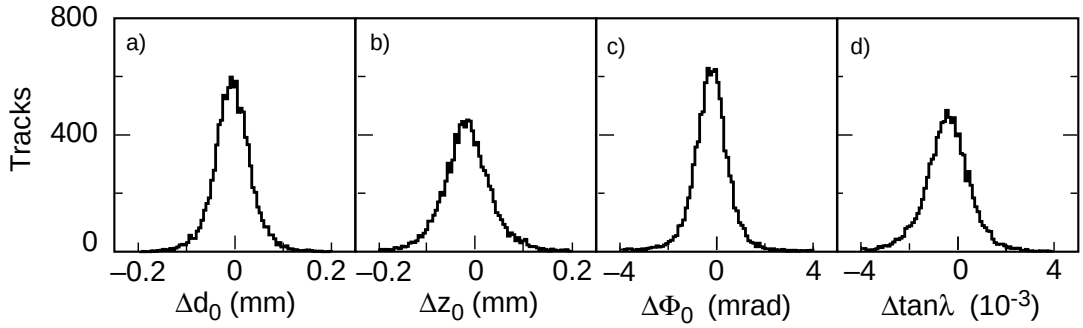

Figure 2.11: Distributions of the differences between the fitted track parameters of the two halves of cosmic ray muons, with transverse momenta above $3\,\mathrm{GeV}/c$.

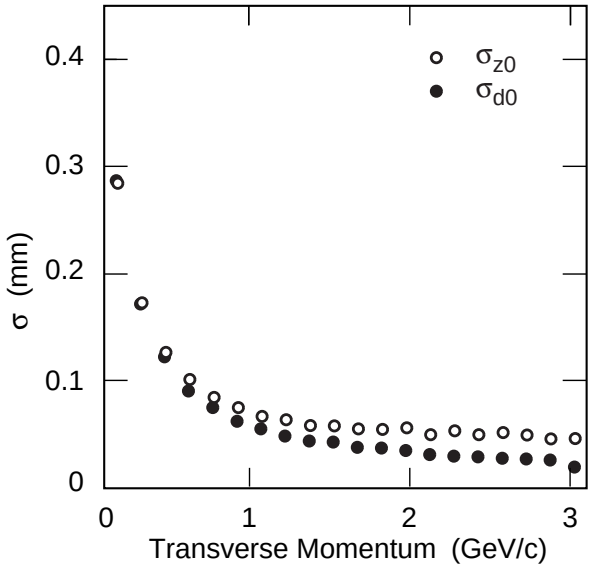

Figure 2.12: Impact parameter resolution of tracks reconstructed in multi-hadron events in the xy plane and along z for tracks in multi-hadron events as a function of transverse momentum.

$\mathrm{d}E/\mathrm{d}x$ resolution

Limited particle ID information for low momentum particles that do not reach the drift chamber and the Čerenkov detector is provided by the SVT through the measurement of the specific ionization loss, $\mathrm{d}E/\mathrm{d}x$, as derived from the total charge deposited in each silicon layer. It is computed as a truncated mean from the lowest 60% of the individual

dE/dx measurements for tracks with at least 4 associated SVT hits. The resulting SVT dE/dx distribution as a function of momentum is shown in Fig. 2.13 [49]. The superimposed Bethe-Bloch curves for the individual particle species have been determined using various particle control samples. The resolution achieved to date is typically about 14% for minimum ionizing particles, and a 2σ separation between kaons and pions can be achieved up to momenta of 500 MeV/c.

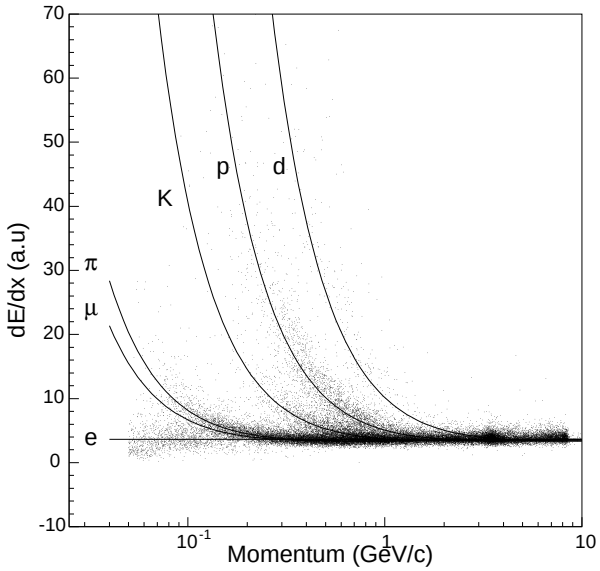

Figure 2.13: Energy loss per unit length (dE/dx) as measured in the SVT as a function of momentum. The enhancement of protons is due to beam-gas interactions. The vertical scale is arbitrary.

2.4 The Drift Chamber

The DCH sub-detector is the main tracking device for charged particles with transverse momenta p_T above $\approx 120\,\mathrm{MeV}/c$, providing the measurement of p_T from the curvature of the particle's trajectory inside the 1.5 T solenoidal magnetic field.

The DCH also allows the reconstruction of secondary vertexes located outside the silicon detector volume, such as those from $K^0_S \to \pi^+\pi^-$ decays. For this purpose, the chamber is able to measure not only the transverse coordinate, but also the longitudinal (z) position of tracks with good ($\sim 1\,\mathrm{mm}$) resolution. Good z resolution also aids in matching DCH and SVT tracks and in projecting tracks to the DIRC and the calorimeter.

For low momentum particles the DCH provides PID by measurement of ionization loss (dE/dx), thus allowing for K/π separation up to $\approx 700\,\mathrm{MeV}/c$. This capability is complementary to that of the DIRC in the barrel region, while it is the only mean to discriminate between different particle hypotheses in the extreme backward and forward directions which fall outside of the geometric acceptance of the DIRC.

Finally, the DCH provides real-time information to the charged particle trigger.

2.4.1 Detector layout

The final design adopted for the Drift Chamber, illustrated in Fig. 2.14, consists of a 280 cm-long cylinder located within the volume inside the DIRC and outside the PEP-II support tube [50]. The inner radius is 23.6 cm and the outer radius is 80.9 cm. To take into account PEP-II's asymmetric boost, the center of the chamber is displaced in the forward direction with respect to the IP by 36.7 cm, thus increasing the acceptance for forward-going tracks. The active volume provides charged particle tracking over the polar angle range $17.2° < \theta_{\rm LAB} < 152.6°$.

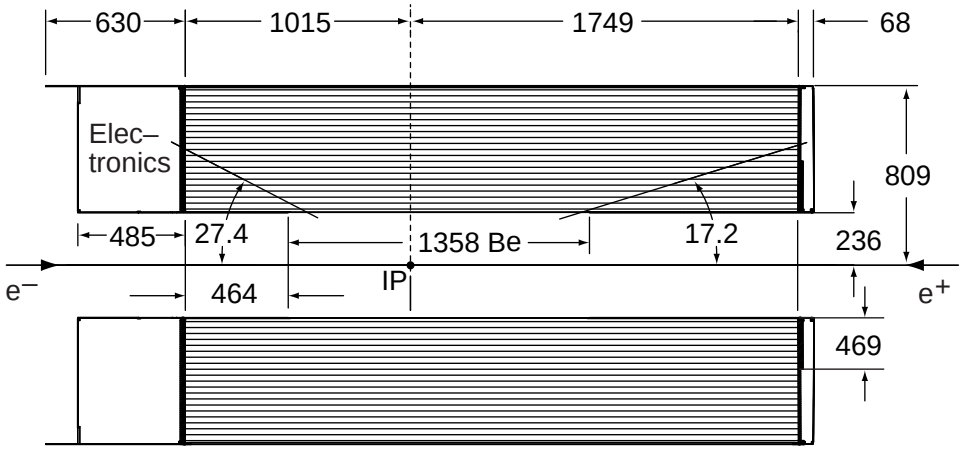

Figure 2.14: *BABAR* DCH side view. Lengths are in mm, angles in degrees.

The drift system consists of 7104 hexagonal cells, approximately 1.8 cm wide by 1.2 cm high, arranged in 40 concentric layers. Each hexagonal cell consist of one sense wire surrounded by six field-shaping wires, as shown in Fig. 2.15.1. In such a configuration, an approximate circular symmetry of the equipotential contours is reached over a large portion of the cell. The field wires are at ground potential while high positive voltage is applied to the sense wire. The 40 layers are grouped by 4 into super-layers. Figure 2.15.2 shows the four innermost super-layers. A complete symmetry along the z-axis does not allow the track position reconstruction along that direction. For this reason two different wire types are used: the type wire A, parallel to the z-axis, provides position measurements in the x-y plane, while longitudinal position information is obtained with wires placed at small angles with respect to the z-axis (U or V wire type) (see Fig. 2.15.2). Sense and field wires have the same orientation in each super-layer and are alternating following the scheme AUVAUVAUVA. Super-layers are also used for a quick local segment finding as the first step in L1 pattern recognition.

The 40 layers provide up to 40 spatial and ionization loss measurements for charged

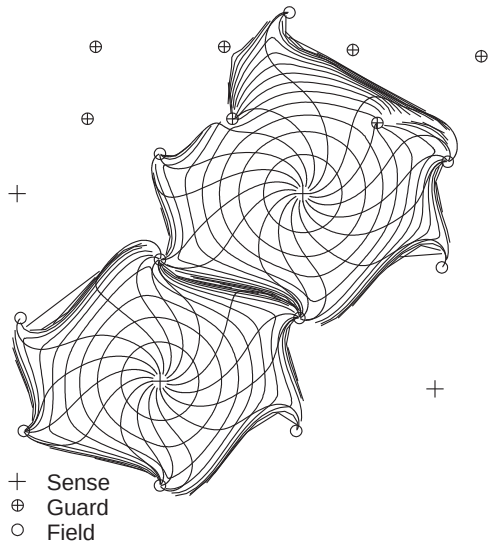

2.15.1: DCH cells structure with 100 ns isochrones.

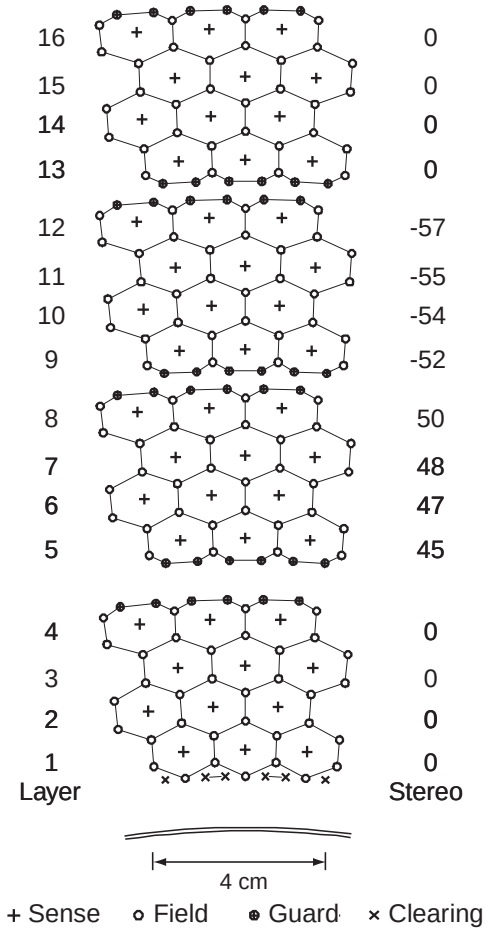

2.15.2: DCH cells configuration in the first 16 layers.

Figure 2.15: *BABAR* DCH cells configuration. The plus signs, open circles, filled circles and crosses denote sense wires, field wires, guard wires and clearing wires, respectively. In the right plot, lines have been added between field wires to aid in visualisation of the cells, and the numbers on its right side give the stereo angles (mrad) of sense wires in each layer. The 1 mm-thick beryllium inner cylinder is also shown inside the first layer.

particles with p_T greater than 180 MeV/c. In order to reduce the impact of multiple scattering on p_T resolution, material within the chamber volume has been minimized (0.2% X_0) using low-mass aluminum field-wires and a helium-based gas mixture. The main properties of the gas system are listed in Table 2.4.1. For the helium-isobutane gas mixtures under consideration, a resolution of around 7% has been achieved for the dE/dx measurement, allowing π/K separation up to 700 MeV/c. The inner wall has been kept thin (0.28% X_0) to improve the contribution of the high-precision measurement in the outer layer of the SVT to the p_T resolution and minimize backgrounds due to photon conversions in the chamber wall. Material in the outer wall has also been minimized (0.6%

X_0) so as not to degrade the DIRC and the EMC performances.

Parameter	Values
Mixture He : C_4H_{10}	80:20
Radiation Length	807 m
Primary Ions (m.i.p.)	21.2/cm
Drift Velocity	22 μm/ ns
Avalanche gain	5×10^4
Lorentz Angle	32°
dE/dx Resolution	6.9%

Table 2.4: Properties of helium-isobutane gas mixture at atmospheric pressure and 20°C (in *BABAR* the gas is operated at a small over pressure of 4 mbar). The drift velocity is given for operation without magnetic field, while the Lorentz angle is stated for a 1.5 T magnetic field. The anode-cathode operating potential difference is 1960 V.

2.4.2 Detector performance

Tracking efficiency and resolution

The drift chamber reconstruction efficiency has been measured on data in selected samples of multi-track events by exploiting the fact that tracks can be reconstructed independently in the SVT and the DCH. The absolute drift chamber tracking efficiency is determined as the fraction of all tracks detected in the SVT which are also reconstructed by the DCH when they fall within its acceptance. Its dependency on the transverse momentum and polar angle is shown in Fig. 2.4.2 [43]. At the design voltage of 1960V the reconstruction efficiency of the drift chamber averages $98 \pm 1\%$ for tracks above 200 MeV/c and polar angle $\theta > 500$ mrad (29°). At the typical operating voltage of 1930V it decreases by about 2%.

The p_T resolution, directly related to the curvature (ω) resolution, is measured as a function of p_T in cosmic ray studies (see Fig. 2.17 [51]). The data are well represented by a linear function:

$$\frac{\sigma_{p_T}}{p_T} = (0.13 \pm 0.01)\% \cdot p_T + (0.45 \pm 0.03)\% \,, \tag{2.1}$$

where p_T is measured in GeV/c. The first contribution, dominating at high p_T, comes from the curvature error due to finite spatial measurement resolution; the second contribution, dominating at low momenta, is due to multiple Coulomb scattering.

dE/dx Resolution

The specific ionization loss dE/dx for charged particles traversing the drift chamber is derived from the total charge deposited in each drift cell. It is computed as a truncated

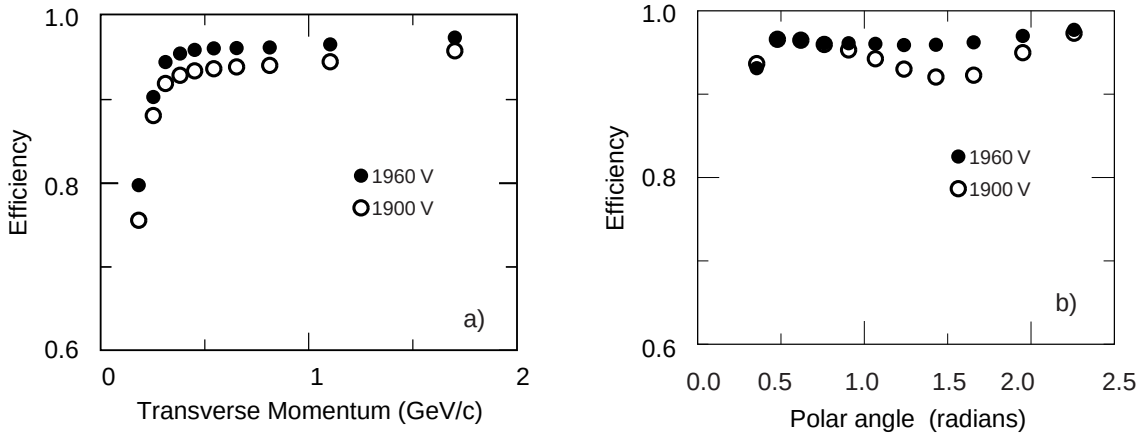

2.16.1: Track efficiency .vs. p_T

2.16.2: Track efficiency .vs. θ

Figure 2.16: Track reconstruction efficiency in the drift chamber at operating voltages of 1900 V and 1960 V, as a function of transverse momentum (p_T) on left plot and of polar angle (θ) on right one.

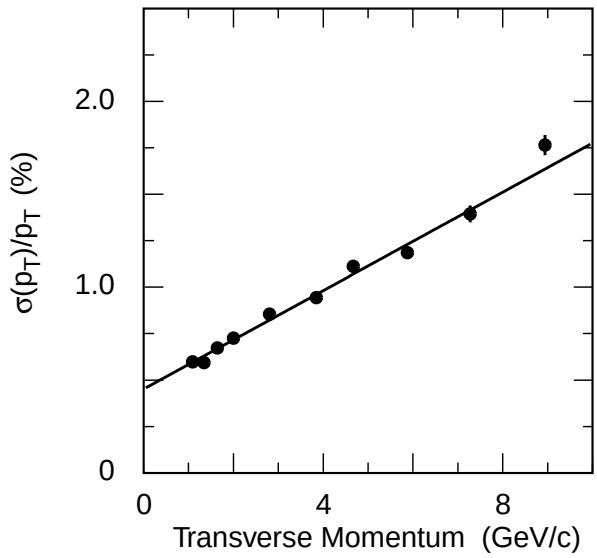

Figure 2.17: p_T resolution determined from cosmic ray muons.

mean from the lowest 80% of the individual $\mathrm{d}E/\mathrm{d}x$ measurements; various corrections are applied to remove several sources of bias (for instance, changes in gas gain due to temperature and pressure variations) that would degrade the accuracy of the primary ionization measurement. Figure 2.18.1 shows the distribution of the reconstructed and corrected $\mathrm{d}E/\mathrm{d}x$ from the drift chamber as a function of track momenta. The superimposed Bethe-Bloch curves for the individual particle species have been determined using various particle control samples. The resolution achieved to date is typically about 7.5% (as shown in the right plot of Fig. 2.18.2 for $e^{\pm}$ from Bhabha scattering), limited by the number of samplings and Landau fluctuations. A 3σ separation between kaons and pions

can be achieved up to momenta of about 700 MeV/c [51].

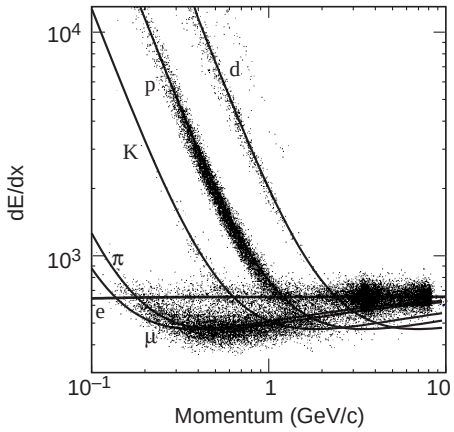

2.18.1: Reconstructed dE/dx as a function of track momenta

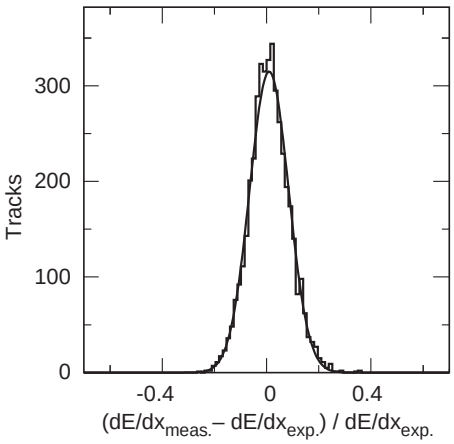

2.18.2: Difference between the measured and expected dE/dx for $e^{\pm}$ from Bhabha scattering

Figure 2.18: dE/dx plots .vs. momentum and resolution.

2.5 The Detector of Internally Reflected Čerenkov radiation

The PID at low momenta exploits primarily the dE/dx measurements in the DCH and SVT. However, above the threshold of 700 MeV/c, the dE/dx information does not allow to separate pions and kaons. *BABAR* has therefore a dedicated PID sub-detector. The DIRC is employed primarily for the separation of pions and kaons from about 500 MeV/c to the kinematic limit of 4 GeV/c. It was designed to be able to provide K/π separation of $\approx 3\sigma$ or greater, for all decay tracks from the pion Čerenkov threshold up to 4.2GeV/c.

2.5.1 Detector layout

The DIRC is a novel type of ring-imaging Čerenkov detector, based on the principle that the magnitudes of angles are maintained upon reflection from a flat surface [52]. Figure 2.19 shows a schematic of the DIRC geometry, while Fig. 2.20 illustrates the principles of light production, transport, and imaging.

The radiator material of the DIRC is synthetic fused silica (refraction index $n = 1.473$) in the form of 144 long, thin bars with regular rectangular cross section. The bars, which are 17 mm-thick, 35 mm-wide and 4.9 m-long, are arranged in a 12-sided polygonal barrel, each side being composed of 12 adjacent bars. The solid angle subtended by the radiator bars corresponds to 94% of the azimuth and 83% of the cosine of the polar angle in the

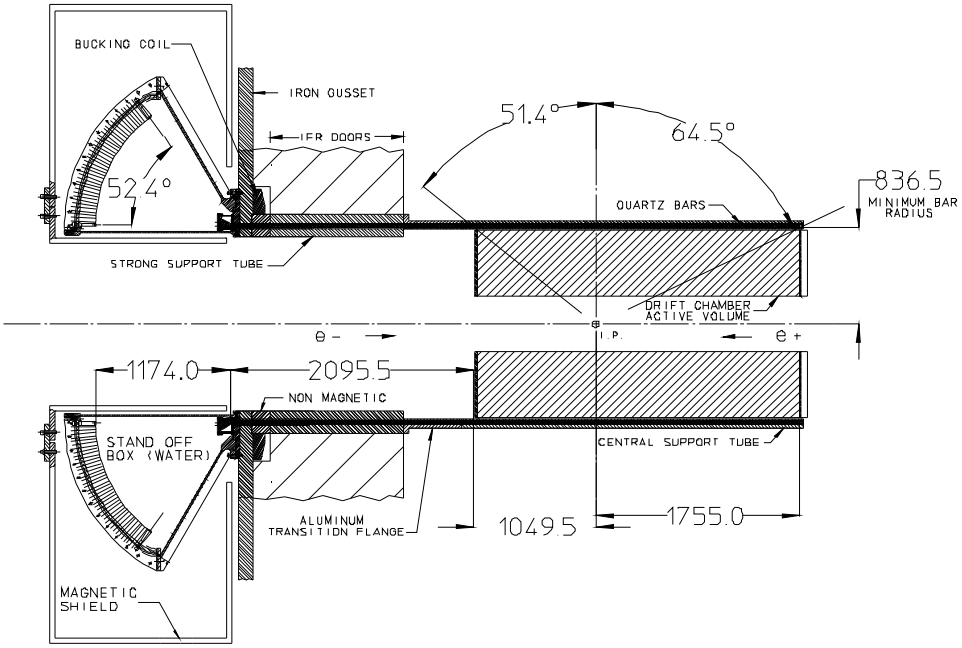

Figure 2.19: Schematics of the DIRC mechanical support structure.

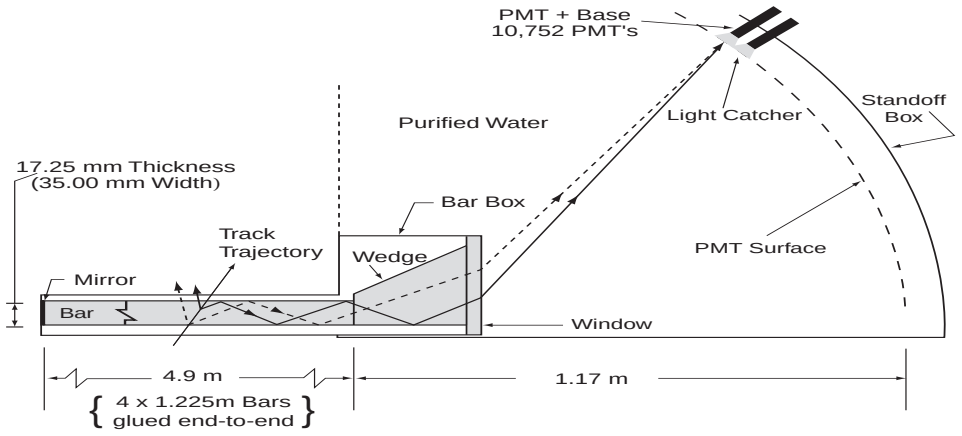

Figure 2.20: Schematics of the DIRC fused silica radiator bar and imaging region.

CM system. The total thickness of the DIRC material (bars and support structure) at normal incidence ($\theta = 90°$) is only 8 cm, corresponding to 17% X_0. Such a thin Čerenkov detector allows, at the same time, a large inner tracking volume, which is needed to achieve the desired momentum resolution and a compact outer electromagnetic calorimeter with improved angular resolution and limited costs.

The bars serve both as radiators and as light pipes for the portion of the light trapped in the radiator by total internal reflection (the internal reflection coefficient of the bar surfaces is greater than 0.9992 per bounce). A charged particle with velocity $v > c/n$, traversing the fused silica bar, generates a cone of Čerenkov photons of half-angle θ_c

with respect to the particle direction, where $\cos\theta_c = 1/\beta n,\ \beta = v/c$. For particles with $\beta \approx 1$, some photons will always lie within the total internal reflection limit and will be transported to either one or both ends of the bar, depending on the particle incident angle. To avoid having to instrument both bar ends with photon detectors, a mirror is placed at the forward end, perpendicular to the bar axis, to reflect incident photons to the backward (instrumented) bar end.

Once photons arrive at the instrumented end, most of them emerge into an expansion region filled with 6000 litres of purified water ($n = 1.346$), called the stand-off box. A fused silica wedge at the exit of the bar reflects photons at large angles and thereby reduces the size of the required detection surface. The photons are detected by an array of densely packed photomultiplier tubes (PMTs), each surrounded by reflecting "light catcher" cones to capture light which would otherwise miss the PMT active area. The PMTs, arranged in 12 sectors of 896 photo-tubes each, have a diameter of 29 mm and are placed at a distance of about 1.2 m from the bar end. The expected Čerenkov light pattern at this surface is essentially a conic section, whose cone opening-angle is the Čerenkov production angle modified by refraction at the exit from the fused silica window.

2.5.2 Detector performance

In the absence of correlated systematic errors the resolution $\sigma_{\theta_C,\mathrm{track}}$ on the track Čerenkov angle scale as

$$\sigma_{\theta_C,\mathrm{track}} = \sigma_{\theta_C,\gamma}/\sqrt{N_\gamma}\ , \tag{2.2}$$

where $\sigma_{\theta_C,\gamma}$ is the single photon Čerenkov angle resolution and N_γ is the number of photons detected.

The single photon Čerenkov angle resolution has been measured in di-muon events to be 10.2 mrad (see left plot on Fig. 2.21 [43]). The main contributions to it come from the geometry of the detector (the size of the bars, the diameter of the PMTs, and the distance between the bars and the PMTs give a 7 mrad contribution) and from the spread of the photon production angle, dominated by a 5.4 mrad chromatic term.

Figure 2.22 shows the number of photons detected as a function of the polar angle. It increases from a minimum of about 20 at the center of the barrel ($\theta \approx 90°$) to well over 50 in the forward and backward directions, corresponding to the fact that the path-length in the radiator is longer for tracks emitted at large dip angles (therefore the number of Čerenkov photons produced in the bars is greater) and the fraction of photons trapped by total internal reflection rises. This feature is very useful in the *BABAR* environment, where - due to the boost of the CM - particles are emitted preferentially in the forward direction. The bump at $\cos\theta = 0$ is a result of the fact that for tracks at small angles internal reflection of the Čerenkov photons occurs in both the forward and backward direction. The small decrease of the number of photons from the backward direction to

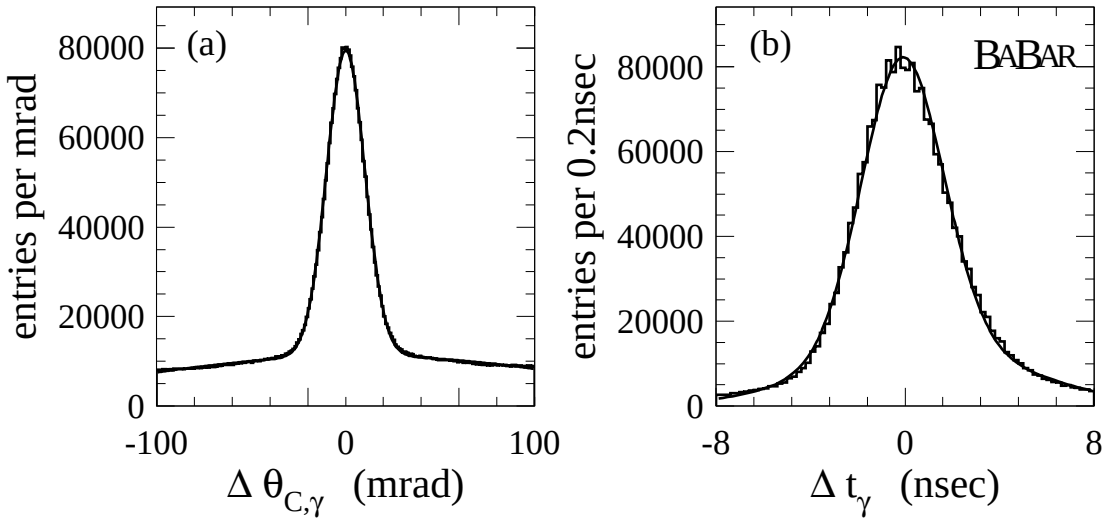

Figure 2.21: Difference between the measured and the expected Čerenkov angle for single photons (left plot) and the measured and expected photon arrival time (right plot), as measured in muons produced in di-muon events.

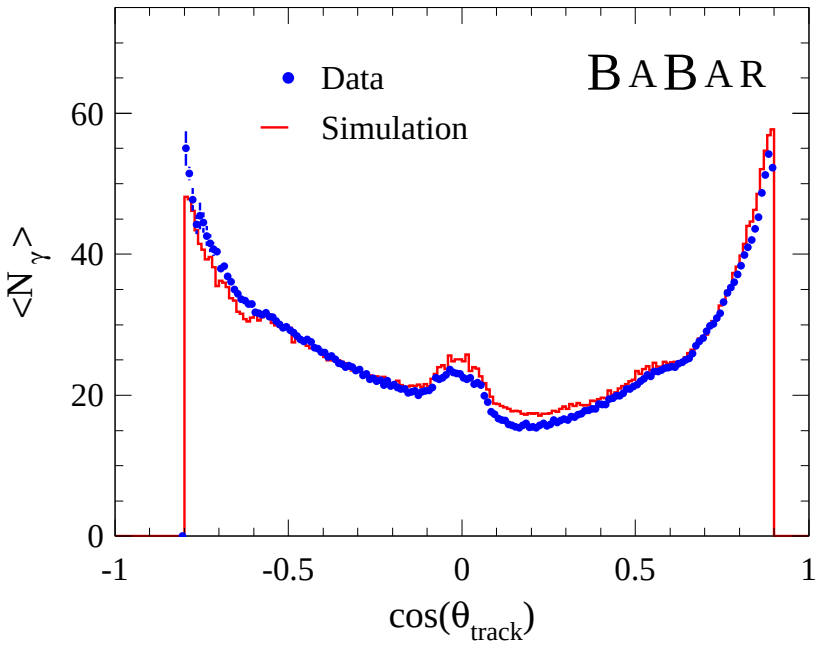

Figure 2.22: Number of detected photo-electrons versus track polar angle for reconstructed di-muon events in data and simulation.

the forward one is a consequence of the photon absorption along the bar before reaching the stand-off box in the backward end.

The combination of the single photon Čerenkov angle resolution, the distribution of the number of detected photons versus polar angle, and the polar angle distribution of

charged tracks yields a typical track Čerenkov angle resolution which is about 2.5 mrad for muons in di-muon events. A similar average resolution is found for charged kaons and pions in a sample of more than 400,000 $D^{*\pm} \to D^0\pi^\pm(D^0 \to K^\mp\pi^\pm)$ decays reconstructed in data, where $K^\mp/\pi^\pm$ tracks are identified through the charge correlation with the $\pi^\pm$ from the $D^{*\pm}$ decay. From the measured single track resolution .vs. momentum and the difference between the expected Čerenkov angles of charged pions (θ_C^π) and kaons (θ_C^K), the pion-kaon separation power of the DIRC, $|\theta_C^K - \theta_C^\pi|/\sigma_{theta_C}$, can be inferred. As shown in Fig. 2.23, the separation between kaons and pions at 3 GeV/c is about 4.3 σ.

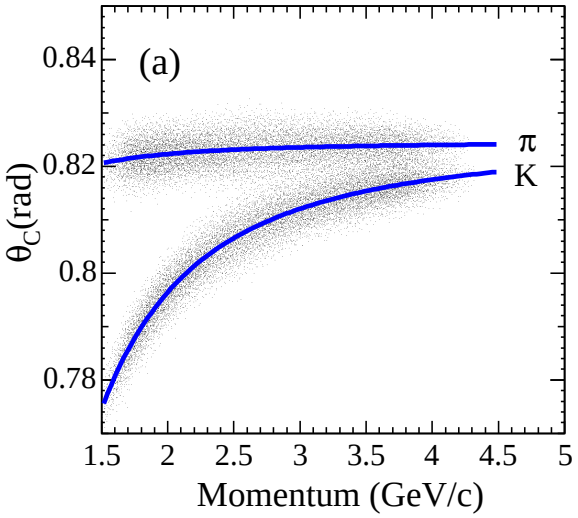

2.23.1: The measured Čerenkov angle for pions (upper band) and kaons (lower band) from $D^* \to D^0\pi, D^0 \to K\pi$ decays reconstructed in data. The curves show the expected angle θ_C as a function of LAB momentum, for the K and π mass hypothesis.

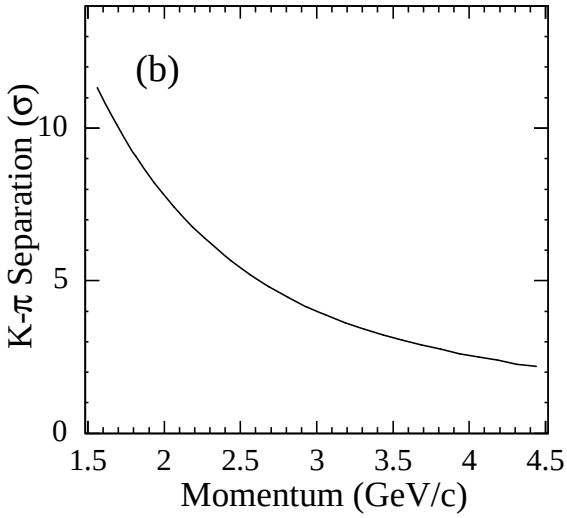

2.23.2: The average difference between the expected value of θ_C for kaons and pions, divided by the uncertainty, as a function of momentum.

Figure 2.23: Plots of K/π separation obtained with DIRC detector

The time taken for the photon to travel from the point of origin to the PMT is also related to the photon propagation angle $(\alpha_x, \alpha_y, \alpha_z)$ with respect to the bar axis. As the track position and angles are known from the tracking system, these three α angles can be used to (over-)determine the Čerenkov angle θ_c. This over-constraint on the angles is particularly useful in suppressing hits from beam-generated background and from other tracks in the same event and also in resolving some ambiguities in the association between the PMT hits and the track (for instance, the forward-backward ambiguity between photons that have or have not been reflected by the mirror at the forward end of the bars). The relevant observable to distinguish between signal and background photons is the difference between the measured and expected photon time, δt_γ. It is calculated for each photon using the track-time of the PMT and the photon propagation time within the bar and the water filled stand-off box. The resolution on this

quantity, as measured in di-muon events (see right plot on Fig. 2.21), is 1.7 ns, close to the intrinsic 1.5 ns transit time spread of the photo-electrons in the PMTs. Applying the time information substantially improves the correct matching of photons with tracks and reduces the number of accelerator induced background hits by approximately a factor 40, as can be seen in Fig. 2.5.2 [53].

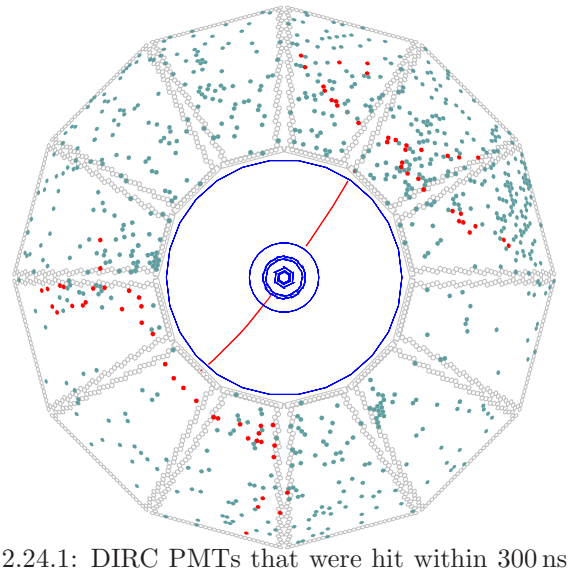

2.24.1: DIRC PMTs that were hit within 300 ns of trigger window.

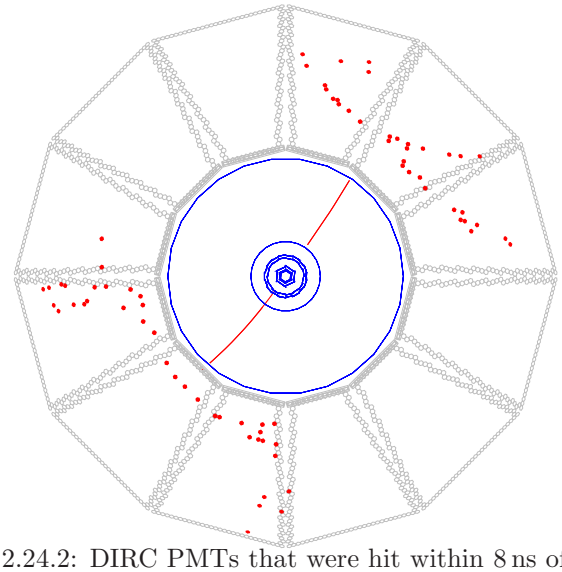

2.24.2: DIRC PMTs that were hit within 8 ns of the expected Čerenkov photon arrival time.

Figure 2.24: Display of the DIRC PMTs for one $e^+e^- \to \mu^+\mu^-$ event reconstructed in *BABAR* with two different time cuts.

2.6 The Electromagnetic Calorimeter

The *BABAR* EMC sub-detector is designed to detect and measure electromagnetic showers with high efficiency and very good energy and angular resolution over an energy range between 20 MeV (low-energy photons from π^0 mesons originating in B decays) and 9 GeV (electrons from Bhabha scattering). It is also the primary sub-detector providing electron-hadron separation.

Energy deposit clusters in the EMC with lateral shape consistent with the expected pattern from an electromagnetic shower are identified as photons when they are not associated with any charged tracks extrapolated from the SVT and the drift chamber. Otherwise they are identified as electrons, if they are matched to a charged track and the ratio between the energy E measured in the EMC and the momentum p measured by the tracking system is $E/p \approx 1$.

The efficient reconstruction of extremely rare decays of B mesons containing π^0's (e.g. $B^0 \to \pi^0\pi^0$) poses the most stringent design requirements on energy resolution of order

1% while excellent photon efficiency at low energy ($\sim$ 20 MeV) is required for efficient reconstruction of B meson decays containing multiple π^0 and η. Similar precision is required for efficient separation of electrons and hadrons with purities required at the 0.1% level for momentum as low as 500 MeV/c. The π^0 mass resolution is dominated by the energy resolution at low energies (below 2 GeV) and by the angular resolution at high energies (above 2 GeV). The angular resolution is required to be a few milliradians in order to maintain good m_π^0 resolution ($\sigma_{m_\pi^0} \approx 6.5$ MeV) at all energies. The need for high efficiency requires hermetic coverage of the acceptance region while excellent resolution is achieved by minimizing the material in front of and between the active detector elements.

2.6.1 Detector layout

The *BABAR* EMC sub-detector is a total-absorption calorimeter composed of 6580 CsI crystals doped with thallium iodide at about 1000 ppm [54]. The main properties of CsI(Tl) are summarized in Table 2.5: the high light yield and small Molière radius give the excellent energy and angular resolution required, while the short radiation length guarantees complete shower containment at *BABAR* energies with a relatively compact design. Furthermore, the high light yield and peak of the emission spectrum permit an efficient use of a silicon photo-diode readout.

Parameter	Value
Radiation Length	1.86 cm
Molière Radius	3.8 cm
Density	4.53 g/ cm^3
Light Yield	50000 γ/ MeV
Light Yield Temperature Coefficient	0.28%/°C
Peak Emission $\lambda_{\max}$	565 nm
Refractive Index ($\lambda_{\max}$)	1.79

Table 2.5: Properties of CsI(Tl).

Each crystal is a truncated trapezoidal pyramid, with thickness between 29.6 cm (16 X_0) and 32.4 cm (17.5 X_0) and typical front face area 5×5 cm^2, as shown in Fig. 2.25. To minimize the material in front of the calorimeter, the support structure of the crystals (which is made in carbon fiber) and the front-end electronics are located at the outer radius of the EMC. To recover the small fraction of light that is not internally reflected by the crystal surface, each crystal is wrapped with a diffuse reflective material (TYVEK). The scintillation light generated inside each crystal is detected by two independent 2×1 cm^2 silicon PIN photo-diodes epoxied to its rear face. The crystals are arranged quasi-projectively in a barrel structure of 48 θ rows by 120 crystals in azimuth (ϕ), with an

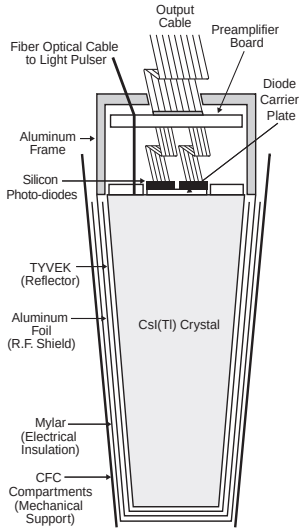

Figure 2.25: Structure of EMC crystal module.

inner radius of 90 cm, as shown in Fig. 2.26. The forward end is closed by a separable

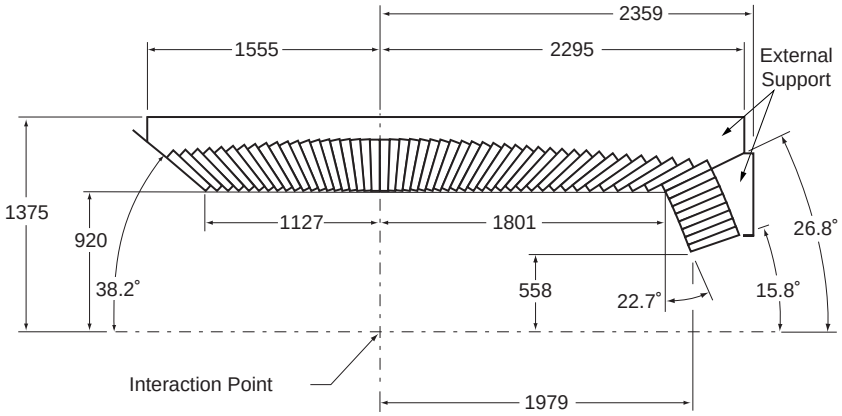

Figure 2.26: EMC side view. Lengths are in mm, angles in degrees.

end-cap capable of holding nine additional rows. This geometry provides full azimuthal coverage, while the polar angle coverage is $15.8^\circ < \theta_{\rm LAB} < 140.8^\circ$.

2.6.2 Detector performance

Energy resolution

The limiting energy resolution of a homogeneous calorimeter is determined by fluctuations in the electromagnetic shower propagation and in the case of the *BABAR* crystal detector is empirically described as the quadratic sum of a stochastic term σ_1 and a constant term σ_2:

$$\frac{\sigma_E}{E} = \sigma_1 \; E^{-\frac{1}{4}} \oplus \sigma_2 \tag{2.3}$$

The stochastic term $\sigma_1 E^{-\frac{1}{4}}$, which is dominant at low energies, arises primarily from fluctuations in photon statistics, but depends also on electronic noise in the readout chain and on the presence of beam-generated background. The constant term σ_2, dominant at higher energies, arises from several effects of which the main are fluctuations in shower containment due to leakage out the rear of the crystal or absorption in the material between and in front of the crystals, as well as uncertainties in the calibrations.

In *BABAR* the energy resolution as a function of energy is measured on data on selected control samples, including electrons and positrons from Bhabha scattering (energies between 3 and 9 GeV), photons from π^0 and η decays (energies below 2 GeV), and from the decay $\chi_{c1} \to J/\psi\gamma$ ($E \approx 500$ MeV). At low energies the resolution is determined through weekly calibrations performed with a radioactive source ($^{16}O^*$) of 6.13 MeV photons. A fit to the resolution dependence on the energy with the empirical parametrization of Equation 2.3, shown in Fig. 2.27.1 [54], yields:

$$\frac{\sigma_E}{E} = \frac{(2.32 \pm 0.30)\%}{\sqrt[4]{E(\mathrm{GeV})}} \oplus (1.85 \pm 0.12)\%, \tag{2.4}$$

The stochastic term is dominant for energies below about 2.5 GeV; above 2.5 GeV the constant term starts to be the limiting factor for the energy resolution.

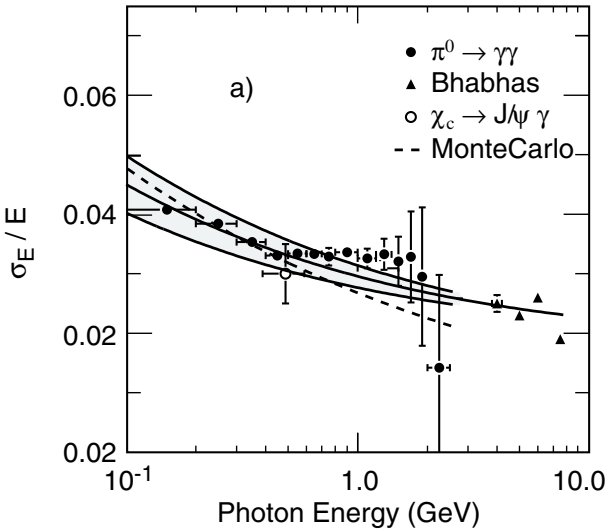

2.27.1: EMC energy resolution measured using photon and electron candidates. The solid curve is a fit to Equation 2.3 and the shaded area denotes the one sigma error on the fit.

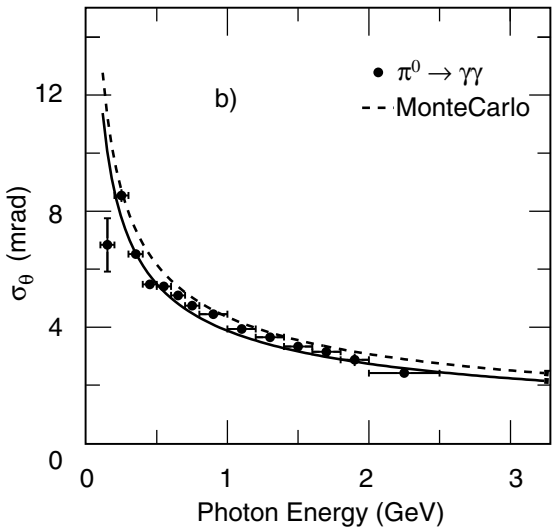

2.27.2: EMC angular resolution measured using photon candidates originating in π^0 and η decays. The solid curve is a fit to Equation 2.5

Figure 2.27: The energy and angular resolution for the *BABAR* EMC.

Angular resolution

The angular resolution is determined by the transverse crystal size and the distance from the interaction point, and improves as the transverse size of the crystal decreases. On the other hand, since the electromagnetic shower has a natural lateral spread of the order of the Molière radius, the energy resolution would degrade if the transverse crystal size were chosen significantly smaller than the Molière radius, due to summing of the electronic noise from several crystals. The best compromise is obtained by choosing the transverse size of the crystals comparable to the Molière radius: this choice allows the required angular resolution (few milliradians) at low energies while maintaining the total number of crystals and readout channels limited to an acceptable noise and cost level.

Figure 2.27.2 [54] shows the angular resolution measured as a function of energy. The decays of π^0 and η candidates in which the two photons in the decay have approximately equal energy are used to infer angular resolution. It varies between about 12 mrad at low energies and 3 mrad at high energy. The data fit the empirical parametrization:

$$\sigma_{\theta,\phi} = \left(\frac{(3.87 \pm 0.07)}{\sqrt{E(\,\mathrm{GeV})}} + (0.00 \pm 0.04) \right) \mathrm{mrad} \tag{2.5}$$

π^0 Mass and Width

Figure 2.28 [43] shows the two-photon invariant mass for π^0 candidates. The π^0 candidates are taken from hadronic B meson decays. The invariant mass is stable to less than 1% over the full photon energy range. The width of 6.9 MeV/c^2 compares to a Monte Carlo estimate of 6.8 MeV/c^2 in hadronic B meson events.

Electron-Hadron separation

Electron-hadron separation is accomplished by use of the shower energy, lateral shower shape and incident track parameters. The comparison of shower energy and incident momentum (E/p) is the most significant separation variable. More details will be given on Sec. 3.2.1. Figure 2.29 [43] shows the typical electron efficiency and pion mis-identification rate versus the track momentum and polar angle. The efficiency of electron identification is measured using electrons from radiative Bhabhas and $\gamma\gamma \to e^+e^-$ events. The pion mis-identification probability is measured in three-prong τ decays.

2.7 The Instrumented Flux Return

The Instrumented Flux Return (IFR) is designed to identify muons and neutral hadrons (primarily K_L^0 and neutrons). The principal requirements for IFR are large solid angle coverage, good efficiency and high background rejection for muons down to momenta

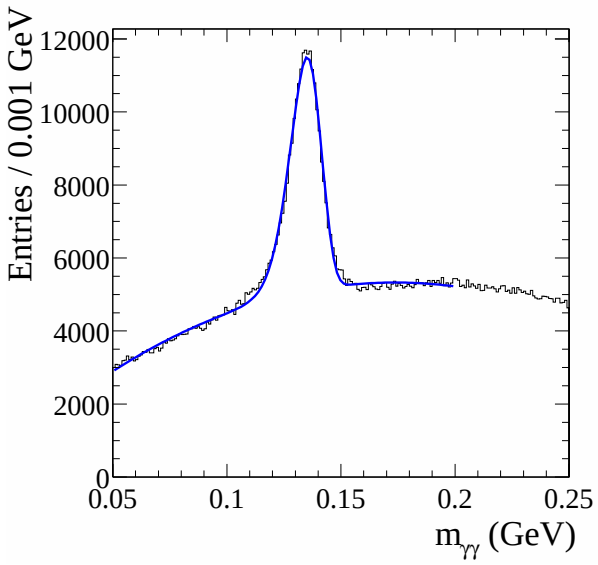

Figure 2.28: The π^0 mass peak reconstructed from photon candidates in hadronic events. The photon candidates are required to have an energy of at least 30 MeV and the energy of the π^0 must be greater than 300 MeV to reduce combinatorial backgrounds. The solid line is a fit to the data.

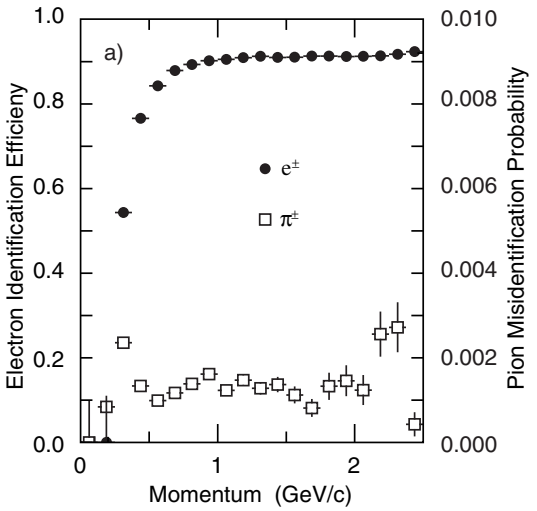

2.29.1: Electron efficiency and pion mis-identification .vs. momenta

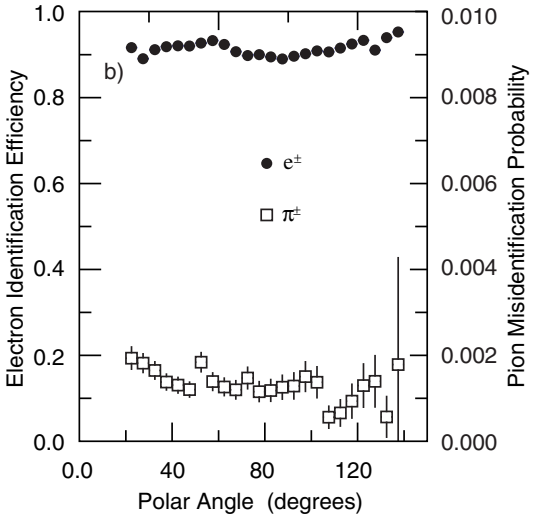

2.29.2: Electron efficiency and pion mis-identification .vs. polar angle

Figure 2.29: The electron efficiency and pion mis-identification rate for different momenta (left) and polar angles (right).

below 1 GeV/c. For neutral hadrons, high efficiency and good angular resolution are crucial.

2.7.1 Detector layout

The IFR uses the steel flux return of the magnet as muon filter and hadron absorber. Single gap resistive plate chambers (RPC) with two-coordinate readout, operated in limited streamer mode constitute the active part of the detector [55]. RPCs detect streamers from ionising particles via capacitive readout strips. They offer the advantage of simple and low cost construction. Further benefits are large signals and fast response allowing for simple and robust front end electronics and good time resolution, typically 1-2 ns. The position resolution depends on the segmentation of the readout; few millimeters are achievable. A cross section of an RPC is shown schematically in Fig. 2.30. The planar RPCs consist of two bakelite sheets, 2 mm thick and separated by a gap of 2 mm. The bulk resistivity of the bakelite sheets has been especially tuned to $10^{11} - 10^{12} \Omega$ cm. The external surfaces are coated with graphite to achieve a surface resistivity of approximately 100 $k\Omega/\,\mathrm{cm}^2$. These two graphite surfaces are connected to high voltage (approximately 8 kV) and protected by an insulating mylar film. The bakelite surfaces facing the gap are treated with linseed oil to improve performance. The modules are operated in limited streamer mode and the signals are read out capacitively, on both sides of the gap, by external electrodes made of aluminium strips on a mylar substrate.

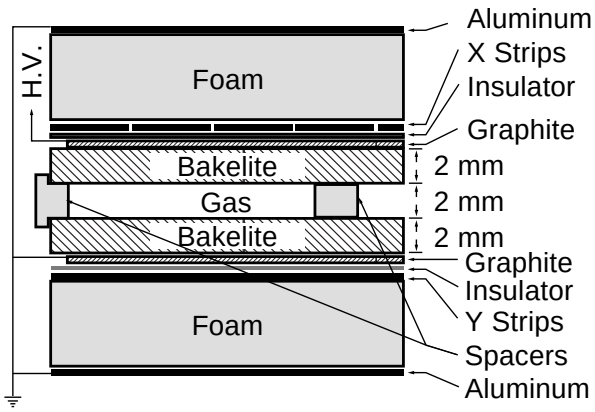

Figure 2.30: Cross section of a planar RPC with the schematics of the HV connection.

The RPC are installed in the gaps of the finely segmented steel of the six barrel sectors and the two end-doors of the flux return, as illustrated in Fig. 2.31. The steel segmentation has been optimised on the basis of Monte Carlo studies of muon penetration and charged and neutral hadron interactions. The steel is segmented into 18 plates, increasing in thickness from 2 cm of the inner 9 plates to 10 cm of outermost plates for a total 65 cm. In addition, two layers of cylindrical RPCs are installed between the EMC and the magnet cryostat to detect particles exiting the EMC.

Soon after the installation (which took place in Summer 1999), the efficiency of a

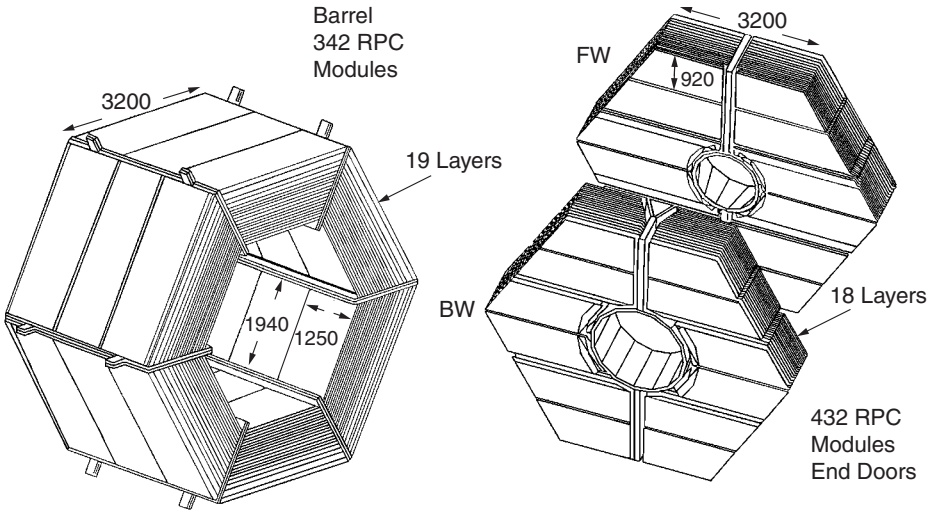

Figure 2.31: Overview of the IFR Barrel sectors and forward and backward end-doors; the shape of the RPC modules and the way they are stratified is shown.

significant fraction of the chambers (initially greater then 90%) has started to deteriorate at a rate of 0.5-1% per month. In order to solve some of the inefficiency problems an extensive improvement program has been developed with multiple solutions. The RPCs in the forward end-cap region have been replaced in Summer 2002 with new ones based on the same base concept but with improved fabrication technique and quality controls. The RPCs in the barrel region have been replaced with limited streamer tube (LST) detectors [56].

The base detector for a limited streamer tube [57] consists of a silver plated wire 100 μm in diameter, located at the center of a squared cell filled with gas. For the *BABAR* LSTs, the cell configuration is 17 mm wide, 15 mm high and 3,8 m long. The wire is gold-plated and six wire holders are equally distributed over the length of a cell to prevent the wire from sagging and touching the cell walls, which are painted with a water-based graphite paint and kept at ground potential. A tube is made of a plastic extruded structure (see a section in Fig. 2.32) consisting of 7 or 8 cells open on the top side and covered with a plastic plane. On the bottom side of this plane conductive strips are installed perpendicular to the wire direction. The extruded structure and the plane are inserted in plastic tubes ("sleeves") of matching dimensions for gas containment. Both end-caps of each tube are equipped with gas connections. Between the cell and the wire a high voltage is applied (5-6 kV) and HV connectors are hosted on one endcap. If a charged particle passes through the cell, the gas is ionised and a streamer builds up, which can be readout from the wire. Simultaneously a signal will be induced on the strips above. The charge on the wire is used for measuring the azimuthal coordinate ϕ coordinate and the induced charge on the strips for the z coordinate, along the beam direction. The r coordinate is taken from the layer position in the segmented steel. Together this gives a

3d information of the hit.

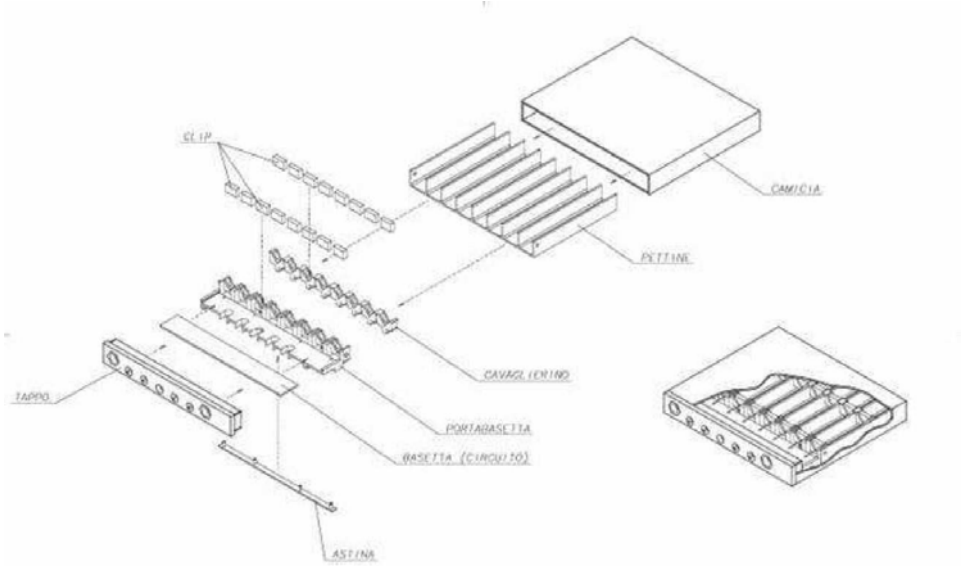

Figure 2.32: Schematic of the "standard" Limited Streamer Tube configuration.

More than one year of R&D studies have been done before choosing the final LST design. R&D program has been concentrated on several critical issues like selection of safe gas mixture, rate capability, wire surface quality and uniformity, aging test and performance of the prototypes. Final results led us to the configuration detailed above and to obtain high performances and to respect the safety requirements it has been chosen a ternary gas mixture of $Ar/C_4H_{10}/CO_2$ (3/8/89)%.

Two of the six sextants of the barrel have been replaced with LSTs in Summer 2004 (affecting data of Run5 and later) while the remaining four sextants have been replaced in Summer 2006 (affecting data of Run6 and later). Extensive quality control studies have been performed before the installation to check the reliability of these detectors, which are expected to operate until the end of the experiment with $\approx 90\%$ efficiency, as measured in cosmic ray runs.

2.7.2 Detector performance

Efficiency

The efficiency of the RPCs and LSTs is evaluated from samples of high momentum muons collected both in normal collision data (from the process $e^+e^- \to \mu^+\mu^-$) and monthly dedicated cosmic ray runs. The efficiency is found by counting the number of times a hit is found in a certain chamber when a charged track is expected to traverse it, based on information from the other chambers and from the tracking system. The absolute efficiency at the nominal working voltage (typically 7.6 kV for RPC, 5.5 kV for LST) is stored in the *BABAR* condition database for use in the event reconstruction software.

Following the installation and commissioning of the IFR system all the RPC modules were tested with cosmic rays and their average efficiency was measured to be approximately 92%, as shown in Fig. 2.33.

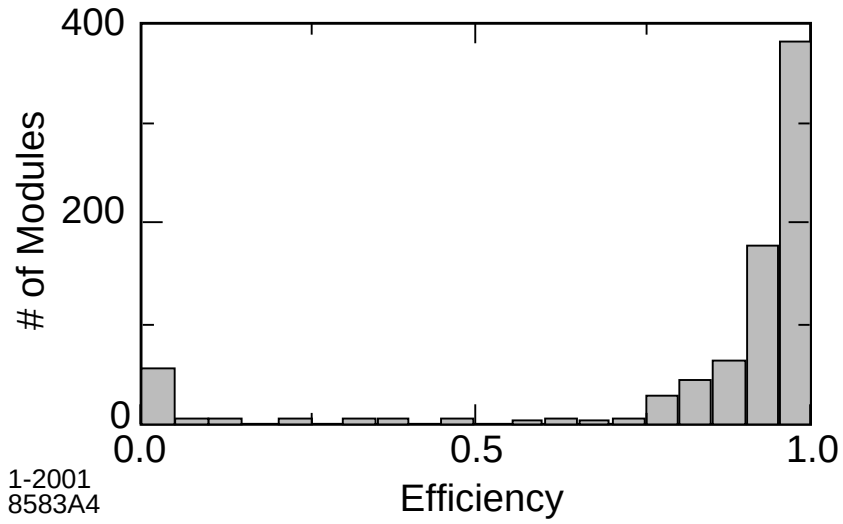

Figure 2.33: Distribution of the efficiency for all RPC modules measured with cosmic rays in June 1999. Some 50 modules were not operational at that time.

As previously said, soon after installation, a progressive, steady efficiency deterioration has been observed in a significant fraction of the RPC chambers. Detailed efficiency studies revealed large regions of very low efficiencies in the modules, but no clear pattern was identified. The overall effects are shown into Fig. 2.34.

Tests to understand the efficiency decrease excluded several possible causes as the primary source of the problem, such as a change in the bakelite bulk resistivity, gas flow or composition. On the other hand, it was found that a number of prototype RPCs developed similar efficiency problems after being operated above a temperature 36°C[3] for a period of two weeks: in some of these modules evidence was found that the linseed oil had accumulated at various spots under the influence of the electric field. After the full installation of the LST detector, a stable muon efficiency was recovered, as shown in Fig. 2.35.

Muon Identification

Muons are identified by measuring the number of traversed interaction lengths in the entire detector and comparing it with the number of expected interaction lengths predicted for a muon of the same momentum. Moreover, the projected intersections of a track with RPC or LST planes are computed and, for each readout plane, all clusters (groups of adjacent

[3]Similar temperatures had been reached inside the iron during the first summer of operations due to the temperature in the experimental hall and the absence of a water cooling system

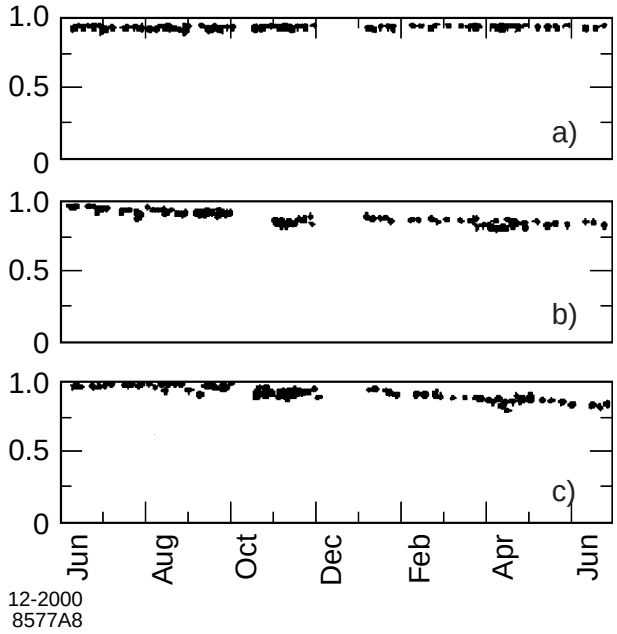

Figure 2.34: Efficiency history for 12 months starting in June 1999 for RPC modules showing different performance. Top: highly efficient and stable. Middle: slow continuous decrease in efficiency. Bottom: faster decrease in efficiency.

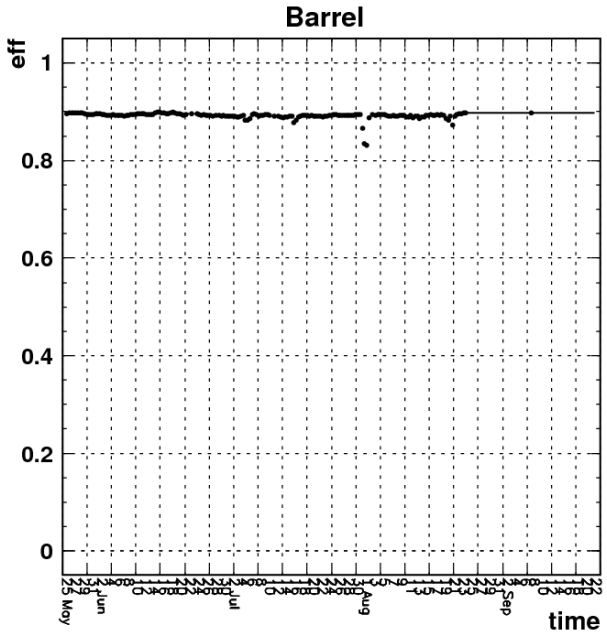

Figure 2.35: Distribution of the efficiency for the LST modules from May 2007 measured with cosmic rays after the full installation.

hits in one of the two readout coordinates) detected within a maximum distance from the predicted intersection are associated with the track. An additional π/μ discriminating power is provided by the average number and the r.m.s. of the distribution of the RPC

and LST hits per layer. The average number of hits per layer is expected to be larger for pions, producing an hadronic interaction, than for muons. Other variables exploiting clusters distribution shapes are constructed and different algorithms, based on all these variables, are applied to select muons. More details will be given on Sec. 3.2.2. The muon selection performance has been tested on samples of kinematically identified muons from $\mu\mu ee$ and $\mu\mu\gamma$ final states and pions from three-prong τ decays and K^0_S decays. The typical muon identification efficiency and the pion mis-identification probability as a function of the track momentum and polar angle are shown in Fig. 2.36.

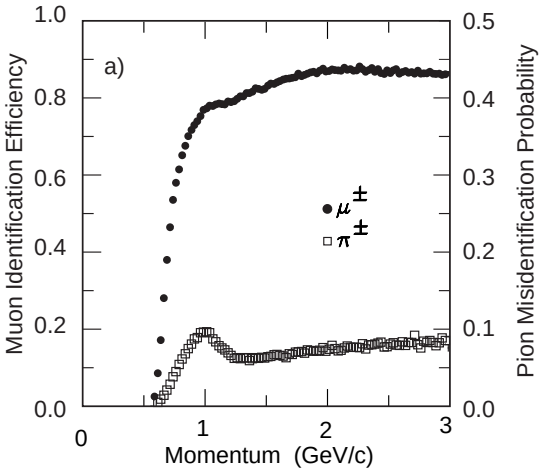

2.36.1: Muon efficiency and pion mis-identification .vs. momenta

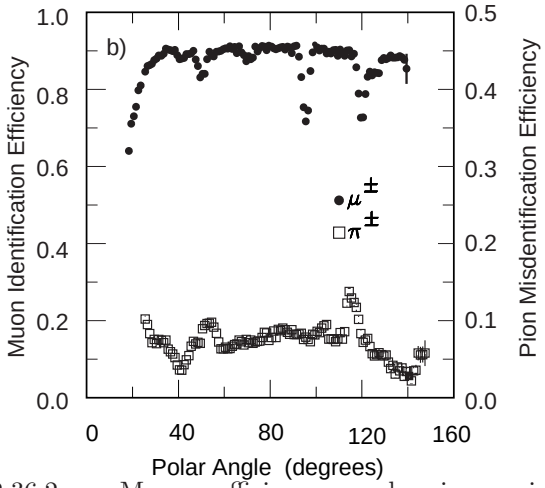

2.36.2: Muon efficiency and pion mis-identification .vs. polar angle

Figure 2.36: The muon efficiency and pion mis-identification rate for different momenta (left) and polar angles (right).

Due to the problems and replacement already described above, the efficiency of IFR detector shows large fluctuations during the years. In Fig. 2.37 the performances on different years data are shown separately for forward endcap and barrel, for low and high momentum tracks.

K^0_L and Neutral Hadron Detection

K^0_L and other neutral hadrons interact in the steel of the IFR and can be identified as clusters that are not associated with a charged track. Since neutral hadrons can interact also in the electromagnetic calorimeter, information from the EMC and the IFR is combined: neutral showers in the EMC are associated with the neutral hadrons detected in the IFR if their production angles, taken from the first interaction point in the detector, are consistent with each other.

The K^0_L detection efficiency and angular resolution are measured on a control sample of K^0_L produced in $e^+e^- \to \phi\gamma \to K^0_L K^0_S \gamma$ processes, where the true K^0_L direction is inferred

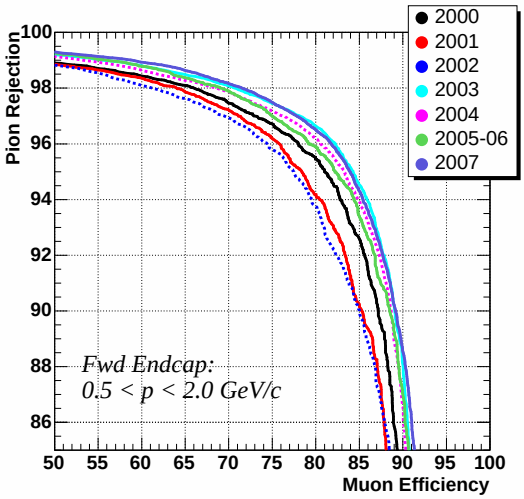

2.37.1: Low momentum track in the forward endcap

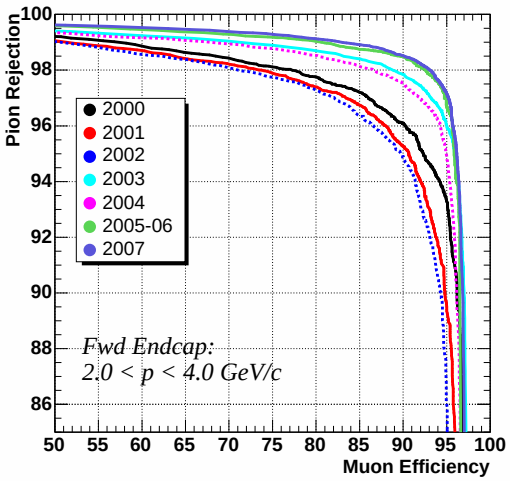

2.37.2: High momentum track in the forward endcap

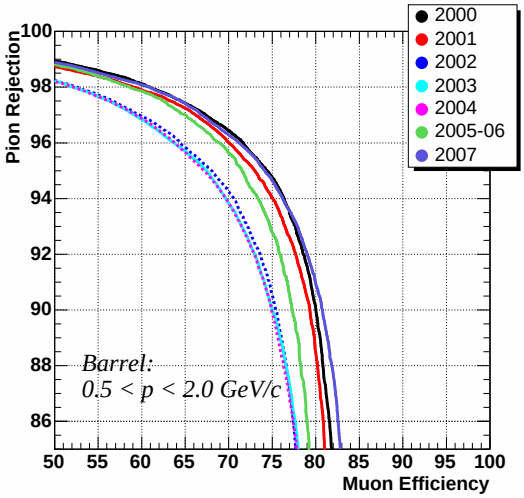

2.37.3: Low momentum track in the barrel

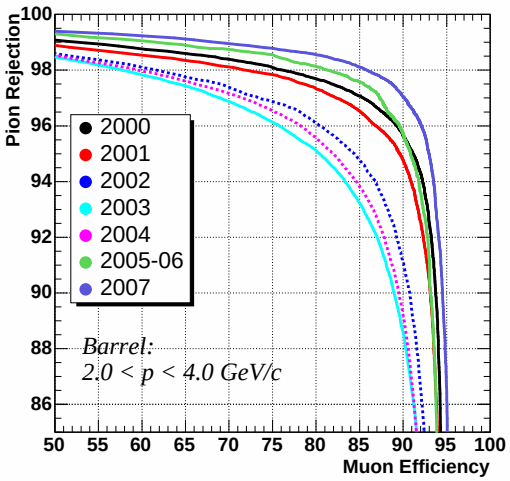

2.37.4: High momentum track in the barrel

Figure 2.37: The muon efficiency .vs. pion mis-identification rate of neural network algorithm for different period of *BABAR* data taking.

from the missing momentum calculated from the particles that are reconstructed in the final state (γ and K^0_S). The K^0_L reconstruction efficiency increases roughly linearly with momentum between 20% at 1 GeV/c and 40% at 4 GeV/c (EMC and IFR combined), and the angular resolution is of the order of 50 mrad.

2.8 The *BABAR* Trigger

The *BABAR* trigger is designed to select a large variety of physics processes rejecting background events and keeping the total event rate around 300 Hz so as not to overload the downstream processing. The trigger must select the physics events of interest with

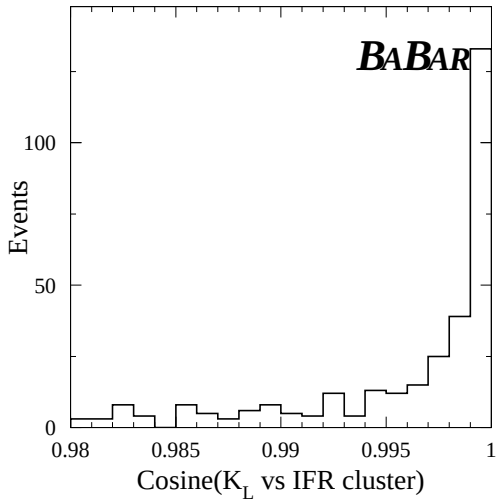

Figure 2.38: Angular difference, $\cos\Delta_\theta$, between the direction of the missing momentum and the closest neutral IFR cluster for a sample of ϕ mesons produced in the reaction $e^+e^- \to \phi\gamma$ with $\phi \to K_L^0 K_S^0$.

very high and/or well understood efficiency, depending on the particular mode. Efficiency, diagnostic and background studies require the trigger to be able to select prescaled samples of Bhabha, di-muon and cosmic events. This kind of studies also demand random beam crossings and events that fail trigger selection criteria.

The trigger system operates as a sequence of two independent stages, the second conditional upon the first. The Level 1 (L1) hardware trigger is performed first at the machine crossing rate. Its goal is to sufficiently reduce that rate to a level acceptable for the Level 3 (L3)[4] software trigger which runs on a farm of commercial processors. The L1 trigger is optimised for simplicity and speed. It consists of a pipelined hardware processor. It is designed to provide an output trigger rate of the order of 5 kHz. The L1 trigger selection is based on a reduced data set from the DCH, EMC and IFR. Its maximum L1 response latency for a given collision is 12 μs. Based on both the complete event and L1 trigger information, the L3 software algorithms select events of interest allowing them to be transferred to mass storage for further analysis. Dedicated L1 trigger processors receive data which is continuously clocked in from the DCH, EMC and IFR detector subsystems. The L1 trigger processor produces a 30 MHz clocked output to the *Fast Control and Timing System* (FCTS) that can optionally mask or prescale input triggers. The arrival of a L1-Accept signal by the data acquisition system causes a window of each sub-system's L1 latency buffer to be read out.

Table 2.6 summarizes the cross sections[5], production rates and L1 trigger rates for the

[4]An intermediate Level 2 software trigger was originally foreseen in the very early step of *BABAR* design, but it was soon merged in the L3 trigger

[5]The e^+e^- cross section refers to events with either the e^+, e^-, or both inside the EMC detection

main physics processes at the $\Upsilon(4S)$ resonance for the luminosity $\mathcal{L} = 3 \cdot 10^{33}$ cm^{-2}s^{-1}.

Event type	Cross section (nb)	Production Rate (Hz)	Level 1 Trigger Rate (Hz)
$\overline{b}$	1.05	3.2	3.2
other $\overline{q}$	3.4	10.2	10.1
e^+e^-	~ 53	159	156
$\mu^+\mu^-$	1.16	3.5	3.1
$\tau^+\tau^-$	0.919	2.8	2.4

Table 2.6: Effective cross sections, production rates and L1 trigger rates for the main physics processes at the $\Upsilon(4S)$ resonance for the luminosity $\mathcal{L} = 3 \cdot 10^{33}\,\mathrm{cm}^{-2}\mathrm{s}^{-1}$.

The Level 3 trigger is implemented as a software that makes use of the complete event information for taking its decision, including the output of the L1 trigger processors and of the FCTS. The selection decision is primarily taken by two set of orthogonal filters, one exclusively based on the DCH information, the other based on the EMC data only. The drift chamber filters select events containing at least one high p_T track ($p_T > 600\,\mathrm{MeV}/c$) or two low p_T tracks, originating from the interaction point. The EMC filters look for events characterized by an effective mass greater than 1.5 GeV. The effective mass is calculated from the cluster energy sums and the energy weighted centroid positions of all clusters in the event in the massless particles hypothesis. The events must also contain at least two clusters with c.m. energy greater than 350 MeV or at least four clusters. Table 2.7 shows the L3 and L1+L3 trigger efficiency for some relevant physics processes, derived from Monte Carlo simulation.

L3 Trigger	$\epsilon_{b\overline{b}}$	$\epsilon_{B\to\pi^0\pi^0}$	$\epsilon_{B\to\tau\nu}$	$\epsilon_{c\overline{c}}$	ϵ_{uds}	$\epsilon_{\tau\tau}$
1 track filter	89.9	69.9	86.5	89.2	88.2	94.1
2 track filter	98.9	84.1	94.5	96.1	93.2	87.6
Combined DCH filters	99.4	89.1	96.6	97.1	95.4	95.5
2 cluster filter	25.8	91.2	14.5	39.2	48.7	34.3
4 cluster filter	93.5	95.2	62.3	87.4	85.5	37.8
Combined EMC filters	93.5	95.7	62.3	87.4	85.6	46.3
Combined DCH+EMC filters	>99.9	99.3	98.1	99.0	97.6	97.3
Combined L1+L3	>99.9	99.1	97.8	98.9	95.8	92.0

Table 2.7: L3 trigger efficiency (%) for various physics processes, derived from Monte Carlo simulation.

volume.

2.9 Conclusion and personal experience

The *BABAR* detector, at the PEP-II B-Factory, is optimized for the study of B physics, with a large B meson sample and excellent vertex resolution, track and photon reconstruction efficiency and charged particle identification. At the same time, wide trigger criteria collect also many other physics events ($c\overline{c}$, $\tau^+\tau^-$, $\mu^+\mu^-$, uds) at a rate comparable with the B's one, allowing to study a large amount of rare τ decays, like $\tau \to lK^0_S$.

During the last years I have been personally involved into the *BABAR* detector operation, specifically concerning the SVT detector. From July until December 2005 I was SVT Operation Manager, taking care of the detector integrity and the quality of collected data. This task requires to reply promptly to any issue arising anytime such as powering, electronics and monitoring problems that could negatively affect the quality of data. Indeed SVT information is crucial for vertex measurement, which is fundamental for many analysis. It is also required to monitor the occupancies and efficiency of the tracker, especially looking for short and long term changes in the electronics noise and in the track reconstruction quality. During this period I participated in running operations, both as regular shifter and as machine-detector liaison, as well as in detector maintenance operations, performed during a one month shutdown.

Starting from January 2006, I am based at SLAC acting as Local System Manager for the SVT detector, reporting directly to the *BABAR* Technical Coordinator. This time includes the periods of data taking for Run6 and Run7 and the start of the decommissioning phase. I have been able to fully understand most of the issue of a running detector and to learn how to work effectively in the team running the *BABAR* detector. This task implied also to manage the activities of two SVT Operation Managers that were working under my responsibility.

Chapter 3

Event Reconstruction

From this chapter we start a detailed description of the various parts of the analysis. A fundamental aspect, described below in this chapter, is the event reconstruction to retrieve measurements of physical quantities using data recorded from the detector. The event reconstruction includes all the basic techniques like tracking, identification of particles and candidates reconstruction. Starting from this chapter charge conjugate decays are implicitly included, if not otherwise specified and we refer to $\tau \to eK^0_S$ decay channel as *electron channel* and to $\tau \to \mu K^0_S$ as *muon channel*.

3.1 Charged particles reconstruction

The charged particle tracks are reconstructed by processing the information from both tracking systems, the SVT and the DCH. The track finding and the fitting procedures use the *Kalman filter algorithm* [58] that takes into account the detailed distribution of material in the detector and the full magnetic field map. After a first processing that produces a raw list of reconstructed track objects, we also apply a refinement procedure using a sequence of modules. The refinement sequence starts by assembling basic information about the event, such as finding the primary and secondary vertexes. Then we run some modules designed to address a particular problem or issue with the tracks found in reconstruction, like tracks due to ambiguity (*ghost*) or tracks that spiral inside DCH (*loopers*). They are able also to improve the resolution of good physics tracks, adding hits not associated in the first processing or removing hits with low probability. Some module can also select some tracks (or couple of tracks that form a secondary vertex) and move them from the *Work* list to sub-lists, so the next modules will ignore them and run faster. The last part of the sequence involves creating the track-based candidate lists used in analysis, starting from the sub-list created by the previous module. Another requirement is then applied on the **polar angle**, in the LAB frame, for each track: $0.41 < \theta_{\rm LAB} < 2.54$ radians, in order to match the acceptance of the detector. This list will be referred to in the following as list of *charged tracks*. Further requirements are then applied to obtain a

list of tracks coming strictly from the IP, called *Good Track Loose* list, that could also be useful in the analysis. The requirements are:

- **Distance of closest approach to the beam-spot (DOCA)**, measured in the x-y plane (d_{xy}) and along the z axis (d_z). Requesting $d_{\rm xy}$ less than 1.5 cm and $d_{\rm z}$ less than 2.5 cm, fake and background tracks not originating near the IP are rejected;

- **Transverse and maximum momentum** in the LAB system $p_\perp$ and $p_{\rm MAX}$. Requesting $p_\perp$ greater than 50 MeV/c and $p_{\rm MAX}$ less than 10 GeV/c, tracks either due to Bhabha process at small angle or not compatible with the beam energy are removed.

3.1.1 Correction Factors for Reconstruction Efficiency

In *BABAR*, the MC simulated sample requires minor tracking efficiency corrections to be consistent with the data. These correction factors are computed selecting a physical process with a fixed multiplicity to determine the absolute efficiency for data and MC samples. The chosen physical process is $\tau^+\tau^-$, where one τ decays in a 3 three hadron mode ($\tau^\pm \to h^\pm h^\mp h^\pm$) and the other one in a leptonic mode ($\tau^\mp \to l^\mp \nu\overline{\nu}$). As described in Sec. 4.4, decay products are back-to-back in the CM frame, because of the high τ momentum, and it is easy to select this type of events. The probability of reconstructing the track is (acceptance is included)

$$\varepsilon = \frac{N_{\rm n\ tracks}}{N_{\rm n\text{-}1\ tracks} + N_{\rm n\ tracks}}, \tag{3.1}$$

where ε is the efficiency of reconstructing a track, $N_{\rm n\ tracks}$ is the number of events where n tracks were reconstructed and $N_{\rm n\text{-}1\ tracks}$ is the number of events where $n-1$ tracks were reconstructed. Then the correction factor is defined as:

$$\Delta = 1 - \frac{\varepsilon_{\rm Data}}{\varepsilon_{\rm MC}}. \tag{3.2}$$

Using this correction factor we compute a weight to apply to each MC event:

$$w = (1-\Delta)^n. \tag{3.3}$$

where n is the number of tracks reconstructed for that event. Correction factors Δ are available separately for different periods of data collection (see Sec. 4.1) to account for changes in the detector through the years. In addition we compute also the uncertainty for those factors summing statistical and systematic errors. The systematic error is due to contamination of the selected sample (τ and non-τ background events), to ghosts and loopers, and to missing kinematic information when the track is not reconstructed. Another systematic uncertainty to be accounted for is the different polar angle distribution

for selected decay modes of the specific analysis. Our $\tau \to lK^0_s$ events are really similar to ones used here, so this systematics will be not added. The weight uncertainty can be written as

$$\Xi = \frac{n\sigma}{(1-\Delta)} \tag{3.4}$$

where σ is the total relevant uncertainty on the correction factor Δ.

3.2 Particle identification

BABAR particle identification is performed using many discriminant variables available from all sub-detectors. A good identification is feasible applying simply requirements for each of those variables, but better results could be obtained using advanced techniques that combine information from different quantities to have a higher discriminant power. Techniques like likelihood ratio, neural network and bagged decision tree are currently used.

Either for simple requirements or advanced technique methods, different levels of efficiency and rejection can be provided modifying parameters and criteria. To make available the PID information in a simple way for different physics analyses, we define selectors. A selector is a category related to a selection method with certain parameters and criteria. For each method you can have more selectors, generally 4, depending if we request a *looser* selection (higher efficiency but also higher mis-identification rate) or a *tighter* selection (lower efficiency but also lower mis-identification rate). Each track satisfies or not a specific selector if it respects its criteria (binary information) and, if a track that satisfies a *tighter* selector, it satisfies also a *looser* one from the same method (i.e. selectors are nested). For each particle category (electron, muons, pions and kaons) we implement few methods and the analyst could choose the best for his analysis without going deeply into the technical details of PID.

In the following we will go through a general description of PID criteria and variables for electron and muon identification and will shown the performances for the selector used in this analysis.

3.2.1 Electron identification

The EMC is crucial for electron identification. Electrons are primarily separated from charged hadrons by taking into account the ratio of the energy E deposited in the EMC to the track momentum p ($\frac{E}{p}$). This quantity should be compatible with the unity for electrons, since all their energy is deposited in the calorimeter. The other charged tracks should appear as minimal ionizing particles, unless they have hadronic interactions in the calorimeter crystals. To further separate hadrons a variable describing the shape of the energy deposition in the EMC (LAT) is used. In addition, the dE/dx energy loss in the

DCH and the DIRC Čerenkov angle are required to be consistent with the values expected for an electron. This offers a good e/π separation in a wide range.

Track selection criteria are tightened for electrons selection to suppress background and to ensure a reliable momentum measurement and identification efficiency. There are requirements in addition for transverse momentum $p_\perp > 0.1\,\mathrm{GeV}/c$, and $N_{\mathrm{DCH}} \geq 12$ for the number of associated drift chamber hits. Furthermore, only electron candidates with a laboratory momentum $p_{\mathrm{LAB}} > 0.5\,\mathrm{GeV}/c$ are considered.

Therefore, electrons are also identified using the a likelihood-based method [59], which use the following discriminating variables:

- $E_{\mathrm{EMC}}/p_{\mathrm{LAB}}$, the ratio of E_{EMC}, the energy deposited in the EMC, and p_{LAB}, the momentum in the laboratory rest frame, measured using the tracking system;
- LAT, the lateral shape of the calorimeter deposit (defined later by Eq. 3.9);
- $\Delta\Phi$, the azimuthal distance between the centroid of the EMC cluster and the impact point of the track on the EMC;
- N_{cry}, the number of crystals in the EMC cluster;
- dE/dx, the specific energy loss in the DCH;
- the Čerenkov angle θ_{C} and N_{C}, the number of photons measured in the DIRC.

First, muons are rejected on the basis of dE/dx ratio value and the shower energy relative to the momentum. For the remaining tracks, likelihood functions are computed assuming the particle is an electron, pion, kaon, or proton. These likelihood functions are based on probability density functions that are derived from pure particle data control samples for each of the discriminating variables. For hadrons, we take into account the correlations between energy and shower-shapes.

Using combined likelihood functions

$$\begin{aligned} L(\xi) &= P(E/p, LAT, \Delta\Phi, dE/dx, \theta_C|\xi) \\ &= P_{\mathrm{EMC}}(E/p, LAT, \Delta\Phi|\xi)\ P_{\mathrm{DCH}}(dE/dx|\xi)\ P_{\mathrm{DIRC}}(\theta_C|\xi) \end{aligned}$$

for the hypotheses $\xi \in \{e, \pi, K, p\}$, the fraction

$$F_{\mathrm{e}} = \frac{f_{\mathrm{e}} L(\mathrm{e})}{\sum_\xi f_\xi L(\xi)}\ , \tag{3.5}$$

is defined, where, for the relative particle fractions, $f_{\mathrm{e}} : f_\pi : f_{\mathrm{K}} : f_{\mathrm{p}} = 1 : 5 : 1 : 0.1$ is assumed. A track is identified as an electron if $F_{\mathrm{e}} > 0.95$.

The electron identification efficiency has been measured using radiative Bhabha events, as function of laboratory momentum $p_{\rm LAB}$ and polar angle $\theta_{\rm LAB}$. The mis-identification rates for pions, kaons, and protons are extracted from selected data samples. Pure pions are obtained from kinematically selected $K^0_s \to \pi^+\pi^-$ decays and three prong τ decays. Two-body Λ and D^0 decays provide pure samples of protons and charged kaons.

3.2.2 Muon identification

Charged particles that are reconstructed in the tracking systems and meet criteria for minimum ionising particles in the EMC (i.e. tracks not depositing large amounts of energy) are potential muon candidates. Their trajectories are extrapolated to the IFR taking into account the non-uniform magnetic field, multiple scattering and the average energy loss. The projected intersections with the RPC or LST planes are computed and for each readout plane all clusters (groups of adjacent hits in one of the two readout coordinates) detected within a maximum distance from the predicted intersection are associated with the track. For each track with associated clusters in the IFR, a number of variables could be computed and used to discriminate muons from charged hadrons:

- tracking variables: transverse momentum $p_\perp$, the number of DCH hits $N_{\rm DCH}$, the polar angle $\theta_{\rm LAB}$ and LAB momentum $p_{\rm LAB}$;
- the energy deposited in the EMC, to be consistent with the minimum ionizing particle hypothesis;
- the number of IFR layers associated with the track;
- the total number of interaction lengths traversed from the IP to the last RPC or LST layer with an associated cluster;
- the difference between this measured number of interaction lengths and the number of interaction lengths estimated for a muon of the same momentum and angle. This interaction lengths estimation takes into account the IFR efficiencies which are routinely measured and stored;
- the average number and the r.m.s. of the distribution of RPC or LST hits per layer;
- the χ^2 for the geometric match between the projected track and the centroids of clusters in different RPC or LST layers;
- the *continuity* of the IFR cluster is defined as $T_c = \frac{N_L}{L-F+1}$, where L and F are the last and first layers with hits. T_c is expected to be 1.0 for muons penetrating an ideal detector whereas is expected smaller for hadrons;

- the quality of a fit made using the strip clusters in the IFR layers combined to form a track and fit to a third degree polynomial;

- χ^2 of cluster centroids compared to the extrapolated charged track.

The performance of muon selection has been tested on samples of muons from $\mu\mu ee$ and $\mu\mu\gamma$ final state events and pions from 3-prong τ decays and $K^0_s \to \pi^+\pi^-$ decays.

For the muon identification, the complex geometry and the high number of available variables make really appealing to put together all the information using a multivariate technique like a neural network or a bagged decision tree. Both of them has been implemented to create efficient selectors that takes in account also the various conditions of data taking, specially due to the major changes in the IFR sub-system. The best performance for muon identification has been obtained using the output of a 30 variables bagged decision tree implemented with the StatPatternRecognition package [60]. Figure 3.1 shows a comparison between the 8 variables neural network and the 30 variables bagged decision tree selectors.

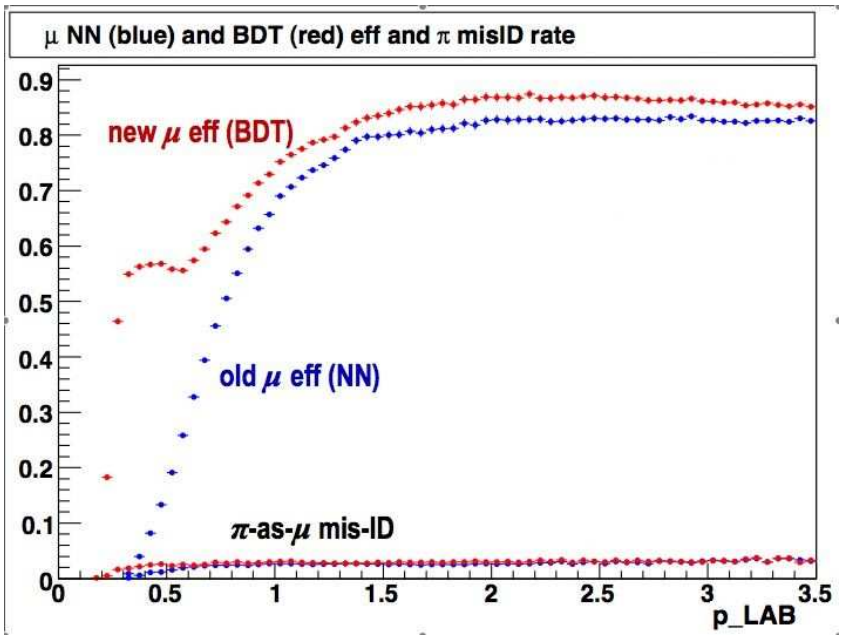

Figure 3.1: Muon identification and pion mis-identification probability for the muon selector based on a neural network (NN) and based on a bagged decision tree (BDT) as a function of momentum.

The improvement has different reasons:

- the better parametrization of detector response, DCH and SVT dE/dx have been greatly improved;

- previously unused quantities classified as *weak variables*), e.g.:

  - number of signal and background photons in the DIRC;
  - last layer hit in the DCH, it helps to catch kaon and pion decays in flight;
  - DIRC Čerenkov angle and DCH $\mathrm{d}E/\mathrm{d}x$;
  - a full set of EMC cluster-shape quantities for all particle types, not just E/p;
  - flattening of the training-sample spectra in momentum, polar angle and charge, so they could be used as normal variables; it allows the use of these variables as input parameters to multivariate classifiers

- new quantities:
  - longitudinal EMC shower depth
  - using geometry to predict *dead spots* in detector acceptance

- advanced statistical techniques from StatPatternRecognition.

3.2.3 Performances of particle identification selectors

For this analysis we use two different selectors for each decay channel: a *loose* selector and a *tight* selector. They are respectively used in the loose and tight selection, described in Chap. 4. For the electron channel a cut-based selector is used as loose selector and a likelihood-based one as tight selector. The performances of these selectors are shown in Fig. 3.2 and Fig. 3.3.

The average efficiency for the loose electron selector is 98% for a LAB momentum $p_{\mathrm{LAB}} > 0.6\,\mathrm{GeV}/c$, whereas the pion mis-identification rate is less than 10%. The average identification efficiency for the tight electron selector with a likelihood-based algorithm is 93% for the same momentum range, whereas the pion mis-identification rate is less than 0.1%.

For the muon channel we used a loose and a tight selectors from the method based on the output of the bagged decision tree algorithm detailed in Sec. 3.2.2. The performances of these selectors are shown in Fig. 3.4 and Fig. 3.5.

The average efficiency for the loose muon selector is 92% for a LAB momentum $p_{\mathrm{LAB}} > 1.4\,\mathrm{GeV}/c$, whereas the pion mis-identification rate is less than 6%. The average identification efficiency for the tight muon selector is 80% for the same momentum range, whereas the pion mis-identification rate is less than 2%.

3.2.4 Correction Factors for Particle Identification

Exactly like the reconstruction efficiency, also PID selectors show a different efficiency for data and MC samples. Therefore, we compute a correction factor to reduce this

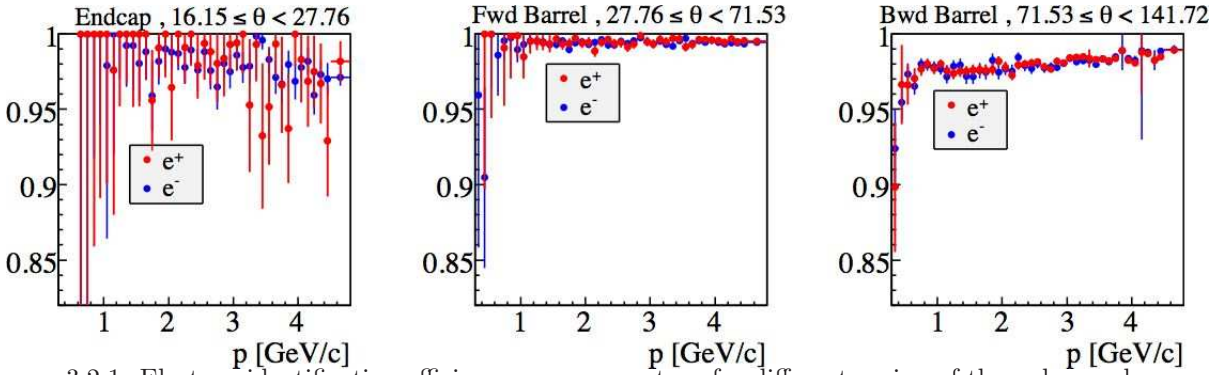

3.2.1: Electron identification efficiency .vs. momentum for different region of the polar angle.

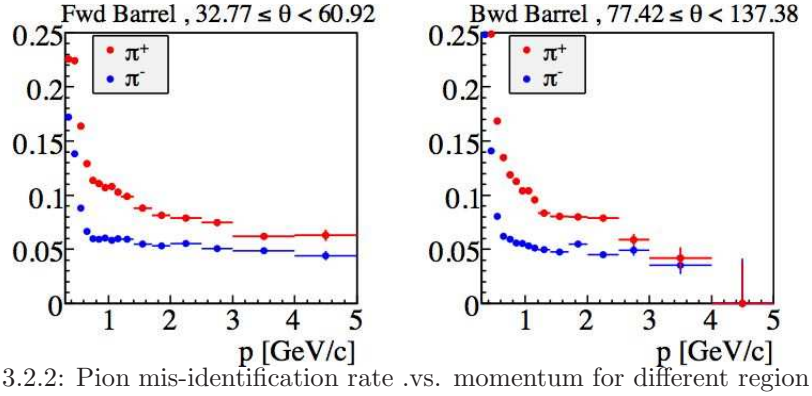

3.2.2: Pion mis-identification rate .vs. momentum for different region of the polar angle.

Figure 3.2: Electron identification and pion mis-identification probability for the cut-based loose electron selector as a function of momentum and polar angle. Note the different scales for identification and mis-identification.

discrepancy. This factor is obtained measuring the efficiency for data and MC events on control samples selected without using PID information.

Given the high correlation between kinematics of selected particle and the identification efficiency, we compute a different factor for each bin of momentum, polar and azimuthal angle in the LAB frame. Observing also variations versus time for efficiencies, we calculate correction factors C separately for different periods of data collection (see Sec. 4.1) to account for changes in the detector through the years. The global corrected MC efficiency for a given selector can be written as

$$\varepsilon^{\mathrm{MC}}_{\mathrm{corrected}} = \frac{\sum_{i=1}^{N_{\mathrm{bins}}} \varepsilon_i^{\mathrm{MC}} \times C_i \times w_i}{\sum_{i=1}^{N_{\mathrm{bins}}} w_i}, \tag{3.6}$$

where

$$C_i = \left(\frac{\varepsilon^{\mathrm{data}}_{\mathrm{ControlSample}}}{\varepsilon^{\mathrm{MC}}_{\mathrm{ControlSample}}} \right)_i \tag{3.7}$$

is the correction factor for the selector in the bin i, $\varepsilon_i^{\mathrm{MC}}$ is the efficiency for the analysis to select the particle in the bin i, and w_i is a weight given by the number of MC particle selected by the analysis. The C_i factor for the used selector can be directly inserted as

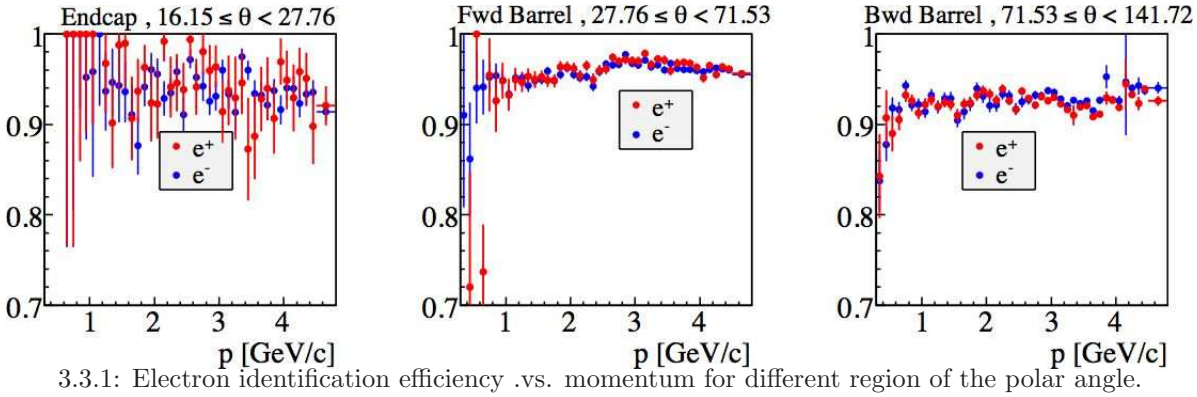

3.3.1: Electron identification efficiency .vs. momentum for different region of the polar angle.

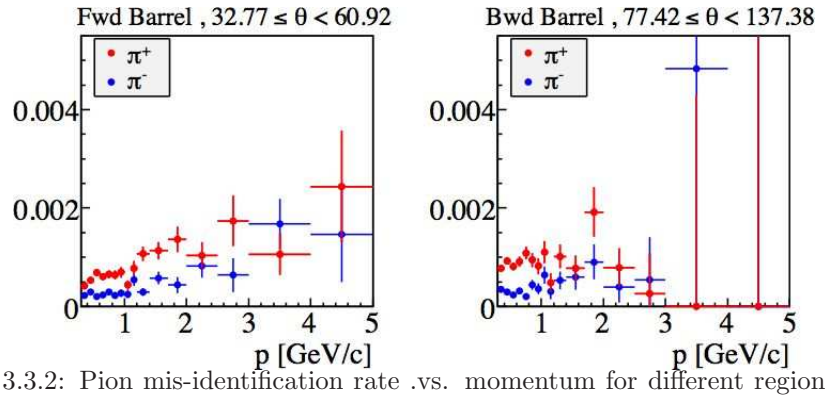

3.3.2: Pion mis-identification rate .vs. momentum for different region of the polar angle.

Figure 3.3: Electron identification and pion mis-identification probability for the likelihood-based tight electron selector as a function of momentum and polar angle. Note the different scales for identification and mis-identification.

a weight for each event where we apply that selector. Each factor has also an associated error due to the statistics and it could large for some bins with few selected events in the control sample. An error for the global corrected efficiency can be written as

$$\sigma^2_{\varepsilon^{\rm MC}_{\rm corrected}} = \frac{\sum_{i=1}^{N_{\rm bins}} \left(\varepsilon_i^{\rm MC} \times \sigma_i \times w_i\right)^2}{\left(\sum_{i=1}^{N_{\rm bins}} w_i\right)^2}, \tag{3.8}$$

where σ_i is the error for the factor C_i.

3.3 Photon reconstruction

Photons are detected in the EMC as clusters of close crystals where energy has been deposited. They are required not to be matched to any charged track extrapolated from the tracking volume to the inner surface of the EMC. Momenta and angles are assigned to be consistent with photons originating from the interaction region. Then photon candidates are required to have an energy $E_\gamma > 30\,\text{MeV}$ in the LAB frame in order to reduce the impact of the sizable beam-related background of low energy photons. Some additional

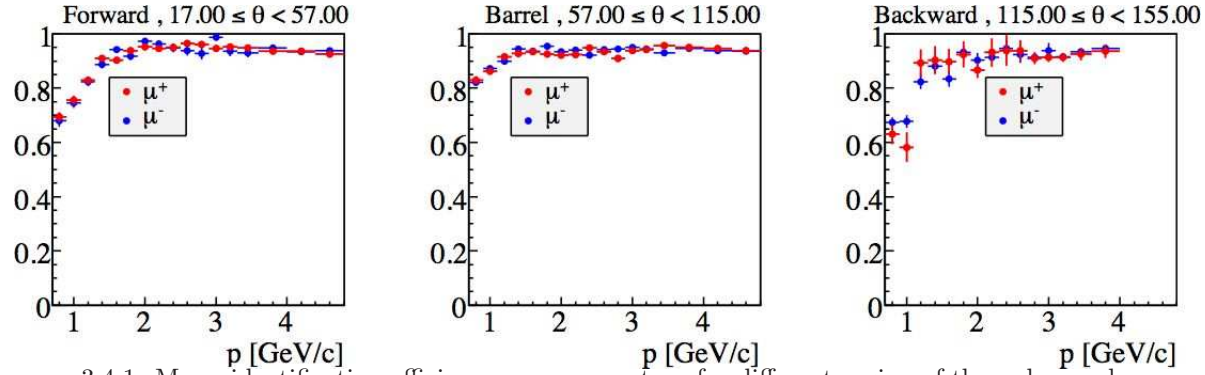

3.4.1: Muon identification efficiency .vs. momentum for different region of the polar angle.

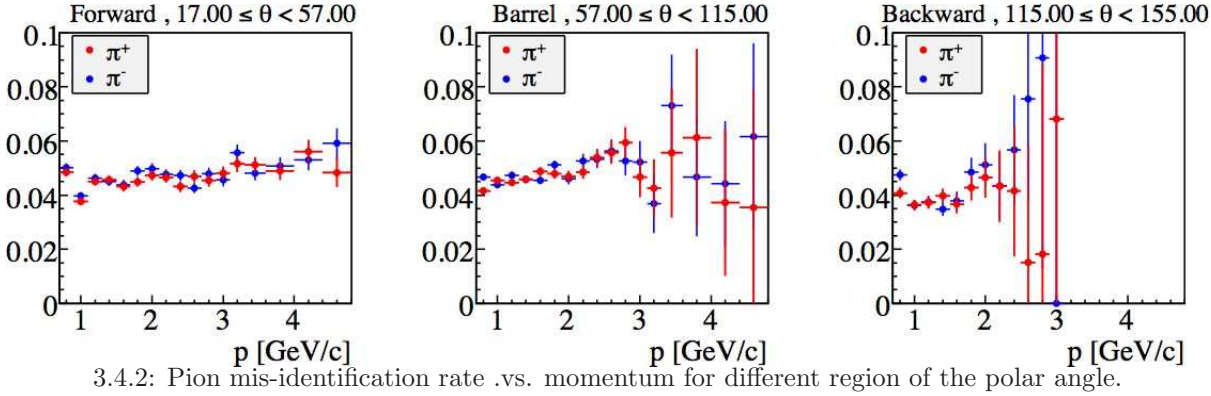

3.4.2: Pion mis-identification rate .vs. momentum for different region of the polar angle.

Figure 3.4: Muon identification and pion mis-identification probability for the loose muon selector as a function of momentum and polar angle. Note the different scales for identification and mis-identification.

backgrounds, due to hadronic interactions, either by K_L^0 or neutrons, can be reduced by applying requests on the shape of the calorimeter clusters.

The variable LAT, used to discriminate between electromagnetic and hadronic showers in the EMC, is defined as

$$LAT = \frac{\sum_{i=3}^{N} E_i r_i^2}{\sum_{i=3}^{N} E_i r_i^2 + E_1 r_0^2 + E_2 r_0^2}, \tag{3.9}$$

where N is the number of crystals associated with the electromagnetic shower, r_0 is the average distance between two crystals, which is approximately 5 cm for the *BABAR* calorimeter, E_i is the energy deposited in the i-th crystal, numbering them such that $E_1 > E_2 > \ldots > E_N$ and r_i, ϕ_i are the polar coordinates in the plane perpendicular to the line pointing from the IP to the shower center centered in the cluster centroid. Considering that the summations start from $i = 3$, they omit the two crystals containing the highest amounts of energy. Since electrons and photons deposit most of their energy in two or three crystals, the value of LAT is small for electromagnetic showers. Multiplying the energies by the squared distances enhances the effect for hadronic showers, compared with electromagnetic ones. Photon candidates are required to have $LAT < 0.8$. In this

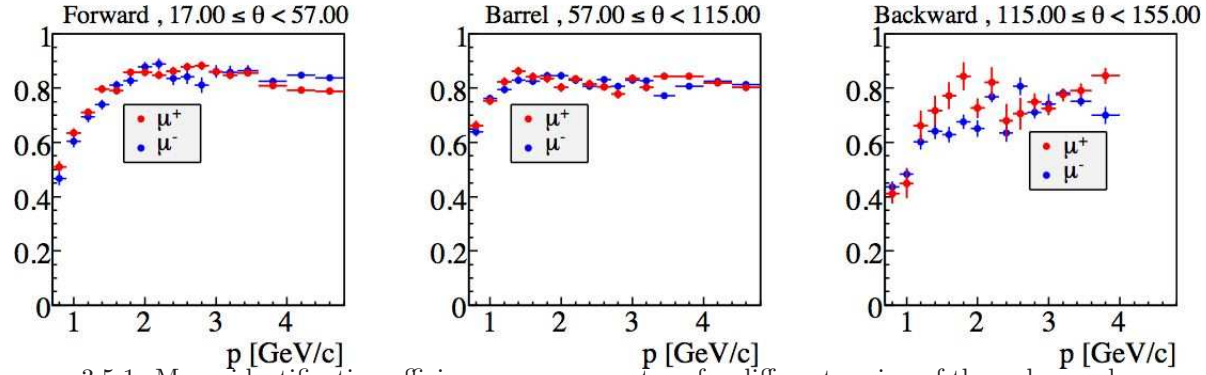

3.5.1: Muon identification efficiency .vs. momentum for different region of the polar angle.

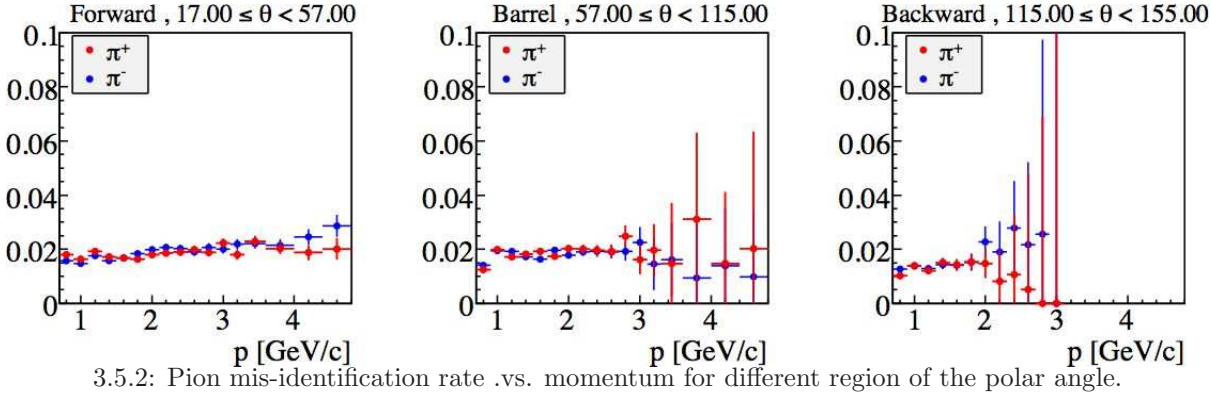

3.5.2: Pion mis-identification rate .vs. momentum for different region of the polar angle.

Figure 3.5: Electron identification and pion mis-identification probability for the likelihood-based tight electron selector as a function of momentum and polar angle. Note the different scales for identification and mis-identification.

analysis, no photons are present in the decay mode but photon candidates are used for bremsstrahlung recovery described in Sec. 3.5 and for rejecting background events during the tight selection (see Sec. 4.5).

3.4 K^0_S reconstruction

K^0_S are reconstructed in the channel $K^0_S \to \pi^+\pi^-$ by pairing all possible tracks of opposite sign and looking for the 3D point (vertex) which is more likely to be common to the two tracks. The algorithm is based on a χ^2 minimization and uses as starting point for the vertex finding the point of closest approach of the two tracks in 3D. No constraint is applied on the invariant mass of the pair, but a $\pm 5\sigma$ cut around the nominal value is imposed: $0.473 < m_{\pi^+\pi^-} < 0.523\,\mathrm{GeV}/c^2$. The invariant mass distribution of the $\pi^+\pi^-$ obtained from data is shown in Fig. 3.6. A comparison between data and Monte Carlo for the K^0_S momentum and polar angle is shown in Fig. 3.7. The channel $K^0_S \to \pi^0\pi^0$ is not used in this analysis.

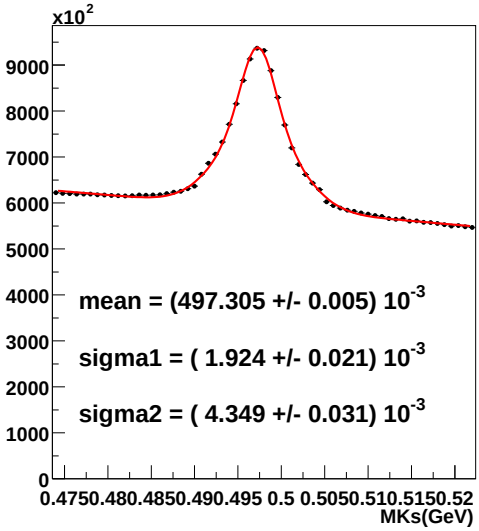

Figure 3.6: Mass distributions for $K^0_S \to \pi^+\pi^-$ on data. The distribution is fitted with a sum of a double Gaussian and a first order polynomial function.

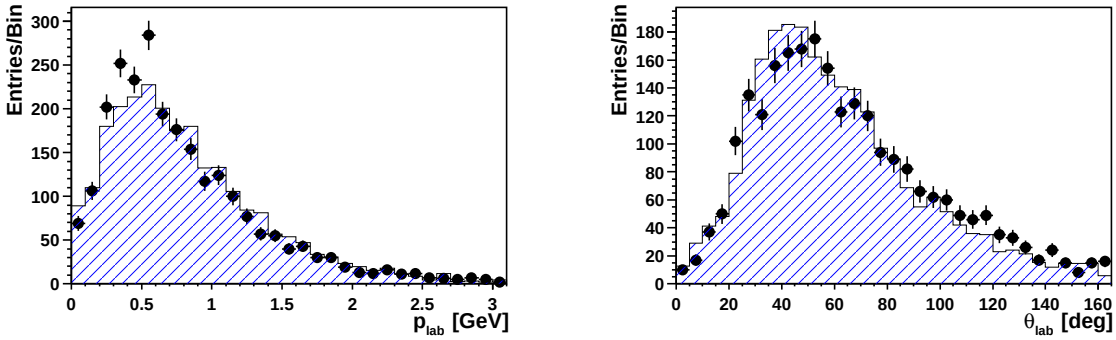

Figure 3.7: K^0_S momentum (left) and polar angle (right) distributions in data (solid markers) and Monte Carlo simulation (hatched histogram), normalized to the same area.

3.5 Reconstruction of the signal τ decay

In this analysis τ signal candidates are reconstructed by combining one K^0_S candidate (as detailed in Sec. 3.4) and one generic track candidate. To reduce the number of combinations, τ's are reconstructed only at the end of the preselection described in Sec. 4.2.

To improve the τ energy resolution for the electron channel, a bremsstrahlung recovery procedure is applied, to take into account possible radiative energy losses suffered by the electrons. The procedure creates new track candidates adding from one to three photons and one track candidate already reconstructed. Photons are added only if the polar (θ) and azimuthal (ϕ) angles between the original track direction and the photon candidate satisfy the following conditions: $\theta < 0.035$ and $\phi < 0.050$.

For each event, we make a τ candidate for each combination of one K^0_S and one track

with assigned the corresponding lepton mass. Two separate candidate lists are created for electron and muon channel and a candidate made from the same track and the same K_S^0 could enter both of them. Only the τ candidates that satisfy these requirements are retained: $|\Delta M_\tau| < 0.35\,\mathrm{GeV}/c^2$ and $|\Delta E_\tau| < 0.4\,\mathrm{GeV}$, where ΔM_τ is defined as the difference between the invariant mass of the reconstructed τ and the world average value [39] and ΔE_τ as the difference between the energy of the reconstructed τ and the expected τ energy, half the CM total energy. Then, only for the selected candidates, we perform for the whole decay tree (tracks from K_S^0, lepton track and bremsstrahlung photons) a geometrical and kinematical fit using the Tree-Fitter algorithm [61]. For this analysis we use two versions of this fit with different constraints, the *standard fit* and the *full fit*. For the *standard fit* the following constraints are applied:

1. the K_S^0 mass is forced to be equal to the world average value [39];
2. the τ reconstructed is forced to originate from the beam-spot taking into account the beam-spot experimental resolution;
3. the track and the K_S^0 must come from the τ decay vertex.

For the *full fit* we apply also constraints on the mass (forced to be equal to the world average value) and on the energy (forced to be equal to half the CM total energy) of τ candidate.

Chapter 4

Event Selection

In this chapter we go through the description of event samples and the selection performed in this analysis. Data and Montecarlo simulation (MC) samples are described in Sec. 4.1. The selection is optimized in a *blind way*, described in Sec. 4.3, and performed in three main stages, described in Sec. 4.2, 4.4 and 4.5:

1. **Preselection stage**, for removing most of background events not coming from $\tau^+\tau^-$ processes. We perform this preselection only for reducing the number of combinations before reconstructing a τ candidate. It retains $\sim 10^{-4}$ of the initial data sample;

2. **Loose selection stage**, aimed at getting a reasonable agreement between data and MC samples with enough statistics to estimate shapes of background distributions. It retains $\sim 10^{-7}$ of the data sample;

3. **Tight selection stage**, optimized to get the lowest value for the sensitivity, defined as the upper limit estimated using background MC samples and assuming no observed events above the residual background. The final background rejection is close to 10^{-8}.

An additional stage, called **final selection**, is applied before estimating the upper limit. Sec. 4.6 describes the final selection, as well as a summary of the performance for each step of the selection. We conclude the chapter describing systematic uncertainties for the number of τ pairs and for the selection efficiency.

Notes about tables and plots

In this chapter tables report the number of selected events and the efficiency for background and signal MC samples, and for data. The equivalent number of background MC events is obtained by rescaling those background MC samples by the respective cross section (see Tab. 2.1) and summing the various components. We show the number of events selected by a specific criterion requiring also all the previous ones to be applied.

Efficiencies are always computed dividing by the total number of events for the respective sample, apart from background MC one, where we use the total number of events from the data sample[1].

During the selection we show only plots for relevant variables, while other plots are available in Sec. A.3. All the distribution plots for data and background MC samples are drawn with the same color legend shown in Fig. 4.1 and the same structure, described below. The legend is repeated for each plot, but background processes with no events at

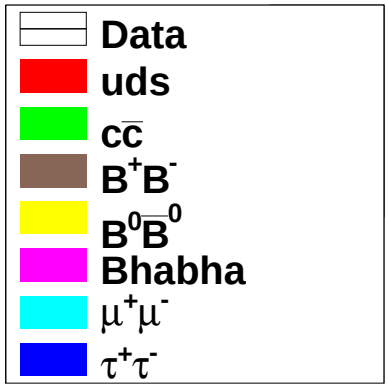

Figure 4.1: Color code used to display data and background MC distributions through all this thesis.

that stage of selection are removed from the box.

In the upper plot we have the data distribution, shown by black points with errors, superimposed to the sum of background MC samples, shown as solid histograms with different colors[2]. Each background MC sample is rescaled according to the corresponding data/MC luminosity ratio (see Tab. 4.3). In the lower plot we have the MC distribution for signal samples (not rescaled). In the middle plot, if present, we have the difference between the sum of rescaled background MC samples and the data divided by the error. The error for each bin is calculated by summing in quadrature the error on data and background MC samples. Under this plot, we report the χ^2 of the distribution, the number of degrees of freedom and the corresponding probability for the χ^2 itself.

In the upper and lower plot, if a selection criterion is applied on the plotted variable, the region selected is shown by one or two dashed black lines with arrows. When the dashed lines are blue, they are showing the blinded region in ΔE_τ and ΔM_τ plots. Details of applied selection criteria are also written in the caption.

Generally, for each group of requirements, the sample shown in a plot is made only by the events that already pass all the previous requirements. This can easily be traced back comparing the number of plot entries reported in the top right box.

[1]This way of compute background MC efficiency is only for a quick comparison with data ones and does not affect in any way the final measurement.

[2]Plots need to be displayed with colors to distinguish the different MC samples.

4.1 Data and Montecarlo simulation samples

The data sample used for this analysis were recorded by *BABAR* starting from October 1999 through September 2007 and corresponds to an integrated luminosity of $469 \pm 2\,\text{fb}^{-1}$ collected from e^+e^- collisions, of which $425\,\text{fb}^{-1}$ at the $\Upsilon(4S)$ resonance and $44\,\text{fb}^{-1}$ 40 MeV below. The total number of τ pairs $N_{\tau\tau}$ is $(4.31 \pm 0.03) \times 10^8$, calculated using the average τ cross section of $0.919 \pm 0.003\,\text{nb}$ estimated with `KK2f` [45]. The number of events and the corresponding luminosities for different periods are detailed in Table 4.1.

		On-peak		Off-peak	
Run-cycle	Period	# evts	$\mathcal{L}$ [fb^{-1}]	# evts	$\mathcal{L}$ [fb^{-1}]
Run 1	Oct 1999 - Oct 2000	2.75281e+08	20.02	3.25566e+07	2.62
Run 2	Feb 2001 - Jun 2002	9.16755e+08	61.08	9.67619e+07	6.92
Run 3	Dec 2002 - Jun 2003	4.78701e+08	31.85	3.41909e+07	2.47
Run 4	Sep 2003 - Jul 2004	1.4829e+09	100.28	1.37207e+08	10.12
Run 5	Mar 2005 - Aug 2006	1.97011e+09	133.26	1.9518e+08	14.49
Run 6	Jan 2007 - Aug 2007	1.22349e+09	78.37	1.11168e+08	7.83
Total	Oct 1999 - Aug 2007	6.34723e+09	424.86	6.07064e+08	44.44

Table 4.1: Number of events and luminosities for the data sample in different periods of data taking.

For this analysis MC simulated samples for signal and background events have been produced to understand background events, to estimate the selection efficiency for the signal events and to validate the procedure for the residual background extrapolation. Anyway the normalization of the final background estimation is made only using information from data. An extensive comparison between data and MC distribution has been performed during each selection stage to ensure that MC samples reproduce properly the shape of data distributions.

MC samples of τ lepton events are produced using the `KK2f` generator [62, 63] and `Tauola` decay library [64, 65]. B meson decays are simulated with the `EvtGen` generator [66], and $q\overline{q}$ events, where $q = u, d, s, c$, with the `JETSET` [67] generator. Two different sample are generated for $q\overline{q}$ events, one for $c\overline{c}$ and one for $u\overline{u}$, $d\overline{d}$ and $s\overline{s}$, generically referred to as *uds* sample. Radiative corrections are simulated using PHOTOS [68]. *Bhabha* events are generated only within the polar angle range from 18 ° to 131 ° in the LAB system and no radiative *Bhabha* events are added. Simulated events are then processed using the detailed model of *BABAR* detector created using the `GEANT4` simulation package [69]. Therefore, for MC samples, all the reconstructed variables are available exactly like real data, plus the information about the original process, decays and kinematical quantities (so called MC-truth). MC samples are produced proportionally to the amount of data

luminosity integrated into each Run-cycle. The *BABAR* experiment has a database that keeps tracks of all the changes in conditions and calibrations occurred during the data taking, not only to correctly process the real data, but also to produce MC simulated events in the conditions as close as possible to real status of detector.

We generate also four signal MC samples with high statistics, one for each combination of lepton type and charge, as detailed in Tab. 4.2. For these samples e^+e^- are forced to produce a τ pair, with one τ decaying into the signal mode and the other one according the standard branching fractions.

Samples	Number of events
$\tau^+ \to e^+ K_S^0$	521568
$\tau^- \to e^- K_S^0$	554908
$\tau^+ \to \mu^+ K_S^0$	520724
$\tau^- \to \mu^- K_S^0$	520944

Table 4.2: Number of generated events for signal MC sample.

Table 4.3 shows the number of events generated for each process in Tab. 2.1. Using the respective cross section, we can compute the equivalent luminosity and the corresponding ratio of MC/data luminosities (shown in the right column), to be used for rescaling background samples to the data one.

Sample	Number of events	$\mathcal{L}_{\rm MC}/\mathcal{L}_{\rm data}$
uds	9.96268e+08	1.02
$c\overline{c}$	1.14943e+09	1.88
B^+B^-	7.00012e+08	2.84
$B^0\overline{B}^0$	7.10674e+08	2.88
Bhabha	4.531e+08	0.04
$\mu^+\mu^-$	5.16528e+08	0.95
$\tau^+\tau^-$	4.01246e+08	0.93

Table 4.3: Number of events generated for background MC samples, with the corresponding ratio between MC and data luminosities.

4.2 Preselection

The purpose of preselection is mainly to reduce the samples removing most of the background events like *Bhabha*, *dimuon*, $b\overline{b}$, *uds* and $c\overline{c}$ applying requirements on basic event variables like numbers of tracks and calorimeter clusters, shape and thrust magnitude.

Then we perform the τ reconstruction (see Sec. 3.5) for selected events ($\sim 1\%$), retaining only those with at least one signal candidates.

4.2.1 Selection of $\tau^+\tau^-$ events

Most of the events in the full *BABAR* data sample are from *Bhabha* processes and can be easily removed making basic requests after a raw reconstruction of tracks and clusters using only DCH and EMC. The following criterion eliminate most of *Bhabha* events while keeping a high efficiency for generic $\tau^+\tau^-$ events.

The first request is that the event passed the L3 trigger as event useful for physics analysis, because in the data sample we have also events for detector studies, diagnostics and online measurements of beam energy, luminosity and hadronic ratio. There are two main categories in the L3 trigger, L3OutDch and L3OutEmc, both highly efficient to select events useful for physics analysis. For the specific definition of those two trigger categories see Sec. A.1. Anyway after requiring this, there is still a considerable percentage of events from *Bhabha* process, as shown in Fig. 4.2 (events on bin 1 passed the requirement). The

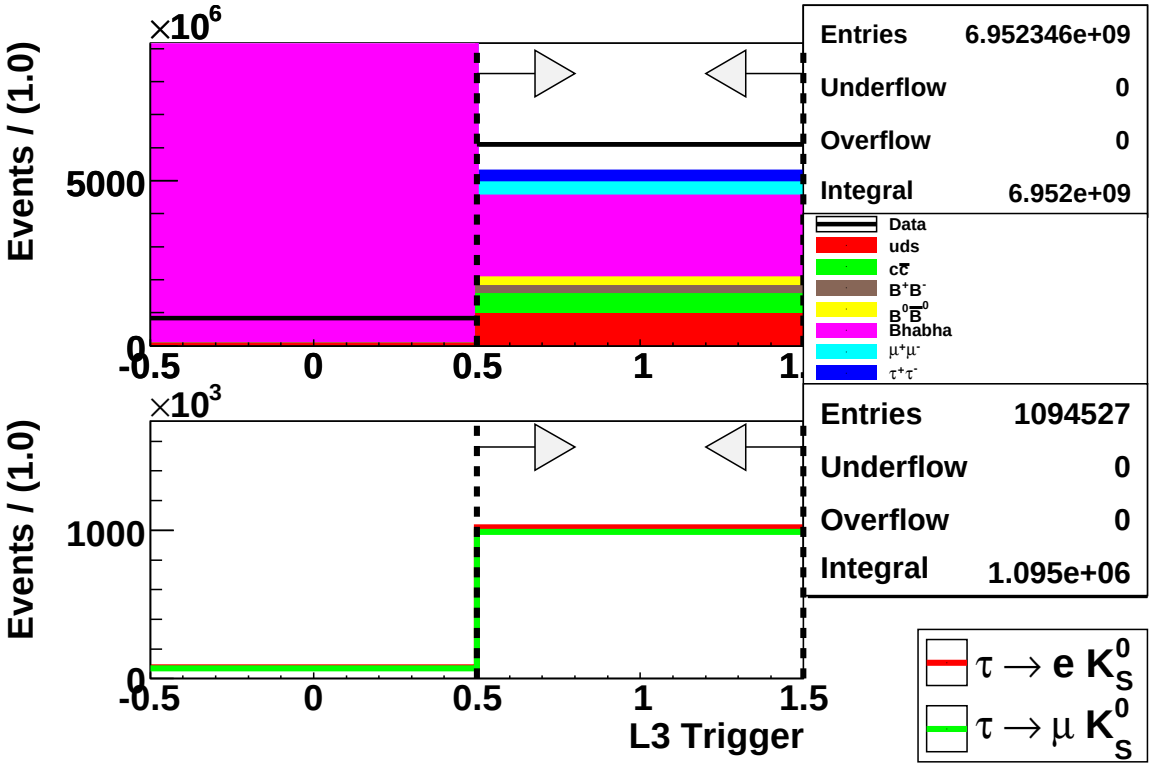

Figure 4.2: Distribution of the L3trigger variable for data (black dots, upper plot), background MC (filled histogram, upper plot) and signal MC (lower plot) samples.

huge amount of *Bhabha* events on the bin at zero in background MC samples, comparing to data, is coming from events that pass L3 trigger under monitoring categories and are not prescaled in the simulated sample.

Other background filters, made using only a raw reconstruction of tracks and clusters, are then available to select events useful for physics analysis and remove the most part of remaining *Bhabha* events. For this analysis events must satisfy the filter for $\tau^+\tau^-$ events or generics ones for hadronic and two-prong events. For details on the definition of those filters see Sec. A.1. The events distribution for these combined filters are shown in Fig. 4.3 and performances of both requests are shown in Tab. 4.4.

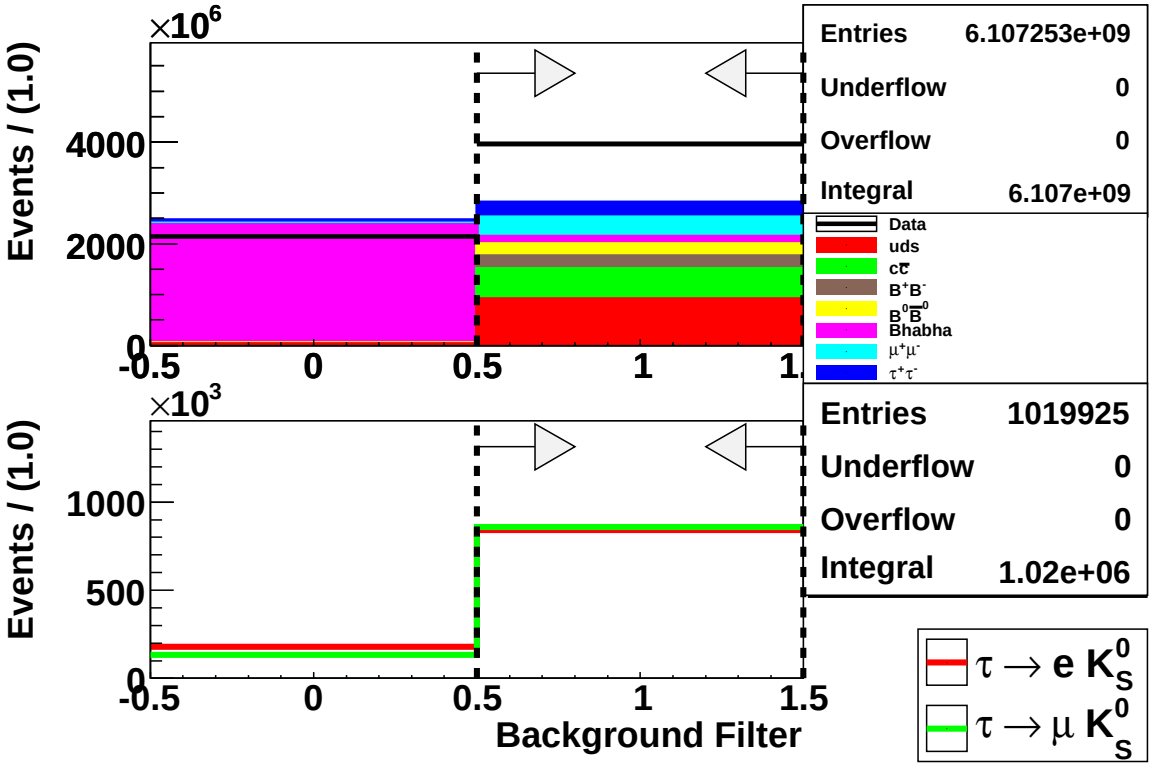

Figure 4.3: Distribution of the background filters variable for data (black dots, upper plot), background MC (filled histogram, upper plot) and signal MC (lower plot) samples just before applying the requirement on the shown variable, but after all the previous ones.

Filter	$\tau \to eK^0_S$	$\tau \to \mu K^0_S$	data	bkg MC (normalized)
Analyzed events	1.07648e+06	1.04167e+06	7.0E+09	–
`L3 Trigger` Applied	94.75%	95.13%	6.1E+09(87.84%)	5.3E+09(76.13%)
`Background Filter` Applied	78.07%	82.43%	4.0E+09(57.04%)	2.8E+09(40.53%)

Table 4.4: Signal MC samples efficiency(ε) after applying selection criteria. Efficiency and number of events are also given for data and background MC samples. Background MC samples have been combined according their respective cross section and their efficiency is computed using the total number of events from data.

4.2.2 Selection of events before τ reconstruction

The data sample is further reduced using other event variables before trying to reconstruct the τ candidates. We start applying requirements directly related to our decay mode, like having **one or two reconstructed** K^0_S, where K^0_S criteria have been defined in Sec. 3.4. K^0_S are reconstructed here only in two charged pions mode (branching fraction is $\sim 69\%$). We have a significant decrease for the number of signal events ($\sim 50\%$) due to select only this decay mode and to the tracking efficiency for these two tracks. Afterwards we use the number of reconstructed track, defined in Sec. 3.1. Most of our signal events have four reconstructed tracks, as shown in Fig. 4.4: three from the τ decaying into the signal mode and one from one-prong decays of the other τ. We apply a loose requirement allowing from **3 to 7 tracks** in the event, removing most of $b\bar{b}$ events (average multiplicity around 10) and half of uds and $c\bar{c}$.

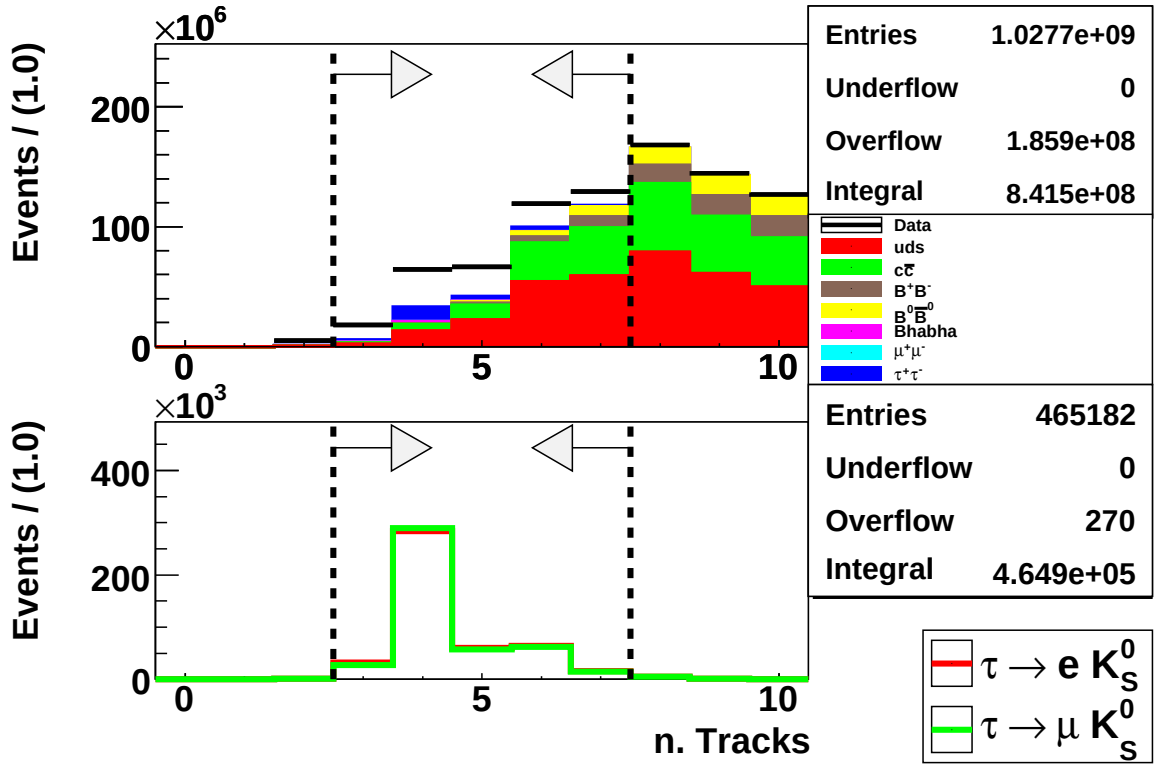

Figure 4.4: Distribution of the number of tracks in the event for data (black dots, upper plot), background MC (filled histogram, upper plot) and signal MC (lower plot) samples just before applying the requirement on the shown variable, but after all the previous ones.

Because of the high CM energy ($\sqrt{s} = M(\Upsilon(4S))$), τ's are produced back-to-back with a high momentum and, given the typical low multiplicity of τ decay modes, products remain close to the original τ direction, making a two jets event. A variable to discriminate events with different shape is the **thrust magnitude**. The thrust axis is the direction which maximizes the sum of momentum modules when they are projected on that direction and the magnitude is obtained by dividing the sum of projections by the sum of

momentum modules [38]. It gives a measure of how much an event is jet-like: 1 means that all tracks are aligned along a preferred direction, 0.5 means that there is no preferred direction. We compute the thrust using tracks and calorimeter clusters (not matched with a track) and request his magnitude to be **between 0.85 and 0.99**. Figure 4.5 shows the distribution to the thrust magnitude, where $\tau^+\tau^-$ events are mostly above 0.9.

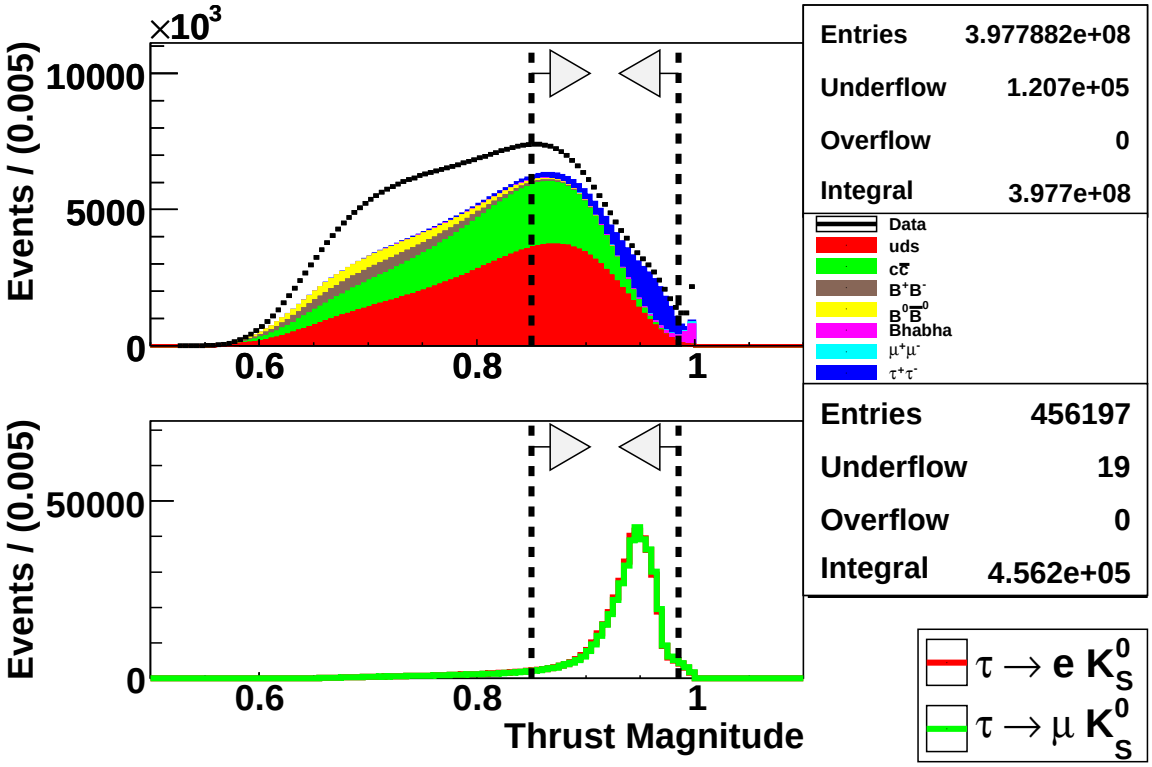

Figure 4.5: Distribution of the thrust magnitude for data (black dots, upper plot), background MC (filled histogram, upper plot) and signal MC (lower plot) samples just before applying the requirement on the shown variable, but after all the previous ones.

The last request is on the momentum of highest momentum track (**MomHighestMomTrk**): **greater than 1.5** GeV/c, to remove other low multiplicity events, and **lower than 4.8** GeV/c, to remove few events with bad reconstructed tracks. Table 4.5 summarizes the requirements, the number of selected events and efficiencies. Figure 4.6 shows distributions of the thrust magnitude after all the previous requirements have been applied, with most of background events coming mainly from uds and $c\overline{c}$ processes, plus a smaller fraction from $\tau^+\tau^-$ events.

After the selection above, we processed the remaining events to reconstruct τ **candidates**, as described in Sec. 3.5 and retain only events with **at least one candidate**. A fraction of signal events is rejected by the cut on ΔM_τ and ΔE_τ made before the fit during the reconstruction. The percentage of remaining events are shown in Tab. 4.6 and the distributions of the number of τ candidates is shown in Figure 4.7.

Most of selected signal events shows two reconstructed τ's because this is the total

Requirements	$\tau \to eK^0_S$	$\tau \to \mu K^0_S$	data	bkg MC (normalized)
Analyzed events	1.07648e+06	1.04167e+06	7.0E+09	–
$1 \leq$ n. $K_S \leq 2$	43.21%	44.12%	1.0E+09(14.78%)	9.1E+08(13.16%)
$3 \leq$ n. Tracks ≤ 7	42.38%	43.32%	4.0E+08(5.72%)	3.0E+08(4.30%)
$0.85 \leq$ Thrust Magnitude ≤ 0.99	38.23%	39.10%	1.3E+08(1.93%)	1.2E+08(1.71%)
$1.5 \leq$ Mom HighestMomTrk ≤ 4.8	36.89%	38.09%	9.2E+07(1.32%)	8.9E+07(1.28%)

Table 4.5: Signal MC samples efficiency(ε) after applying selection criteria. Efficiency and number of events are also given for data and background MC samples. Background MC samples have been combined according their respective cross section and their efficiency is computed using the total number of events from data.

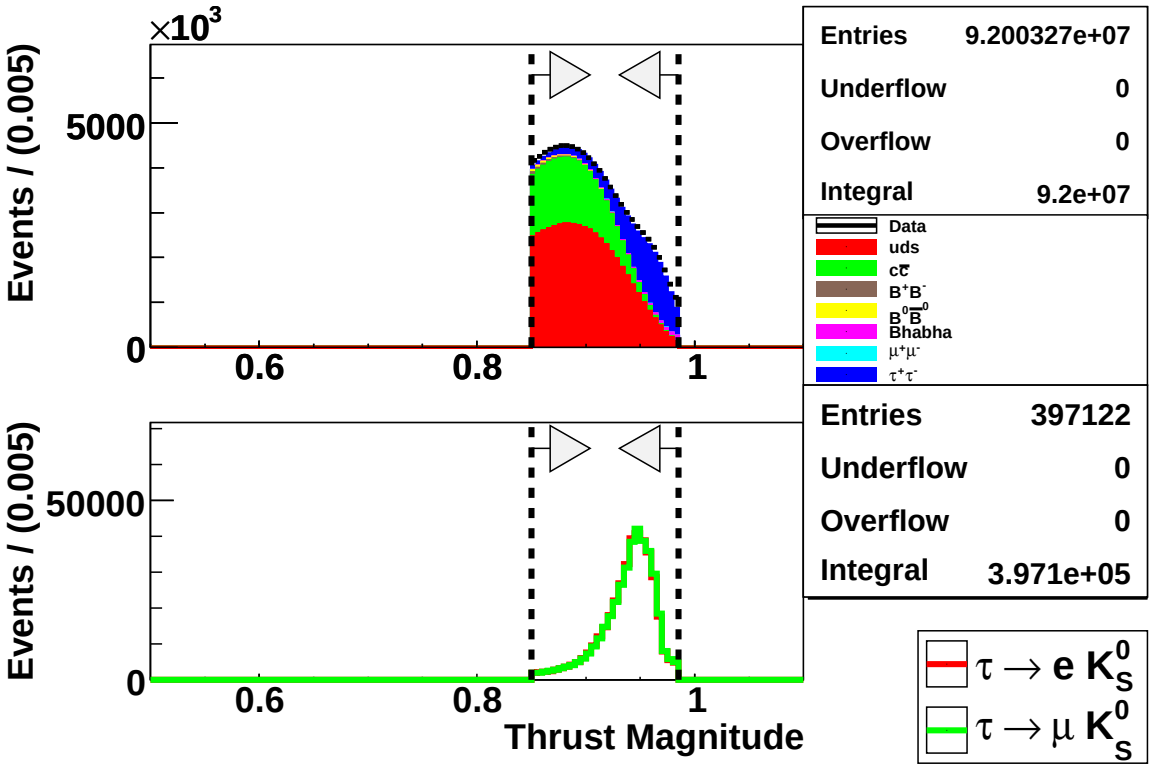

Figure 4.6: Distribution of the thrust magnitude for data (black dots, upper plot), background MC (filled histogram, upper plot) and signal MC (lower plot) samples after having applied all the previous requirements of the preselection.

number of reconstructed candidates in electron and muon channel lists and the same candidate could enter on both of them (candidates are reconstructed with a generic track and PID request is not yet applied). Until this point there is no difference between the selection of the two decay channels and all the τ candidates are kept. Later we consider only one τ candidate, the one with the highest χ^2 of the vertex fit in the list of the requested channel.

Requirements	$\tau \to eK^0_s$	$\tau \to \mu K^0_s$	data	bkg MC (normalized)
Analyzed events	1.07648e+06	1.04167e+06	7.0E+09	–
`n. τ Cands` ≥ 1	25.62%	27.89%	5.1E+05(7.29E-05)	4.9E+05(7.01E-05)

Table 4.6: Signal MC samples efficiency(ε) after applying selection criteria. Efficiency and number of events are also given for data and background MC samples. Background MC samples have been combined according their respective cross section and their efficiency is computed using the total number of events from data.

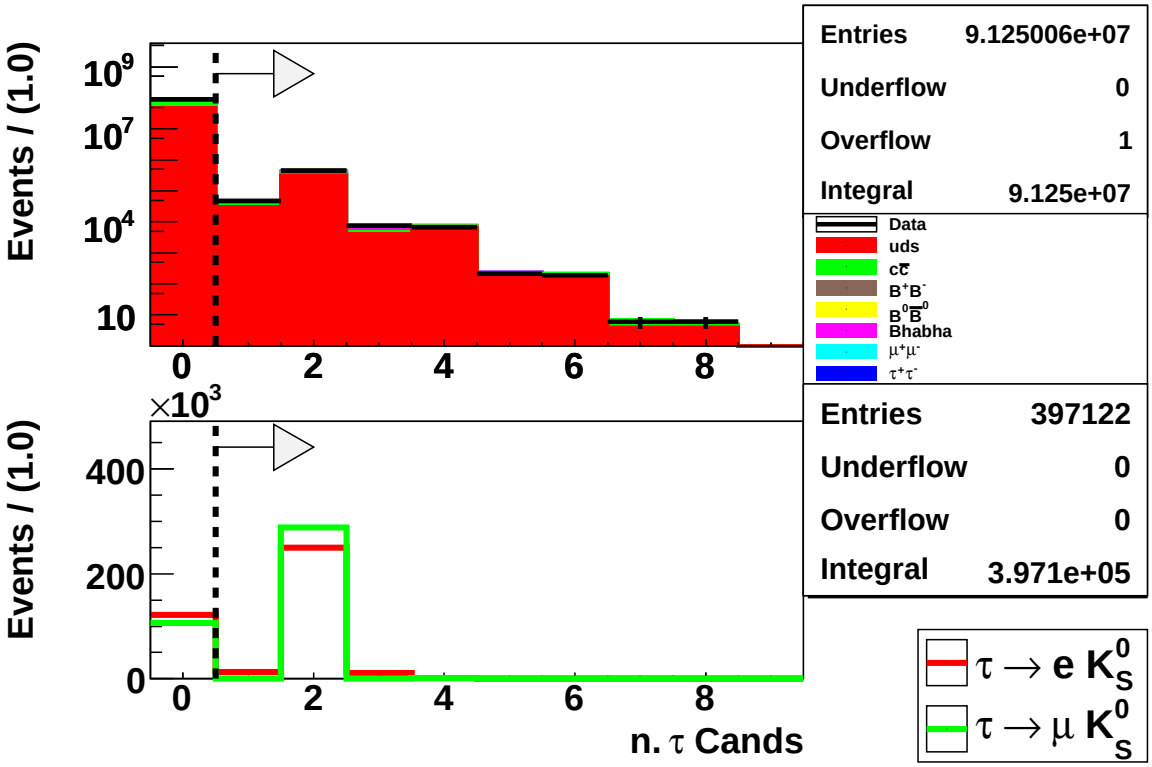

Figure 4.7: Distribution for the number of the reconstructed τ candidates for data (black dots, upper plot), background MC (filled histogram, upper plot) and signal MC (lower plot).

4.3 Blinding procedure for the final signal region

For the loose and tight selection, this analysis adopts for the data sample a blinding procedure designed to avoid any bias in choosing requirements, which could come from knowledge of the data distributions. Therefore data events were removed from the final signal region defined as a rectangular box on the $\Delta E_\tau/\Delta M_\tau$ plane (see Sec. 3.5 for a definition of ΔM_τ and ΔE_τ). According the signal MC sample, that region contains more than 90% of signal events. When all the selection criteria and the estimation procedure for the upper limits is completely defined (optimized, tested on the MC samples, and approved), those events are reinserted into the data sample to calculate the final results

for the upper limit.

Considering MC samples, ΔE_τ and ΔM_τ variables show a clear peak close the axes origin for signal events, while the distributions are flat or much wider for background ones, as shown in Fig. 4.8. The approximate resolutions of these variables are computed fitting each distribution with a bifurcated Gaussian excluding the radiative tail ($\Delta M_\tau > -50\,\mathrm{MeV}/c^2$, $\Delta E_\tau > -50\,\mathrm{MeV}$). The resolution are $\sigma_{\Delta M_\tau} = 16/8\,\mathrm{MeV}/c^2$ and $\sigma_{\Delta E_\tau} = 35/25\,\mathrm{MeV}$, where the two values are respectively for left and right side of the function. In $\Delta E_\tau/\Delta M_\tau$ plots distribution tails are due to events with initial state radiation (right mass and wrong energy) and, for the electron channel only, to the bremsstrahlung radiation of the electron itself (wrong mass and energy with a clear correlation between them). We choose the size of region to blind roughly $\pm 4\sigma_{\Delta \mathrm{X}}$. The blinded region size is slightly different between the two channels and their boundaries are detailed in Table 4.7. A 2-dimensional plot of $\Delta E_\tau/\Delta M_\tau$ distribution is shown in Fig. 4.9.

Channel	ΔM_τ (GeV/c^2)		ΔE_τ (GeV)	
$\tau \to e K_S$	-0.03	0.03	-0.14	0.10
$\tau \to \mu K_S$	-0.03	0.03	-0.13	0.10

Table 4.7: Values for boundaries of blinded region.

In the following we retain only events with ΔM_τ within $\pm 0.3\,\mathrm{GeV}/c^2$ and ΔE_τ within $\pm 0.4\,\mathrm{GeV}$. The blinded region corresponds to the final signal region for the modifies frequentist analysis method and events outside that region will be used for the background estimation. We perform also an upper limit estimation with another method, using different regions for signal and background estimation, for cross-checking the first result. The cross-check method will consider, as final signal region, an elliptical region included into the blinded one, while for the background estimation we used two box on the left and right side of the blinded one, to be referred to as *sidebands*. Figure 4.10 shows again $\Delta E_\tau/\Delta M_\tau$ distributions of signal MC samples, with superimposed the blinded region (blue box), the sidebands region (purple box) and the final signal region (red ellipsis) used for this cross-check method.

4.4 Loose Selection

The purpose of the loose selection is to further reduce the number of background events and obtain a reasonable agreement between data and background MC shapes, while keeping enough statistics to estimate those shapes. For this step of selection we apply the loose PID selector, plus requirements on event shape, on the K_S^0 and on the τ candidates. From this point the selection is slightly different for each decay channel, but we use generally the same variables. If more than one τ candidate exists in the event, only the one with

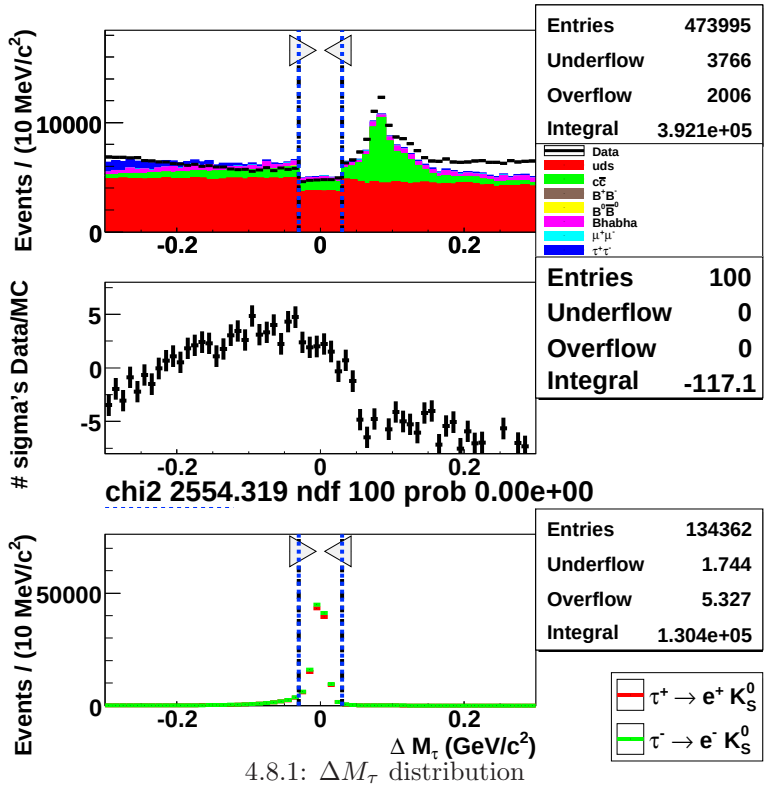

4.8.1: ΔM_τ distribution

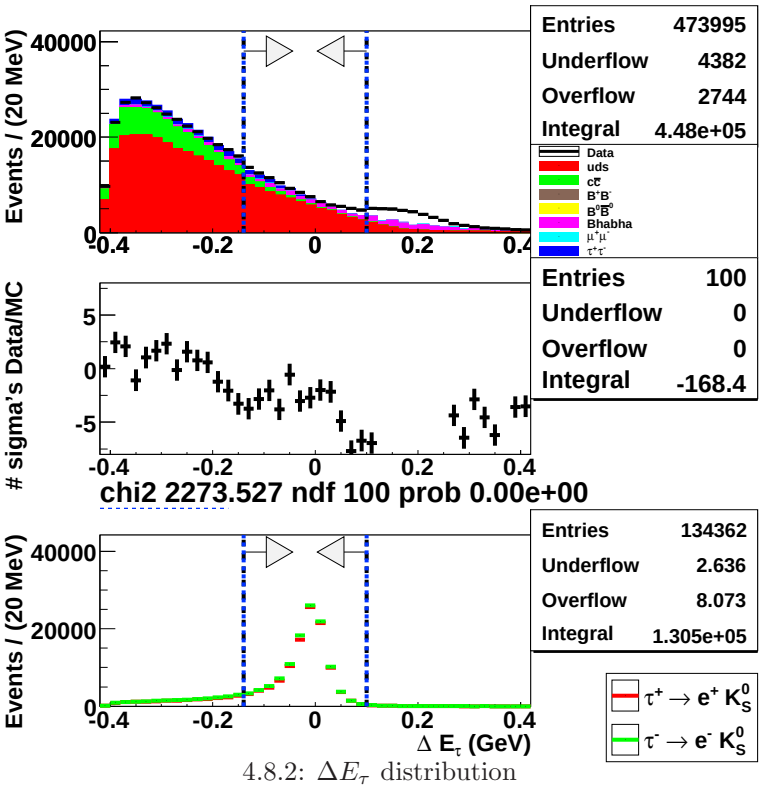

4.8.2: ΔE_τ distribution

Figure 4.8: ΔM_τ and ΔE_τ distributions for background and signal MC samples for the electron channel. Vertical dashed blue lines and arrows show the blinded region. Data in the blinded region are removed during the analysis optimization.

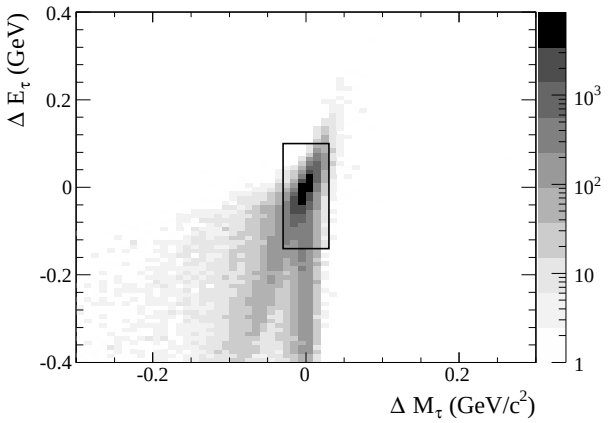

4.9.1: $\tau \to eK^0_S$

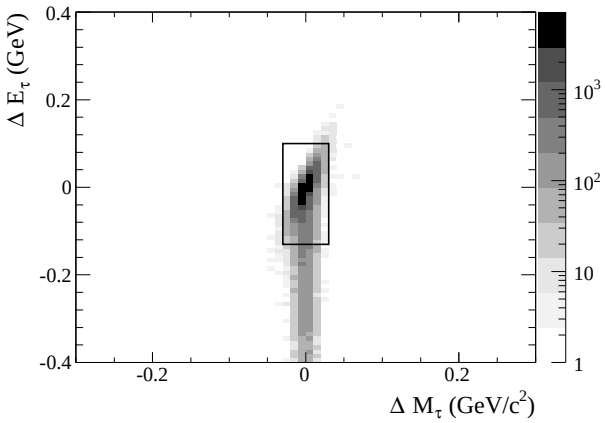

4.9.2: $\tau \to \mu K^0_S$

Figure 4.9: $\Delta E_\tau / \Delta M_\tau$ distributions for signal MC samples. The blinded region is shown by the black square. The z-axis scale is logarithmic.

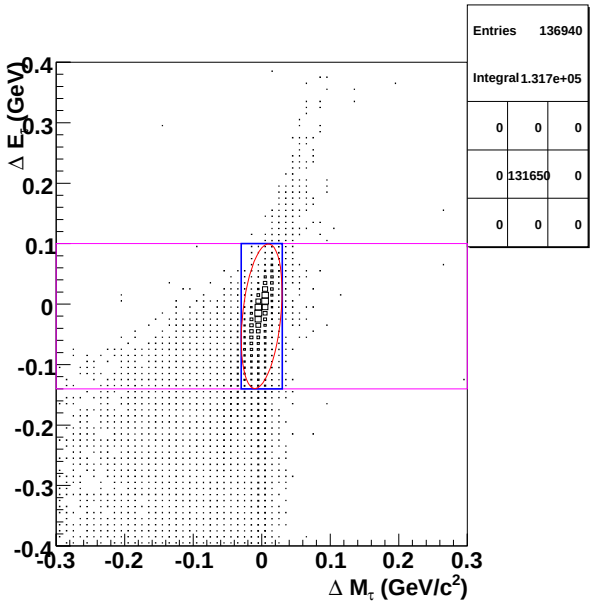

4.10.1: $\tau \to eK^0_S$

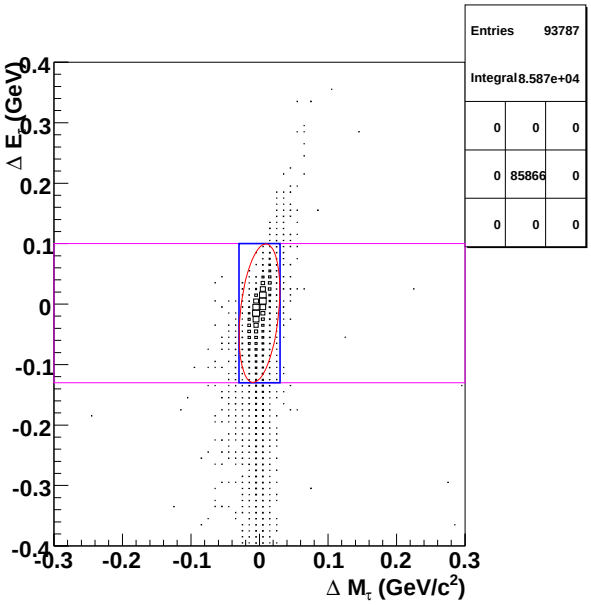

4.10.2: $\tau \to \mu K^0_S$

Figure 4.10: $\Delta E_\tau / \Delta M_\tau$ distributions for signal MC samples. The blue square is the blinded region. The red ellipsis is final signal region. Purple squares show the sideband regions.

the highest χ^2 probability of vertex fit is chosen. In the following the track and the K^0_S candidates used to reconstruct the best τ candidate will be referred to generically as *reconstructed lepton* and *reconstructed* K^0_S.

As previously mentioned in Sec. 3.1.1 and 3.2.4, correction factors are available to reduce discrepancies between data and MC samples due to different efficiency for reconstruction and particle identification. Therefore, starting from from this point of the selection, we apply a weight factor for each event of MC samples computed multiplying Δ and C_i factors[3]

The first request of the loose selection is that the reconstructed lepton passes the **loose PID selector** described in Sec. 3.2.3. This PID selector is really efficient, keeping more than 90% of selected signal events while rejecting most of the background, as shown in Fig. 4.11 and 4.12. (figures to be changed with other ones showing only the used selector in a binary way)

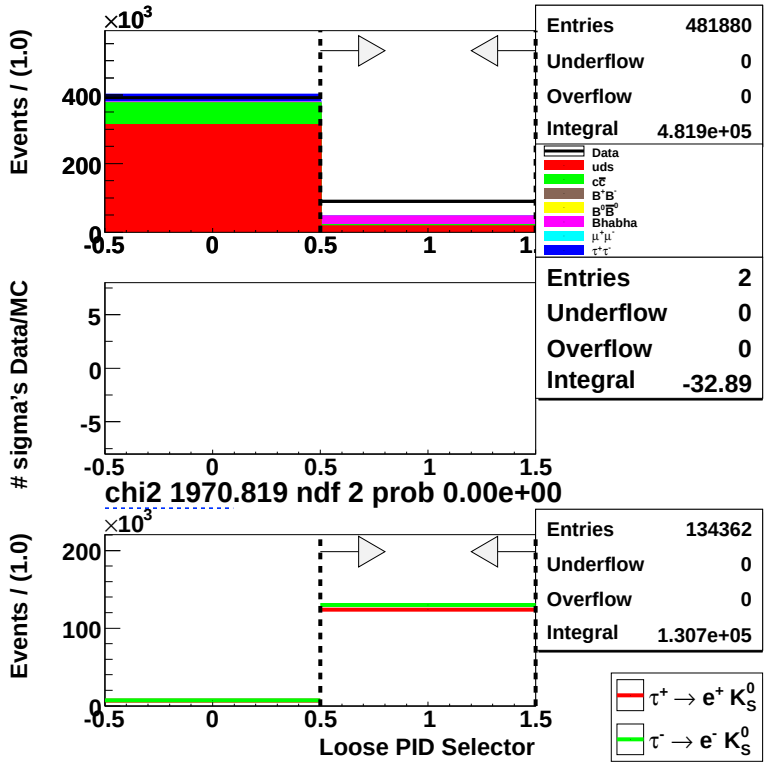

Figure 4.11: Distribution of the loose PID selector in the $\tau \to eK^0_S$ channel for data (black dots, upper plot), MC (filled histo, upper plot), MC signal (lower plot). In the middle plot the difference between data MC divided by the error is shown. Vertical dashed lines and arrows show the selected region.

At this stage, while most of remaining background events for muon channel is from *uds* events, the electron channel background is coming also from *Bhabha* processes and shows a big discrepancy between data and MC. This discrepancy is mainly due to an insufficient MC *Bhabha* sample, but those processes will be completely removed later during the loose selection. For the muon channel only, an additional request is performed before applying the PID selector: the **momentum of reconstructed K^0_S in LAB frame** must

[3]For background MC samples there is an additional rescaling factor due to equivalent generated luminosities. This factor is applied through all the selection.

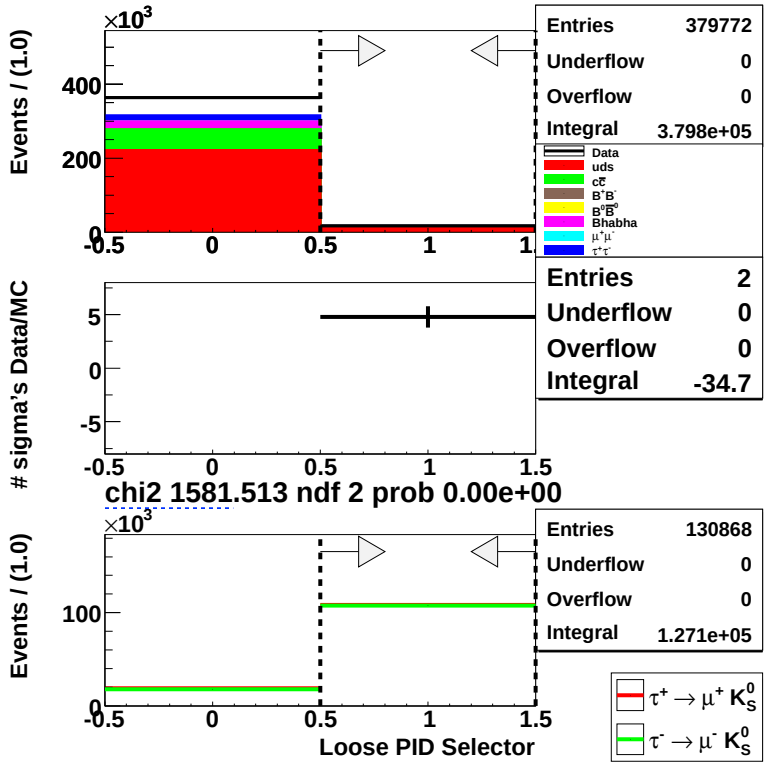

Figure 4.12: Distribution of the loose PID selector in the $\tau \to \mu K_S^0$ channel for data (black dots, upper plot), MC (filled histo, upper plot), MC signal (lower plot). In the middle plot the difference between data MC divided by the error is shown. Vertical dashed lines and arrows show the selected region.

be **greater than 1** GeV/c, to reduce the background from events with a slow K_S^0.

As said above, the thrust axis is the preferred direction for decay products in $\tau^+\tau^-$ events. Therefore, if we consider the plane perpendicular to this axis and divide each event in two hemispheres in the CM frame, all the decay products from one τ are likely to be in the same hemisphere. We define the hemisphere that contains the signal τ candidate as the **signal side** and the other one as the **tag side**, as shown into Fig. 4.13, and request to have only **three tracks on the signal side** and **one on the tag side**. We also request that the **total charge of the events must be zero**. This request is really efficient, but requesting only one track on tag side remove many signal events with three-prong decays on tag side. So for the electron channel we retain also events with **three tracks on the tag side**, because in this channel we have less background from the three-prong events on tag side than the muon one, as shown in Fig. 4.14 and Fig. 4.15.

Because of allowing also three tracks on the tag side, an additional request is made for the electron channel only, to have **at maximum four tracks** reconstructed as **Good Track Loose** ones. As described in Sec. 3.1, these tracks have a small distance of closest approach to the beam-spot and they are likely to be produced close to the beam-spot. When there are six tracks in the event, three on each side, two of them are forced by this

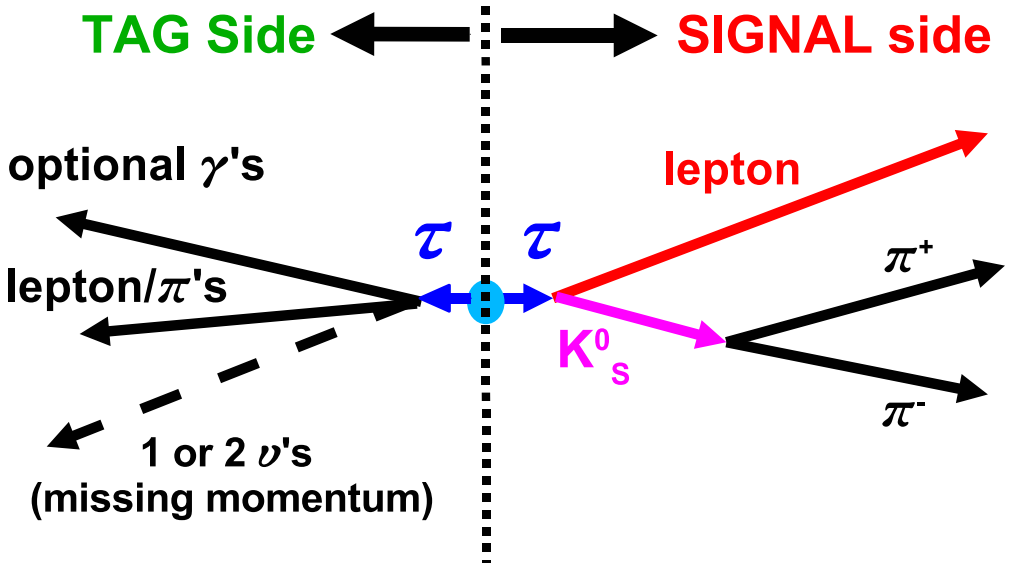

Figure 4.13: Scheme of a typical signal event divided into signal and tag side.

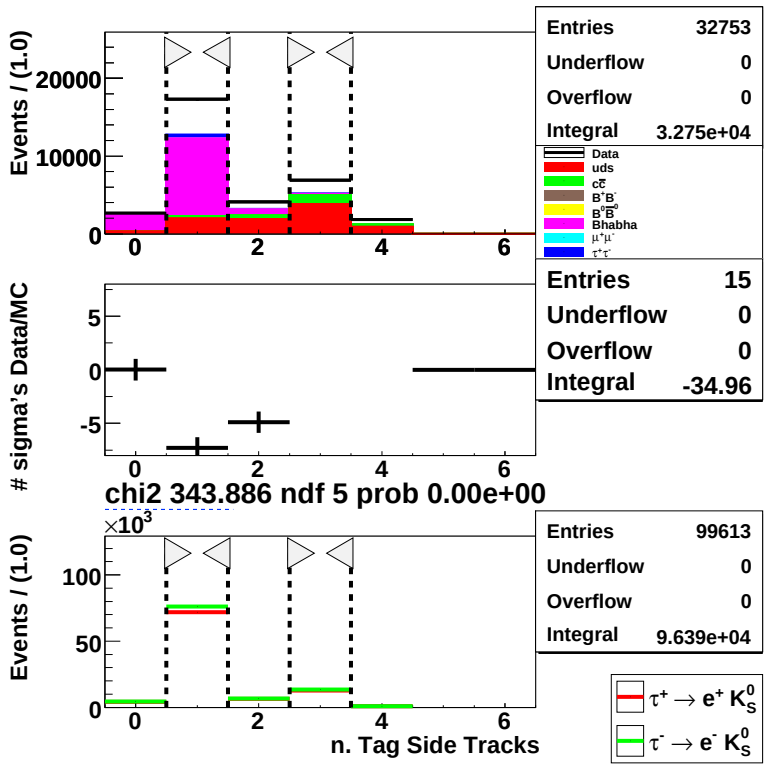

Figure 4.14: Distribution of the number of tracks on the **tag** side in the $\tau \to eK^0_S$ channel for data (black dots, upper plot), MC (filled histo, upper plot), MC signal (lower plot). In the middle plot the difference between data MC divided by the error is shown. Vertical dashed lines and arrows show the selected region.

request to be originated far from the beam-spot, generally the two from a K^0_S decaying far from the IP. So this criterion removes events where all the six tracks are produced close to the beam-spot, mostly events from uds and $c\bar{c}$.

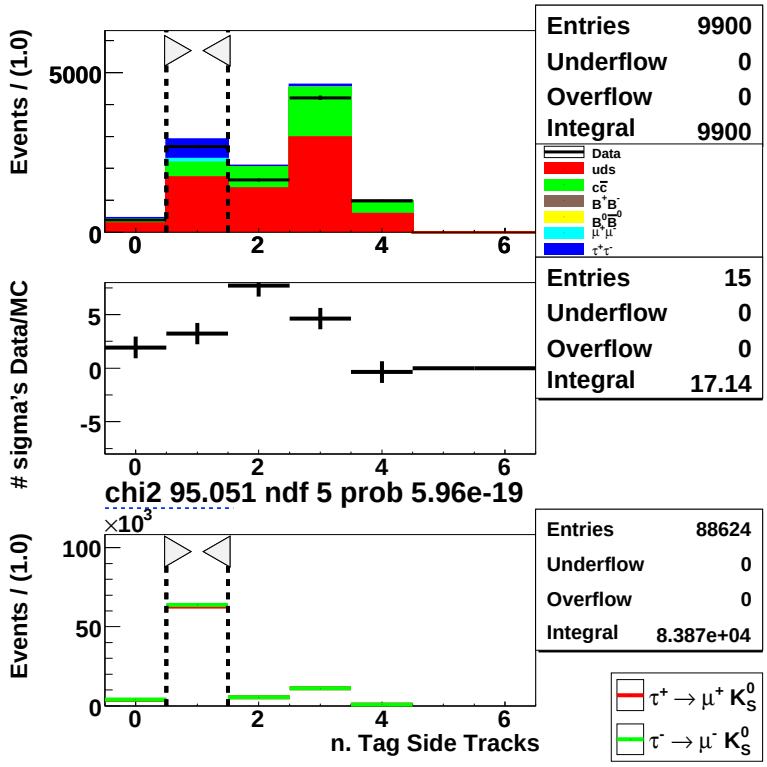

Figure 4.15: Distribution of the number of tracks on the **tag** side in the $\tau \to \mu K^0_S$ channel for data (black dots, upper plot), MC (filled histo, upper plot), MC signal (lower plot). In the middle plot the difference between data MC divided by the error is shown. Vertical dashed lines and arrows show the selected region.

For many τ candidates the vertex fit has converged but its quality is not so good. To remove events with a poor quality fit, we require the **probability of χ^2 for τ vertex fit** to be **more than 1%**. Then, only for the muon channel, we make a tighter request on the **thrust magnitude**, selecting events with a magnitude between **0.88 and 0.97**. After having applied all the previous criteria, all the selected events for the muon channel show a reasonable agreement between data and background MC samples, e.g. looking at the ΔM_τ variable, as shown in Fig. 4.16.

Instead, in the electron channel we still have a considerable amount of background from *Bhabha* events. To strongly reject them, we apply two more requirements. The first is on the total calorimeter energy for clusters associated with a track in the LAB frame (**Total Charged Tracks Energy**). For selected events this energy must be **less than 9** GeV, because for *Bhabha* processes almost all the available energy is released in the calorimeter with two or more clusters each associated with a track. Figure 4.17 shows the distribution for this variable. The second requirement is on the invariant mass of tracks used to reconstructed the K^0_S. If the invariant mass of those tracks, assigning them the mass of the electron, is close to zero, the two tracks are likely to be generated by a photon conversion into electron and positron. So we request that this invariant mass

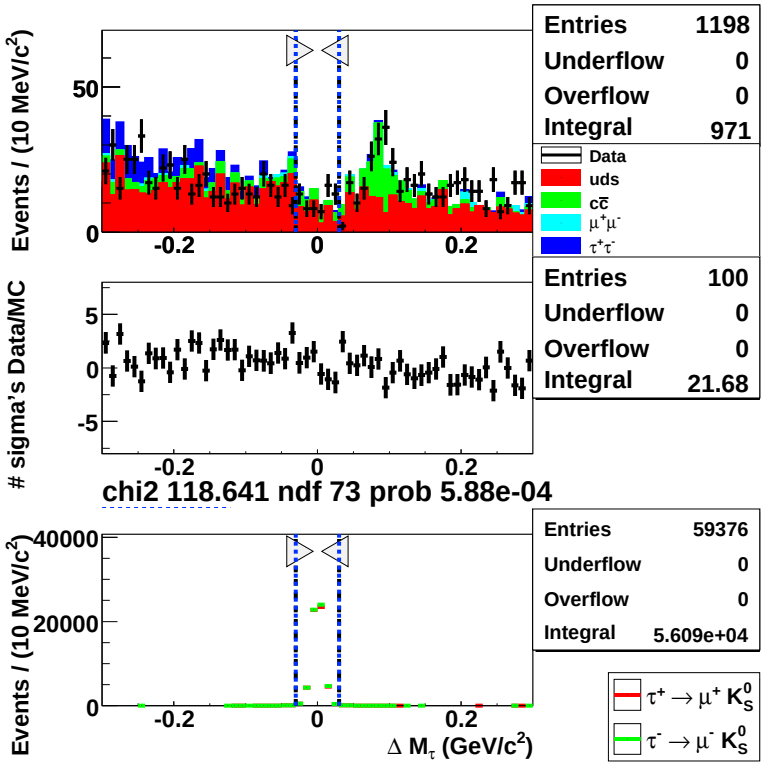

Figure 4.16: ΔM_τ distribution after the loose selection for $\tau \to \mu K_S^0$ channel.

(K_S^0 **DaughterAsElectron Mass**) must be greater than **100** MeV/c^2. Then to remove other background events in which we have a fake reconstructed K_S^0 generated by any random combination of two tracks, we require that the K_S^0 **flight significance** has to be **greater than 3** and the K_S^0 **invariant mass** between **0.48 and 0.51** GeV/c^2. The flight significance of a candidate is defined as the distance between the mother and the reconstructed decay vertex divided by its error. Here also the agreement between data and MC distribution of electron channel is satisfactory, as shown in Fig. 4.18. Table 4.8 shows a summary of the requirements applied for the loose selection.

Looking at the MC samples, we can argue that the residual background is now made by two main component: a flat one coming from the *uds* combinatorial and another one peaking $\sim 90\,\text{MeV}$ above the τ mass. This latter is coming from $D \to K_S^0\pi$ decays. Few events from $\tau^+\tau^-$ and *dimuon* processes are still present, while $b\bar{b}$ and *Bhabha* have been completely removed.

4.5 Tight selection

After we get a reasonable data/MC shape agreement, we can use the MC samples to obtain a hypothetical value for the upper limit, assuming that no events are found over the expected background. This upper limit value is generally called *sensitivity* and we

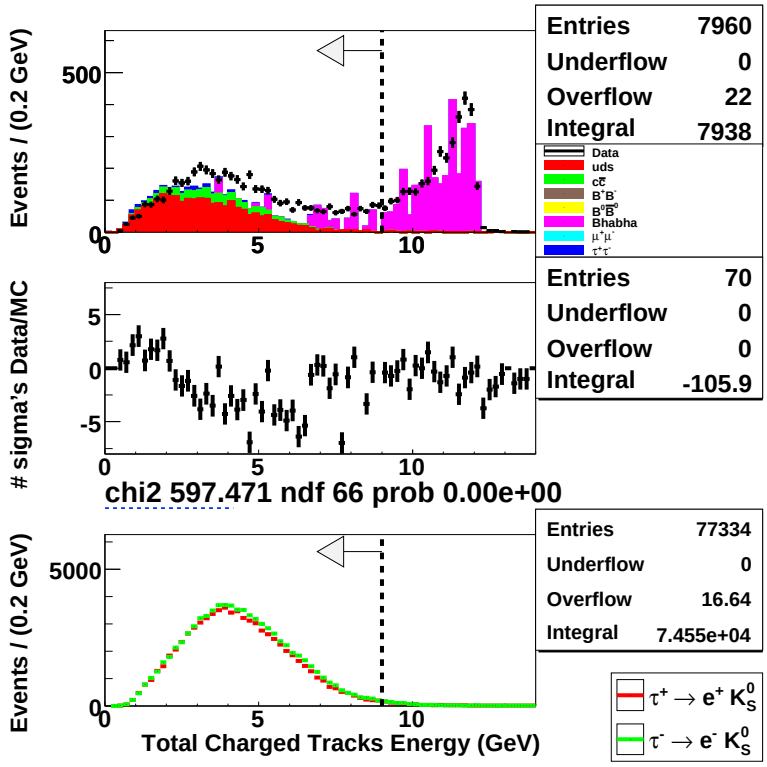

Figure 4.17: Distribution of the Total Charged Tracks Energy in the $\tau \to eK^0_S$ channel for data (black dots, upper plot), MC (filled histo, upper plot), MC signal (lower plot). In the middle plot the difference between data MC divided by the error is shown. Vertical dashed lines and arrows show the selected region.

Loose Selection criteria	$\tau \to eK^0_S$	$\tau \to \mu K^0_S$
Loose PID selector	Applied	Applied
K_S Momentum (GeV/c)	–	≥ 1.0
n. Signal Side Tracks	3	3
n. Tag Side Tracks	1 or 3	1
Event Charge	0	0
τ Vertex Fit χ^2 Probability	≥ 0.01	≥ 0.01
n. Good Tracks Loose	≤ 4	–
Thrust Magnitude	–	$0.88 \div 0.97$
Total Charged Tracks Energy (GeV)	≤ 9.0	–
K_S DaughtersAsElectrons Mass (GeV/c^2)	≥ 0.1	–
K_S Flight Significance	≥ 3.0	–
K_S Mass (GeV/c^2)	$0.482 \div 0.514$	–

Table 4.8: Summary of requirements for the loose selection. Bounds are included.

compute it with the same method used for the final result (see Chap.5). More information to discriminate signal from background is still available using the missing momentum and other variables related to the event and to the τ candidate. Criteria used for this last step

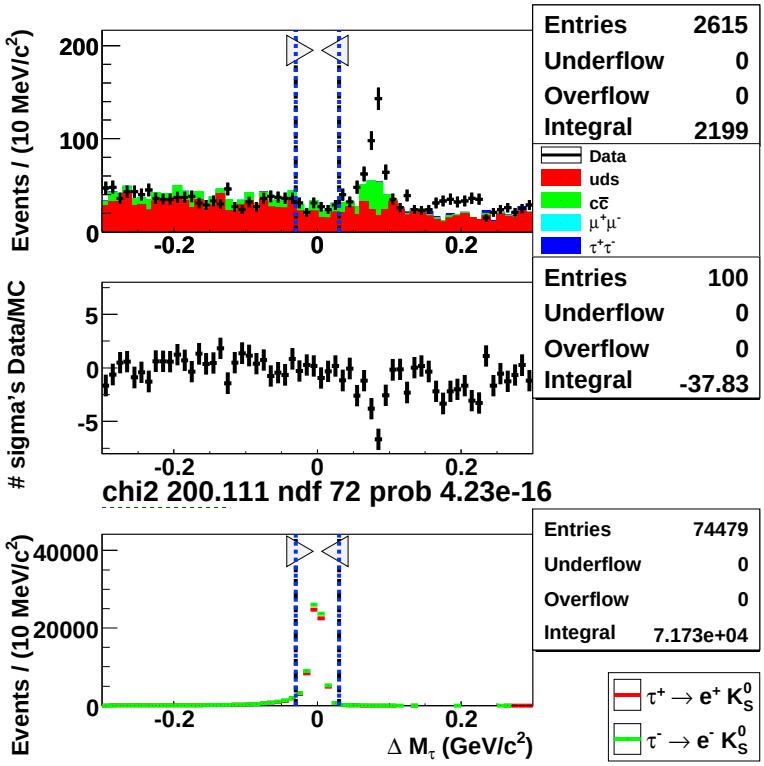

Figure 4.18: ΔM_τ distribution after the loose selection for $\tau \to eK^0_S$ channel.

of the selection are optimized to obtain the best sensitivity. Before applying requirements on new variables, we apply to the muon channel the same requirements on the flight significance and on the invariant of K^0_S used in the electron channel at the end of the loose selection. We avoid to use them before for this channel just to keep a reasonable number of events for estimating the background shape since the data/MC comparison is good for the muon channel even without these requirements.

Looking at Fig. 4.13, signal events have one or two neutrino always only on the tag side, so an event missing momentum is supposed to be different from zero and close to the trust axis, in the opposite direction compared to the τ signal candidate. Here the missing momentum is computed subtracting from the $\Upsilon(4S)$ momentum all the momenta of reconstructed tracks and clusters. We require that the **transverse component of missing momentum** must be **greater than 0.1** GeV/c for the electron channel and **greater than 0.2** GeV/c for the muon one. The distributions plot of the transverse missing momentum is shown in Fig. 4.19 for the muon channel. We choose the transverse component because this variable is less correlated than its module with particles lost out of the acceptance, close to the beams direction. We apply also another requirement related to the detector acceptance: **the cosine of the missing momentum polar angle** ($cos(\theta_{MissMom})$) must be **less than 0.95**, to remove background events again with lost particles. Regarding the direction of missing momentum, we request, only for the

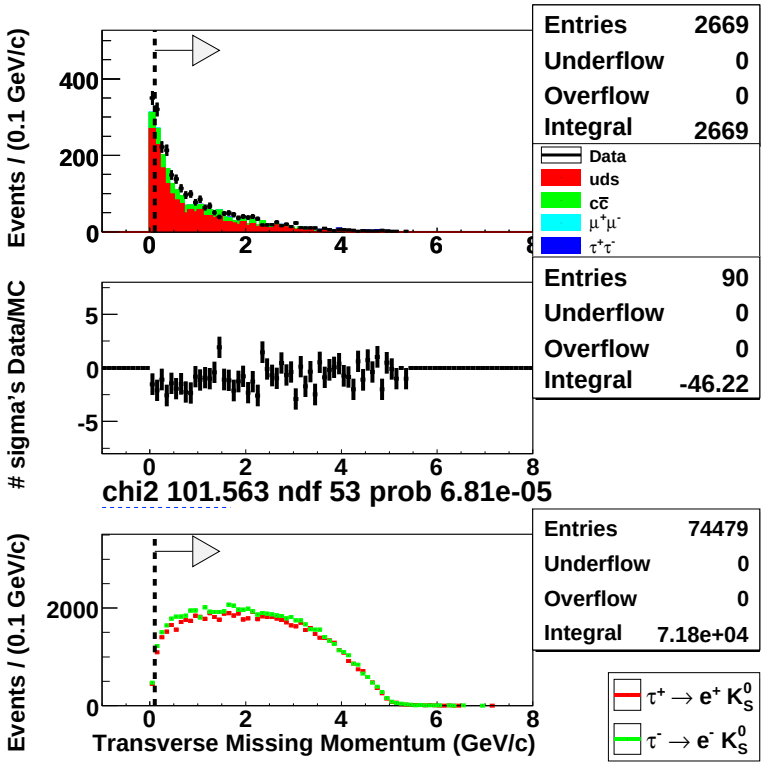

Figure 4.19: Distribution of the transverse missing momentum in the $\tau \to eK_S^0$ channel for data (black dots, upper plot), MC (filled histo, upper plot), MC signal (lower plot). In the middle plot the difference between data MC divided by the error is shown. Vertical dashed lines and arrows show the selected region.

muon channel, that **the cosine of the angle between the direction of τ candidate and the missing momentum must be positive**.

Assuming that the tag side contains a τ lepton with the same momentum of the signal candidate (but opposite in direction) and decaying mainly into hadrons, the squared invariant mass of the hadronic system on the tag side is computed by subtracting from the τ 4-momentum the neutrino 4-momentum that corresponds to the event missing momentum. As shown on Fig. 4.20, this squared mass peaks at small values (around $0.1(\,\mathrm{GeV}/c^2)^2$) for the signal events and at the squared τ mass for the background events with missing momentum close to zero. For the signal sample the tail on the right is due to events with two neutrinos and the small peak around 0.6 to τ decays with a ρ and one neutrino. For background samples the tail on the left is due to events with missing energy from lost photons. We required this **squared invariant mass of the hadronic system on the tag side** to be **less than 2.6** $(\,\mathrm{GeV}/c^2)^2$ for both channels.

Events from *uds* and $c\bar{c}$ processes have a higher average **number of reconstructed photons on the tag side**, so we request that the number of those photons must be less than 6 for both channels. As last step of tight selection we require that the reconstructed

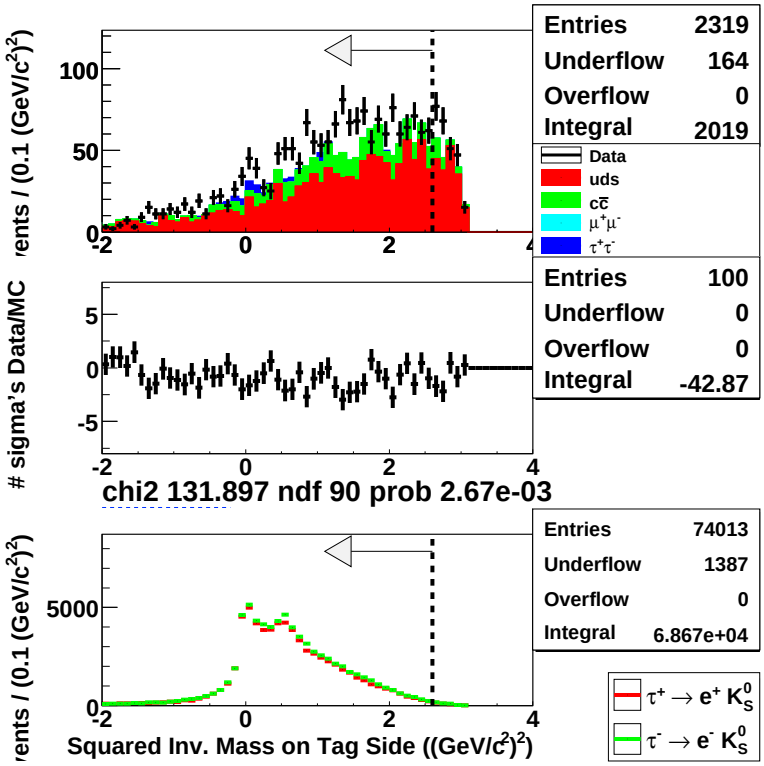

Figure 4.20: Distribution of the squared invariant mass of the hadronic system on the **tag** side in the $\tau \to eK^0_S$ channel for data (black dots, upper plot), MC (filled histo, upper plot), MC signal (lower plot). In the middle plot the difference between data MC divided by the error is shown. Vertical dashed lines and arrows show the selected region.

lepton for selected events must pass the tight PID selector. Table 4.9 show a summary of all the requirement values applied here.

Tight Selection criteria	$\tau \to eK^0_S$	$\tau \to \mu K^0_S$
K_S Flight Significance	-	≥ 3.0
K_S Mass (GeV/c^2)	-	$0.482 \div 0.514$
Transverse Missing Momentum (GeV/c)	≥ 0.1	≥ 0.2
$cos(\theta_{\tau/MissMom})$ (CM)	–	≤ 0.0
Squared Inv. Mass on Tag Side $((GeV/c^2)^2)$	≤ 2.6	≤ 2.6
n. Tag Side Photon	≤ 6	≤ 6
$cos(\theta_{MissMom})$	≤ 0.95	≤ 0.95
PID Tight selector	Applied	Applied

Table 4.9: Details of requirements values, bounds are included.

Figure 4.21 shows $\Delta E_\tau / \Delta M_\tau$ 2-dimensional distributions after the tight selection. Note that in the blinded region data was invisible throughout the analysis optimization process, and was unblinded only after careful scrutiny of the upper limit estimation

method by a review committee.

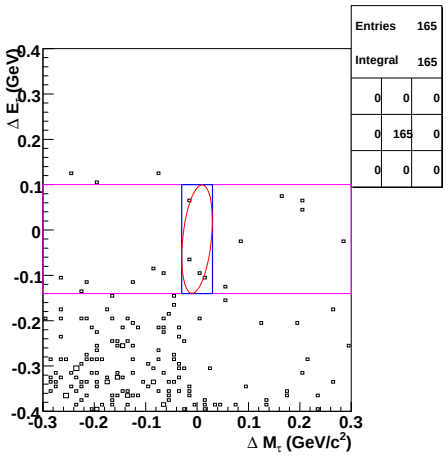

4.21.1: $\tau \to eK^0_S$

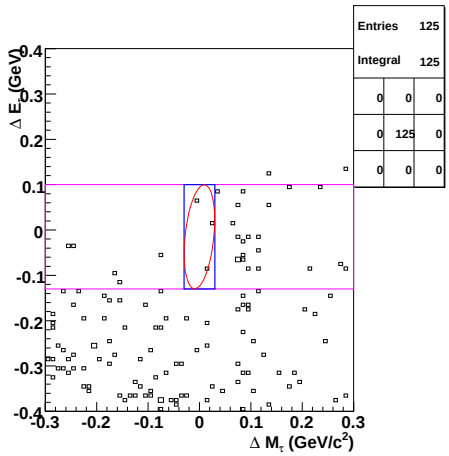

4.21.2: $\tau \to \mu K^0_S$

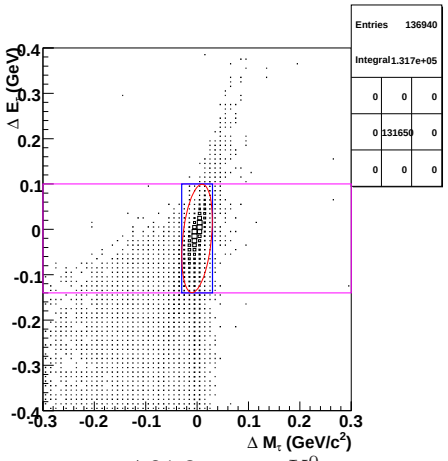

4.21.3: $\tau \to eK^0_S$

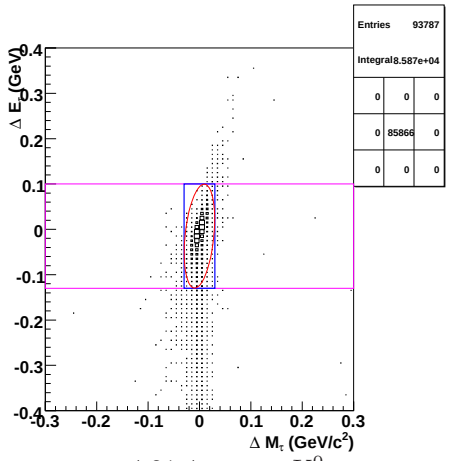

4.21.4: $\tau \to \mu K^0_S$

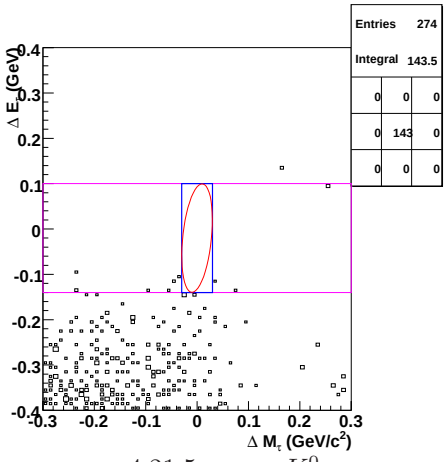

4.21.5: $\tau \to eK^0_S$

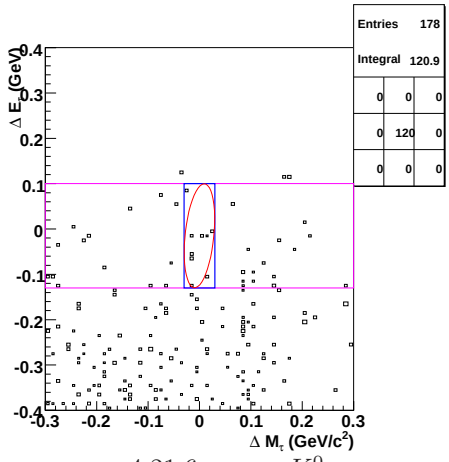

4.21.6: $\tau \to \mu K^0_S$

Figure 4.21: $\Delta E_\tau / \Delta M_\tau$ plots for data, signal and background MC after the tight selection. Blue squared is the blinding region.

4.6 Final selection and summary

After the tight selection, we perform an additional selection for the final step of upper limit estimation and only events inside the blinded region and with a χ^2_{full} **less than 50** are retained[4]. We refer to these last requirements as the **final selection**. Table 4.10 and 4.11 show a summary of the number of selected events and efficiencies for all the samples after each of the three main steps of selection. In addition tables provide the same quantities also after having applied final selection requirements.

Sample	**Events**			
	Total	Loose selection	Tight selection	Final selection
Data	6.95234e+09	2669.00(3.84E-07)	165.00(2.37E-08)	1.00(1.44E-10)
$\tau^+ \to e^+ K^0_S$	521568	71799.90(13.77%)	64098.90(12.29%)	49305.00(9.45%)
$\tau^- \to e^- K^0_S$	554908	75969.60(13.69%)	67555.20(12.17%)	51880.00(9.35%)
Total	1.07648e+06	1.5E+05(13.73%)	1.3E+05(12.23%)	1.0E+05(9.40%)
uds	9.96268e+08	1702.28(1.71E-06)	12.65(1.27E-08)	0.0(<1.00E-09)
$c\overline{c}$	1.14943e+09	454.58(3.95E-07)	126.39(1.10E-07)	0.0(<8.70E-10)
B^+B^-	7.00012e+08	0.0(<1.43E-09)	0.0(<1.43E-09)	0.0(<1.43E-09)
$B^0\overline{B}^0$	7.10674e+08	0.0(<1.41E-09)	0.0(<1.41E-09)	0.0(<1.41E-09)
$Bhabha$	4.531e+08	0.0(<2.21E-09)	0.0(<2.21E-09)	0.0(<2.21E-09)
$\mu^+\mu^-$	5.16528e+08	1.76(3.41E-09)	0.0(<1.94E-09)	0.0(<1.94E-09)
$\tau^+\tau^-$	4.01246e+08	42.38(1.06E-07)	4.51(1.12E-08)	0.0(<2.49E-09)

Table 4.10: Summary of efficiency at various levels of event selection for $\tau \to eK^0_S$ channel. In addition to the efficiency after the loose and tight selection, we show also the final efficiency after requirements of the final selection.

Looking at those table and at the whole selection, we can make the following remarks:

- after the loose selection, we obtain a reasonable shape agreement between data and MC samples. The overall normalization is not fully compatible but we will not rely on MC samples for the normalization of residual background estimation;

- after the tight selection, we completely remove events from $b\overline{b}$, *Bhabha* and *dimuon* processes. Main contributes to the background are from uds and $c\overline{c}$ processes plus few events from $\tau^+\tau^-$ one;

- after the tight selection, for the electron channel the background is mostly due to $c\overline{c}$ events, especially $D \to K^0_S e\nu$. This last background component is irreducible;

[4] This is the χ^2 of the vertex fit with additional constraints on τ energy and invariant mass, see Sec. 3.5.

Sample	Events			
	Total	Loose selection	Tight selection	Final Selection
Data	6.95234e+09	1225.00(1.76E-07)	125.00(1.80E-08)	2.00(2.88E-10)
$\tau^+ \to \mu^+ K_S^0$	520724	56086.40(10.77%)	42462.50(8.15%)	36167.50(6.95%)
$\tau^- \to \mu^- K_S^0$	520944	56815.00(10.91%)	43404.60(8.33%)	37000.30(7.10%)
Total	1.04167e+06	1.1E+05(10.84%)	85867.10(8.24%)	73167.80(7.02%)
uds	9.96268e+08	878.12(8.81E-07)	70.05(7.03E-08)	5.20(5.22E-09)
$c\overline{c}$	1.14943e+09	229.62(2.00E-07)	41.72(3.63E-08)	0.0(<8.70E-10)
B^+B^-	7.00012e+08	0.0(<1.43E-09)	0.0(<1.43E-09)	0.0(<1.43E-09)
$B^0\overline{B}^0$	7.10674e+08	0.0(<1.41E-09)	0.0(<1.41E-09)	0.0(<1.41E-09)
$Bhabha$	4.531e+08	0.0(<2.21E-09)	0.0(<2.21E-09)	0.0(<2.21E-09)
$\mu^+\mu^-$	5.16528e+08	31.89(6.17E-08)	0.0(<1.94E-09)	0.0(<1.94E-09)
$\tau^+\tau^-$	4.01246e+08	242.93(6.05E-07)	9.12(2.27E-08)	0.0(<2.49E-09)

Table 4.11: Summary of efficiency at various levels of event selection for $\tau \to \mu K_S^0$ channel. In addition to the efficiency after the loose and tight selection, we show also the final efficiency after requirements of the final selection.

- after the tight selection, for the muon channel the background is made mostly by uds events with a real K_S^0 and a pions mis-identified as a muon. Also $D \to K_S^0\pi$ events are still present for the same reason. Our PID muon selector has worse performances compared to the electron one;

- after the final selection, all the background MC events have been removed, apart from 5 events from uds for the muon channel;

- we reinsert the blinded events in the data sample and we found, after the final selection, one and two events respectively on electron ad muon channel.

4.7 Study of systematic uncertainties

During the running of *BABAR* experiment, the detector simulation has been continuously improved to obtain background and signal MC samples as similar as possible to data. Anyway there are still some discrepancies and many studies have been performed to have a good estimation of these discrepancies to be accounted as systematic errors.

For this analysis we consider only systematic uncertainties related to the number of τ pair and to the signal efficiencies and a detailed description of them is provide in this section, with a summary table at the end. Systematic uncertainties are ordered from the greatest contribute to the smallest one. The final systematics value is computed summing in quadrature all the contributes. For the background samples, the number of selected events is small and statistics uncertainties dominate over the systematic ones. An accurate

estimation of uncertainties on background samples is different for each method of upper limit calculation and we describe them in detail in Chap. 5 and 6.

4.7.1 Particle identification

In this analysis the difference between the PID in data and MC sample has been accounted applying an additional weight on each MC event according the used selector, as described in Sec. 3.2.4. The PID systematic error is estimated summing two contributes: one is coming from statistical errors on the control sample used to calculate the weight factor and one from the difference between this control sample and the sample selected in this analysis. The second contributes generally is larger than the first one.

The first component is obtained summing the uncertainties for the PID correction factors. As previously said, these factors are given for different bin of momentum, polar and azimuthal angle for the track in the LAB system and their uncertainties are weighted according the number of events selected for this analysis in each bin.

The PID correction factor is the ratio between the efficiencies for a certain selector on data and MC samples and these efficiencies are computed using samples that in general are different from specific analysis ones. The second component is the variation on the selection efficiency when PID corrections are computed using this analysis events as MC control sample. This efficiency corrected for a different event environment is calculated using Eq. 3.6 and replacing $\varepsilon^{MC}_{\mathrm{ControlSample}}$ in Eq. 3.7 with

$$\left(\varepsilon^{\mathrm{MC}}_{\mathrm{AnalysisSelector}}\right)_i = \left(\varepsilon^{\mathrm{MC}}_{\mathrm{ControlSample}}\right)_i \times \frac{\left(\frac{N^{\mathrm{AnalysisMC}}_{\mathrm{PIDSelected}}}{N^{\mathrm{AnalysisMC}}_{\mathrm{Truth}}}\right)_i}{\left(\frac{N^{\mathrm{ControlSampleMC}}_{\mathrm{PIDSelected}}}{N^{\mathrm{ControlSampleMC}}_{\mathrm{Truth}}}\right)_i} \tag{4.1}$$

where $N^{\mathrm{AnalysisMC}}$ is the number of events in this analysis and $N^{\mathrm{ControlSampleMC}}$ is the number in the control sample used for the PID correction. This second component is larger that the first one for our analysis.

These two components are then summed in quadrature and final relative errors due to the PID are 0.4% and 5.1% respectively for electron and muon channels.

4.7.2 Tracking efficiency

In this analysis the difference between the tracking efficiency in data and MC sample has been accounted applying an additional weight on each MC event according the number and the type of tracks, as described in Sec. 3.1.1. Each of this correction factor has its own error and the average error for events after the final selection is taken as systematic uncertainty for the tracking efficiency. The average relative error is 1.7% and 1.6% respectively for electron and muon channels.

4.7.3 K_S^0 reconstruction

Correction factors to reduce the discrepancy between data and MC samples are available also for effect due to the K_S^0 reconstruction. These factors are computed for each bin of transverse flight length, transverse momentum and polar angle in LAB system and they are computed separately for each Run-cycle. Instead of apply them, we choose to take them as a systematic error. Therefore the values for each period are summed together, weighting over the luminosity of the period itself. The final value is for the systematic error due to K_S^0 reconstruction is 1.0% for both channels.

4.7.4 Luminosity and cross section

For this analysis we use the cross section for τ production at the $\Upsilon(4S)$ estimated with `KK2f` MC to be 0.919 ± 0.003 nb in [45], with a relative error of 0.31%. The luminosity of the data sample for the *BABAR* experiment is computed using *Bhabha*, *dimuon* and two-photons events and cross sections of those processes are known from MC studies with estimated uncertainties of 0.5% for *Bhabha*, 1.4% for *dimuon* and 2.0% for two-photon events. After combining these uncertainties with the error on efficiencies to select those process we obtain a relative error on the luminosity of 0.94% for Run-cycle 1,2 and 3 and 0.7% for Run-cycle 4,5 and 6. When combining the two groups of Run-cycles, we assume they share a 100% correlated uncertainty that can be estimated to be 0.5% due to the *Bhabha* cross section error. The remaining uncertainties are assumed to be uncorrelated. Therefore we separate the uncorrelated contributions, obtaining 0.8% for Run-cycle 1,2 and 3 and 0.49% for Run-cycle 4,5 and 6. These values are weighted for the luminosities of included Run-cycles, summed in quadrature and then we add in quadrature the correlated uncertainty subtracted before. For this analysis the resulting uncertainty is 0.7% for both channels.

4.7.5 Beam energy scale and energy spread

Studies on the beams energy spread have revealed that systematic uncertainties in the CM are expected to be ~ 2 MeV. A shift in the beams energy affects the reconstructed energy of the τ candidate, directly related to ΔE_τ. This is evident in figure 4.9 where initial state radiation induces visible shift in the reconstructed energy not correlated with a shifts in ΔM_τ. We estimate the systematic error for this effect by shifting the center of final signal region in ΔE_τ by ± 2 MeV and determining the change for the signal efficiency. This effect produce a tiny change in the efficiencies, below 0.1%, that produce no change on the final value when summed in quadrature with the other systematics.

4.7.6 Summary

Table 4.12 shows a summary of various systematic uncertainties that have been described above and will be included into the final results using different procedures for each upper limit estimation method. We will detail those procedures in chapters where methods are described.

Systematic source	$\tau \to eK_S^0$	$\tau \to \mu K_S^0$
Particle identification (ε)	0.4%	5.1%
Tracking efficiency (ε)	1.7%	1.6%
K_S reconstruction (ε)	1.0%	1.0%
Luminosity and Cross Section ($\#\tau$)	0.7%	0.7%
Beam energy scale and energy spread (ε)	$< 0.1\%$	$< 0.1\%$
Total	**2.1%**	**5.5%**

Table 4.12: Relative systematic errors (%) associated with luminosity, τ cross section and signal efficiency.

Chapter 5

Modified Frequentist Analysis

In this chapter we describe the method used in this analysis to extract an upper limit estimation for $\tau \to lK^0_S$ decay mode. We will give a brief technical description of this method, how we estimate the efficiency and the residual background and then the result. More details about the method could be found in [40, 70, 71]. In the following we refer to this method as **modified frequentist analysis** or $CL_{\rm s}$ **method**.

5.1 Overview of the analysis method and implementation

In the recent years, most search experiments estimate confidence intervals for physical constants using the *Feldman and Cousins* approach [42]. This approach is based on a classical frequentist estimation that could produce apparently unintuitive results. For example, if we have two experiments with identical efficiencies and numbers of observed events, the experiment with the largest expected background can have a better sensitivity for the upper limit. The *modified frequentist analysis* has been developed to avoid this behaviour, but also to have the possibility of combining more search results and their uncertainties from different experiments. The basic goal of the method is to allow a strong exclusion of a signal (or a strong evidence for an existing signal) while providing a consistent tool to avoid statements concerning regions where the signal+background hypothesis cannot be discriminated against the background only one (i.e. when going significantly below the sensitivity of the analysis). The basic ingredients of this method are a different definition of signal confidence level and a test-statistics which ranks experiments from the least to most signal-like or most to least background-like. This method was used originally to set lower bounds on the Higgs boson mass and partially in other *BABAR* analysis like the search for $\tau \to \mu\gamma$ [15].

Introducing CL_s

The analysis of search results can be formulated in terms of a hypothesis test. The null hypothesis is that the signal is absent and the alternate hypothesis is that it exists. An analysis of search results is simply a formal definition of the procedure which quantifies the degree to which the hypotheses are favored or excluded by an experimental observation. The first step in defining an analysis of search results is to identify observables in the experiment which include search results. The next step is to define a test-statistic or function of the observables and the model parameters (particle mass, production rate, etc.) of the known background and hypothetical signal which ranks experiments from the least to most signal-like (most to least background-like). The last step is to define rules for exclusion and discovery i.e. specify ranges of values of the test-statistic in which observations will lead to one conclusion or the other. In other words a confidence level for the exclusion will be quoted. A confidence limit for exclusion is defined as the value of a population parameter (such as a particle mass or a production rate) which is excluded at a specified confidence level. A confidence limit is a lower (upper) limit if the exclusion confidence is greater (less) than the specified confidence level for all values of the population parameter below (above) the confidence limit. For convenience the test-statistic Q is constructed to increase monotonically for increasingly signal-like (decreasingly background-like) experiments so that the confidence in the signal+background hypothesis is given by the probability that the test-statistic is less than or equal to the value observed in the experiment, $Q_{\rm obs}$:

$$CL_{\rm s+b} = P_{\rm s+b}(Q \leq Q_{\rm obs}), \tag{5.1}$$

where

$$P_{\rm s+b}(Q \leq Q_{\rm obs}) = \int_{-\infty}^{Q_{\rm obs}} \frac{dP_{\rm s+b}}{dQ} dQ, \tag{5.2}$$

and where $dP_{\rm s+b}/dQ$ is the probability distribution function (pdf) of the test-statistic for signal+background experiments. Small values of indicate poor compatibility with the signal+background hypothesis and favor the background hypothesis. Similarly, the confidence in the background hypothesis is given by the probability that the test-statistic is less than or equal to the value observed in the experiment, $Q_{\rm obs}$:

$$CL_{\rm b} = P_{\rm b}(Q \leq Q_{\rm obs}) = \int_{-\infty}^{Q_{\rm obs}} \frac{dP_{\rm b}}{dQ} dQ, \tag{5.3}$$

where again $dP_{\rm b}/dQ$ is the pdf of the test-statistic for background-only experiments. Values of $CL_{\rm b}$ very close to 1 indicate poor compatibility with the background hypothesis and favor the signal+background hypothesis.

Taking into account the presence of background in the data may result in a value

of the estimator of a model parameter which is unphysical, e.g. observing less than the mean expected number of background events could be accommodated better if the signal rate was negative. One possible technique for dealing with this situation is to normalize the confidence level observed for the signal+background hypothesis, $CL_{\mathrm{s+b}}$, to the one observed for the background-only hypothesis, CL_{b}. This is a generalization of the modified classical calculation of confidence limits for single channel counting experiments presented in [72]. This also makes it possible to obtain sensible exclusion limits on the signal even when the observed rate is so low that the background hypothesis is called into question. We are also aware that a low background confidence may also indicate underestimated or forgotten systematic errors. It may be said that this modified frequentist or CL_{s} procedure (as it will be called here) is performed in order to obtain conservative limits on the signal hypothesis. The modified frequentist re-normalization described above is simply

$$CL_{\mathrm{s}} \equiv CL_{\mathrm{s+b}}/CL_{\mathrm{b}}. \tag{5.4}$$

Although is not, strictly speaking, a confidence (it is a ratio of confidences), the signal hypothesis will be considered excluded at the confidence level when

$$1 - CL_{\mathrm{s}} \leq CL. \tag{5.5}$$

The consequence of not being a true confidence is that the hypothetical false exclusion rate is generally less than the nominal rate of $1-CL$. The difference between CL_{s} and the actual false exclusion rate will in fact increase as the pdf's of the signal+background and background hypotheses become more and more similar. Thus the use of CL_{s} increases the coverage of the analysis, i.e. the range of model parameters for which an exclusion result is possible is reduced, but it also avoids the undesirable property for which, between two experiments with the same (small) expected signal rate but different backgrounds, the experiment with the larger background may have a better expected performance.

The Likelihood Ratio Test-Statistics

It is well known that an optimal choice for such a test-statistic is represented by the likelihood ratio Q:

$$Q = \mathcal{L}(S+B)/\mathcal{L}(B) \tag{5.6}$$

between the likelihood $\mathcal{L}(S+B)$ for the signal+background hypothesis and the likelihood $\mathcal{L}(B)$ for the background-only hypothesis. The likelihood ratio for an experiment with independent channels is simply a product of the likelihood ratios of the individual channels, so that the combination of additional histogram bins, independent search channels, experiments or center-of-mass energies is straightforward and unambiguous. The likelihood ratio Q for experiments with independent search channels and measurements of a

discriminating variable for each candidate, and where the absolute signal and background rates are known, can be written as

$$Q = \frac{\prod_{i=1}^{N_{\rm chan}} \frac{e^{-(s_i+b_i)}(s_i+b_i)^{n_i}}{n_i!}}{\prod_{i=1}^{N_{\rm chan}} \frac{e^{-b_i} b_i^{n_i}}{n_i!}} \frac{\prod_{j=1}^{n_i} \frac{s_i S_i(x_{ij}) + b_i B_i(x_{ij})}{s_i+b_i}}{\prod_{j=1}^{n_i} B_i(x_{ij})} \tag{5.7}$$

which can be simplified to

$$Q = e^{-s_{tot}} \prod_{i=1}^{N_{\rm chan}} \prod_{j=1}^{n_i} \left(1 + \frac{s_i S_i(x_{ij})}{b_i B_i(x_{ij})}\right), \tag{5.8}$$

where n_i is the number of observed candidates in each channel, x_{ij} is the value of the discriminating variable measured for each of the candidates, s_i and b_i are the integrated signal and background rates per channel, s_{tot} is the total signal rate for all channels, and $S_i(x)$ and $B_i(x)$ are the probability distribution functions of the discriminating variable for the signal and background of i channel respectively.

If the p.d.f.s of the discriminating variable are identical for the signal and background, if none is measured or if the distributions are expressed as binned histograms, the likelihood ratio simplifies further to

$$Q = e^{-s_{tot}} \prod_{i=1}^{N_{\rm chan}} \left(1 + \frac{s_i}{b_i}\right)^{n_i}. \tag{5.9}$$

Implementation for this analysis

In the present analysis an interesting example of a strongly discriminating variable is offered by the χ^2 of a geometrical and kinematic fit imposing further constraints, already defined in Sec. 3.5 as the *full fit*. For this fit, in addition to constrain the K^0_S mass to the nominal value, the τ vertex to the beam-spot and K^0_S and lepton to come from τ decay vertex, we request also that the reconstructed τ candidate has the nominal τ mass and the expected energy for a $\tau^+\tau^-$ process in our experiment, exactly half of the CM energy. This variable, that accounts simultaneously for all kinematic discrepancies between the measured and fitted quantities and the respective errors, will be referred from now on as χ^2_{full}. Fig.5.1 shows simulated distributions of these variables at the loose selection stage for the two decay channels respectively. For better readability the background samples are rescaled by a factor 100.

The pdf distribution of χ^2_{full} is estimated for signal and background events in the range from 0 to 50 divided in 100 bins and respective uncertainties are included into them, as described in Sec. 5.2. Each of these bins is accounted as a single experiment result and the errors are treated as fully correlated, because due mainly to normalization uncertainties. After estimating pdf distributions, several possible values of the $\tau \to lK^0_S$

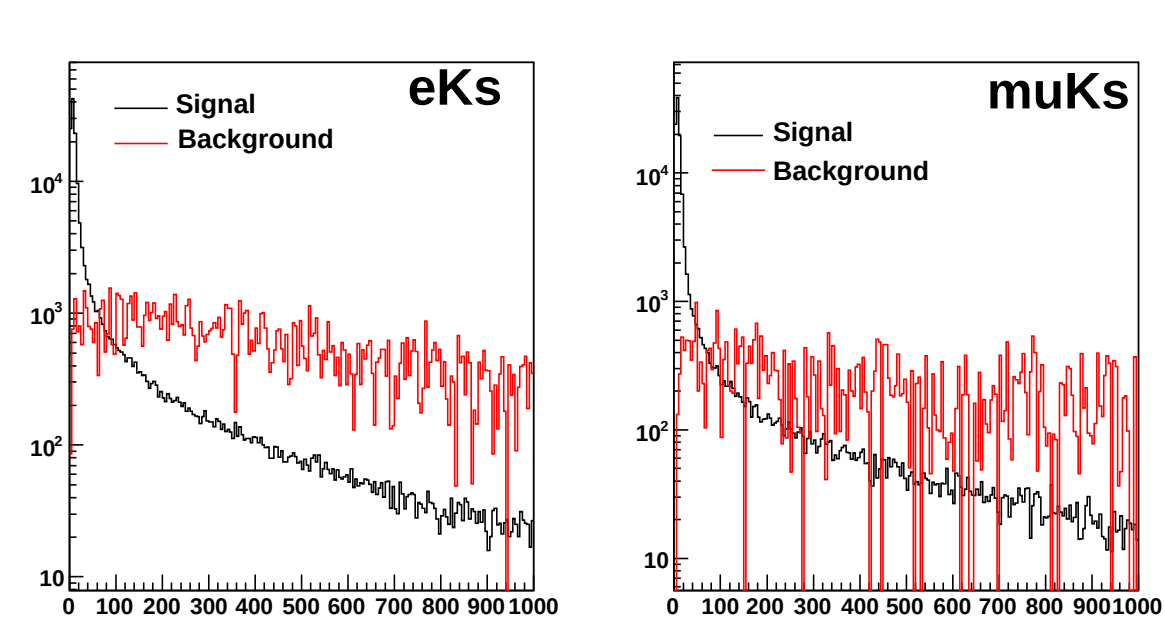

Figure 5.1: Distributions of χ^2_{full} for simulated background and signal samples. The background events are rescaled by a factor 100 for a better readability.

branching fraction are chosen in turn and for each of them a series of MC experiments for signal+background and background only is performed. Uncertainties are accounted in the procedure smearing for each experiment efficiencies and background rates: each rate is randomly generated according a Gaussian distribution with the original rate value as mean and the uncertainty as sigma. For each simulated experiment the likelihood ratio is evaluated and compared to the real data one allowing to evaluate $CL_{\rm b}$ and $CL_{\rm s+b}$ values. At the end the $CL_{\rm s}$ value is obtained as ratio of $CL_{\rm s+b}$ to $CL_{\rm b}$. An expected value is computed on the basis of the median value of $CL_{\rm s+b}$ obtained using other background only simulated experiments instead of the real data one. This values is what we referred to as sensitivity in Sec. 4.5.

5.2 Estimation of signal and background distributions

Probability density functions (pdf) of the discriminating variable χ^2_{full} for signal and background are retrieved using the MC samples. For this analysis we applied the $CL_{\rm s}$ method considering those distributions only in the range between 0 and 50, divided in 100 bins, because it contains more than 90% of the signal sample.

For the signal we consider events after the final selection because we still have enough statistics. Systematic errors are assigned to bin contents for the efficiency pdf according

the uncertainties quoted in Sec. 4.7 and these errors are added in quadrature to to the statistical ones. Distributions for both channel are shown in Fig. 5.2.

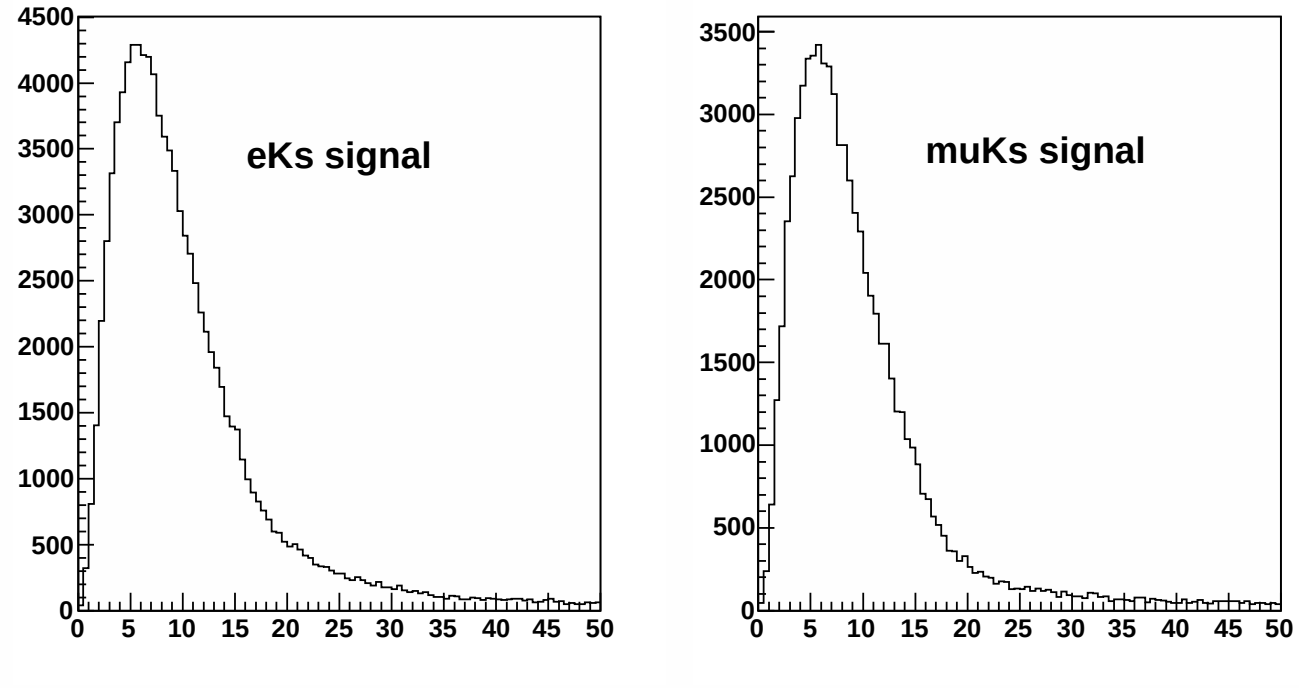

Figure 5.2: Signal χ^2_{full} distributions after the final selection.

The direct evaluation of the background distribution is more problematic because the number of events in background MC samples at the final selection stage is very low (actually zero for $\tau \to eK^0_S$). Therefore we use events at loose and tight selection stages (see Sec. 4.4 and 4.5) in an extended range of χ^2_{full}, between 0 and 1000. In addition we define a new selection stage, called **loose-plus** that retains events, after the loose selection stage, inside the blinded box with a χ^2_{full} between 0 and 50.

As a first step an estimate of the expected total number of background events at final stage has to be obtained indirectly, based on some sensible hypotheses. This is done separately for *uds* and $c\bar{c}$ components of the background. They are the only ones surviving after the loose selection inside the blinding box and have non compatible distributions, as can be seen in Fig. 5.3.

Apart form the case of *uds* component for $\tau \to \mu K^0_S$ channel, we have no events after the final selection. So for each component, we take the number of events at loose and tight selection stage and compute the ratio between them. Assuming that the fraction of events inside the blinded region is the same for the loose and tight stages of selection, we multiply the number of events at the loose-plus selection stage by the ratio calculated

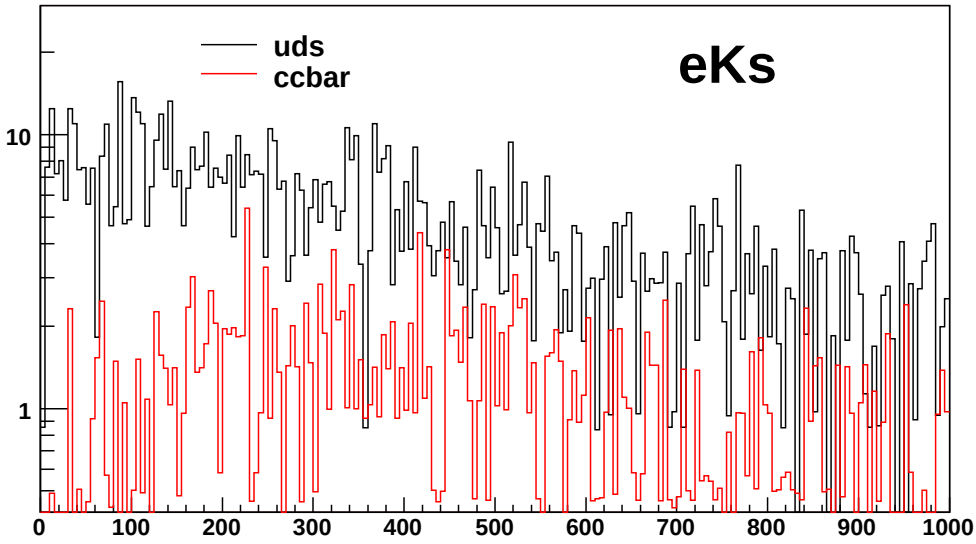

Figure 5.3: Distributions of χ^2_{full} for the different background samples after the loose selection.

before and we obtain an estimation of background events in the final signal region. In fact the final signal region corresponds exactly to the tight selection stage plus the request for the events to be inside the blinded box and to have a χ^2_{full} between 0 and 50. The error is computed with the standard propagation from Poissonian uncertainties of each number of events used in the calculation. So we use the estimation procedure described above for all the components but the *uds* one for $\tau \to \mu K^0_S$ channel. Value used for the total estimation are bold in Tab. 5.1, that summarize the number of events for each component and for different selections.

Although the hypothesis of equal fraction is somehow arbitrary, the statistical error is so large to account for any discrepancy. As a check, the same estimate applied to signal events turns out to agree at the 1% level with the actual observed number for both channels. A further issue to be discussed is the agreement of the MC background simulations with the data. This can be done using events after the tight selection outside the blinded region. In case of the $\tau \to eK^0_S$ channel the number of events is ~ 95, a bit less than the real ones (107) so the original background normalization is rescaled by the data/MC ratio leading to a final corrected estimate of 1.0 ± 0.4, as shown in Tab. 5.1. On the other hand for the $\tau \to \mu K^0_S$ channel 48 events in the MC samples have to be compared to 53 real events. As the difference is statistically negligible, the lower MC background estimation is used since it is the most conservative when establishing upper limits, but a systematic 10% error is added in quadrature, leading to a final corrected estimate of 5.3 ± 2.2.

				Final Selection	
Component	Loose Sel	Loose-plus Sel	Tight Sel	Estimation	Observed
$\tau \to eK_s^0$					
uds	963.7	42.1	9.2	$\mathbf{0.40 \pm 0.13}$	0
$c\overline{c}$	232.0	1.4	82.8	$\mathbf{0.5 \pm 0.3}$	0
Total Bkg Estimation				0.9 ± 0.3	
Corrected Bkg Estimation				0.9 ± 0.3	
$\tau \to lK_s^0$					
uds	333.1	23.6	34.9	2.5	$\mathbf{5.2 \pm 2.1}$
$c\overline{c}$	75.5	0.45	17.7	$\mathbf{0.10 \pm 0.06}$	0
Total Bkg Estimation				5.3 ± 2.1	
Corrected Bkg Estimation				5.3 ± 2.1	

Table 5.1: Summary of numbers of events after various selections used for computing the estimation of background normalization. In addition we report also the corrected estimation used as final normalization value (see text for details).

After the normalization, i.e. the expected number of background events, the shape of the background distribution has to be fixed. The way to determine it is based on the observation that selection criteria applied for tight selection do not change significantly the shape of the χ^2_{full} distribution. This is illustrated in Fig. 5.4, where it can be observed that the ratio of the distributions at loose and tight selection levels for signal events does not exhibit important structures, with respect to the very large statistical errors.

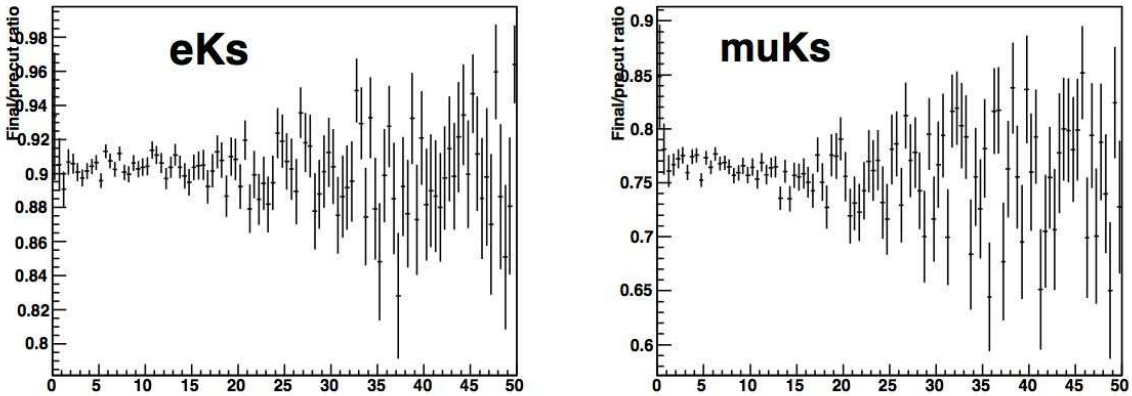

Figure 5.4: Ratio of signal χ^2_{full} distributions after the final selection and after loose selection.

Since the different background components show a different behavior (see Fig. 5.3) and progressing with the selection the relative contributions of these components vary significantly, it is not possible to assume the overall background distribution at loose

selection level as representative (in shape) of the distribution at final selection level. The way to determine the background shape is then to use estimates of the contribution at final level from uds and $c\bar{c}$ and use these as weights to combine respective distributions extracted at the loose selection level. The resulting distribution for $\tau \to eK_S^0$ is presented with an arbitrary normalization in Fig. 5.5.

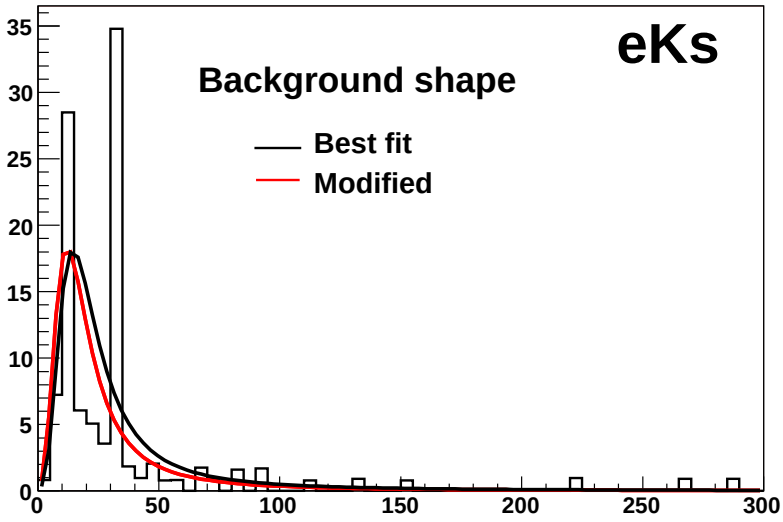

Figure 5.5: Background χ^2_{full} distribution at final selection for $\tau \to eK_S^0$. The superimposed curve is the result of the fit described in the text.

The spikes are due to a few $c\bar{c}$ events with a high relative contribution. To avoid discontinuities due to single events, the background will be described by a function, defined as the product of a Landau times a straight line, fitted on top of this histogram. The fit results are shown as well in Fig. 5.5 The same procedure is applied to the $\tau \to \mu K_S^0$ channel, as shown in Fig. 5.6

Figures 5.5 and 5.6 show also alternative background shapes in addition to the best fit ones. They were obtained with changes in the range of one to two σ's in the fitted parameters. These modified shapes have been introduced in order to check the stability of the results, since the low MC statistics does not allow a precise determination of the background. For the upper limit estimation, a systematic error is added in quadrature to the statistical one for each bin content, according the normalization error quoted above.

5.3 Results

Expected limits can be evaluated using signal efficiency and background pdf's described above. Total errors (statistical plus systematic) in the different bins can be treated in the implementation of CL_s method as correlated or uncorrelated. As in this case for both

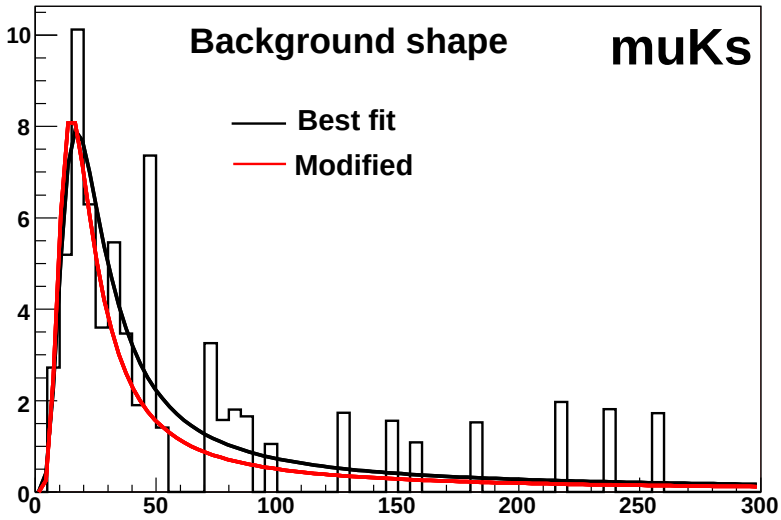

Figure 5.6: Background χ^2_{full} distribution at final selection for $\tau \to \mu K^0_S$. The superimposed curve is the result of the fit described in the text.

efficiency and background they represent mainly a normalization uncertainty, they have been treated as fully correlated. As detailed in Sec. 4.6, we found one and two events respectively for electron and muon channels after the final selection of the data sample. The obtained behavior for the expected $CL_{\rm s}$ is shown in Fig. 5.7 as a function of the branching fraction for the two channels.

The dashed line is the average expected confidence level, computed assuming we observe exactly the expected background distribution. The points where the dashed curves are crossed by the horizontal line define the sensitivity for the 90% confidence level upper limits: 3.0×10^{-8} for $\tau \to eK^0_S$ and 4.8×10^{-8} for $\tau \to \mu K^0_S$. The full line is the confidence level computed using the observed events The final resulting ULs can be extrapolated as following: $\mathcal{B}(\tau \to eK^0_S) < 3.3 \times 10^{-8}$ and $\mathcal{B}(\tau \to \mu K^0_S) < 4.0 \times 10^{-8}$. As anticipated in the previous section, alternative background shapes, as shown in Figs. 5.5 and 5.6 have been tested. In both channels no noticeable change in the results was observed.

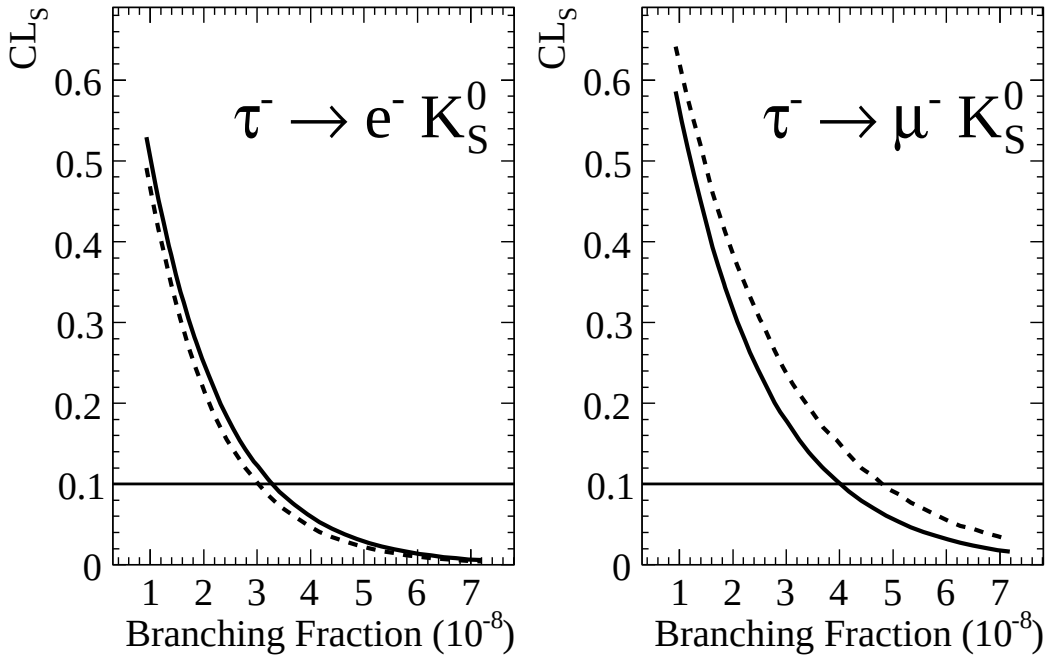

Figure 5.7: Expected (dashed line) and observed (full line) CL_s as a function of the branching fraction (10^{-8}) for the decays $\tau \to eK^0_S$ and $\tau \to \mu K^0_S$. The horizontal line defines the 90% confidence level value.

Chapter 6

Another Approach for the Upper Limit Estimation

In this chapter we describe an alternative approach to calculate the upper limit estimation. This approach is taken only as a cross-check for the CL_{s} method, because it gives a lower sensitivity. The approach is more classical: we use a slightly tighten selection, described in Sec. 6.1, and estimate the total number of residual background events with a maximum likelihood fit (Sec. 6.2). The upper limit estimation is performed with Feldman and Cousins method including experimental uncertainties [41].

6.1 Event selection for the alternative method

For this alternative method we tighten requirements for the loose selection described in Sec. 4.4 and re-optimize criteria for the tight selection described in Sec. 4.5. The optimization is performed again looking for the best sensitivity, but the upper limit is now computed with the method described in the following sections. Compared to the selection used for the CL_{s} method, this one allows a stronger rejection of the background events, which is essential for this different approach.

While preselection criteria are applied without changes, few requirements are modified in the alternative version of loose selection, as detailed in the following. The thrust magnitude must be **smaller than 0.97** and, only for the muon channel, also **greater than 0.91**. In addition, for the electron channel, the **Total Charged Tracks Energy** has to be **smaller than 8.0** GeV and the K_S^0 **flight significance greater than 4**. Regarding the tight selection, for the muon channel, the requirement on the K_S^0 flight significance is modified, as already specified above, and the **maximum number of reconstructed photons on the tag side is 5**. Also the requirement on the **squared invariant mass of the hadronic system on the tag side** is changed: for the electron channel must be **less than 1.8** and for the muon one **less than 1.5** $(\,\mathrm{GeV}/c^2)^2$. Here for the tight

selection on muon channel the criterion on **the cosine of the missing momentum polar angle** is not applied, while for the muon channel the allowed range for the same variable is **between -0.76 and 0.92**. All the modified requirements are summarized in Tab. 6.1.

Selection criteria	$\tau \to eK_S$	$\tau \to \mu K_S$
Thrust Magnitude	≤ 0.97	$0.91 \div 0.97$
Total Charged Tracks Energy (GeV)	≤ 8.0	–
K_S^0 Flight Significance	≥ 4	–
K_S^0 Flight Significance	–	≥ 4
Squared Invariant Mass on Tag Side ((GeV/c^2)^2)	≤ 1.8	≤ 1.5
n. Tag Side Photons	≤ 6	≤ 5
$cos(\theta_{MissMom})$	–	$-0.76 \div 0.92$

Table 6.1: Summary of modified requirements for the alternative selection.

After the loose selection, we obtain a reasonable shape agreement between data and MC samples also with this selection. Processes that contribute to final selected background samples are substantially same ones already mentioned for the original selection.

For the estimation of residual background the cross-check method takes in account only events inside sidebands or inside the blinded region, while the **final selection region** is the elliptical one already defined at the end of Sec. 4.3. Final signal efficiencies for signal events inside the ellipse are 9.1% and 6.1% respectively for electron and muon channels. Figures 6.1 and 6.2 show ΔM_τ distributions after the tight selection.

6.2 Background estimation

The background estimation for the final signal region is extrapolated using the ΔM_τ distribution in sidebands region defined in Sec. 4.3. In this chapter all the ΔM_τ distributions will be shown using events only from the blinded region plus the sidebands. For this estimation we use only events from the data sample and the MC one will be considered only as check.

Looking at ΔM_τ distributions for the sidebands and the blinded region after the tight selection, Fig. 6.3, we have not enough events to perform a reasonable maximum likelihood fit and estimate directly the residual background.

Assuming that selection criteria applied for tight selection do not change significantly the shape of ΔM_τ, we can perform the fit at the loose selections stage and then fit with the same functions the ΔM_τ distribution after the tight selection. Distributions for ΔM_τ after the loose selection are shown in Fig. 6.4.

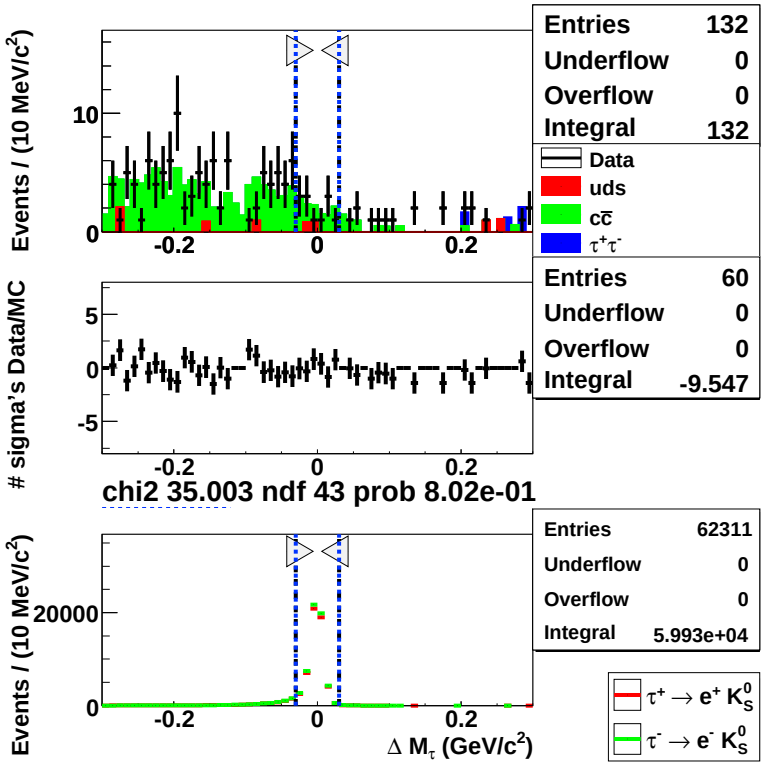

Figure 6.1: ΔM_τ distribution after alternative tight selection for $\tau \to eK_S^0$ channel.

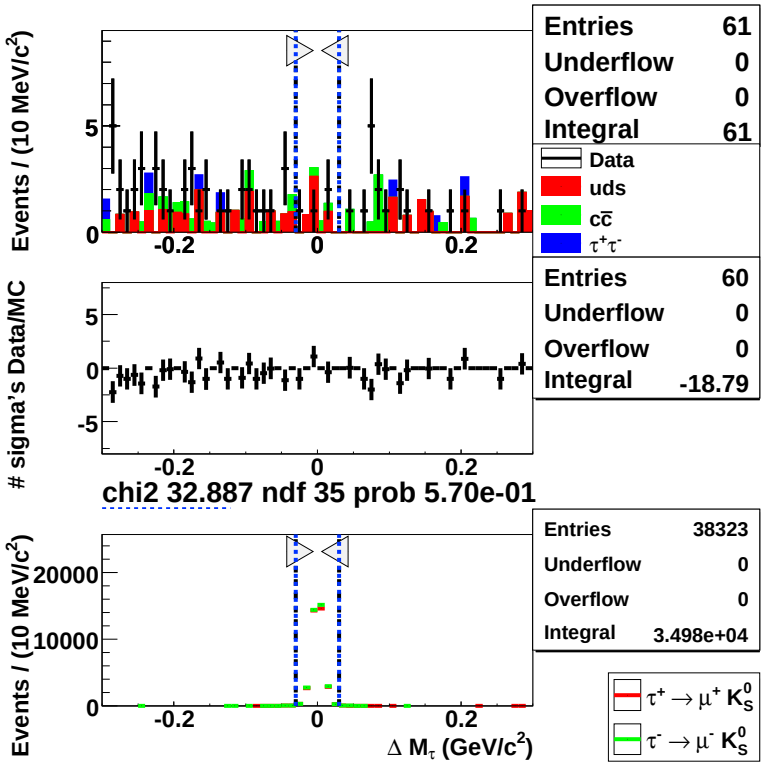

Figure 6.2: ΔM_τ distribution after alternative tight selection for $\tau \to \mu K_S^0$ channel.

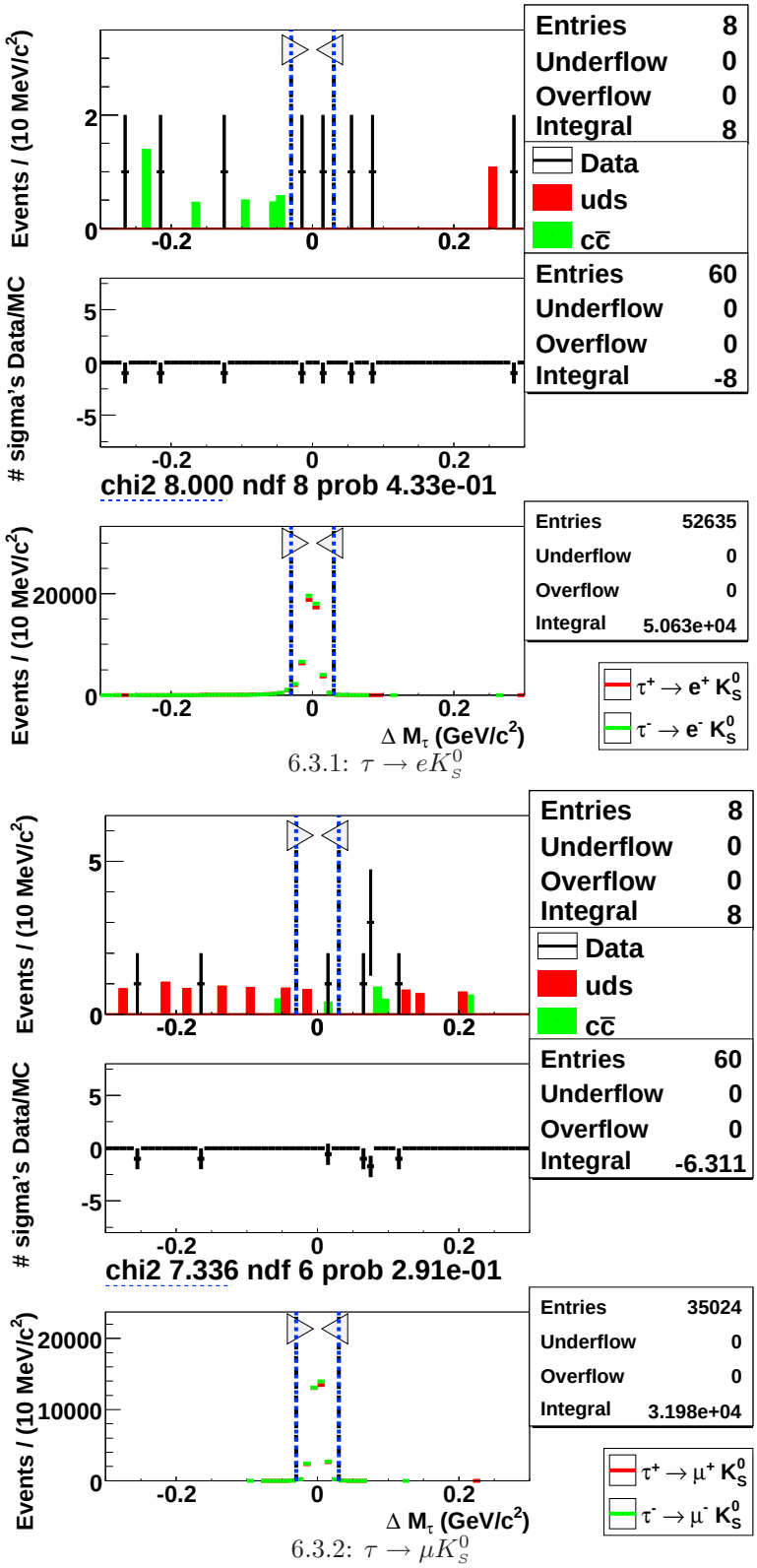

6.3.1: $\tau \to eK^0_S$

6.3.2: $\tau \to \mu K^0_S$

Figure 6.3: ΔM_τ distributions after the tight selection only in the sidebands and blinded region.

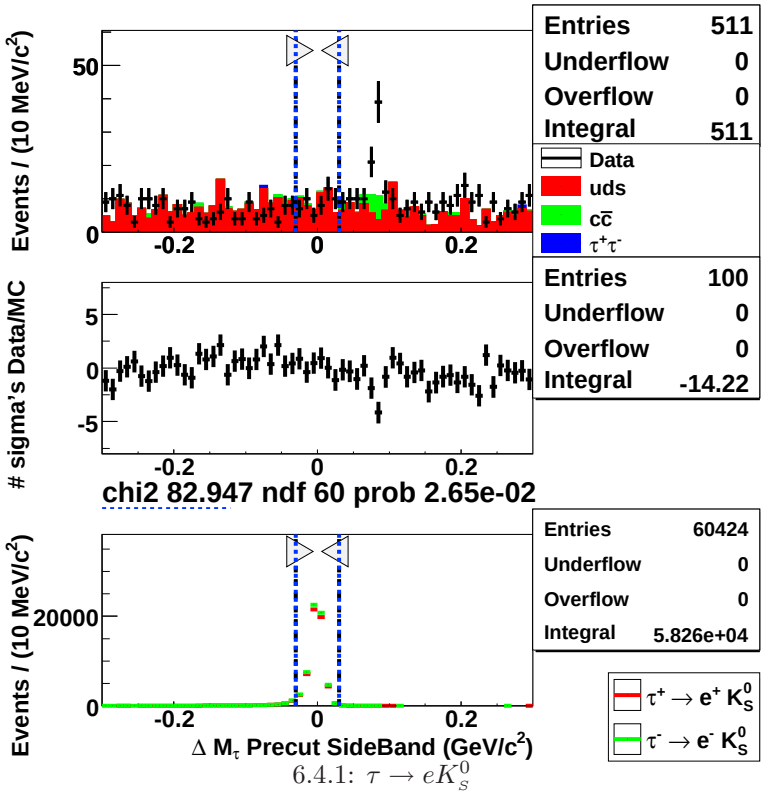

6.4.1: $\tau \to eK_S^0$

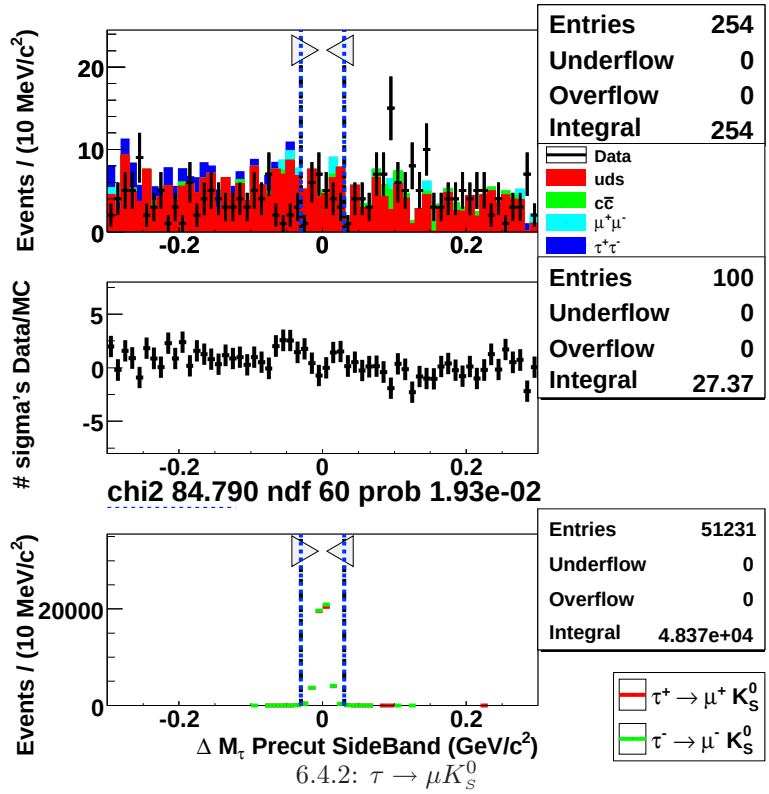

6.4.2: $\tau \to \mu K_S^0$

Figure 6.4: ΔM_τ distribution after the loose selection only in the sidebands and blinded region.

According the simulated sample, background events are only from *uds* and $c\overline{c}$ processes and the distribution could be fit using as fit function a first degree polynomial (referred to below as *poly1*) plus a Gaussian function. The peak is due to $D \to K^0_S\pi$ decays, where a pion is mis-identified as a lepton[1]. The blinded ΔM_τ region is always excluded in all the fits. Figure 6.5 shows the fit results for data events at the loose selection stage.

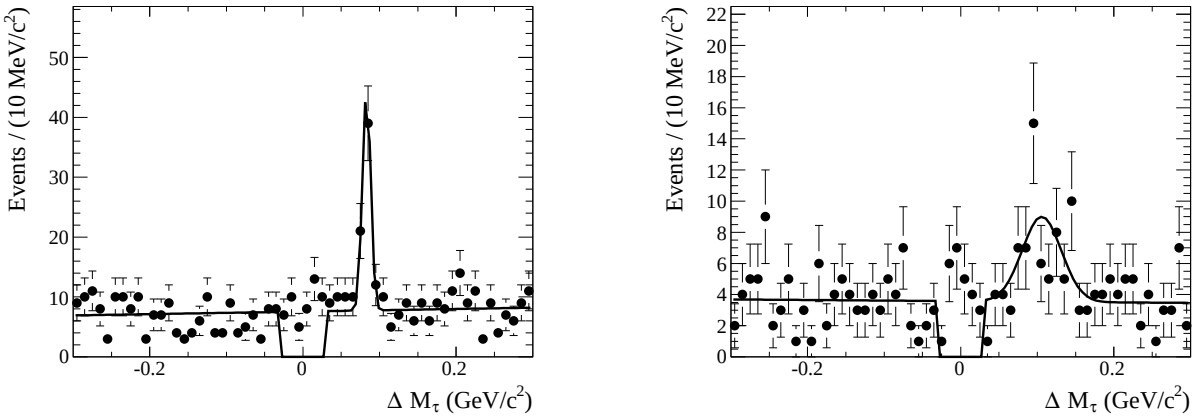

6.5.1: $\tau \to eK^0_S$ 6.5.2: $\tau \to \mu K^0_S$

Figure 6.5: Fit results for data events after the loose selection. We use a first degree polynomial plus a Gaussian as fit function.

The fit is then repeated after the full selection, fixing the function parameters, to compute the normalization factor for each component. These factors could be different (and in fact they are) because there is no reason to have *uds* and $c\overline{c}$ component suppressed at the same rate by the last step of selection. This procedure is based only on the assumption that the tight selection reduces the number of events without modifying the background shape of each component within the errors. A residual small disagreement will be accounted later as systematic error. Figure 6.6 shows the fit results for data events after the tight selection.

The expected number of background events in the blinded region can be computed directly from the integral of the final fit function including the normalization from the last fit, but for the uncertainty we need to consider errors from both fits. Using an ensemble of 5000 sets of function parameters generated according to the multi-Gaussian distribution of covariance matrix eigen-values, we can obtain a distribution of the integral value. Assuming to have a Gaussian distribution, we can take the distribution RMS as uncertainty of the integral. Therefore, we compute the integral value with its error separately for each component from the distribution obtained using the covariance matrix from the first fit. Then we rescale these two integral values by normalization factors found using the second fit and sum them together. We take the error on normalization factors

[1]At this stage of selection only a loose PID is applied

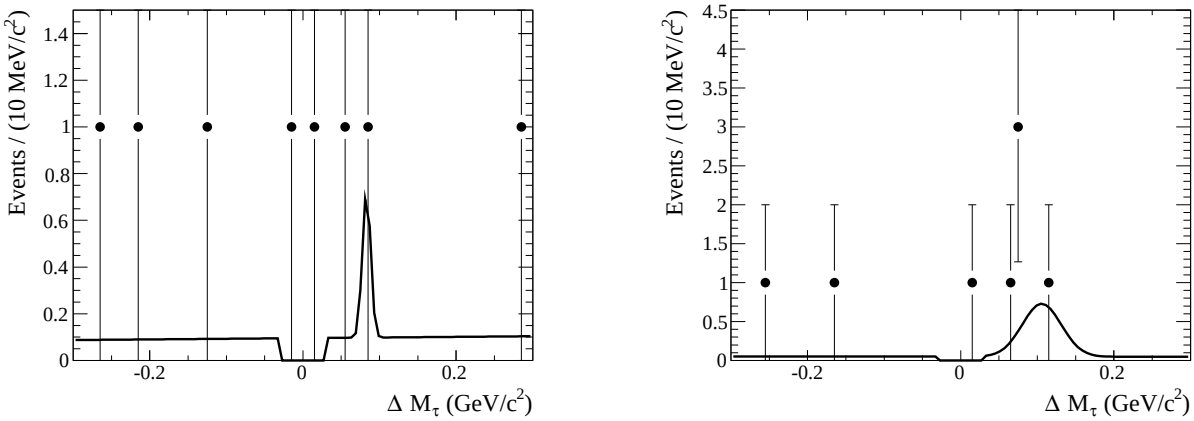

6.6.1: $\tau \to eK_S^0$ 6.6.2: $\tau \to \mu K_S^0$

Figure 6.6: Fit results for data events after the loose selection. Parameters of the straight line and the Gaussian are not refit but the two functions are simply rescaled to model the background.

from the second fit and the final error is computed using the standard error propagation. The real and estimated values for the number of events inside the blinded region at different stages of selection is shown in Tab. 6.2. In the same table we report also the

	data		bkg MC	
Channel, Selection	Real evts	Estim. evts	Real evts	Estim. evts
$\tau \to eK_S$				
Loose Selection	53.00 ± 7.28	45.39 ± 2.34	56.24 ± 7.26	40.10 ± 5.43
Tight selection	2.00 ± 1.41	0.57 ± 0.26	0.0 ± 0.0	0.49 ± 0.24
$\tau \to \mu K_S$				
Loose Selection	26.00 ± 5.10	21.51 ± 3.63	38.97 ± 5.89	32.23 ± 2.37
Tight selection	1.00 ± 1.00	0.34 ± 0.24	1.17 ± 0.88	1.00 ± 0.35

Table 6.2: Real and estimated number of events inside blind box for data and background MC samples, at loose and tight selection levels.

result for the estimation procedure applied to background MC samples. Distributions with the fit for background MC samples are shown in Fig. 6.7.

Looking at the table above, we have a numerical discrepancy between data and MC samples, but this does not affect our estimation that use only data events. On the other hand, considering the number of events estimated from MC samples and the real one, we notice again a discrepancy. In particular, our procedure underestimates the number of expected background events. Therefore, we rescale our estimation according the ratio between the real and the expected number of events at the loose selection stage for MC samples. To be also more conservative, we add a systematic error to the estimation equal

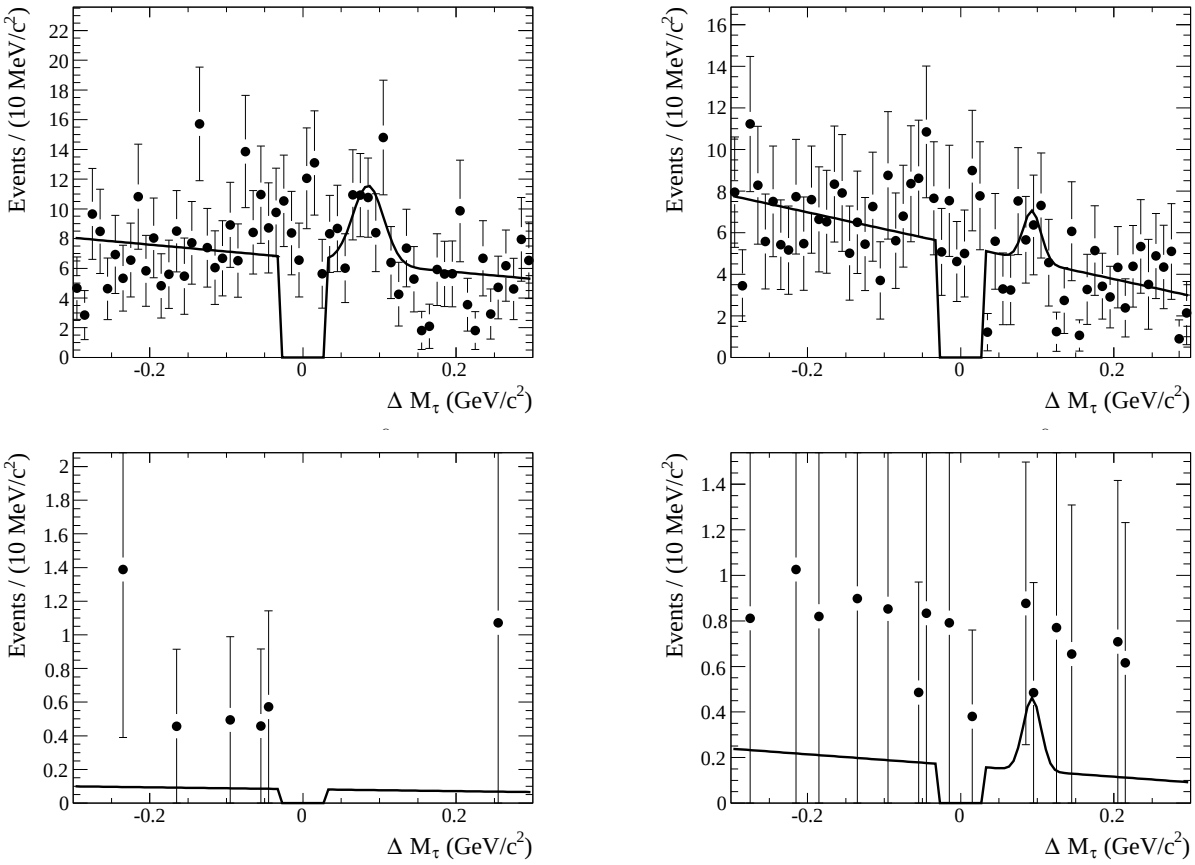

6.7.3: $\tau \to eK_S^0$ 6.7.4: $\tau \to \mu K_S^0$

Figure 6.7: Fit results for background MC samples after the loose (top) and the tight (bottom) selection. The fit function is again a straight line plus a Gaussian.

to the difference between that previous and the new value of the estimation itself. So the final values for the background estimation inside the blinded region is $0.80 \pm (0.26 \oplus 0.23)$ for the electron channel and $0.41 \pm (0.24 \oplus 0.07)$ for the muon one, including the statistical and systematic errors.

The final signal region is the ellipse already defined in Sec. 4.3 and, for estimating the expected background over there, we simply rescale the estimation by the ratio between ellipse and blinded region area. This last step relies on an hypothetical flatness of background on the blind region, but any discrepancy can be accounted by the large statistical error. The final values for background estimation in the final selection region are $0.59 \pm (0.19 \oplus 0.17)$ for $\tau \to eK_S^0$ and $0.30 \pm (0.17 \oplus 0.05)$ for $\tau \to \mu K_S^0$.

6.3 Upper limit estimation and results

Using the signal efficiency, the background estimation and the number of observed events after the final selection we can compute the upper limit estimation using the Feldman

and Cousins technique [42]. This is obtained using the POLE algorithm [41] that allows to extend the construction of the confidence level proposed by Feldman and Cousins incorporating systematic uncertainties of the measurement for both signal and background efficiencies. Because of assuming a pdf which parametrizes our knowledge about the uncertainties and integrating over this pdf, this algorithm is often referred to as *semi-Bayesian*.

For this analysis the distribution of uncertainties is assumed to be Gaussian and not correlated between signal and background. The option called *conditioning* is not applied. Considering the final signal region for this method, we find one event on both channels and a summary of results is shown in Tab. 6.3. The upper limit estimation is compatible

				Upper limit (10^{-8})	
Channel	$\varepsilon(\%)$	Estim. bkg evts	Obs. evts	Sensitivity	Measured
$\tau \to eK_S$	$9.06 \pm (0.04 \oplus 0.19)$	$0.59 \pm (0.19 \oplus 0.17)$	1	3.7	**4.8**
$\tau \to \mu K_S$	$6.14 \pm (0.03 \oplus 0.34)$	$0.30 \pm (0.17 \oplus 0.05)$	1	5.1	**7.6**

Table 6.3: Final results for the upper limit estimation using the alternative approach. Efficiencies, estimated backgrounds and observed events after the final selection are also shown. On the last two columns, we show the values for the expected sensitivity and the measured upper limit. The uncertainty for efficiency and estimation are shown in the usual way: $\pm$ (statistical error $\oplus$ systematic error).

with the one found with the CL_{s} method, within the statistical fluctuation of the observed background. The upper limit sensitivity, used for the selection optimization, is calculated using again a Feldman and Cousins technique, but without including uncertainties. This technique requests an integer value for the observe background and we compute an interpolated value, summing all the upper limits for integer values from 0 to 10 weighted by Poissonian probability of a distribution with expected background as mean.

Conclusions

In this thesis we present the search for the lepton flavour violating decay $\tau \to lK_S^0$ with the *BABAR* experiment data. This process and many other lepton flavour violating τ decays, like $\tau \to \mu\gamma$ and $\tau \to lll$, are one of the most promising channel to search for evidence of new physics. According the Standard Model and the neutrino mixing parameters, branching fractions are estimated well below 10^{-14}, but many models of new physics allow for branching fractions values close to the present experimental sensitivity.

This analysis is based on a data sample of $469\,\text{fb}^{-1}$ collected by *BABAR* detector at the PEP-II storage ring from 1999 to 2007, equivalent to 431 millions of τ pairs. The *BABAR* experiment, initially designed for studying CP violation in B mesons, has demonstrated to be one of the most suitable environment for studying τ decays. The tracking system, the calorimeter and the particle identification of *BABAR*, together with the knowledge of the τ initial energy, allow an extremely powerful rejection of background events that, for this analysis, is better than 10^{-9}.

Being $\tau \to lK_S^0$ a decay mode without neutrinos, the signal τ decay can be fully reconstructed. Kinematical constraints are used in a fit that provides a decay tree reconstruction with a high resolution. For this analysis MC simulated events play a decisive role for estimating the signal efficiency and study the residual background. High statistics MC sample are produced simulating detector conditions for different periods of data collection, in order to reduce any discrepancies with the data. When discrepancies can not be removed, we perform studies to compute a correction factor or an estimation of systematic errors, that need to be included in the final measurement.

Most of the selection is performed in a *blind way*, i. e. removing data events from a selected region where is more than 90% of the signal, according signal MC samples. This allows us to optimize selection criteria on background MC samples without introducing any bias due to a previous knowledge of data, specially when we have few selected events. The optimization is performed following the criteria of highest sensitivity, where the sensitivity is the upper limit estimation obtained supposing to observe only the estimated background. At the energy of $\Upsilon(4S)$ resonance, $\tau^+\tau^-$ events are back-to-back with an high momentum and the event can be divided in two hemispheres using the thrust axis. Applying requirements on the number of tracks on each side and on other event shape variables allows us to select signal candidates with high efficiency. Another big fraction

of the background is removed using the particle identification. Unfortunately the identification of muons suffers of a high mis-identification rate and the efficiency on muon channel is lower than electron one. The final efficiency is $(9.40 \pm 0.20)\%$ for $\tau \to eK^0_S$ and $(7.02 \pm 0.39)\%$ for $\tau \to \mu K^0_S$. The error is substantially systematic due to discrepancy between data and MC sample for the particle identification and the track reconstruction. An intermediate stage of selection is used to obtain the shape of background distribution with an high statistics, reducing the uncertainty on the final background estimation: 1.0 ± 0.4 and 5.3 ± 2.2 respectively for electron and muon channels.

A modified frequentist analysis, or $CL_{\rm s}$ method, is used to estimate the final upper limit. This method use the likelihood ratio of a discriminant variable as test-statistics to compute the confidence level of two different hypotheses: the signal+background hypothesis and the background only one. For estimating the limit, the method uses the ratio of these two confidence levels and avoids statements concerning regions where the signal+background hypothesis cannot be discriminated against the background only one. Confidence levels are estimated with a series of MC experiments where efficiency and background are smeared by a Gaussian distribution, for taking into account any experimental uncertainties. As discriminant variable we choose the χ^2 of the kinematical fit for the τ decay tree with all the constraints: masses of K^0_S and τ are constrained to the nominal value, the τ energy is constrained to half of the center-of-mass energy, the τ must originate in the interaction point, and the K^0_S and the lepton must come from τ decay vertex. This method is able to use all the information from the χ^2 distribution for signal and background and has a high sensitivity. The final result for the upper limit estimation is:

$$\mathcal{B}(\tau \to eK^0_S) \;<\; 3.3 \times 10^{-8} \tag{6.1}$$

$$\mathcal{B}(\tau \to \mu K^0_S) \;<\; 4.0 \times 10^{-8} \tag{6.2}$$

and it clearly confirms and improves the result already obtained by Belle Collaboration: $\mathcal{B}(\tau \to eK^0_S) < 5.6 \times 10^{-8}$ and $\mathcal{B}(\tau \to \mu K^0_S) < 4.9 \times 10^{-8}$ [5]. An alternative estimation is performed but it is used only as a cross-check. Using a tightened selection, we increase the background rejection and simply estimate the final number of background events. The selection is again optimized calculating the upper limit estimation with a Feldman and Cousins method, but the reached sensitivity is lower than the one with $CL_{\rm s}$ method. The final upper limit estimation is computed using the same Feldman and Cousins method, but including also uncertainties and the results of the this approach is compatible with the other one.

A significant improvement of the current result can be reached only with a higher statistics and, therefore, with a new collider providing a luminosity from 10 to 100 times more than PEP-II. A new detector, with improved performance and able to collect data

in a high background environment, is also requested to fully exploit the capability of such amount of data. In fact, only keeping the efficiency and the background as similar as possible to present ones, we will able to scale almost linearly the estimated upper limit according the luminosity. The strong potential of improvement for the search of lepton flavour violation τ decays makes the building of such a machine highly desirable.

Appendix A

Additional Analysis Details and Plots

In this appendix we describe some technical details of the analysis that not necessary for a global comprehension of the work, but could interesting for future reference. In addition we show also the distributions for all the selection variables.

A.1 Trigger and background filters

The full *BABAR* data sample contains not only events from useful for physics analysis but also a lot of background events and others for monitoring and diagnostic purpose. Most of the background events can be removed using simple requests on the L3 trigger category and on raw information from the event. In the following we define these allowed trigger categories and applied background filters.

A.1.1 L3trigger filter

In the L3 trigger we have different categories, called also trigger lines, used for selecting events to store for further analysis. Some of them select events interesting for detector studies, diagnostics and online measurements of beam energy, luminosity and hadronic ratio, while other ones events useful for physics analysis. The two main categories for useful events are:

1. **L3OutDch** events category, it select events that pass the following criteria:
   - DCH-one-track criterion: require at least 1 track with transverse momentum $p_\perp > 600\,\mathrm{MeV}/c$, transverse distance of closest approach $d_{\mathrm{xy}} < 1\,\mathrm{cm}$, and distance of closest approach along z axis $d_{\mathrm{z}} < 7\,\mathrm{cm}$ with respect to the IP;
   - DCH-two-tracks criterion: require at least 2 tracks with $p_\perp > 250\,\mathrm{MeV}/c$ and $d_{\mathrm{xy}} < 1.5\,\mathrm{cm}$, $d_{\mathrm{z}} < 10\,\mathrm{cm}$ with respect to the IP;

2. **L3OutEmc** events category, it select events that pass the following criteria:

   - EMC-high-energy criterion: require at least 2 clusters with $E_{\mathrm{c.m.}} > 350\,\mathrm{MeV}$ and an event invariant mass of at least $1.5\,\mathrm{GeV}/c^2$;
   - EMC-high-multiplicity criterion: require at least 4 clusters (with an implicit 100 MeV energy cut) with an event invariant mass of at least $1.5\,\mathrm{GeV}/c^2$.

Requesting only events selected by at least one of these, we remove background events and reduce the processing time for the whole data sample.

A.1.2 Background filter

For further reduce the number of selected events to be processed, we can make request on raw variables of the event before of a full reconstruction. The groups of criteria, called background filters, available to select interesting events are: **BGFMultiHadron**, **BGFNeutralHadron**, **BGFTau**, **BGFMuMu** and **BGFTwoProng**, and they are described below. Only tracks that satisfy the DCH-two-tracks criteria are considered here and quantities below with 1 or 2 as subscript refer to the first and the second highest momentum tracks. Some filters make a request also on R2, the ratio of 2^{nd} to 0^{th} Fox-Wolfram moments [73] computed in the CM frame. This quantity gives a measure of sphericity of the event: events with 2 jet tend to give a value of 1, more spherical events tend to give a value of 0. Specific criteria for each filter are:

1. **BGFMultiHadron**: it requires at least three tracks and R2 less than 0.98. Most of the hadronic events in the physics sample are passed through this filter;

2. **BGFNeutralHadron**: this filter complements BGFMultiHadron for certain hadronic modes that feature many neutrals but less than three charged tracks. The selection defines two categories of clusters: low-energy clusters with $E > 100\,\mathrm{MeV}$ and high-energy clusters with $E_{\mathrm{CM}} > 500\,\mathrm{MeV}$. In both cases the clusters are required not to be matched to a charged track. The requirements are as follows:

   - Two tracks and at least 3 low-energy clusters, including 2 high-energy clusters;
   - One track and at least 4 low-energy clusters, including 2 high-energy clusters;
   - No tracks and at least 6 low-energy clusters, including 3 high-energy clusters.

   In addition, R2 calculated from all the tracks and clusters with $E > 100\,\mathrm{MeV}$ must be less than 0.95.

3. **BGFMuMu**: this filter requires the momenta for the two highest momentum tracks to be $p_1 > 4\,\mathrm{GeV}$ and $p_2 > 2\,\mathrm{GeV}$, while the sum of polar angles of the same tracks satisfies $2.8 < \theta_1 + \theta_2 < 3.5$. The total energy of clusters associated to these tracks must be less than 2 GeV;

4. **BGFTau**: requires at least two tracks. The sum of momenta of the two highest momentum tracks must be $p_1 + p_2 < 9\,\mathrm{GeV}/c$ and the sum of associate clusters energy for the same tracks $E_1 + E_2 < 5\,\mathrm{GeV}$. The ratio between the momentum and cluster energy p/E for the first or the second highest momentum track must be less than 0.8 and the total charge of the event must be zero. The difference between the CM energy and $p_1 + p_2$ must be positive and the sum of transverse momenta $p_{\perp 1} + p_{\perp 2}$ divided by that difference must be greater than 0.07;

5. **BGFTwoProng**: requires at least two track and the charge of the events must be zero. At least p_1 or p_2 must be greater than $1\,\mathrm{GeV}/c$ and the energies of the two highest momentum tracks E_1 and E_2 must be smaller than 3 GeV. To reject events from cosmics the module of the sum $cos(\theta_{p_1}) + cos(\theta_{p_2})$ is required to be greater than 0.1. The highest momentum track is required to be within the acceptance of the EMC ($cos(\theta_{p_1}) > -0.75$). The last requirement is to have at least one track with a momentum greater than $4\,\mathrm{GeV}/c$ or that the module of the difference between the transverse momenta of the two highest momentum tracks smaller than $0.3\,\mathrm{GeV}/c$.

A.2 Details of the final signal region and sidebands for cross-check method

At the end of Sec. 4.3 we define the final signal region for the cross-check method. The parameter for this elliptical region are detailed in Tab. A.1 for both channels.

Channel	x_0	y_0	r_x	r_y	Rotation angle(°)
$\tau \to eK_S$	0.0	-0.02	0.03	0.12	-5
$\tau \to \mu K_S$	0.0	-0.01	0.03	0.12	-5

Table A.1: Parameters for signal region ellipse.

In the same section we introduce also the sidebands region. The distribution of events in those sidebands are used to extrapolate the residual background under the blinded region. The parameter for the sidebands region are detailed in Tab. A.2 for both channels.

Channel	ΔM_τ (GeV/c^2)		ΔE_τ (GeV)	
$\tau \to eK_S$	-0.30	0.30	-0.14	0.10
$\tau \to \mu K_S$	-0.30	0.30	-0.13	0.10

Table A.2: Values for side bands region.

A.3 Additional plots for the selection

This section contains plots for all the distributions of variables used for the event selection. These distribution are not relevant for understanding the analysis but could interesting for some readers. Plots are displayed as described in Chap. 4: in the upper plot data sample is represented by black dots, while the background MC one as filled histograms; in the middle plot the difference between data MC divided by the error is shown and signal MC samples are shown in the lower plot.

A.3.1 Preselection

In Figs. A.1, A.2, A.3, A.4, A.5, A.6, and A.7 we show distributions for all the variables used for the preselection. Each distribution shows selected events after having applied the previous criteria.

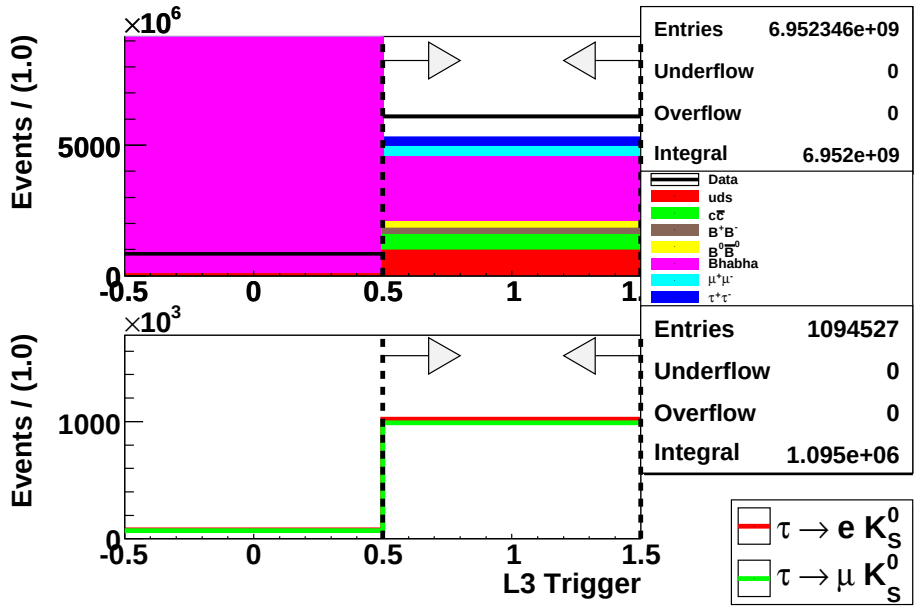

Figure A.1: Distribution of the L3 Trigger categories for data (black dots, upper plot), background MC (filled histogram, upper plot) and signal MC (lower plot) samples during the preselection just before applying the requirement on the shown variable, but after all the previous ones.

In Fig. A.8 we show the ΔM_τ and ΔE_τ distributions for muon channel and in Fig. A.3.1 the 2-dimensional distribution of ΔE_τ versus ΔM_τ on both channels after the preselection for data, signal and background MC samples.

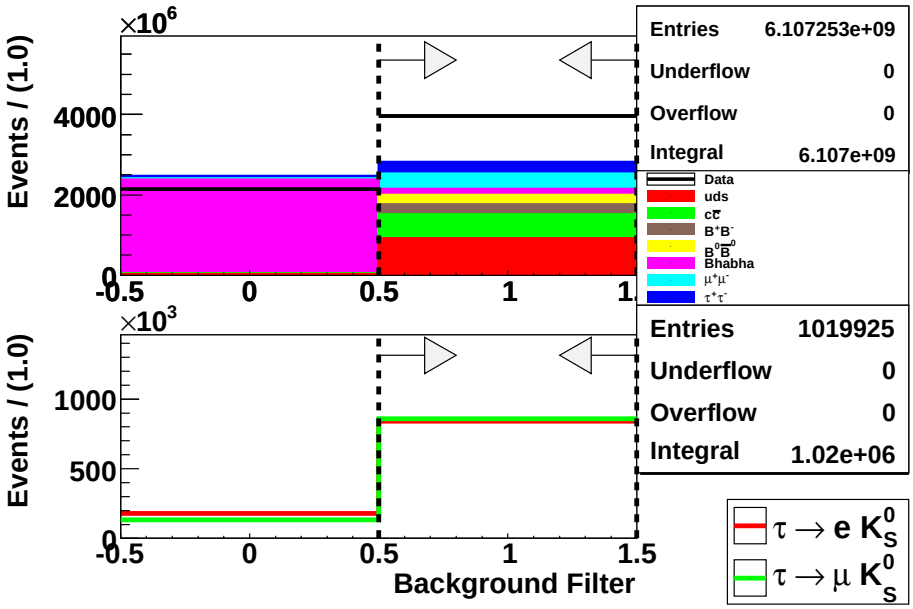

Figure A.2: Distribution of the Background filter for data (black dots, upper plot), background MC (filled histogram, upper plot) and signal MC (lower plot) samples during the preselection just before applying the requirement on the shown variable, but after all the previous ones.

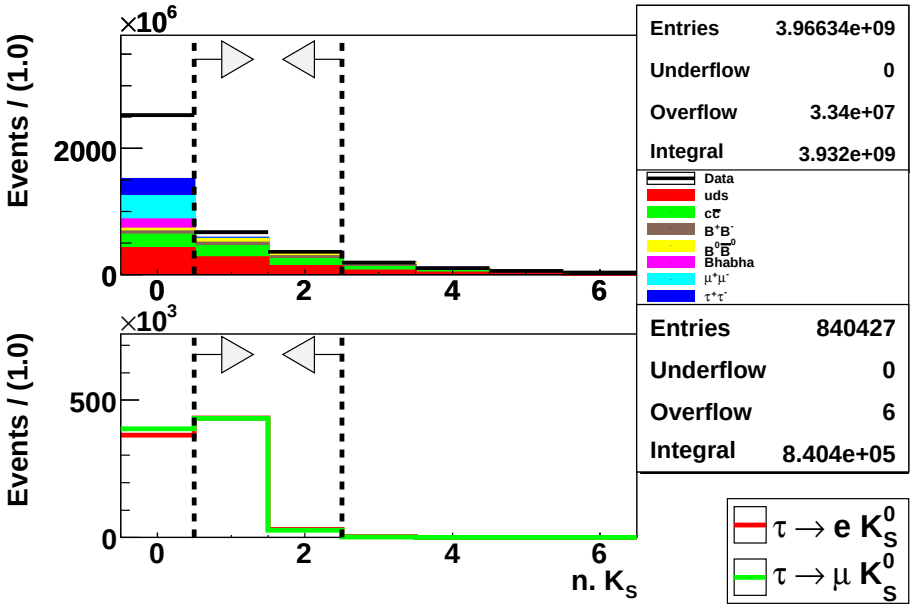

Figure A.3: Distribution of the number of K_S^0 for data (black dots, upper plot), background MC (filled histogram, upper plot) and signal MC (lower plot) samples during the preselection just before applying the requirement on the shown variable, but after all the previous ones.

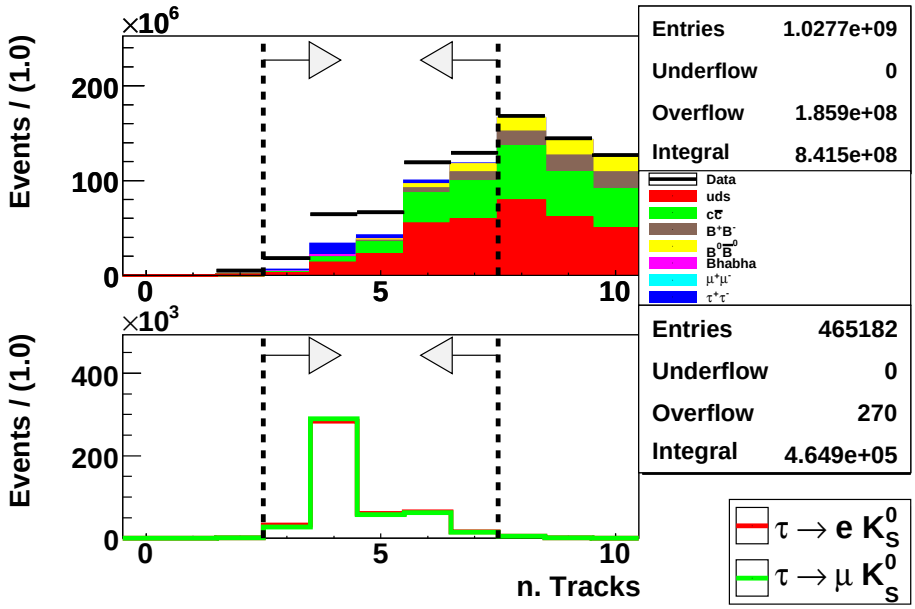

Figure A.4: Distribution of the number of reconstructed tracks for data (black dots, upper plot), background MC (filled histogram, upper plot) and signal MC (lower plot) samples during the preselection just before applying the requirement on the shown variable, but after all the previous ones.

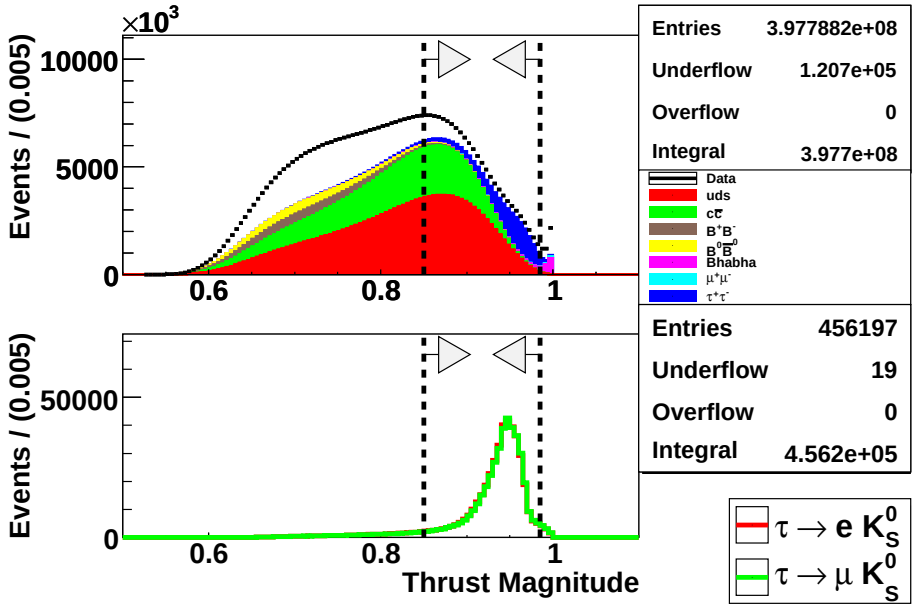

Figure A.5: Distribution of the thrust magnitude for data (black dots, upper plot), background MC (filled histogram, upper plot) and signal MC (lower plot) samples during the preselection just before applying the requirement on the shown variable, but after all the previous ones.

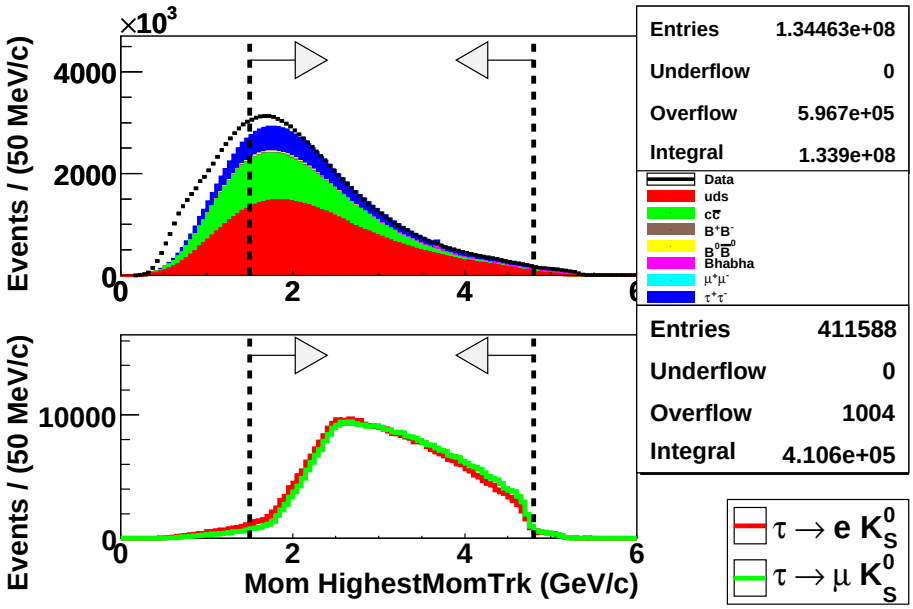

Figure A.6: Distribution of the momentum for the highest momentum tracks for data (black dots, upper plot), background MC (filled histogram, upper plot) and signal MC (lower plot) samples during the preselection just before applying the requirement on the shown variable, but after all the previous ones.

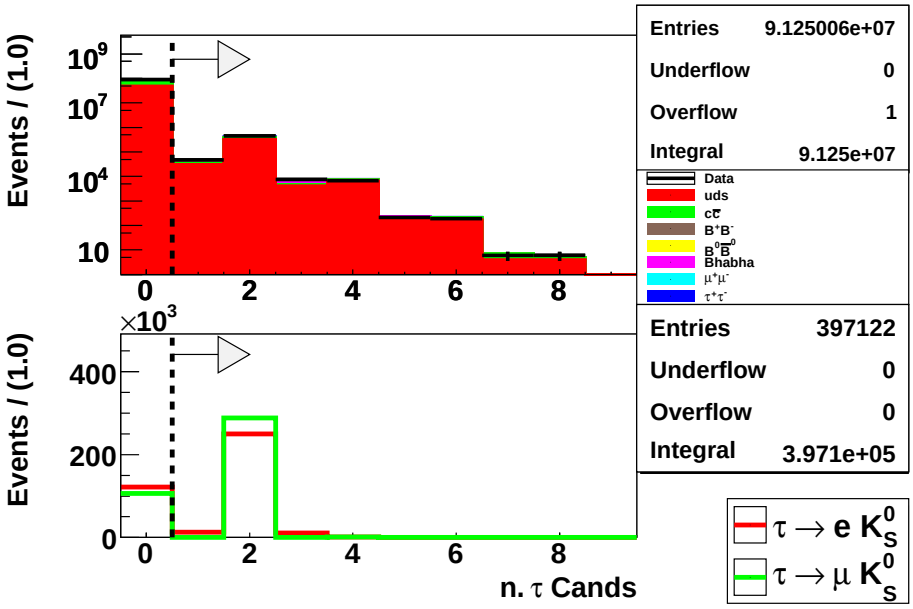

Figure A.7: Distribution of the number of reconstructed τ candidate for data (black dots, upper plot), background MC (filled histogram, upper plot) and signal MC (lower plot) samples during the preselection just before applying the requirement on the shown variable, but after all the previous ones.

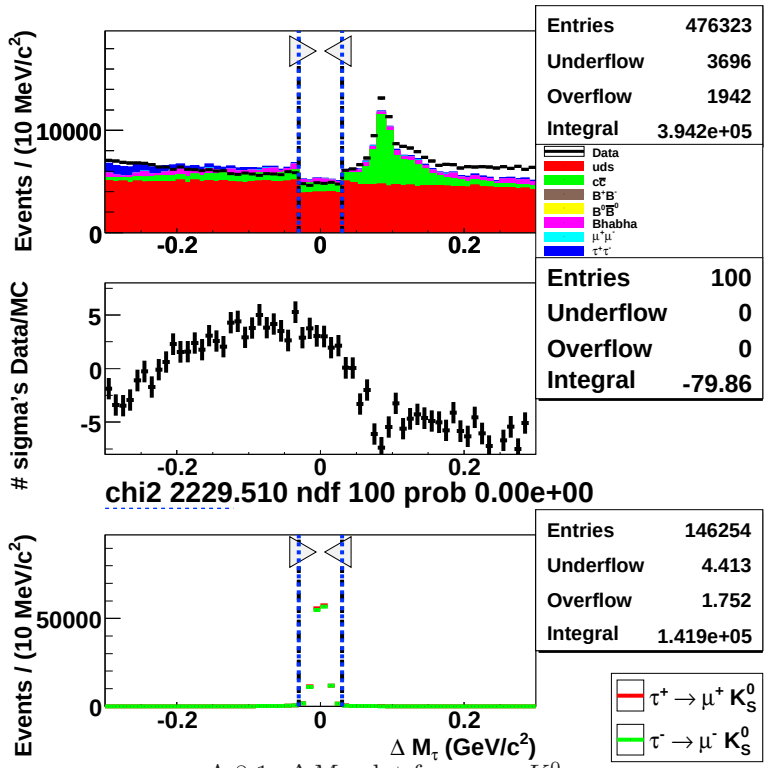

A.8.1: ΔM_τ plot for $\tau \to \mu K_S^0$

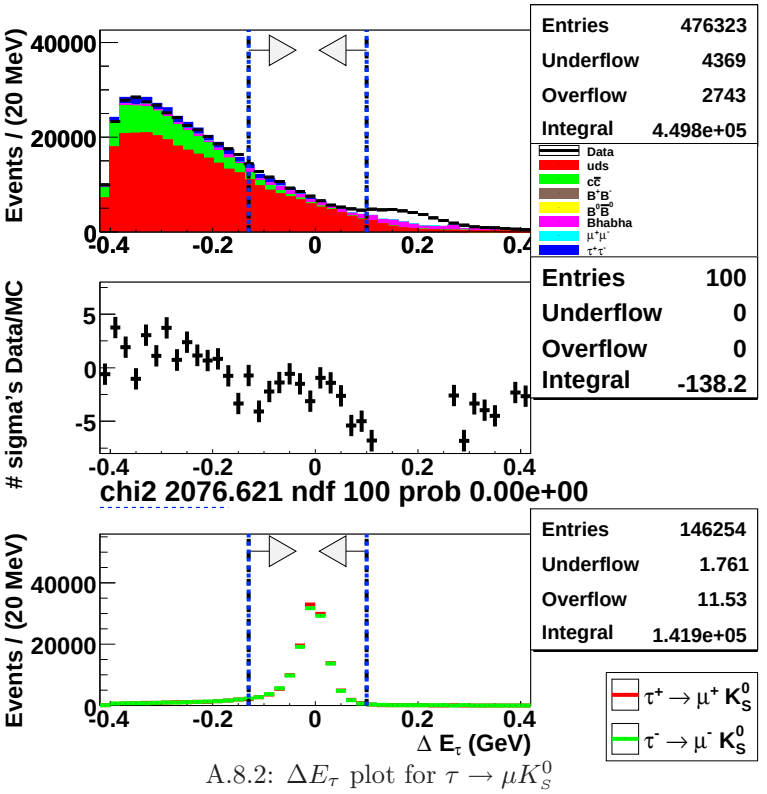

A.8.2: ΔE_τ plot for $\tau \to \mu K_S^0$

Figure A.8: ΔM_τ and ΔE_τ distributions for background and signal MC samples for the muon channels. Vertical dashed blue lines and arrows show the blinded region. Data in the blinded region are removed during the analysis optimization.

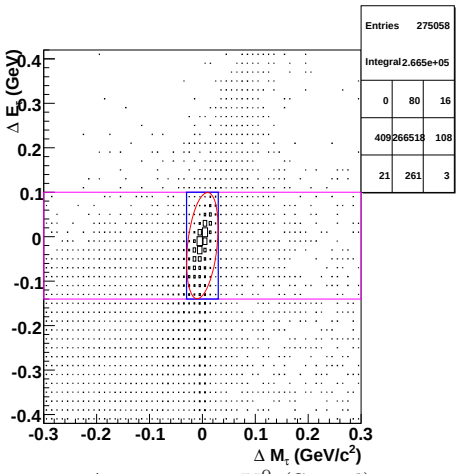

A.9.1: $\tau \to eK^0_S$ (Signal)

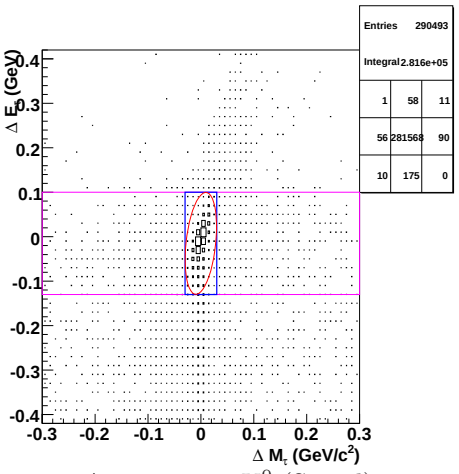

A.9.2: $\tau \to \mu K^0_S$ (Signal)

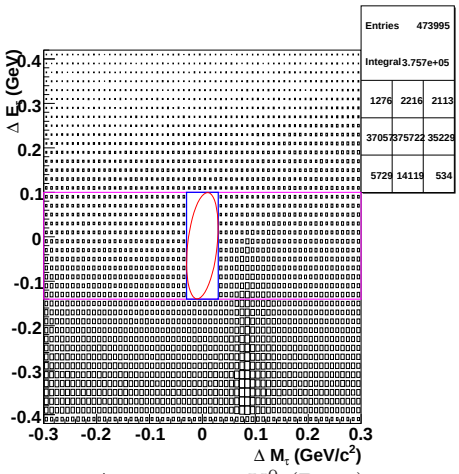

A.9.3: $\tau \to eK^0_S$ (Data)

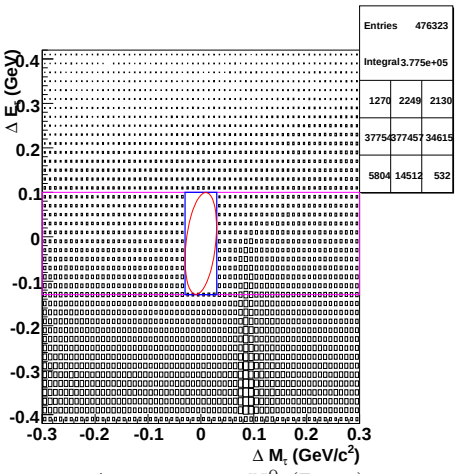

A.9.4: $\tau \to \mu K^0_S$ (Data)

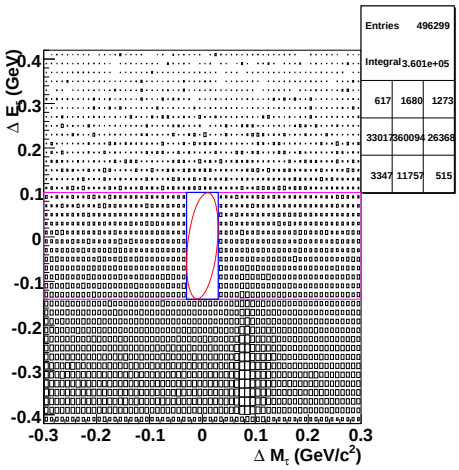

A.9.5: $\tau \to eK^0_S$ (MC)

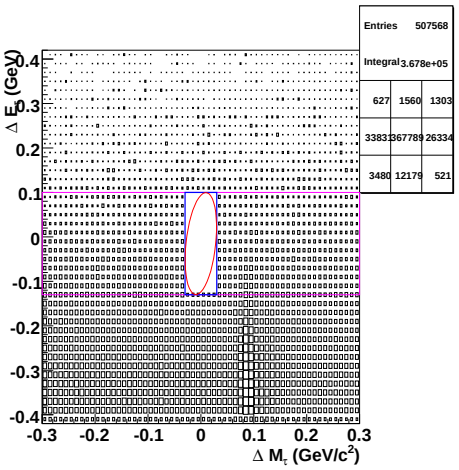

A.9.6: $\tau \to \mu K^0_S$ (MC)

Figure A.9: Distributions of $\Delta E_\tau / \Delta M_\tau$ after the preselection for signal MC, data and background MC samples. Data and background MC events are removed from the blinded region. The blue square is the blinded region, while the red ellipsis and the purple square are respectively sidebands and final signal regions for the cross-check method.

A.3.2 Loose selection

In Figs. A.10, A.11, A.12, A.13, A.14, A.15, A.16, A.17, A.18, and A.19 we show distributions of all the variables used in the loose selection for electron channel, while in Figs. A.20, A.21, A.22, A.23, A.24, A.25, and A.26 distributions of all the variable used for muon channel. Each distribution shows selected events after having applied the previous criteria.

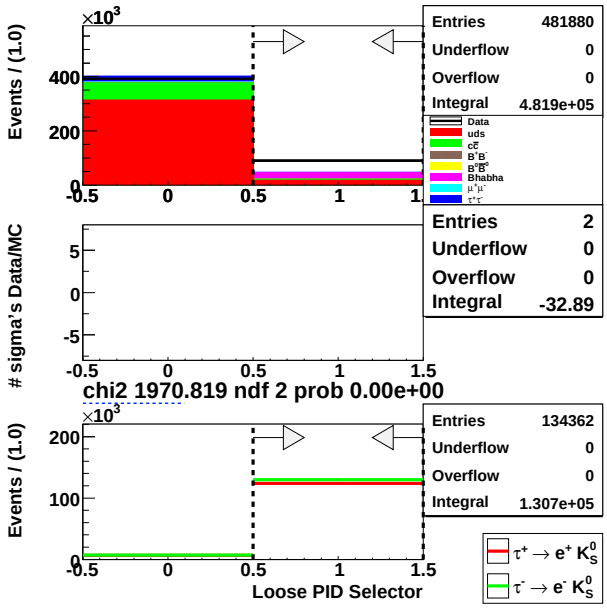

Figure A.10: Distribution of the loose selector variable for $\tau \to eK^0_S$ during the loose selection just before applying the requirement on the shown variable, but after all the previous ones.

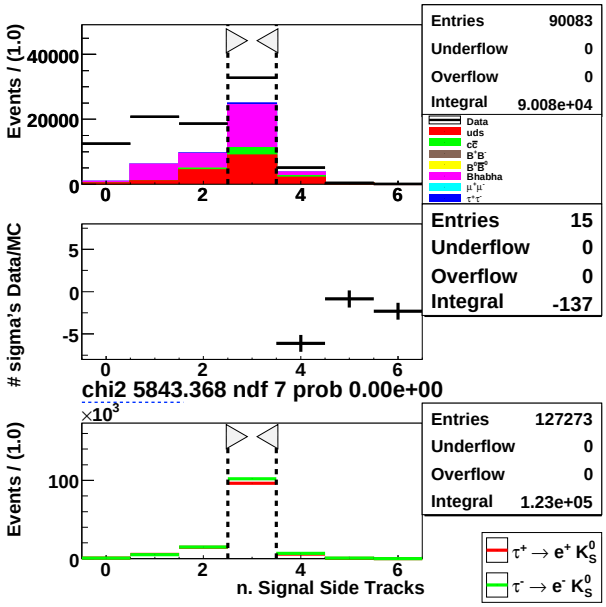

Figure A.11: Distribution of the number of tracks on the signal side for $\tau \to eK_S^0$ during the loose selection just before applying the requirement on the shown variable, but after all the previous ones.

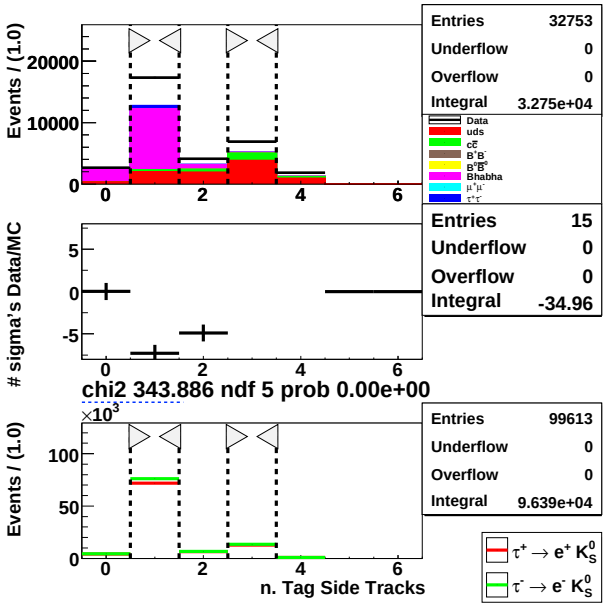

Figure A.12: Distribution of the number of tracks on the tag side for $\tau \to eK_S^0$ during the loose selection just before applying the requirement on the shown variable, but after all the previous ones.

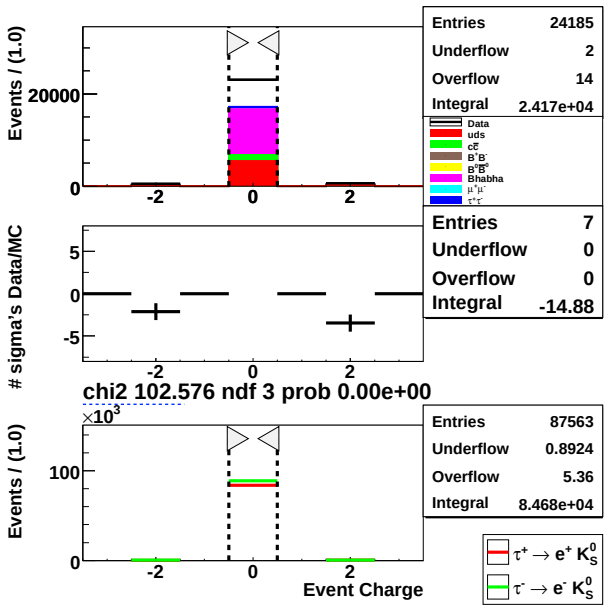

Figure A.13: Distribution of the total charge of event for $\tau \to eK_S^0$ during the loose selection just before applying the requirement on the shown variable, but after all the previous ones.

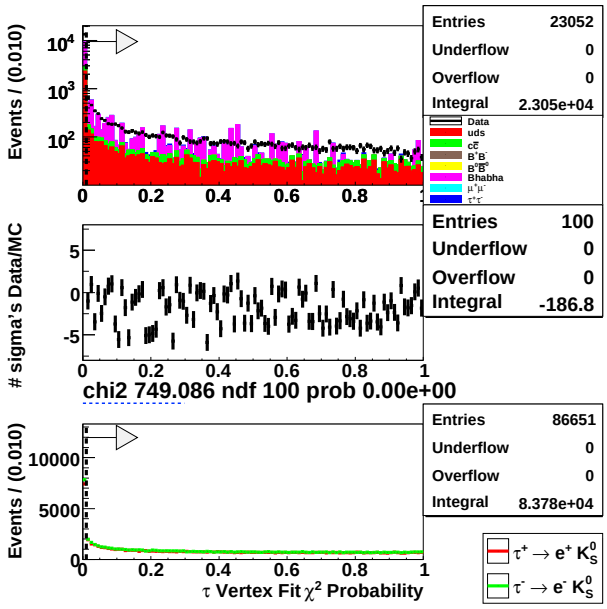

Figure A.14: Distribution of χ^2 probability of vertex fit for $\tau \to eK_S^0$ during the loose selection just before applying the requirement on the shown variable, but after all the previous ones.

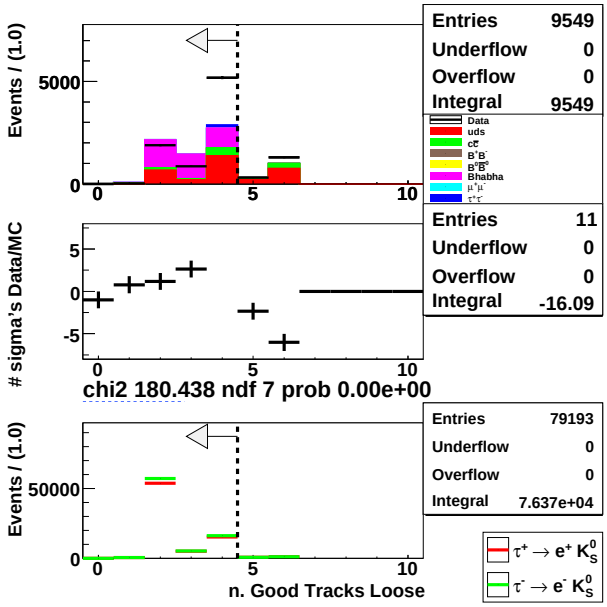

Figure A.15: Distribution of the number of *Good Track Loose* tracks for $\tau \to eK_S^0$ during the loose selection just before applying the requirement on the shown variable, but after all the previous ones.

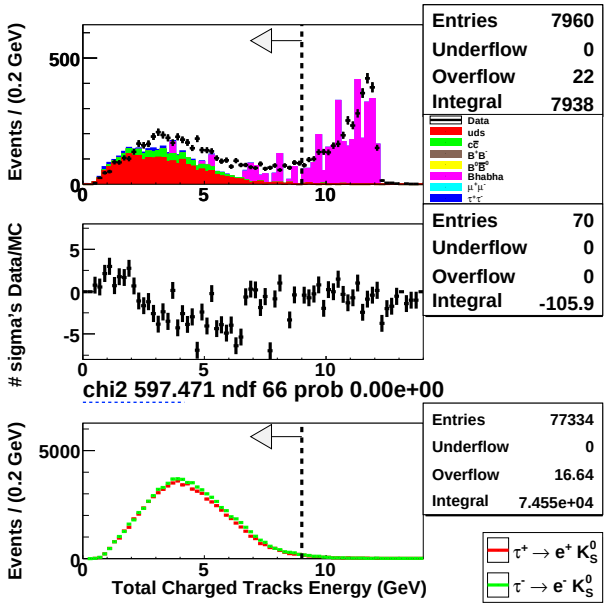

Figure A.16: Distribution of the total calorimeter energy (made using only clusters associated with a track) for $\tau \to eK_S^0$ during the loose selection just before applying the requirement on the shown variable, but after all the previous ones.

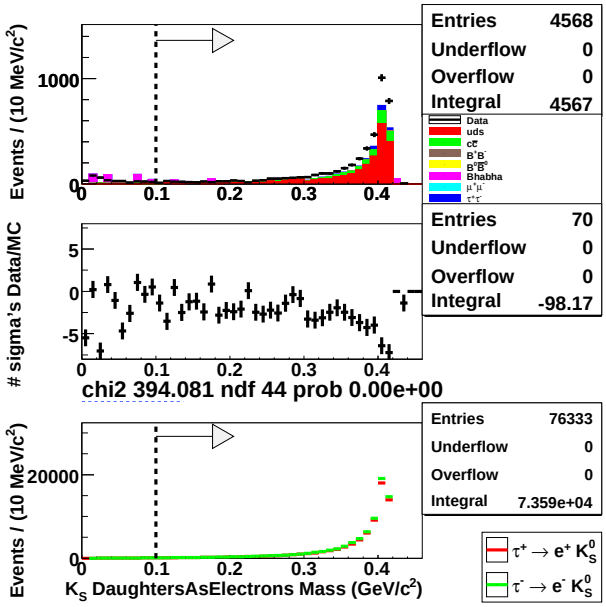

Figure A.17: Distribution of the invariant mass of K_S^0 daughter tracks (assuming for each of them the electron mass) for $\tau \to eK_S^0$ during the loose selection just before applying the requirement on the shown variable, but after all the previous ones.

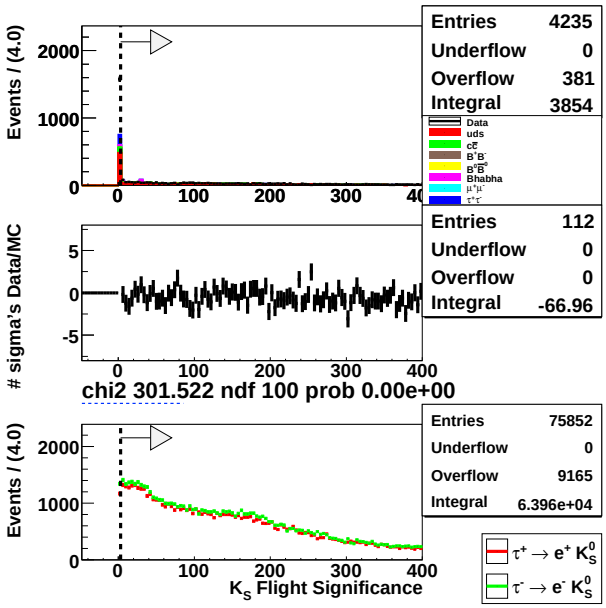

Figure A.18: Distribution of K_S^0 flight significance for $\tau \to eK_S^0$ during the loose selection just before applying the requirement on the shown variable, but after all the previous ones.

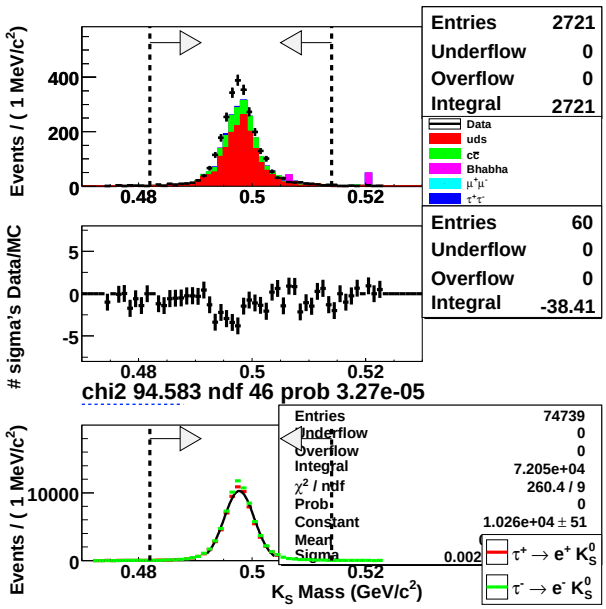

Figure A.19: Distribution of the K_S^0 invariant mass number for $\tau \to eK_S^0$ during the loose selection just before applying the requirement on the shown variable, but after all the previous ones.

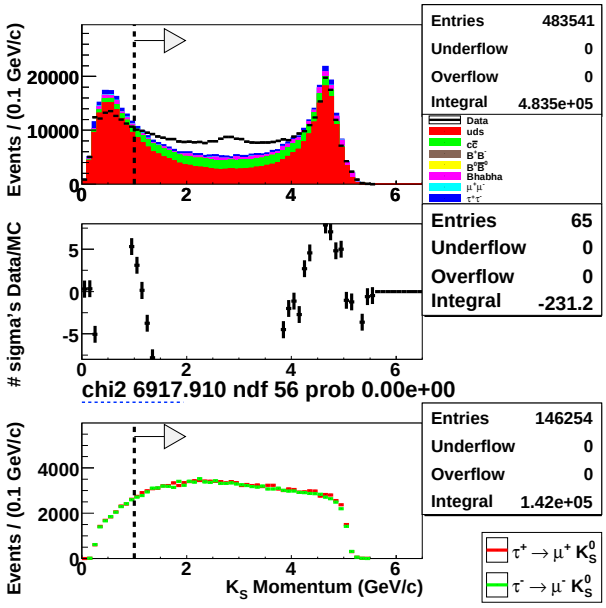

Figure A.20: Distribution of the K_S^0 momentum for $\tau \to \mu K_S^0$ during the loose selection just before applying the requirement on the shown variable, but after all the previous ones.

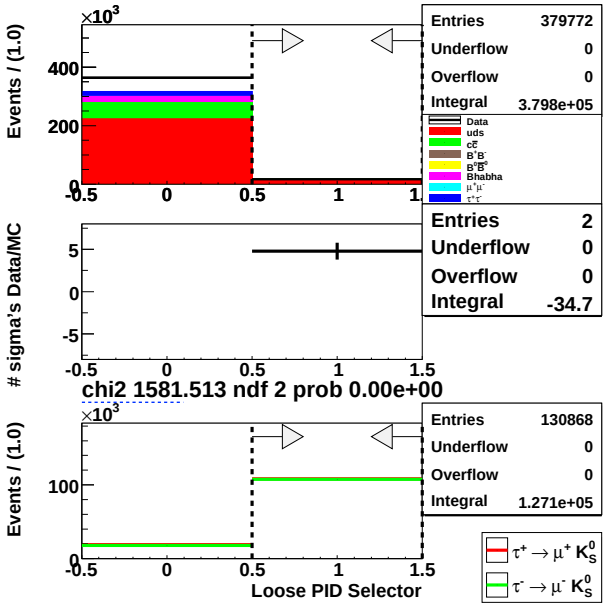

Figure A.21: Distribution of the loose selector variable for $\tau \to \mu K_S^0$ during the loose selection just before applying the requirement on the shown variable, but after all the previous ones.

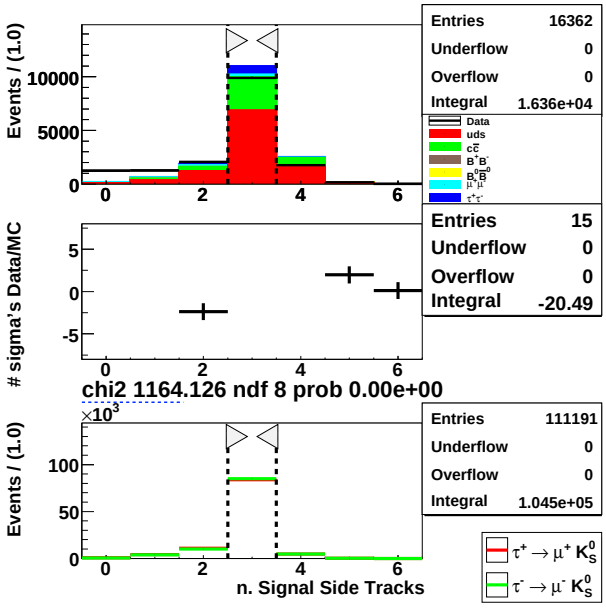

Figure A.22: Distribution of the number of tracks on the signal side for $\tau \to \mu K_S^0$ during the loose selection just before applying the requirement on the shown variable, but after all the previous ones.

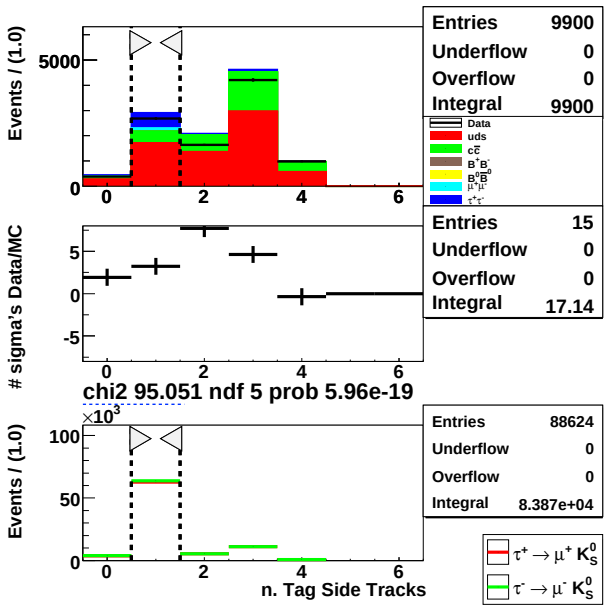

Figure A.23: Distribution of the number of tracks on the tag side for $\tau \to \mu K_S^0$ during the loose selection just before applying the requirement on the shown variable, but after all the previous ones.

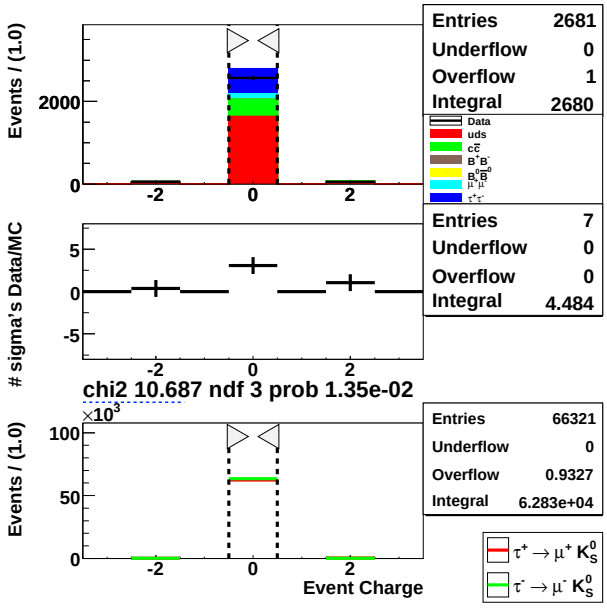

Figure A.24: Distribution of the total charge of event for $\tau \to \mu K_S^0$ during the loose selection just before applying the requirement on the shown variable, but after all the previous ones.

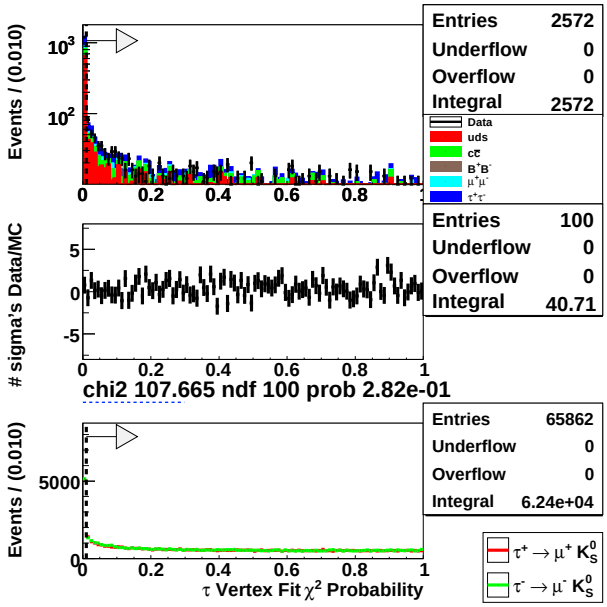

Figure A.25: Distribution of χ^2 probability of vertex fit for $\tau \to \mu K_S^0$ during the loose selection just before applying the requirement on the shown variable, but after all the previous ones.

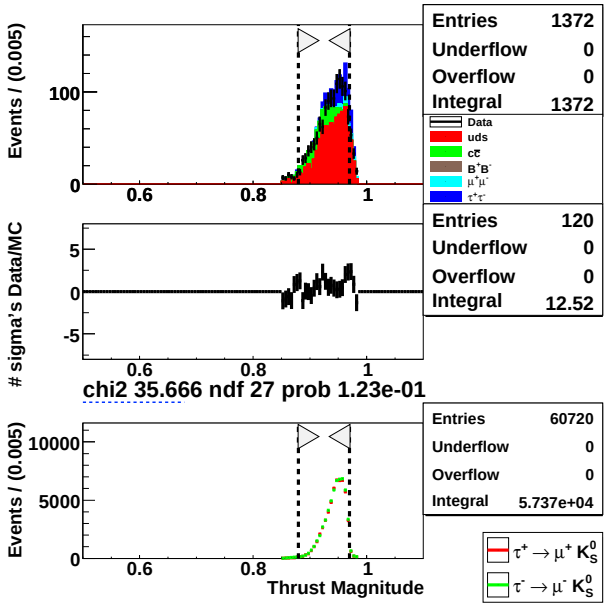

Figure A.26: Distribution of the thrust magnitude for $\tau \to \mu K_S^0$ during the loose selection just before applying the requirement on the shown variable, but after all the previous ones.

A.3.3 Tight selection

In Figs. A.27, A.28, A.29, A.30, and A.31 we show distributions of all the variables used in the loose selection for electron channel, while in Figs. A.32, A.33, A.34, A.35, A.36, A.37, A.38, and A.39, distributions of all the variable used for muon channel. Each distribution shows selected events after having applied the previous criteria.

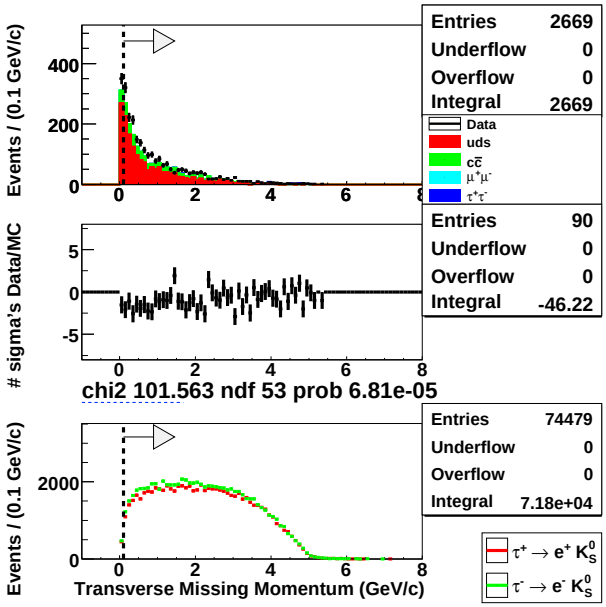

Figure A.27: Distribution of the transverse missing momentum for $\tau \rightarrow eK^0_S$ during the tight selection just before applying the requirement on the shown variable, but after all the previous ones.

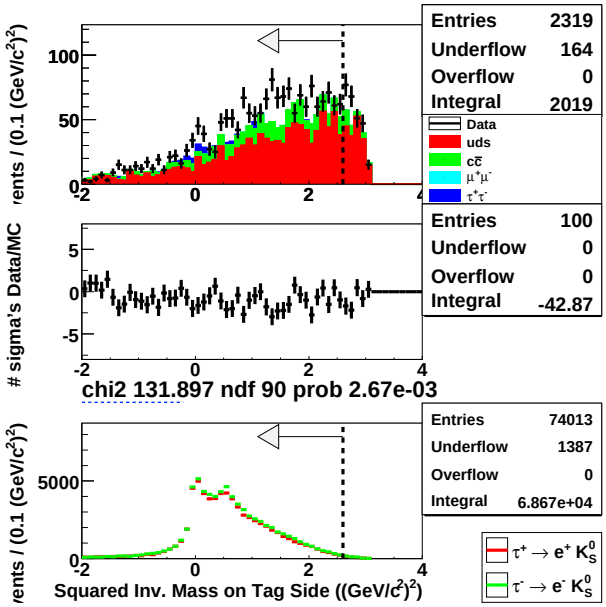

Figure A.28: Distribution of the squared invariant mass of hadronic system on tag side for $\tau \to eK^0_S$ during the tight selection just before applying the requirement on the shown variable, but after all the previous ones.

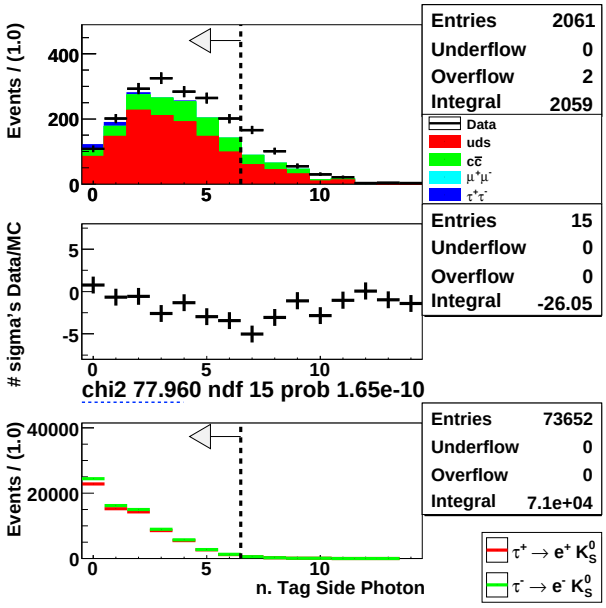

Figure A.29: Distribution of the number of photons on the tag side for $\tau \to eK^0_S$ during the tight selection just before applying the requirement on the shown variable, but after all the previous ones.

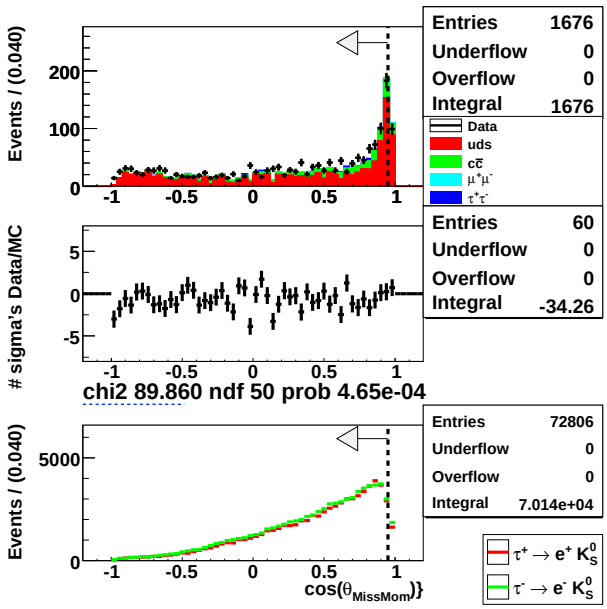

Figure A.30: Distribution of cosine of the polar angle of missing momentum for $\tau \to eK_S^0$ during the tight selection just before applying the requirement on the shown variable, but after all the previous ones.

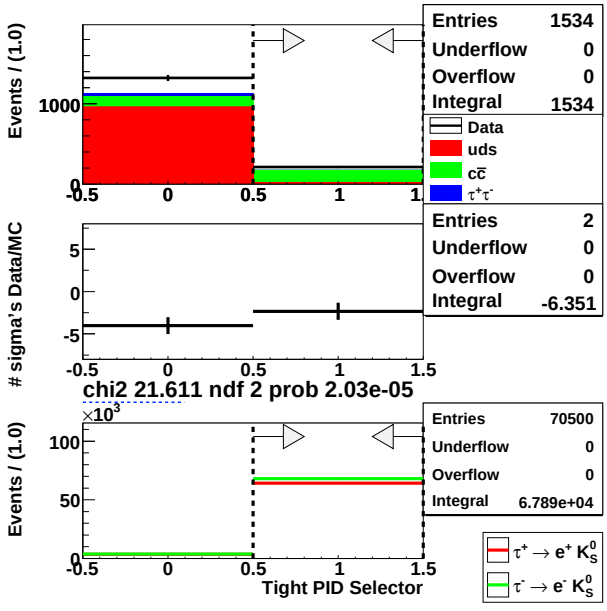

Figure A.31: Distribution of the tight selector variable for $\tau \to eK_S^0$ during the tight selection just before applying the requirement on the shown variable, but after all the previous ones.

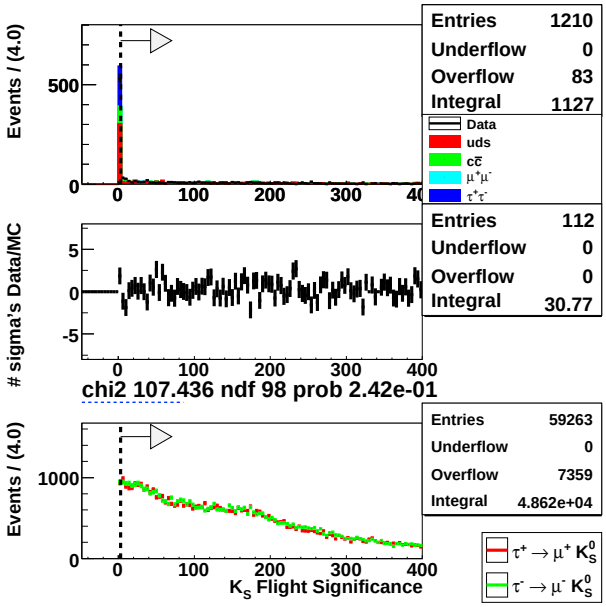

Figure A.32: Distribution of K_S^0 flight significance for $\tau \to \mu K_S^0$ during the tight selection just before applying the requirement on the shown variable, but after all the previous ones.

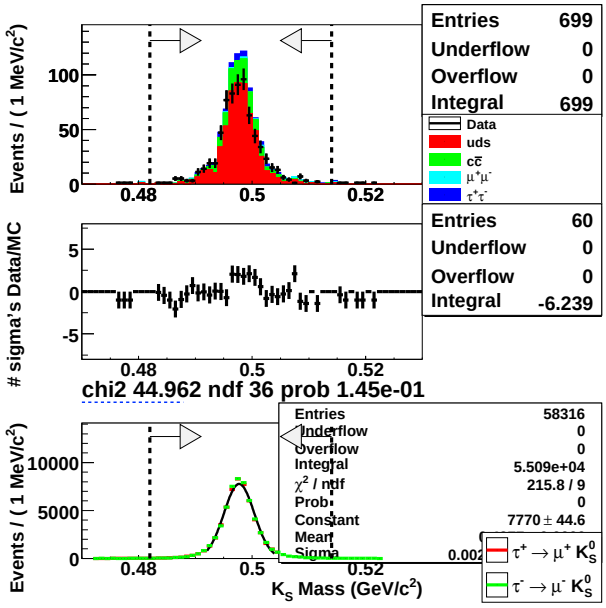

Figure A.33: Distribution of the K_S^0 invariant mass number for $\tau \to \mu K_S^0$ during the tight selection just before applying the requirement on the shown variable, but after all the previous ones.

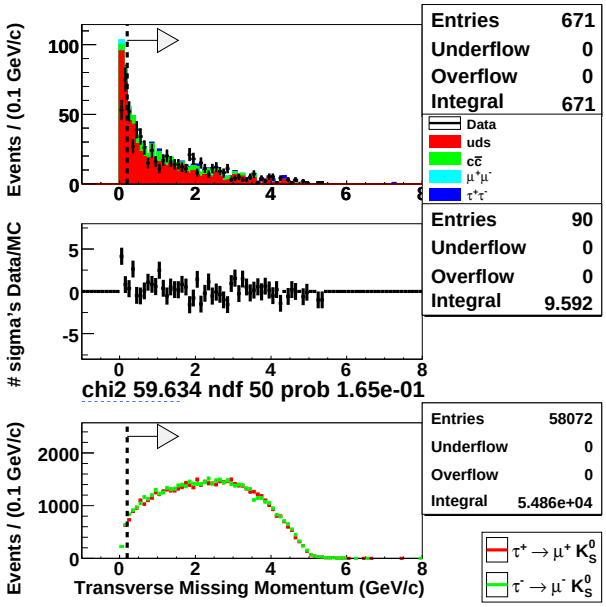

Figure A.34: Distribution of the transverse missing momentum for $\tau \to \mu K_S^0$ during the tight selection just before applying the requirement on the shown variable, but after all the previous ones.

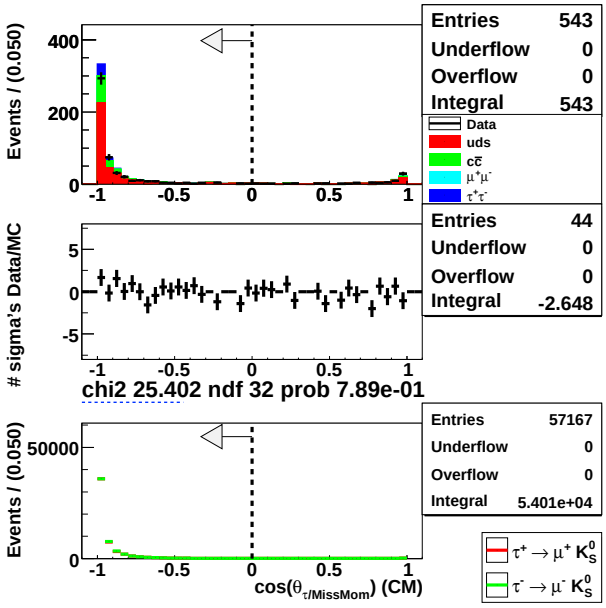

Figure A.35: Distribution of cosine of the angle between the τ candidate and the missing momentum for $\tau \to \mu K_S^0$ during the tight selection just before applying the requirement on the shown variable, but after all the previous ones.

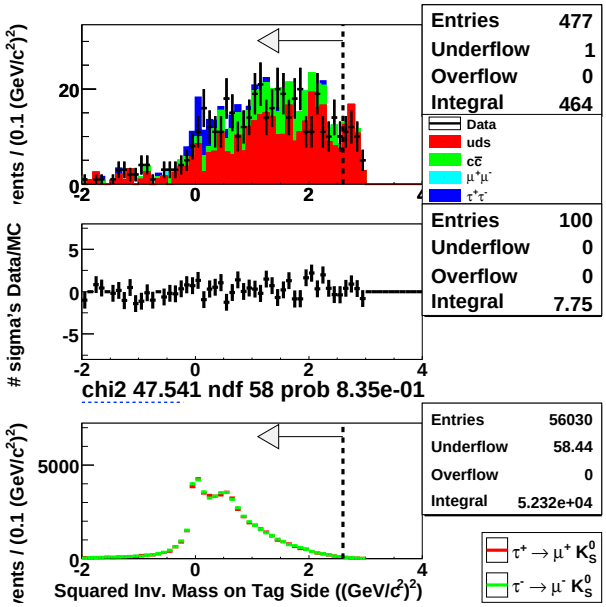

Figure A.36: Distribution of the squared invariant mass of hadronic system on tag side for $\tau \to \mu K_S^0$ during the tight selection just before applying the requirement on the shown variable, but after all the previous ones.

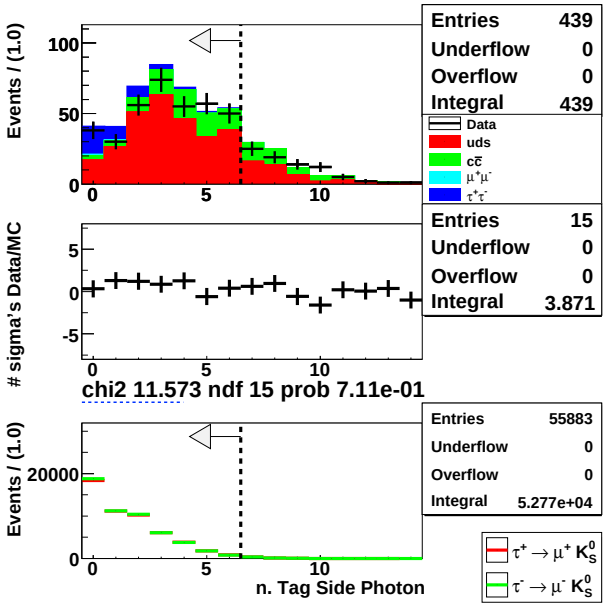

Figure A.37: Distribution of the number of photons on the tag side for $\tau \to \mu K_S^0$ during the tight selection just before applying the requirement on the shown variable, but after all the previous ones.

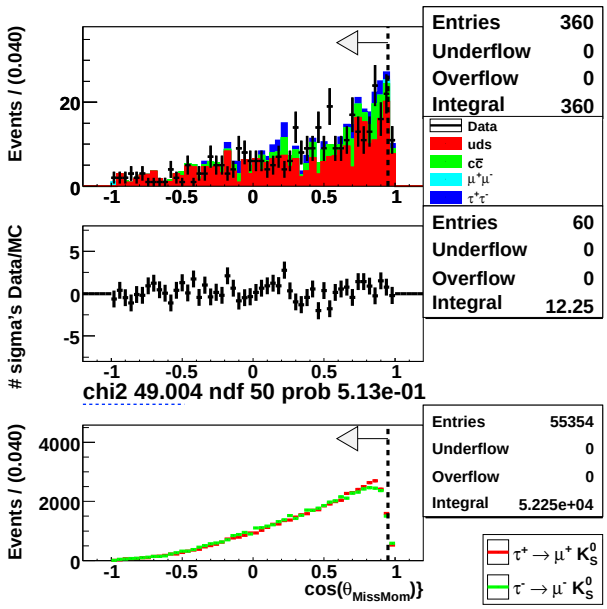

Figure A.38: Distribution of cosine of the polar angle of missing momentum for $\tau \to \mu K_S^0$ during the tight selection just before applying the requirement on the shown variable, but after all the previous ones.

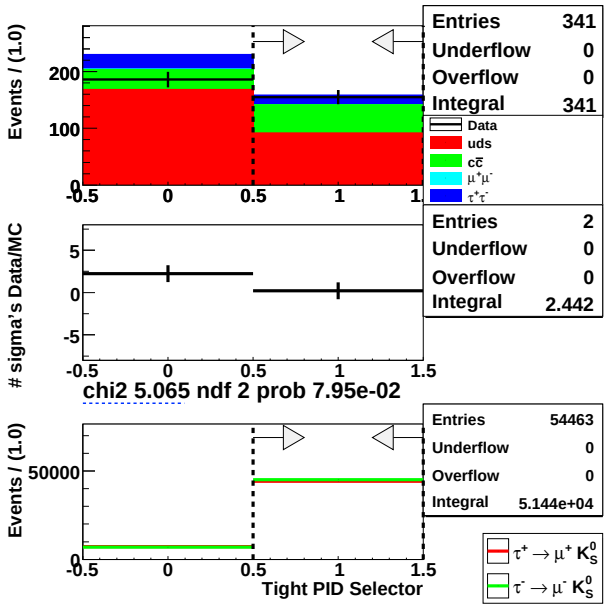

Figure A.39: Distribution of the tight selector variable for $\tau \to \mu K_S^0$ during the tight selection just before applying the requirement on the shown variable, but after all the previous ones.

In Figs. A.40 and A.41 we show the distribution after the tight selection for ΔM_τ and ΔE_τ.

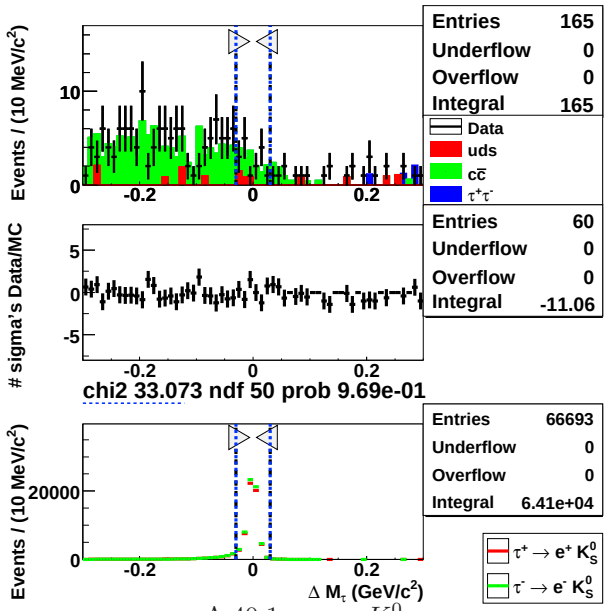

A.40.1: $\tau \to eK^0_S$

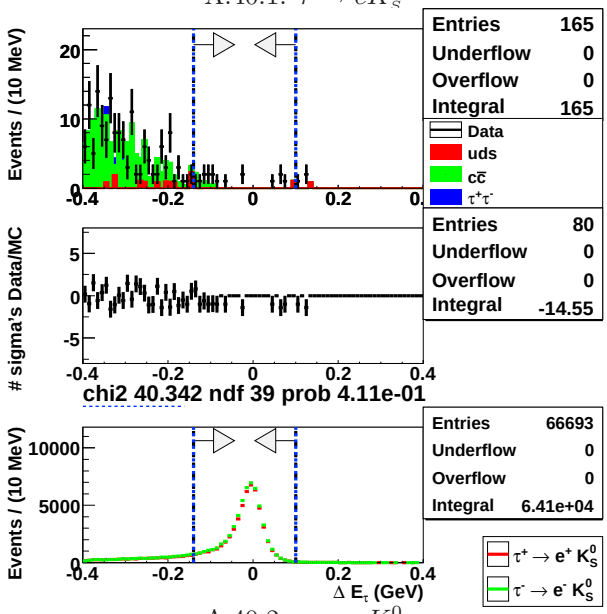

A.40.2: $\tau \to eK^0_S$

Figure A.40: Distributions of ΔM_τ and ΔE_τ after the tight selection for $\tau \to eK^0_S$. In each sub-figure, in the upper plot data sample is represented by black dots, while the background MC one as filled histograms. In the middle plot the difference between data MC divided by the error is shown. Signal MC samples are shown in the lower plot.

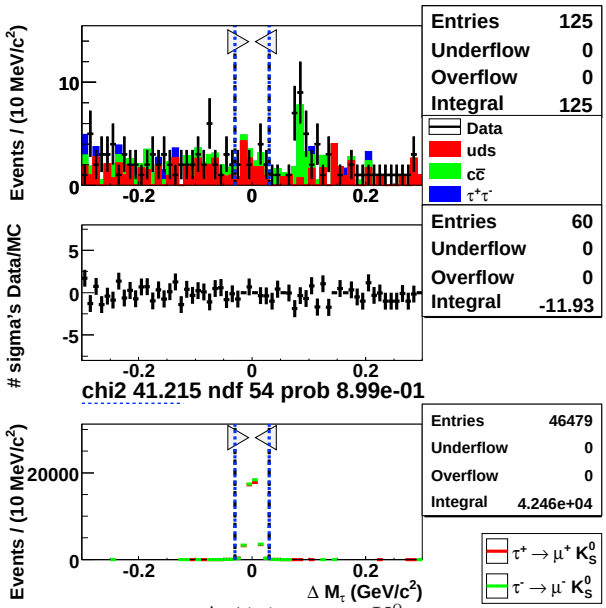

A.41.1: $\tau \to \mu K_s^0$

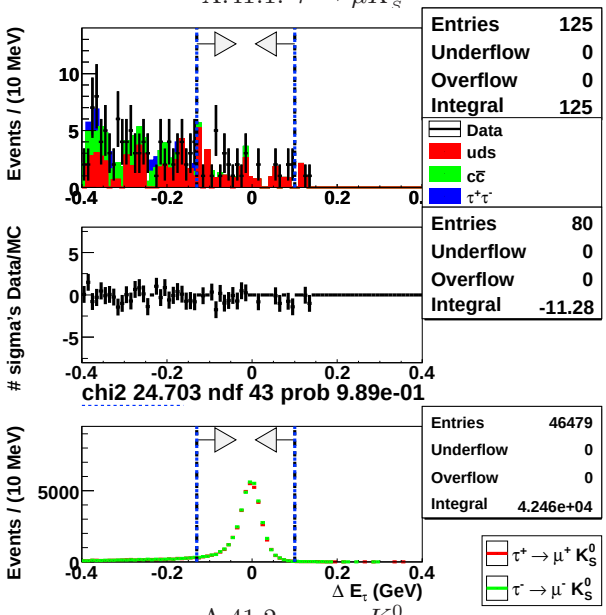

A.41.2: $\tau \to \mu K_S^0$

Figure A.41: Distributions of ΔM_τ and ΔE_τ after the tight selection for $\tau \to eK_S^0$. In each sub-figure, in the upper plot data sample is represented by black dots, while the background MC one as filled histograms. In the middle plot the difference between data MC divided by the error is shown. Signal MC samples are shown in the lower plot.

Bibliography

[1] Y. Fukuda et al. Evidence for oscillation of atmospheric neutrinos. *Phys. Rev. Lett.*, 81:1562–1567, 1998, hep-ex/9807003.

[2] Q. R. Ahmad et al. Direct evidence for neutrino flavor transformation from neutral-current interactions in the Sudbury Neutrino Observatory. *Phys. Rev. Lett.*, 89:011301, 2002, nucl-ex/0204008.

[3] *The MEG experiment at PSI*, 2007. Prepared for 12th International Workshop on Neutrinos Telescopes: Twenty Years after the Supernova 1987A Neutrino Bursts Discovery, Venice, Italy, 6-9 Mar 2007.

[4] Xuan-Yem Pham. Lepton flavor changing in neutrinoless τ decays. *Eur. Phys. J.*, C8:513–516, 1999, hep-ph/9810484.

[5] Y. Miyazaki et al. Search for lepton flavor violating τ-decays with a K_S^0 meson. *Phys. Lett.*, B639:159–164, 2006, hep-ex/0605025.

[6] M. Bona et al. SuperB: A High-Luminosity Asymmetric e^+e^- Super Flavor Factory. Conceptual Design Report, 2007, arXiv:0709.0451 [hep-ex].

[7] G. Rizzo et al. A novel monolithic active pixel detector in 0.13 μm triple well CMOS technology with pixel level analog processing. *Nucl. Instrum. Meth.*, A565:195–201, 2006.

[8] M. Raidal et al. Flavour physics of leptons and dipole moments, 2008, arXiv:0801.1826 [hep-ph].

[9] N. Arkani-Hamed, A. G. Cohen, E. Katz, and A. E. Nelson. The littlest Higgs. *JHEP*, 07:034, 2002, hep-ph/0206021.

[10] Monika Blanke, Andrzej J. Buras, Bjoern Duling, Anton Poschenrieder, and Cecilia Tarantino. Charged Lepton Flavour Violation and $(g-2)_\mu$ in the Littlest Higgs Model with T-Parity: a clear Distinction from Supersymmetry. *JHEP*, 05:013, 2007, hep-ph/0702136.

[11] J. A. Casas and A. Ibarra. Oscillating neutrinos and $\mu \to e\gamma$. *Nucl. Phys.*, B618:171–204, 2001, hep-ph/0103065.

[12] John R. Ellis and Martti Raidal. Leptogenesis and the violation of lepton number and CP at low energies. *Nucl. Phys.*, B643:229–246, 2002, hep-ph/0206174.

[13] M. Maltoni, T. Schwetz, M. A. Tortola, and J. W. F. Valle. Status of three-neutrino oscillations after the SNO-salt data. *Phys. Rev.*, D68:113010, 2003, hep-ph/0309130.

[14] S. Eidelman et al. Review of particle physics. *Phys. Lett.*, B592:1, 2004.

[15] B. Aubert et al. Search for lepton flavor violation in the decay $\tau \to \mu\gamma$. *Phys. Rev. Lett.*, 95:041802, 2005, hep-ex/0502032.

[16] Anna Rossi. Supersymmetric seesaw without singlet neutrinos: Neutrino masses and lepton-flavour violation. *Phys. Rev.*, D66:075003, 2002, hep-ph/0207006.

[17] F. R. Joaquim and Anna Rossi. Phenomenology of the triplet seesaw mechanism with gauge and Yukawa mediation of SUSY breaking. *Nucl. Phys.*, B765:71–117, 2007, hep-ph/0607298.

[18] R. Barbier et al. R-parity violating supersymmetry. *Phys. Rept.*, 420:1–202, 2005, hep-ph/0406039.

[19] K. S. Babu and Christopher Kolda. Higgs-mediated $\tau \to 3\mu$ in the supersymmetric seesaw model. *Phys. Rev. Lett.*, 89:241802, 2002, hep-ph/0206310.

[20] Athanasios Dedes, John R. Ellis, and Martti Raidal. Higgs mediated $B^0_{s,d} \to \mu\tau, e\tau$ and $\tau \to 3\mu, e\mu\mu$ decays in supersymmetric seesaw models. *Phys. Lett.*, B549:159–169, 2002, hep-ph/0209207.

[21] Andrea Brignole and Anna Rossi. Anatomy and phenomenology of mu tau lepton flavour violation in the MSSM. *Nucl. Phys.*, B701:3–53, 2004, hep-ph/0404211.

[22] Paride Paradisi. Higgs-mediated $\tau \to \mu$ and $\tau \to e$ transitions in II Higgs doublet model and supersymmetry. *JHEP*, 02:050, 2006, hep-ph/0508054.

[23] Paride Paradisi. Higgs-mediated $e \to \mu$ transitions in II Higgs doublet model and supersymmetry. *JHEP*, 08:047, 2006, hep-ph/0601100.

[24] A. Ilakovac. Lepton flavor violation in the standard model extended by heavy singlet dirac neutrinos. *Phys. Rev.*, D62:036010, 2000, hep-ph/9910213.

[25] Enrico Nardi, Esteban Roulet, and Daniele Tommasini. Limits on neutrino mixing with new heavy particles. *Phys. Lett.*, B327:319–326, 1994, hep-ph/9402224.

[26] Jyoti Prasad Saha and Anirban Kundu. Constraints on R-parity violating supersymmetry from leptonic and semileptonic τ, B_d and B_s decays. *Phys. Rev.*, D66:054021, 2002, hep-ph/0205046.

[27] Robert D. Cousins and Virgil L. Highland. Incorporating systematic uncertainties into an upper limit. *Nucl. Instrum. Meth.*, A320:331–335, 1992.

[28] K. Hayasaka et al. New search for $\tau \to \mu\gamma$ and $\tau \to e\gamma$ decays at Belle. *Phys. Lett.*, B666:16–22, 2008, 0705.0650.

[29] B. Aubert et al. Search for lepton flavor violation in the decay $\tau^{\pm} \to e^{\pm}\gamma$. *Phys. Rev. Lett.*, 96:041801, 2006, hep-ex/0508012.

[30] Y. Miyazaki et al. Search for Lepton Flavor Violating tau Decays into Three Leptons. *Phys. Lett.*, B660:154–160, 2008, 0711.2189.

[31] B. Aubert et al. Improved Limits on the Lepton-Flavor Violating Decays $\tau^- \to l^- l^+ l^-$. *Phys. Rev. Lett.*, 99:251803, 2007, 0708.3650.

[32] Y. Miyazaki et al. Search for lepton flavor violating τ^- decays into $l^-\eta, l^-\eta', l^-\pi^0$. *Phys. Lett.*, B648:341–350, 2007, hep-ex/0703009.

[33] B. Aubert et al. Search for lepton flavor violating decays $\tau^{\pm} \to l^{\pm}\pi^0, l^{\pm}\eta, l^{\pm}\eta'$. *Phys. Rev. Lett.*, 98:061803, 2007, hep-ex/0610067.

[34] Y. Miyazaki et al. Search for Lepton Flavor Violating τ Decays at Belle. *Tau08*, 2008. Prepared for 10th Internation workshop on τ Lepton Phyics, Novosibirsk, Russia, 22-25 Sep 2008.

[35] B. Aubert et al. Search for lepton-flavor and lepton-number violation in the decay $\tau^- \to \ell^{\mp} h^{\pm} h'^{\pm}$. *Phys. Rev. Lett.*, 95:191801, 2005, hep-ex/0506066.

[36] M. Roney et al. Search for LFV Decays $\tau \to l K^0_S$ and $\tau \to l(\rho^0, K^{*0}, \overline{K}^{*0}, \phi)$. *Tau08*, 2008. Prepared for 10th International workshop on τ Lepton Physics, Novosibirsk, Russia, 22-25 Sep 2008.

[37] Y. Nishio et al. Search for lepton-flavor-violating $\tau \to \ell V^0$ decays at Belle. *Phys. Lett.*, B664:35–40, 2008, 0801.2475.

[38] S. Brandt, C. Peyrou, R. Sosnowski, and A. Wroblewski. The principal axis of jets. An attempt to analyze high-collisions as two-body processes. *Phys. Lett.*, 12:57–61, 1964.

[39] W. M. Yao et al. Review of Particle Physics. *J. Phys.*, G33:1–1232, 2006.

[40] Thomas Junk. Confidence level computation for combining searches with small statistics. *Nucl. Instrum. Meth.*, A434:435–443, 1999, hep-ex/9902006.

[41] Jan Conrad, O. Botner, A. Hallgren, and Carlos Perez de los Heros. Including systematic uncertainties in confidence interval construction for Poisson statistics. *Phys. Rev.*, D67:012002, 2003, hep-ex/0202013.

[42] Gary J. Feldman and Robert D. Cousins. A Unified approach to the classical statistical analysis of small signals. *Phys. Rev.*, D57:3873–3889, 1998, physics/9711021.

[43] B. Aubert et al. The *BABAR* detector. *Nucl. Instrum. Meth.*, A479:1–116, 2002, hep-ex/0105044.

[44] *PEP-II: An Asymmetric B Factory. Conceptual Design Report. June 1993*, 1993. SLAC-418, LBL-PUB-5379.

[45] Swagato Banerjee, Bolek Pietrzyk, J. Michael Roney, and Zbigniew Was. τ and μ pair production cross-sections in electron-positron annihilations at $\sqrt{s} = 10.58$ GeV. *Phys. Rev.*, D77:054012, 2008, 0706.3235.

[46] *Results and plans of the PEP-II B Factory*, 2004. Presented at 9th European Particle Accelerator Conference (EPAC 2004), Lucerne, Switzerland, 5-9 Jul 2004.

[47] C. Bozzi et al. The *BABAR* silicon vertex tracker. *Nucl. Instrum. Meth.*, A435:25–33, 1999.

[48] V. Re et al. Status and future plans of the *BABAR* silicon vertex tracker. *Nucl. Instrum. Meth.*, A511:1–5, 2003.

[49] V. Re et al. Performance of the *BABAR* silicon vertex tracker. *Nucl. Instrum. Meth.*, A501:14–21, 2003.

[50] G. Sciolla et al. The *BABAR* drift chamber. *Nucl. Instrum. Meth.*, A419:310–314, 1998.

[51] Michael H. Kelsey. Performance and aging of the *BABAR* drift chamber. *Nucl. Instrum. Meth.*, A535:206–211, 2004.

[52] I. Adam et al. Dirc, the internally reflecting ring imaging Čerenkov detector for *BABAR*. *IEEE Trans. Nucl. Sci.*, 45:657–664, 1998, hep-ex/9712001.

[53] *Operation of the Čerenkov detector DIRC of BABAR at high luminosity*, 2000. Talk given at IEEE Nuclear Science Symposium and Medical Imaging Conference, Lyon, France, 15-20 Oct 2000.

[54] B. Lewandowski. The *BABAR* electromagnetic calorimeter. *Nucl. Instrum. Meth.*, A494:303–307, 2002.

[55] F. Anulli et al. The muon and neutral hadron detector for *BABAR*. *Nucl. Instrum. Meth.*, A409:542–546, 1998.

[56] W. Menges. The *BABAR* muon system upgrade. *IEEE Nucl. Sci. Symp. Conf. Rec.*, 5:1470–1474, 2006, physics/0609039.

[57] G. Battistoni, E. Iarocci, M. M. Massai, G. Nicoletti, and L. Trasatti. Operation Of Limited Streamer Tubes. *Nucl. Instr. Meth.*, 164:57, 1979.

[58] Pierre Billoir. Track Fitting With Multiple Scattering: A New Method. *Nucl. Instrum. Meth.*, A225:352–366, 1984.

[59] Thorsten Brandt. Likelihood-based Electron Identification. *BABAR* Analysis Document 396, 2002.

[60] I. Narsky. StatPatternRecognition: A C++ Package for Statistical Analysis of High Energy Physics Data, 2005, physics/0507143.

[61] Wouter D. Hulsbergen. Decay chain fitting with a Kalman filter. *Nucl. Instrum. Meth. A*, 552:566–575, 2005, physics/0503191.

[62] S. Jadach, B. F. L. Ward, and Z. Was. The precision Monte Carlo event generator KK for two- fermion final states in e^+e^- collisions. *Comput. Phys. Commun.*, 130:260–325, 2000, hep-ph/9912214.

[63] B. F. L. Ward, S. Jadach, and Z. Was. Precision calculation for $e^+e^- \to 2f$: The K K MC project. *Nucl. Phys. Proc. Suppl.*, 116:73–77, 2003, hep-ph/0211132.

[64] S. Jadach, Z. Was, R. Decker, and Johann H. Kuhn. The τ decay library TAUOLA: Version 2.4. *Comput. Phys. Commun.*, 76:361–380, 1993.

[65] Elisabetta Barberio and Zbigniew Was. PHOTOS: A Universal Monte Carlo for QED radiative corrections. Version 2.0. *Comput. Phys. Commun.*, 79:291–308, 1994.

[66] D. J. Lange. The EvtGen particle decay simulation package. *Nucl. Instrum. Meth.*, A462:152–155, 2001.

[67] Torbjorn Sjostrand, Stephen Mrenna, and Peter Skands. PYTHIA 6.4 physics and manual. *JHEP*, 05:026, 2006, hep-ph/0603175.

[68] P. Golonka et al. The tauola-photos-F environment for the TAUOLA and PHOTOS packages, release II. *Comput. Phys. Commun.*, 174:818–835, 2006, hep-ph/0312240.

[69] S. Agostinelli et al. GEANT4: A simulation toolkit. *Nucl. Instrum. Meth.*, A506:250–303, 2003.

[70] *Workshop on confidence limits, CERN, Geneva, Switzerland, 17-18 Jan 2000: Proceedings*, 2000. CERN-2000-005.

[71] Alexander L. Read. Presentation of search results: The CL(s) technique. *J. Phys.*, G28:2693–2704, 2002.

[72] Gunter Zech. Upper Limits in Experiments with Background Or Measurement Errors. *Nucl. Instrum. Meth.*, A277:608, 1989.

[73] Geoffrey C. Fox and Stephen Wolfram. Event Shapes in e^+e^- Annihilation. *Nucl. Phys.*, B149:413, 1979.

Acknowledgements

This thesis summarizes my work from the last five years. This work would not have been possible without the help of many people. A lot of support came from the people that worked with directly, but also from people I met during those years and with which I shared my life.

At first, I must thank my advisor, Prof. Francesco Forti, who gave me the opportunity to do this work, to join the *BABAR* Pisa group, to spend more than two years at SLAC and to work on new silicon detectors. He should be also credited with helping improve my skills not only as a physicist, but even in the everyday working life. Through him, I was introduced to the people of *BABAR* group in Pisa. Many of these are now good friends of mine, but I would like to thank everyone for their kind support and advices.

Then I have to thank all the people from the *BABAR* Collaboration and especially from Tau/QED analysis working group. A special mention is for Prof. Roberto Contri who provided a fundamental contribution for this work. Another mention is for all the people who reviewed this work, from the first stages until the final steps before publication and also the people who acted as referees for this thesis. The last mention is for the people working for INFN-Pisa and SLAC administration: their support was always essential.

Regarding the people I have met during those years from around the world, not directly involved in this work, the list is really too long to be written down. I can barely remember all the names, all the places, all the days and the nights we spent together. I would say only that everyone I met along the way, they are going to change me, either for good or bad, but their legacy is what I am right now. I hope to meet them again sometime to say thanks.